STRUCTURE AND GAS ADSORPTION BEHAVIOUR

OF

SPECTRALLY SELECTIVE FILMS

by

Paul J. Pigram

A thesis submitted in fulfilment
of the requirements for the degree of
Doctor of Philosophy

School of Physics
University of Sydney
Sydney Australia

October 1991

The University of Sydney

Copyright in relation to this Thesis

Under the Copyright Act 1968 (several provision of which are referred to below), this material must be used only under the normal conditions of scholarly fair dealing for the purposes of research, criticism or review. In particular no results or conclusions should be extracted from it, nor should it be copied or closely parahrased in whole or in part without the written consent of the author. Proper written acknowledgement should be made for any assistance obtained from this material.

Under Section 35 (2) of the Copyright Act 1968 'the author of a literary, dramatic, musical or artistic work is the owner of any copyright subsisting in the work'. By virtue of Section 32 (1) copyright 'subsists in an original literary, dramatic, musical or artistic work that is unpublished' land of which the author was an Australian citizen, an Australian protected person or a person resident in Australia.

The Act, by Section 36 (1) provides : 'Subject to this Act, the copyright in a literary, dramatic, musical or artistic work is infringed by a person who, not being the owner of the copyright and without the licence of the owner of the copyright, does in Australia, or authorises the doing in Australia of, any act comprised in the copyright'.

Section 31 (1) (a) (i) provides that copyright includes the exclusive right to 'reproduce the work in a material form'. Thus, copyright is infringed by a person who, not being the owner of the copyright, reproduces or authorises the reproduction of a work, or of more than a reasonable part of the work, in a material form, unless the reproduction is a 'fair dealing' with the work 'for the purpose of research or study' as further defined in Sections 40 and 41 of the Act.

Section 51 (2) provides that "Where a manuscript, or a copy, of material of other similar literary work that has not been published is kept in a library of a university or other similar institution or in an archives, the copyright in the material or other work is not infringed by the making of a copy of the material or other work by or on behalf of the officer in charge of the library or archives if the copy is supplied to a person who satisfies an authorized officer of the library or archives that he requires the copy for the purpose of research or study'.

* Thesis' includes ' treatise', ' dissertation' and other similar productions.

ABSTRACT

An understanding of the physical mechanisms underlying the operation of temperature limited solar thermal collectors has been developed in this study. A number of interrelated problems concerning the behaviour of spectrally selective stainless steel/carbon cermet films are addressed. These include the affect of annealing on film composition and structure; the relationship between film morphology and gas adsorption; and the energetic characteristics of the adsorption process.

Evacuated tubular solar thermal collectors are constructed like a dewar flask. They consist of two concentric glass tubes, sealed at both ends, with a vacuum in the intervening, annular space. A spectrally selective film is deposited on the outer surface of the inner glass tube. The film consists of a graded stainless steel/carbon cermet layer, a copper layer and an adhesion promoting layer. In non - concentrated sunlight these collectors can reach a maximum temperature of approximately 570K if no heat is removed from the inner tubes.

For domestic applications, it is desirable to limit the temperature of the collector to less than 350K without substantially degrading the efficiency at lower temperatures. A gas adsorption/desorption temperature limitation mechanism has been proposed and demonstrated. A small amount of a condensable gas is incorporated into the collector vacuum space during manufacture. At temperatures less than 350K, the gas adsorbs on the spectrally selective film, leaving the level of vacuum unaffected. When the collector temperature rises above a threshold temperature, desorption occurs which degrades the vacuum, providing a conductive heat loss path.

It is shown that the surface of the graded outer layer of the spectrally selective film is composed of carbon, with oxygen, argon and nitrogen contaminants. Carbon and oxygen are both present in a number of bonding configurations in as - prepared film surfaces. Annealing significantly reduces the level of surface contamination.

It is shown that the depth dependence of composition of the spectrally selective film changes in response to thermal annealing. Factors such as the composition of the substrate material and the thickness of the constituent layers have a significant effect on the magnitude of the changes observed.

Adsorption studies of the spectrally selective film were undertaken in clean and controlled ultrahigh vacuum conditions. Gas desorption has been studied using thermal desorption spectroscopy. It is shown that benzene adsorption on the spectrally selective film is characterised by two adsorption processes. Estimations are made of the activation energies of each of the processes using Arrhenius plots. A comparison is made with complementary data obtained previously from adsorption isotherms. A simple, single pore gas adsorption model has been developed and used to estimate pore sizes and activation energies. Changes in benzene desorption behaviour with changes in film thickness are also discussed.

The gas adsorption behaviour of amorphous carbon films has also been studied using a Kelvin probe. It is shown that benzene adsorption occurs predominantly in the bulk of the film rather than on the surface. Data are presented showing adsorption of gases such as oxygen and nitrogen. Proposals for adsorption mechanisms are also included.

Thermal desorption spectroscopy and the Kelvin method of measuring work function behaviour are sensitive to very small changes in adsorption. In addition, surface and bulk adsorption effects can be studied independently using these techniques in combination.

Acknowledgements

I wish to express my great appreciation to my family and friends for their understanding and encouragement throughout my studies. Special thanks to Bel, John, Jen, Kate, Suze and Mark.

I wish to thank my supervisors, Professor R.E. Collins, Dr. R.N. Lamb and Dr. B.A. Pailthorpe for their advice and assistance during the research programme and thesis preparation period. Thanks also to Mr. Barry Wood for educating me in the art of surface analysis and Professor D.B. Hibbert for assistance with computer modelling.

I wish to thank all of the technical staff of the Department of Applied Physics for their professional approach to the construction of complicated equipment and their willing assistance during the research programme.

This work has been supported by:

His Royal Highness Prince Nawaf bin Abdul Aziz of the Kingdom of Saudi Arabia through the Science Foundation for Physics within the University of Sydney;

The Energy Research and Development Corporation (ERDC); and

The Australian Research Council (ARC).

Author's Contributions

Chapters 1 and 2 form an introduction and review of the current state of the subject matter. They are entirely the responsibility of the author. Chapters 3 and 4 detail investigations of film composition using several electron spectroscopies. The bulk of the experimental work was undertaken at the Brisbane Surface Analysis Facility, University of Queensland by the author. Technical assistance and advice was provided by Mr. Barry Wood. The experiments described in section 3.5.2 were undertaken at the Surface Science and Technology Centre, University of New South Wales by the author. Chapter 5 is primarily the work of the author with the exception of the computational analysis in section 5.7.1. This analysis was undertaken with the assistance of Professor D.B. Hibbert, University of New South Wales. Chapter 6 is primarily the work of the author. The Kelvin probe apparatus was designed in conjunction with Professor R.E. Collins. Chapter 7 is entirely the responsibility of the author

Professor R.E. Collins, Dr. R.N. Lamb and Dr. B.A. Pailthorpe (the project supervisors) freely discussed many aspects of the experimental work and the thesis manuscript with the author during the course of the research programme.

Author's Publications

The following papers have been submitted for publication at the time of submission of this thesis.

P.J. Pigram, R.N. Lamb, B.J. Wood and R.E. Collins, "Structure and Surface Composition of Graded Amorphous Carbon/Stainless Steel Cermet Films", *Applied Physics A* , 52, 145 (1991).

P.J. Pigram, R.N. Lamb, R.E. Collins and B.A. Pailthorpe, "Gas Adsorption Behaviour of Amorphous Carbon Films", submitted to *Journal of Vacuum Science and Technology A*, October 1991.

CONTENTS

Page

1. Introduction

1.1 Evacuated Tubular Collectors 1
1.2 Temperature Limitation in Evacuated Tubular Collectors 2
1.3 Aims of this Research Programme 4

2. Review of Structure and Gas Adsorption Behaviour of Amorphous Carbon and Graded Stainless Steel/Carbon Cermet Films

2.1 Introduction 7
2.2 Structure and Bonding in Amorphous Carbon Films 8
2.3 Methods of Film Preparation 11
2.4 Preparation of Amorphous Hydrogenated Carbon and Graded Stainless Steel/Carbon Cermet Films 14
2.4.1 Reactive D.C. Magnetron Sputtering 14
2.4.2 Deposition Apparatus 15
2.5 Microstructural Analysis 16
2.5.1 Macroscopic Properties 17
2.5.2 Electron Spectroscopies 17
2.5.3 Other Spectroscopies 19
2.6 Gas Adsorption Behaviour 20
2.6.1 Morphology and Microporosity 20
2.6.2 Physical Adsorption of Gases 22
2.6.3 Experimental Studies of Gas Adsorption 25
2.7 Summary 28

3. Structure and Surface Composition of Amorphous Carbon and Graded Stainless Steel/Carbon Cermet Films

3.1 Introduction 36

3.2 X-ray Photoelectron Spectroscopy 37

3.3 Film Preparation 40

3.4 Experimental Method 42

3.5 Semiquantitative Analysis of XPS Data 42

3.6 Results and Discussion 45

3.6.1 Surface Composition of Stainless Steel/Carbon Cermet Films 45

3.6.2 Surface Structure of Amorphous Carbon Films 48

3.7 Summary 51

4. Layer Composition and Depth Profile of Graded Stainless Steel/Carbon Cermet Films

4.1 Introduction 55

4.2 Auger Electron Spectroscopy 56

4.3 Experimental Method 57

4.4 Determination of Depth Profile and Film Thickness 58

4.5 Results and Discussion 60

4.5.1 Comparison of Spectrally Selective Films 60

4.5.2 Effect of Annealing Conditions on Optical Properties and Layer Profile 62

4.5.3 Interlayer Diffusion 64

4.6 Summary 65

5. Thermal Desorption Behaviour of Amorphous Carbon Films

5.1	Introduction	69
5.2	Thermal Desorption Spectroscopy	70
5.3	Ultrahigh Vacuum System	72
	5.3.1 Design and Construction	72
	5.3.2 Sample Mounting and Manipulation	73
	5.3.3 Gas Dosing Facilities	74
5.4	Design and Construction of Thermal Desorption System	75
	5.4.1 Design and Construction	75
	5.4.2 Data Acquisition and Testing	76
5.5	Experimental Method	76
5.6	Semiquantitative Analysis of TDS Data	78
	5.6.1 Arrhenius - Redhead Analysis	78
	5.6.2 Modelling Thermal Desorption Behaviour	82
5.7	Results and Discussion	88
	5.7.1 Determination of Activation Energies using Arrhenius Analysis	88
	5.7.2 Discussion of Desorption Modelling	91
	5.7.3 Discussion of Thermal Desorption Behaviour	92
5.8	Summary	96

6. Work Function Studies of Gas Adsorption Behaviour of Amorphous Carbon Films

6.1	Introduction	101
	6.1.1 Introduction	101
	6.1.2 Work Function	102
6.2	Methods of Measuring Work Function	103
	6.2.1 Absolute Methods	103
	6.2.2 Relative Methods	104
6.3	The Kelvin Method	106
	6.3.1 Implementations of the Kelvin Method	106
	6.3.2 Theoretical Description of the Kelvin Method	108

6.4 Design and Construction of Kelvin Probe 111
6.4.1 Guarded Electrode Design 111
6.4.2 Signal Detection and Data Acquisition 113
6.5 Optimising Kelvin Probe Performance 115
6.5.1 Shielding and Filtering 115
6.5.2 Setting Up the Kelvin Probe 118
6.5.3 Kelvin Probe Performance Tests 120
6.6 Experimental Method 122
6.7 Results and Discussion 124
6.7.1 Preliminary Adsorption Studies 124
6.7.2 Work Function Response of a-C:H films to Different Adsorptives 125
6.7.3 Comparison of Thermal Desorption and Work Function Results 129
6.8 Summary 131

7. Conclusions 136

CHAPTER 1

Introduction

1.1 Evacuated Tubular Collectors

Solar thermal collectors are used to generate heat from sunlight. Many different collector designs have been developed, differing in construction, application and efficiency. All collectors, however, are designed to maximise collection of solar radiation and the efficiency with which thermal energy is removed from the collector. Collector design also seeks to minimise the rate of energy loss to the surroundings as the collector temperature exceeds the environmental temperature. The energy loss mechanisms are radiation, conduction and convection.

The energy distribution in the solar spectrum is peaked in the visible region whilst energy losses due to thermal radiation occur at wavelengths in the infra - red. Spectrally selective films which have a high absorptance in the visible region and a low emittance in the near infrared region are used to coat the absorbing surface of collectors. Energy capture is maximised while radiative losses are minimised. Losses due to conduction and convection are reduced using glass cover plates and convection barriers in flat plate collectors. In evacuated tubular collectors, the absorbing surface is encapsulated in a vacuum envelope.

All-glass evacuated tubular collectors (ETCs) are constructed like a dewar flask, as shown in figure 1.1(a). The collectors developed at the University of Sydney consist of two concentric borosilicate glass tubes with a vacuum ($< 10^{-3}$ torr) in the intervening space. A spectrally selective, high absorptance, low emittance film is deposited onto the outer, vacuum side of the inner glass tube using reactive d.c. magnetron sputtering, as discussed in Chapter 2.

The spectrally selective film is baked (770K, 60 minutes) under vacuum before final sealing of the ETC. Degassing by heating is necessary to maintain a sufficiently high vacuum in the ETC to ensure efficient operation over its lifetime (~ 20 years). Such heating, however, has also been shown to affect the structure and

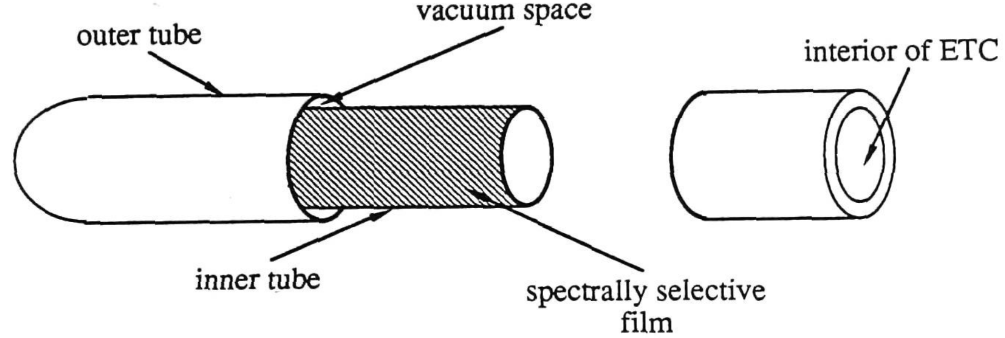

Figure 1.1(a) Schematic diagram of an evacuated tubular collector

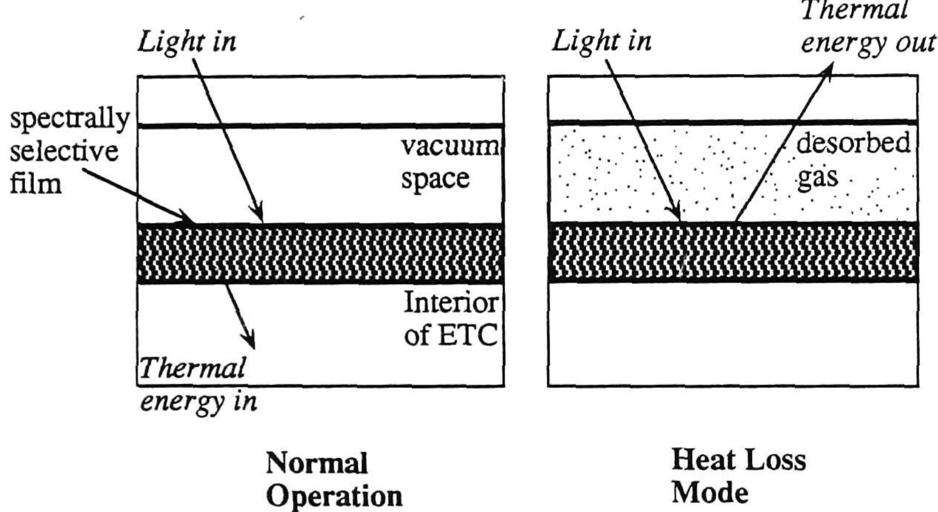

Figure 1.1(b) Schematic description of the principal features of the temperature limitation mechanism

performance of the spectrally selective film [1-3]. Continued thermal cycling of films deposited on certain metal substrates leads to changes in structure and the eventual breakdown of film adhesion and cohesion [4]. A barium - aluminium getter is evaporated inside the collector vacuum space after sealing to assist in maintaining satisfactory vacuum levels in commercially produced ETCs.

ETCs employing the design developed at the University of Sydney have been manufactured commercially by Nitto Kohki Corporation and Shiroki Corporation in Japan and by Rheem Australia Pty Ltd, in Australia. Examples of ETC dimensions are:

	Shiroki	Rheem
Length:	1400mm	1750mm
Inner tube diameter:	30mm	44mm
Outer tube diameter:	38mm	50mm

In typical applications, ETCs are used to heat water, oils and other liquids. The hot liquid or vapour is then used directly to supply heat or passed through a heat exchanger. ETCs are most commonly used to heat water for use in domestic (< 350K) and medium temperature (~ 570K) applications. Heating applications include hot water services, space heating, steam cookers and hot plates and sterilisation. Other possible applications include refrigeration, electricity generation and conversion to mechanical energy.

1.2 Temperature Limitation in Evacuated Tubular Collectors

Domestic solar water heating systems are designed to maximise energy collection under a range of weather conditions. An objective of this optimisation is to provide a useful energy output under reduced ambient light conditions. The ETCs described above can reach temperatures as high as 570K when no energy is removed from the device. This condition is referred to as collector stagnation; the rate of energy collection equals the rate of energy loss by radiation.

In domestic water heating applications it is desirable to limit ETC stagnation temperature to a range of 350 - 420K using a temperature limitation mechanism. Higher temperatures lead to accelerated degradation of the water heating system and excess pressures. A significant safety hazard is created if steam is formed in a system designed to operate at atmospheric pressure [5]. Over - temperature protection is generally costly, has adverse reliability implications and can significantly reduce the low temperature efficiency of the system. The essential features of any temperature limitation mechanism for ETCs are:

(i) reduction of ETC stagnation temperature to 350 - 420K;
(ii) preservation of low temperature operating efficiency;
(iii) low cost; and
(iv) simple and reliable operation.

It has been proposed and demonstrated [6-8] that a gas adsorption/desorption switching mechanism can be incorporated into the vacuum space of ETCs. At temperatures less than 350K, the gas is adsorbed on the spectrally selective film, resulting in a high level of vacuum. When the ETC temperature rises above a threshold temperature, desorption degrades the vacuum, providing a conductive heat loss path to the surroundings [7]. A typical temperature limited ETC operates over a pressure range of ~ 10^{-4} torr to ~ 10^{-1} torr. The temperature limitation mechanism is shown in figure 1.1(b). The optimal thermal switch requires desorption to be strongly dependent on temperature and to occur over a narrow temperature range in the vicinity of 350K. The implementation and optimisation of a thermal switching mechanism requires an understanding the relationship between adsorption processes and film structure and morphology.

A range of gases, principally organic vapours, have been investigated for suitable adsorption behaviour [5, 7-9]. Benzene appears to be most appropriate for the application and therefore has been the focus of this research programme. A number of temperature limited ETCs have been constructed [9] which show non - linear, conductive heat losses as the collector temperature increases. Maximising the rate at which the desorption increases with temperature is an ongoing concern. Limiting factors include the intrinsic statistical thermodynamics of the adsorption/desorption process, impurities in the desorbable gas and long - term changes in film structure.

1.3 Aims of this Research Programme

The aim of this research programme was to investigate the structure and gas adsorption behaviour of the spectrally selective films incorporated in ETCs. A number of interrelated aspects concerning the behaviour of the stainless steel/carbon cermet film are addressed. These include the effect of annealing on film composition and structure; the relationship between film morphology and gas adsorption; and the energetic characteristics of the adsorption process. The thermal switch mechanism is dependent on adsorption behaviour and the way in which adsorption is affected by changes in film composition, thickness and film annealing. This study seeks to increase the understanding of the processes underlying the temperature limitation mechanism.

Chapter 2 provides an introduction to the fabrication, analysis and behaviour of amorphous carbon and graded stainless steel/carbon cermet films. The methods used to fabricate the films used in this study are described. They are identical to those used in previous work undertaken in this laboratory and are representative of a class of deposition techniques. Film morphology and porosity are also discussed in the context of gas adsorption and the thermal switch. An outline of the theoretical aspects of gas adsorption is presented, along with examples of previous adsorption studies.

Chapter 3 presents the experimental data for X - ray photoelectron studies of the surface composition of the spectrally selective films. Differences in the surface structure of amorphous carbon films produced using different deposition techniques are also experimentally investigated and discussed.

Chapter 4 presents the experimental data for Auger electron spectroscopy studies of the layer profile of the spectrally selective films. Changes in layer profile, observed in response to heat treatment, have important implications for the optical performance and life expectancy of this type of ETC. The layer profile of the spectrally selective film has been optimised to provide satisfactory optical behaviour. Changes in film structure resulting from annealing and ageing have been investigated with an emphasis on coincident changes in the optical properties. The choice of substrate material is shown to be a key factor in the subsequent thermal degradation of the film. Diffusion of film components is also discussed with reference to interlayer adhesion and film stability.

Structure, morphology and annealing dominate gas adsorption behaviour [9]. A principal motivation for this study was to seek experimental evidence that the dominant adsorption mechanism occurs wthin the bulk of the film rather than on the surface. Previous adsorption studies [9,10] of these amorphous carbon and graded stainless steel/carbon cermet films have employed techniques commonly used in the characterisation of bulk adsorbent materials such as molecular sieves. These techniques measure absolute adsorption as a function of gas pressure over the surface, expressing the results as an adsorption isotherm, and can not differentiate between a single adsorption process and a number of simultaneous processes. The spectroscopic adsorption studies discussed in this thesis complement the adsorption isotherms previously obtained. The experimental methods and the clean and controlled ultrahigh vacuum conditions used are, however, significantly different.

The design and construction of an ultrahigh vacuum system and thermal desorption apparatus are discussed in Chapter 5. The benzene desorption behaviour of amorphous carbon films is discussed along with the semiquantitative analytical techniques employed in thermal desorption studies. The design and construction of a Kelvin probe and the associated instrumentation is described in Chapter 6. A detailed optimisation was undertaken and an assessment made of resulting instrument performance. The Kelvin probe has been used to study the gas adsorption behaviour of amorphous carbon films. Data are presented showing adsorption of benzene, oxygen and nitrogen along with proposals for adsorption mechanisms.

Thermal desorption spectroscopy reveals the activation energies of individual binding states. The Kelvin probe detects changes resulting from surface adsorption processes, thereby distinguishing such effects from adsorption processes occurring exclusively in the pore space of the film. Thermal desorption spectroscopy and the Kelvin method of measuring variations in work function are sensitive to very small changes in adsorption. Surface and bulk adsorption effects can be studied independently using these techniques in combination.

References - Chapter 1

[1] G.L. Harding, S. Craig and B. Window, Appl. Surf. Sci., 11/12, 315 (1982).

[2] S.P. Chow and G.L. Harding, Sol. Energy Mater., 11, 123 (1984).

[3] G.L. Harding and B. Window, Sol. Energy Mater., 7, 101 (1982).

[4] P.J. Pigram, R.N. Lamb, B.J. Wood and R.E. Collins, Appl. Phys. A, 52, 145 (1991).

[5] S. O'Shea, D.N. Furlong, B.A. Pailthorpe and R.E. Collins, Adsorption Science and Technology, 4, 275 (1987).

[6] G.L. Harding and B. Window, Sol. Energy Mater., 4, 421 (1981).

[7] B.A. Pailthorpe, R.E Collins and S. O'Shea, Sol. Energy, 39, 73 (1987).

[8] B.A. Pailthorpe, R.E Collins and S. O'Shea, Aust. J. Phys., 40, 643 (1987).

[9] S. O'Shea, PhD thesis, Department of Applied Physics, University of Sydney, 1989.

[10] Y. Yin, R.E. Collins and B.A. Pailthorpe, J. Appl. Phys., submitted December 1990.

CHAPTER 2

Review of Structure and Gas Adsorption Behaviour of Amorphous Carbon and Graded Stainless Steel/Carbon Cermet Films

2.1 Introduction

Spectrally selective films are an integral part of efficient photothermal collector systems. A variety of spectrally selective films has been reported including black chrome [1], black copper [2], homogeneous and multi - layer metal/carbon cermets [3-6] and other composite films [7,8].

A multi - layer film has been optimised for spectral selectivity. The film consists of a graded stainless steel/carbon cermet layer (140nm), deposited over a low emittance copper base layer (300nm) and an adhesion layer (60nm), as seen in figure 2.1. The outer surface of the film consists of pure amorphous hydrogenated carbon (a-C:H). The selective films are deposited onto glass tubes by reactive and non - reactive d.c. magnetron sputtering [9], in batches of 20 - 50 tubes. The film is graded from metal rich at the copper film to carbon rich at the top surface. The film has an absorptance of $\approx$ 0.93 and an emittance of $<$ 0.04 at low temperatures [3,4,10-13].

The method of fabrication was selected over others for a number of reasons including suitability for industrial production and for tailoring film composition. Producing ETCs commercially requires large production runs, good quality control and relatively simple operation. The sputtering system devised for film production has been successfully scaled up in size from a single glass tube to 50 tubes. The method of fabrication and the sputtering system are described in more detail in section 2.4.

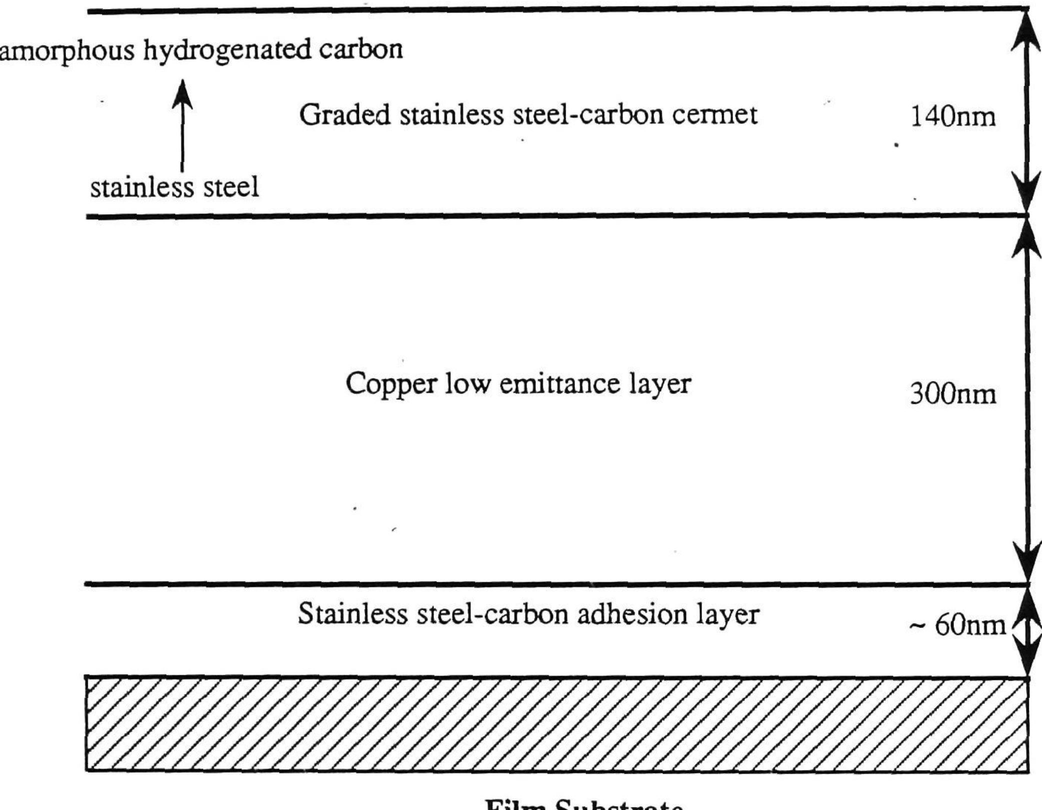

Figure 2.1 Schematic diagram of the layer profile of the spectrally selective film incorporated in solar collectors developed by the University of Sydney. The film comprises a graded stainless steel/carbon cermet layer, a copper base layer and an adhesion promoting layer.

One of the advantages of using materials in thin film form is that the physical properties of the film can be controlled and modified by the type of deposition and by varying process parameters during deposition. The complex layer structure of the spectrally selective film used in this study was produced during a single process using two cathodes and controlled gas dosing into the sputter zone of the coater.

The optical properties of the film are optimised by varying the elemental composition and adjusting the various layer thicknesses. The mechanical strength and interlayer adhesion must also be considered in this process. The provision of an adhesion promoting layer is an essential part of the deposition process. The interface between the copper low emittance layer and the borosilicate glass substrates is a potential source of adhesion failure in the multi - layer films. Adhesion is significantly improved by separating the two layers with a thin stainless steel/carbon layer [13].

This chapter discusses film properties and deposition processes. Relevant aspects of amorphous carbon film structure and behaviour are also considered. The relationship between film morphology and gas adsorption behaviour is discussed in the context of the proposed thermal switch mechanism and previous investigations of gas adsorption behaviour.

2.2. Structure and Bonding in Amorphous Carbon Films

Amorphous carbon (a-C) and amorphous hydrogenated carbon (a-C:H) films have been the subject of intensive research. Different methods of film fabrication give rise to films with a wide range of physical characteristics and lead to a variety of applications [14]. One form of amorphous carbon displays extreme hardness and high density, and is used as a transparent coating material [15], while amorphous hydrogenated carbons have potential applications in microelectronics as insulating films or as semiconducting films doped with Group III and Group V impurities [14]. These films are also used as solar spectrally selective absorbers [14] and as sensors [16].

The method of fabrication determines the composition and bonding and influences the physical properties of the film. Sputtered films are generally composed of amorphous hydrogenated carbon, while films formed using ion beam techniques can be tailored to produce harder and denser amorphous carbon films [17]. In order to understand better the nature of the various forms of amorphous carbon several structural models have been developed [14].

The diversity in the structure of carbon films arises from the different types of bonding behaviour of the carbon atom. This sets carbon apart from other Group IV elements such as silicon and germanium [18]. The approximate valence electron orbitals and bonding angles are shown in figure 2.2 [15]. The sp^3 bond configuration is characterised by tetrahedrally oriented σ bonds. This type of single bonding is found in saturated hydrocarbons and diamond. It is commonly referred to as tetrahedral or diamond structure [19]. In the sp^2 configuration, three valence electrons form planar trigonally directed σ bonds with neighbouring atoms. The remaining valence electron lies in a delocalised π bonding orbital which is normal to the σ bonding plane [15]. In ring structures, such as graphite, the σ bonds link neighbouring atoms in the same plane forming extensive sheets of material. These sheets are interlinked by much weaker Van der Waals interactions between adjacent planes [20]. Triple bonded materials contain sp^1 bonded carbon atoms. Two valence electrons form σ bonds, while the remaining electrons lie in π bonding orbitals in a plane normal to the σ bonds [15].

The structure of amorphous carbon is determined by two factors: the carbon bonding configuration and the hydrogen content of the film. Carbon bonding is confined to varying ratios of sp^3 and sp^2 bonding as there is little evidence for sp^1 bonding [15]. The ratio of sp^3/sp^2 bonding is often used as an indicator of the properties expected in a carbon film. Values of $sp^3/sp^2 \geq 5$ are found in diamond - like carbon (DLC) films whereas values ≤ 0.1 are found in graphitised films and glassy carbons. Mixtures of the two bonding configurations give amorphous carbon films with a variety of intermediate properties.

Glassy carbon and carbon fibres, while having markedly different overall structure, show quite similar bonding behaviour. Figures 2.3(a) and (b) show the structures proposed for the two materials [20]. Glassy carbon consists of narrow intertwined ribbons of graphite - like material about 30Å wide, defining pores with diameters of about 50 - 100Å. Progressive thermal annealing of the film up to around 3000K removes all local defects in the network leaving all the carbon atoms

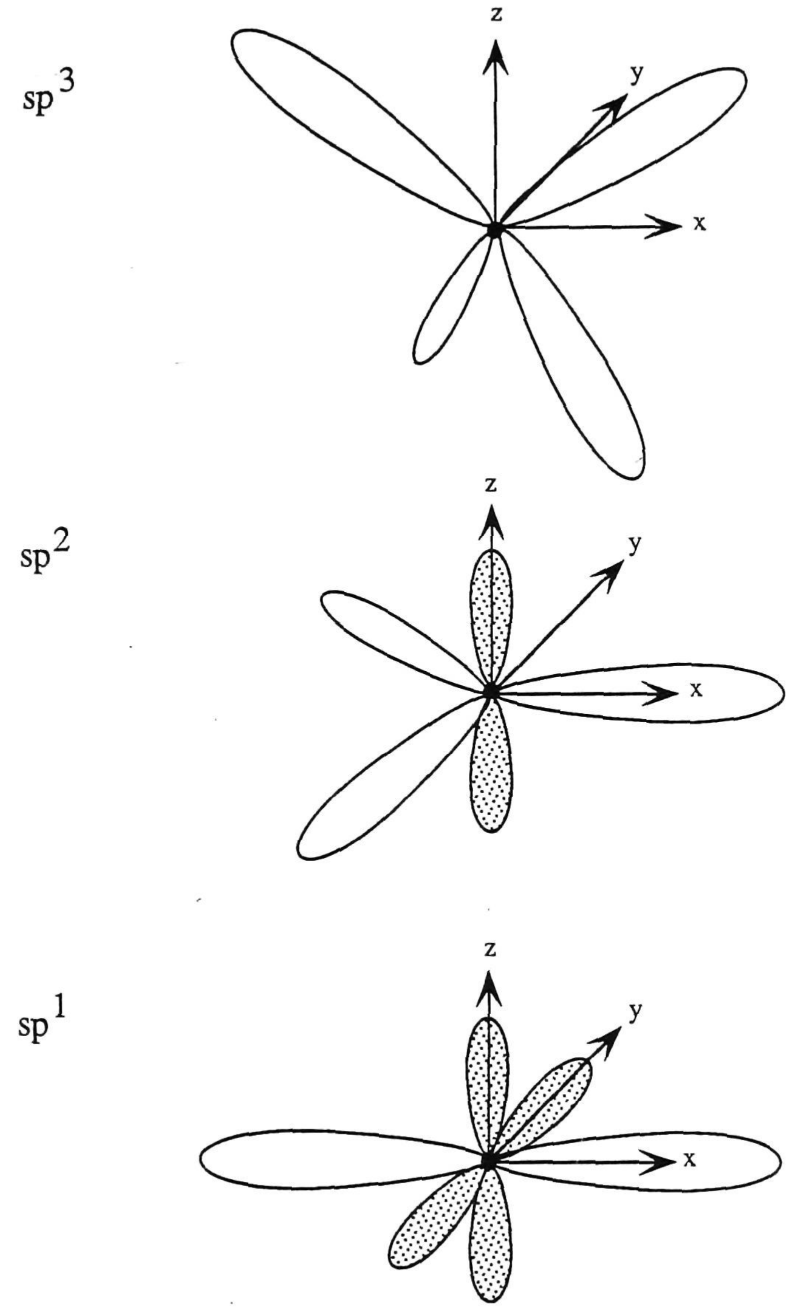

Figure 2.2 Schematic representation of sp^3, sp^2 and sp^1 hybridised atoms

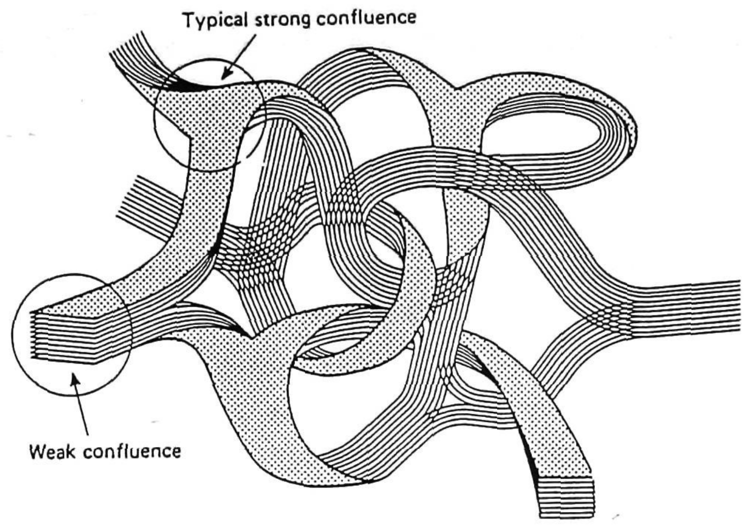

Figure 2.3(a) Schematic structural model for glassy carbon [reprinted from ref. 20]

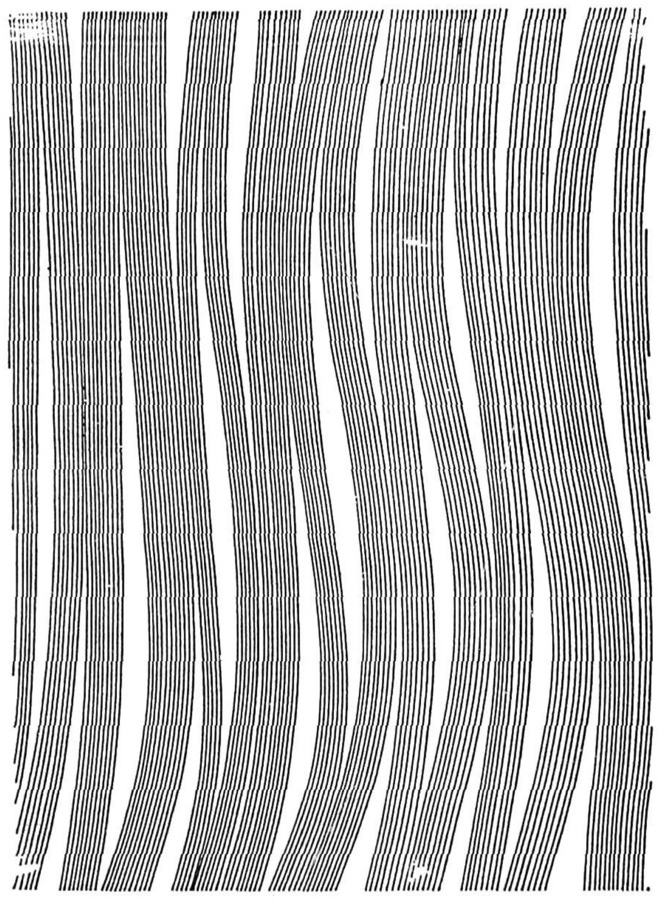

Figure 2.3(b) Schematic structural model for high modulus carbon fibres [reprinted from ref. 20]

in the sp^2 state [20]. Carbon fibres show very similar graphitic layering to the glassy carbons. The ribbons, however, are arranged in long, approximately parallel strips. Small angle X - ray scattering has shown that pores are defined in the structure with elongated dimensions of about 15Å x 300Å. Carbon fibres appear to be almost entirely composed of sp^2 bonded material and therefore the sp^3/sp^2 ratio for both glassy carbon and carbon fibres is < 0.1 [20].

Amorphous carbon can exist in a variety of different physical forms depending on the method of film preparation. Thermally evaporated amorphous carbon is similar in structure to glassy carbon, however, sp^2 bonded regions are linked with regions of sp^3 bonded material [18]. Amorphous carbon films made using vacuum arc techniques show quite different properties. Films produced using very low or very high ion energies are graphitic whereas films produced using intermediate ion energies are very hard and display predominantly sp^3 bonding [21].

Increases in hydrogen content of amorphous carbon films are generally reflected by increases in the proportion of sp^3 bonding in the film. During film growth hydrogen may be incorporated into the film to passivate "dangling" sp^3 carbon bonds. Random film growth often leads to bonding imperfections with graphitic regions being linked by regions of sp^3 bonded material or dangling sp^3 bonds. Consequences of hydrogen incorporation into the film are film stability and chemical neutrality. Much of this hydrogen may be subsequently driven out of the voided film structure during an annealing process. This compacts and further stabilises the film by eliminating imperfections left by the film formation process.

Carbon bonding and hydrogen content define short range order in amorphous carbon films; they do not entirely define its structure, however. There is definite medium range order over distances of about 10 Å in amorphous carbon films. Some amorphous carbon films are composed of clusters of warped graphitic layers. These clusters are joined by regions of sp^3 bonded material in which dangling bonds are passivated by the incorporation of hydrogen [15].

Thermal annealing is an integral part of many film formation processes, acting as a catalyst for structural changes during and after deposition. This process promotes long term stability, resistance to atmospheric attack and degassing of the film. Volatile contaminants are removed from micropores in the film bulk by the sustained application of heat in vacuum. This process energetically activates the micropores for gas adsorption in carbon absorbent materials and thermal switching

solar ETCs [16,22]. Gas adsorption studies of the a-C:H films used in this study have been carried out using a quartz crystal microbalance technique. The results strongly suggest that the dominant process in thermal degassing of these films is the removal of oxygen atoms in the form of CO and CO_2 [23]. Thermomanometric analysis of a-C:H films shows the evolution of CO and H_2 and lesser amounts of CO_2 and H_2O in response to heating [24,25]. There is no evidence of the evolution of CH_4, C_2H_6 or similar gases.

Annealing can also provide the activation energy for changes in bonding and structural rearrangement. This is a source of intrinsic stress relief within the film as atoms adopt lower energy bonding arrangements. A consequence of this behaviour is that film/substrate adhesion of a-C:H films is improved by moderate annealing [26].

2.3 Methods of Film Preparation

Methods of depositing carbon films have been developed in parallel with advances in the understanding of film structure and behaviour. Enhanced deposition rates and uniformity are required for many commercial applications of carbon film technology. Studies of the effects of deposition method on film properties have required a higher degree of control of deposition parameters. Sophisticated deposition techniques, such as mass selected ion beam deposition, have been developed to tailor film properties for specific applications.

Basic carbon processing methods involve modifying solid polymeric resins into chars, glassy carbons and fibres. Pyrolysis is one such technique where the precursors are carbonised, dehydrogenated and annealed by heating in an inert atmosphere to form a wide range of materials depending on the processing techniques and the precursor structure. Long chain polymers are transformed into complex intertwined networks of material in the form of fibres and films. For example, natural polymeric cellulose fibres are used as a precursor for carbon fibres and various polymeric hydrocarbon resins are used as precursors for glassy carbons [20].

Amorphous carbon films with a range of properties can be produced by evaporative deposition in vacuum. Heat is injected into the starting material with the film being deposited by evaporation onto a nearby substrate. Methods of heating include furnaces, passing high currents through carbon electrodes and bombarding a carbon target with an electron beam. These methods give some control over deposition parameters with vacuum deposition minimising hydrogen and oxygen contamination [18].

Advanced methods of carbon film production involve the modification of the starting material into neutral or ionised carbonaceous fragments or carbon atoms and the subsequent deposition of this material onto a substrate. Plasma and ion beam deposition are types of deposition in common use both individually and in combination. Plasma deposition can be used to produce a variety of carbon films from almost any hydrocarbon starting material. Commonly used materials include methane (CH_4), ethane (C_2H_6), ethylene (C_2H_4), acetylene (C_2H_2) and benzene (C_6H_6). A glow discharge is sustained in the hydrocarbon atmosphere using d.c., r.f., microwave or pulsed excitation. Hydrocarbons are ionised or dissociated in the glow space by electrons which are accelerated across the potential difference near the cathode [27]. These ions and atoms can then be condensed onto a nearby substrate to form a film. Film properties can be modified by substrate heating and biasing (positive and negative). Film structure can incorporate high proportions of hydrogen from the starting material.

Carbon films can also be produced by chemical vapour deposition (CVD). In this process, a hot filament and plasma decompose and dissociate the hydrocarbon starting materials into reactive fragments which are condensed to form a film [28,29]. Substrate heating, light absorption and range of other methods can also be used to activate the CVD process.

High energy electrons within a plasma can interact with, and modify a growing film [30]. In contrast, ion beam deposition (IBD) gives more control over deposition parameters than plasma deposition techniques. This is possible because the ion source and the film substrate are separated, with only the ion beam affecting film growth. In IBD, ions are formed remotely in an ion gun. An argon plasma is used to ionise CH_4 or to sputter a cathode - mounted carbon target. An ion beam is extracted from the gun and directed at the substrate using a series of accelerating grids [30,31]. Control of the ion energy and the ion beam composition gives the

ability to tailor film properties. Alternatively, ions produced in the plasma can be used to create an ion beam by sputtering a target outside the gun.

Magnetron sputtering (discussed in detail in section 2.4.1) and ion beam sputtering are examples of ion assisted deposition (IAD). IAD can be used to modify growing films. Low energy ion beams (< 40eV) will preferentially sputter substrate contaminants and assist the formation of adhesion promoting interfacial layers. Higher energy ions cause lattice motion increasing surface atom motion and diffusion. Other effects include preferential etching of unwanted film structures (such as graphitic regions in DLC) and structural damage [30]. Controlled microstructural changes can be made in growing films using IAD. Computer simulation of 2 - dimensional film growth indicates that columnar film structure, typical in many carbon films, can be disrupted by ion bombardment resulting in a denser film structure, as seen in figure 2.4 [32]. The source of bombarding ions can be from the starting material itself, the plasma or an independent ion gun directed at the substrate.

Further progress in controlling deposition parameters with IBD can be made by altering the ion beam downstream from the source. Electrostatic and magnetic filtering and mass selection techniques can be used to determine accurately the geometric, energetic and ionisation characteristics of the ion beam reaching the substrate. Film purity can be significantly improved by separating the ion source and substrate by a filtering line and depositing films under ultrahigh vacuum conditions [33]. This form of deposition is limited to beams of small cross - section and low deposition rates, and is therefore difficult to implement in commercial deposition applications.

Cathodic vacuum arcs are used as high current ion sources for filtered beam systems. This method produces very hard carbon films at high deposition rates with an ion beam free from macroparticles and neutrals [17,34]. The beam of carbon ions emanating from the arc is filtered by a curved magnetic solenoid, removing neutrals and leaving only singly and doubly ionised atoms which then condense onto a substrate to form a film [35]. It has been shown that this material is composed of almost pure sp^3 bonded carbon and is termed "amorphous diamond" or "diamond - like carbon", (DLC) [21,36].

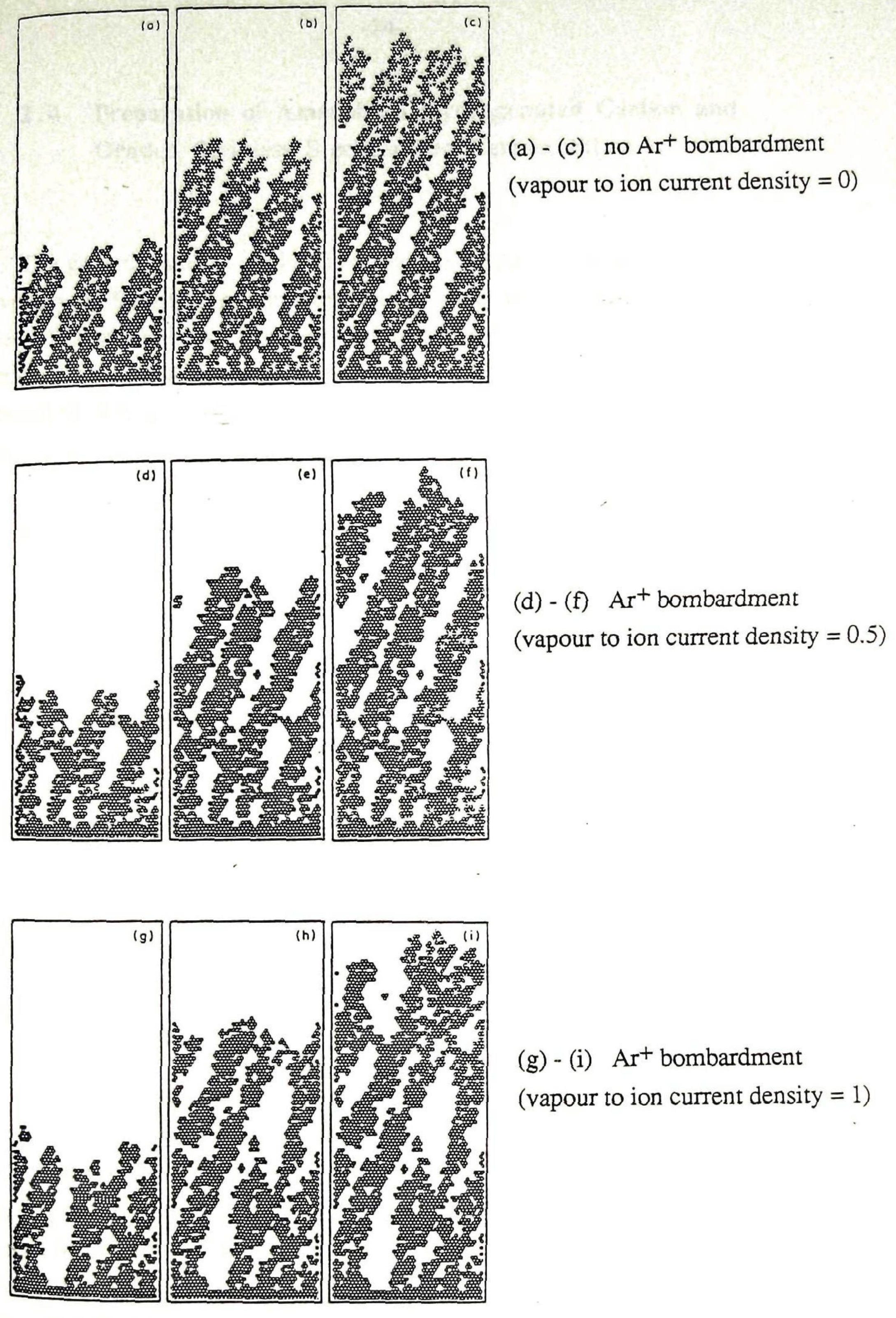

Figure 2.4 Computer simulation of 2 - dimensional film growth demonstrating the relationship between columnar structure and ion bombardment. The microstructure of a vapour deposited film with low adatom mobility is shown during three different stages of growth and argon ion bombardment.
[reprinted from ref. 32]

2.4 Preparation of Amorphous Hydrogenated Carbon and Graded Stainless Steel/Carbon Cermet Films

The graded stainless steel/carbon spectrally selective films developed at the University of Sydney are fabricated using a reactive d.c. magnetron sputtering process. The spectrally selective films used in this study were fabricated using this process in the original sputter coating apparatus. The following discussion of sputter deposition is included as a review of the fabrication methods used in this work and as an example of a widely used, industrially compatible fabrication method.

2.4.1 Reactive D.C. Magnetron Sputtering

High purity carbon films can be produced by sputtering a carbon cathode. A large number of particles (predominantly neutrals) are produced in this process and can be condensed to form a film on a nearby substrate. Sputtering describes a process in which energetic ions bombard a target (cathode) surface, dislodging material via a momentum transfer process. The energetic ions originate, in the case of magnetron sputtering, from a glow discharge around the cathode. The number of atoms dislodged per incident ion is referred to as the sputter yield and is a function of the target type and the energy of the incident ion (typically many hundreds of electron volts) [37].

Secondary electrons are emitted from the negatively biased cathode as a result of ion impact. These are accelerated away from the cathode through the cathode dark space and into the negative glow where they collide with gas atoms producing more ions. This process can sustain a glow discharge if the gas pressure and ionisation efficiency are sufficiently high. Ionisation efficiency can be increased if electrons are closely confined to the cathode using magnetic confinement [38]. Planar magnetron sputtering systems use an array of permanent magnets beneath the target for plasma confinement. Electron drift is confined to a series of loops, forming a ring or rings on the cathode depending on the arrangement of the magnets [38]. Cylindrical magnetron sputtering systems use analogous confinement techniques but with an axial field directed parallel to the cathode surface.

Reactive magnetron sputtering produces amorphous hydrogenated carbon films at significantly faster deposition rates than conventional sputtering [30]. Hydrocarbon reactive gases are injected into the plasma along with a sputtering gas (generally Ar) where they are decomposed and incorporated into the growing film. Other reactive gases in common use include oxygen and nitrogen which are used in the production of metal oxides and nitrides [39]. Reactive sputtering is a very versatile method of film deposition as it allows the simultaneous use of both solid and gaseous starting materials with good control over deposition parameters. The sputter deposition of metal oxide films, for example, is greatly simplified if a metal target and an Ar/O_2 sputter gas mixture is used in preference to a metal oxide target and Ar gas alone. The sputtering process can be further controlled by the interaction of the reactive gas with the cathode. When the flow of reactive gas into the sputter chamber exceeds a threshold value, the sputter rate of the cathode is greatly reduced or ceases, leaving the reactive gas as the primary source of ions. This is caused by two processes: an increase in cathode secondary emission coefficient causing a decrease in voltage; and the formation of compounds on the cathode surface. Surface compounds often have a significantly lower sputter yield than the cathode material itself [38].

2.4.2 Deposition Apparatus

Cylindrical magnetrons have two standard configurations (see figure 2.5): cylindrical - post cathode and cylindrical - hollow cathode. The batch coater used to fabricate films for the experiments discussed in this thesis is a dual cathode, cylindrical - post cathode magnetron and has a form similar to that shown in figure 2.5(c). The advantages of magnetron sputtering over other forms of deposition such as evaporation or ion beam techniques include good film uniformity over lengths of 2m, ease of fabrication of long - life cathodes from commercially available metals, the ability to form composite materials via the introduction of reactive gases and good control of operating parameters and hence film characteristics including thickness and microstructure [13].

The batch coating system is fully described in references [13] and [40]. Sectional views of the system are shown in figure 2.6. Twenty, 1.5m long glass tubes can be coated simultaneously with multi - layer films or pure a-C:H. The tubes rest on rotating posts which move around the perimeter of the chamber. This enhances film uniformity. The sample substrates are fixed to the posts during deposition. Two 2m long cathodes are placed axially in the chamber, separated by a

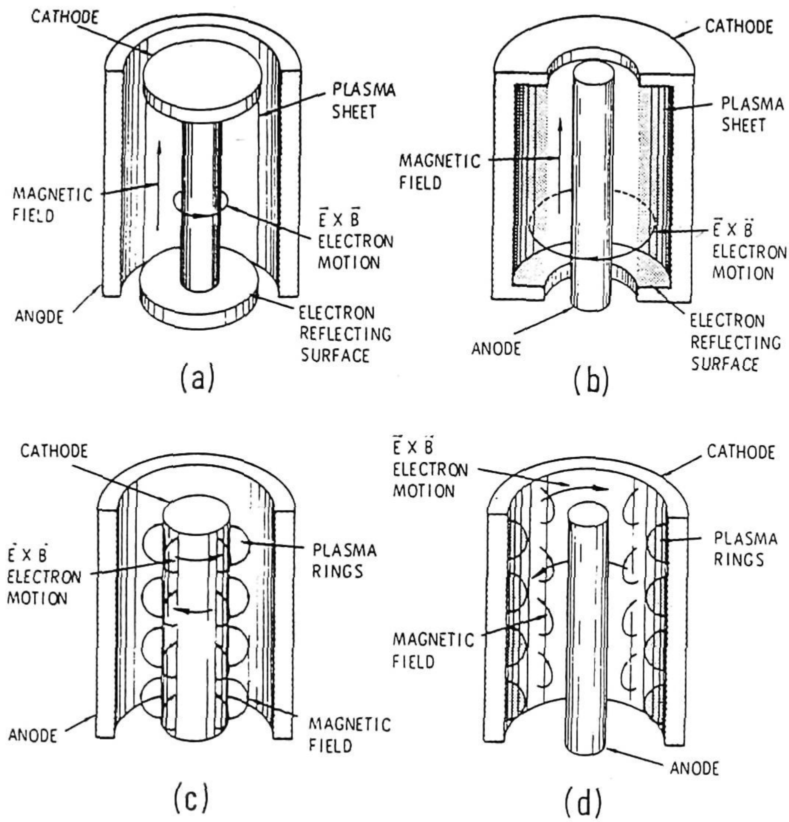

Figure 2.5 The configuration of various cylindrical magnetron sputtering sources:

(a) cylindrical - post magnetron with electron reflecting wings

(b) cyindrical - hollow magnetron with electron reflecting ends

(c) cylindrical - post magnetron

(d) cyindrical - hollow magnetron

[reprinted from ref. 38]

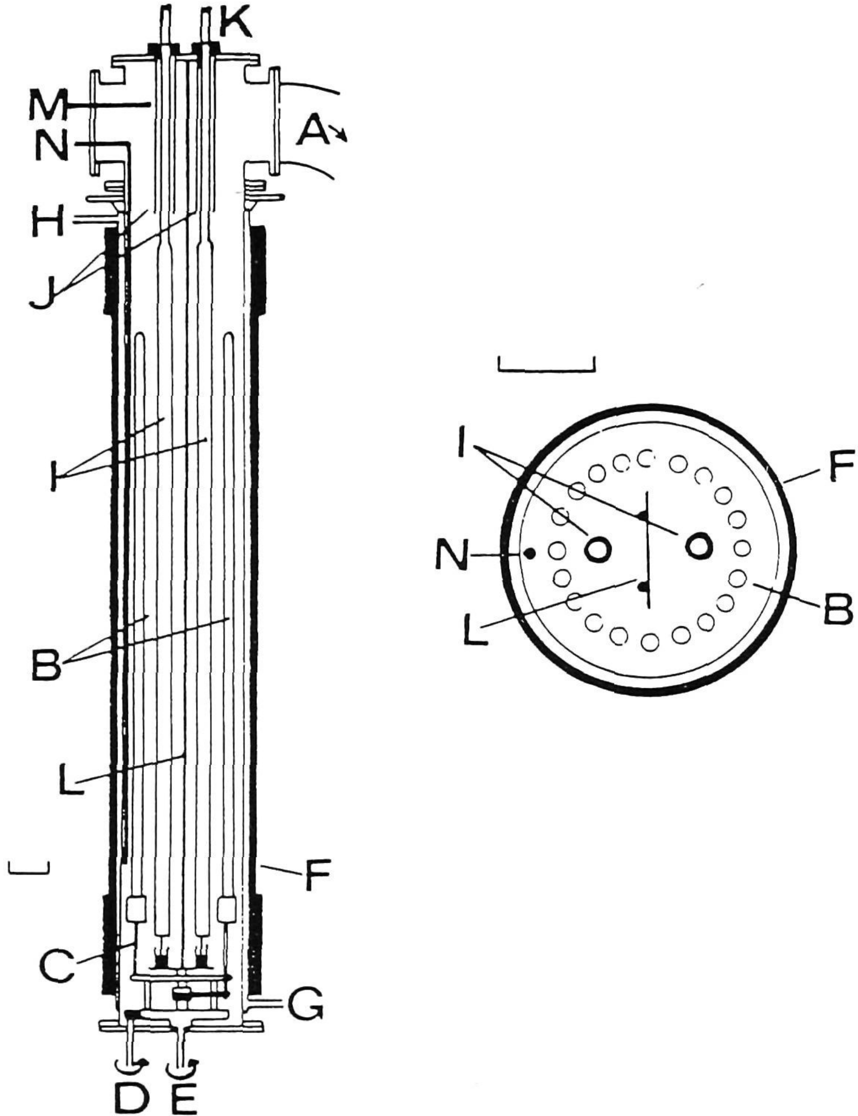

Figure 2.6 Sectional views of the batch coater. A: to pumps; B: glass tubes; C: carousel; D: carousel rotation drive; E: tube rotation drive; F: magnetic field coil; G: water jacket inlet; H: water jacket outlet; I: sputtering electrodes; J: guard rings; K: high voltage connections and water cooling for electrodes; L: water cooled screen; M: argon inlet; and N: reactive gas inlet. The scale indicates 100mm. [reprinted from ref. 13]

water cooled screen to prevent cross contamination [40]. The cathodes are made from oxygen free, high conductivity (OFHC) type copper and 316 type stainless steel.

The plasma is confined by a water cooled magnetic field coil wound around the outside of the chamber. Extra turns are wound at either end to enhance the uniformity of the magnetic field [13]. Soft iron sections are included at each end of the cathodes to concentrate the magnetic field and confine the plasma to the length of the cathode [40].These act in a similar fashion to the cathode wings found in other forms of cylindrical magnetron. The intensity of the magnetic field along the length of the chamber is shown in figure 2.7.

Gases are admitted to the chamber via a tube with about a dozen evenly spaced, fine holes along its length. The holes are directed at the chamber wall to provide an even flux of molecules and to prevent clogging caused by deposition of sputtered material. The flow rate of gases is controlled with a series of flow regulating valves and needle valves. The flow rate is measured with a micromanometer and flow transducers (Matheson, Model 8141). Argon is used as the sputtering gas and acetylene as the reactive gas. The chamber is vented after each run using dry nitrogen.

2.5 Microstructural Analysis

Methods for investigating the microstructure of amorphous carbon films range in complexity and the type of information produced. If film deposition processes are well characterised then accurate predictions of film properties are possible. Macroscopic film properties such as electrical resistivity, film hardness and film density can be measured using straightforward experimental techniques; it is more difficult to probe the underlying film microstructure. One of the primary means of deducing structural information is to determine the sp^3/sp^2 ratio. It requires analysis of electron diffraction data, however, to confirm that very hard DLC films consist of a network of tetrahedrally bonded carbon atoms.

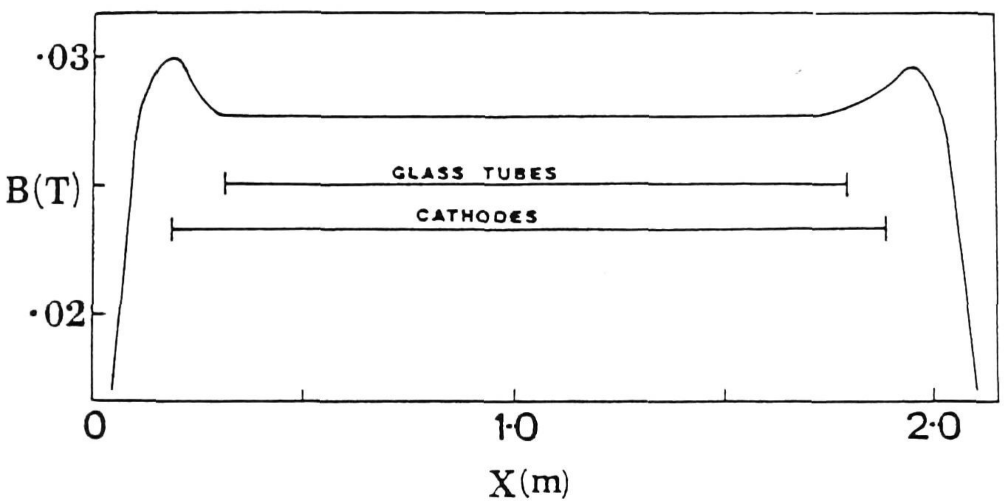

Figure 2.7 Magnetic field B versus distance X along the chamber for coil current of 50A, (X=0 corresponds to the base plate of the chamber). The positions of the glass tubes and sputtering electrodes are shown. [reprinted from ref. 13].

2.5.1 Macroscopic Properties

Measurements of film thickness are a useful starting point for film analysis. A variety of straightforward methods exist including the use of stylus instruments (Taylor - Hobson Talystep profilometer, for example) to measure step heights defined by masking or selective film removal. Quartz crystal microbalance (QCM) techniques, laser interferometry, laser ellipsometry and X - ray photoelectron spectroscopy (XPS) can be used to measure thickness, in situ, during film deposition. Film thickness is deduced using XPS by determining the attenuation of a characteristic substrate photoemission peak by the film deposited on the substrate.

Measurements of hardness and density are also useful for testing and characterising film properties. Hardness is determined using scratch and indent tests with reference to standard tables or samples. Density is determined using float/sink methods or calculations using film volume and weight. Measurements of electrical resistivity as a function of temperature or specific deposition parameters provide information about the electrical properties of the film and the overall film bonding arrangement [14,41]. The behaviour of simple thin film devices can be analysed by creating I - V and C - V curves [21,42].

Internal film stress is an important parameter for controlling phase transitions in growing films, film/substrate and interlayer adhesion and film hardness. Stress can be determined by measuring substrate bending relative to an optical flat [43,44]. This measurement is usually performed interferometrically. Alternatively, the deflection can be detected of a beam coated with material on one side [45,46]. It has been recently shown that carbon films deposited using a cathodic vacuum arc under conditions favouring high compressive stress form a stable phase with a local diamond structure [21].

2.5.2 Electron Spectroscopies

High resolution electron micrographs are important in the initial stages of film analysis and will often suggest the direction that other analyses should take. High magnification reveals film morphology, clustering and the presence of lattice dislocations. Electron diffraction and electron energy loss spectroscopy (EELS) have also been used extensively in the investigation of the composition and structure of different forms of amorphous carbon. These techniques reveal the bonding structure present in the film, in particular, ring structures, layering and bonding

concentrations. Numerical analysis of electron diffraction data allows the co - ordination numbers of the various structures to be calculated.

Electron energy loss spectroscopy (EELS) has been used to analyse four types of carbon using scanning transmission electron microscopy (STEM) with 100keV electrons [17]. The low energy loss parts of the spectra collected are shown in figure 2.8. The most significant feature of the four spectra is the 6.2eV peak for graphitised carbon. This arises from the π to π^* energy excitation of the π bonding in this material. A band diagram for carbon in shown in figure 2.9. The principal difference between the diamond and DLC spectra is the shifting of the large plasmon peak in the DLC spectrum to a slightly lower energy. This arises because the DLC has a slightly lower density than diamond due to its amorphous structure and the presence of some sp^2 bonding. The sp^3/sp^2 ratio can be determined with some degree of accuracy using the carbon K edge. Integrating the area under the peak corresponding to the transition gives a result proportional to the quantity of sp^2 bonded material in the film. If this quantity is compared to the peak area of graphitised carbon, (that is, entirely sp^2 bonded carbon), the ratio can be deduced. In this case it was found that there was approximately 15% sp^2 bonded material and 85% sp^3 bonded material present in the film. The high proportion of sp^3 bonded carbon gives the material its diamond - like characteristics, in particular, its exceptional hardness [17].

Electron spin resonance (ESR) studies of a-C:H reveal changes in film structure resulting from heat treatment. Ring structures were detected with a high carbon - to - hydrogen (C:H) ratio and associated delocalised electrons. Lower molecular weight aliphatic material with a lower C:H ratio was also detected. Heat treatment caused gas evolution from the film and converted some of the aliphatic material into an aromatic form [47].

X - ray photoelectron spectroscopy (XPS) provides a chemical analysis of surface. X - rays (~ 1200 - 1400eV) irradiate the sample, ejecting core level photoelectrons with characteristic kinetic energies. The escape depth of the photoelectrons collected by the electron energy analyser can be adjusted by varying the substrate/analyser angle to generate depth sensitive spectra. Carbon spectra can be deconvoluted by curve fitting to give information about bonding states and interfacial structure. The chemical environment of the atom causes shifts in the peak energy. The proportional contributions of each chemical state can be quantified by calculating and comparing the corresponding peak areas.

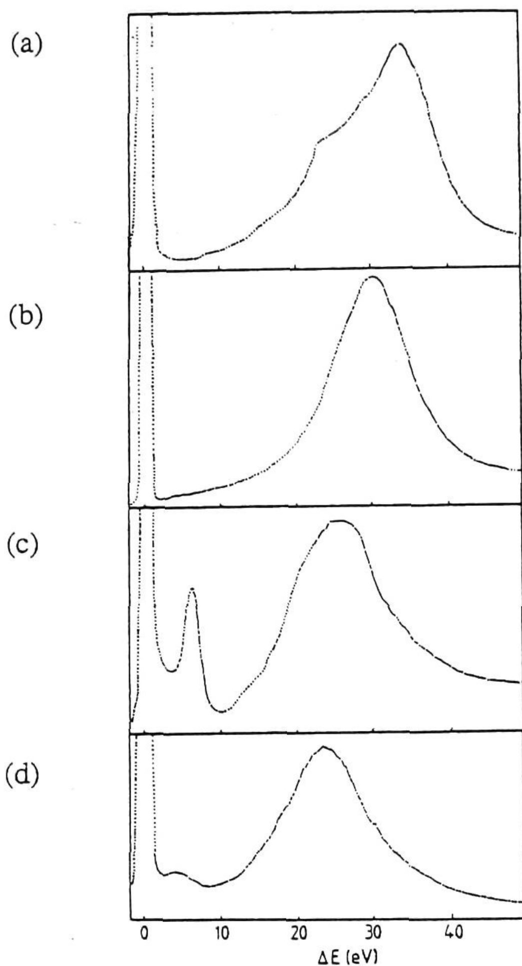

Figure 2.8 Electron energy-loss spectra in low-loss region from (a) diamond, (b) a-D, (c) graphitised carbon and (d) a-C. [reprinted from ref. 17]

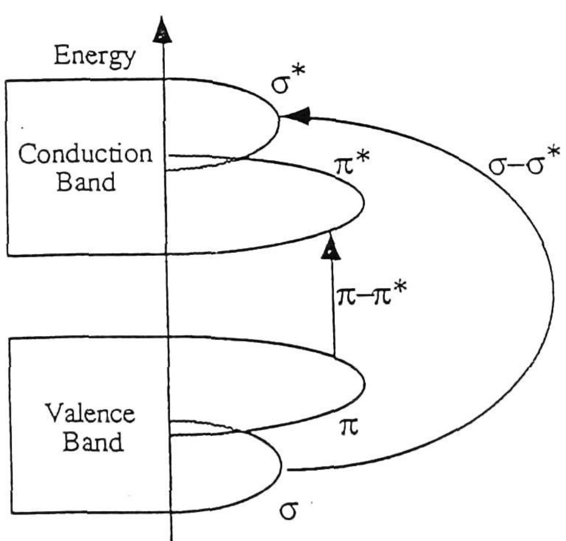

Figure 2.9 A schematic representation of the density of states of carbon showing the relationship between the π and σ bonding orbitals and the π* and σ* anti-bonding orbitals. [reprinted from ref. 18]

Auger electron spectroscopy (AES) involves electron beam induced ejection of Auger electrons from the valence bands. This technique is also highly surface sensitive, producing elemental rather than chemical information [48,49]. Depth profiles of complicated film structures can be produced by combining XPS or AES with ion beam etching [50]. Depth profiling using a well characterised ion gun is a useful method for investigating multi - layer structures, film adhesion and degradation [51]. Scanning XPS and scanning AES produce compositional maps of the sample surface. Electron lenses are used to raster scan the electron collection point (XPS) and electron beam (AES). Electrons are energy analysed using the standard, static mode of operation. The chemical information contained in the XPS spectra can be used to map regions containing different phases of a given material.

XPS and AES have been used to investigate the properties of the films produced for this study. The results are presented in Chapters 3 and 4. The physical processes and practical implementation of the two techniques are also discussed.

2.5.3 Other Spectroscopies

Solid state ^{13}C NMR has been used to investigate the structure of a-C:H prepared using a number of different techniques and starting materials. Quantitative assessments of the amount of sp^2 bonded carbon present were made. The concentration of sp^2 bonded sites was found to be dependent on the deposition conditions and the hydrogen content of the film [15,52]. Spectra are characterised by two broad peaks corresponding to sp^3 bonded material (40ppm) and sp^2 bonded material (130ppm) in a range of bonding configurations [18]. Spectra for as - prepared films show mainly sp^3 bonded material. Heat treatment results in the formation of sp^2 bonded ring structures and a decrease in the concentration of sp^3 bonded material [21].

Infrared and Raman vibrational spectroscopies, using the position and size of absorption peaks, identify different types of carbon - carbon and carbon - hydrogen bonding and bending modes [53]. Experiments were performed over a range of annealing temperatures and durations, giving a detailed description of changes in carbon and hydrogen bonding. Relative concentrations of the various types of bonding can be deduced with reasonable accuracy by comparing the integrated intensity of the corresponding peaks [18].

The optical properties of amorphous carbon films can be used to deduce structural and bonding states. Measurements of transmission and reflectance as a function of wavelength quantify the performance and suitability of anti - reflection and optically selective films. The evaluation of the complex dielectric function ($\varepsilon = \varepsilon_1 + i\varepsilon_2$) using optical methods provides information about the valence band structure, optical gap and, in the case of carbon films, the sp^3/sp^2 ratio [53]. Some difficulties arise, however, when this type of analysis is applied to a-C:H films as there is no clear separation between the π and σ absorption regions [18].

2.6 Gas Adsorption Behaviour

2.6.1 Morphology and Microporosity

Film morphology is a significant determinant of the adsorption/desorption behaviour observed in amorphous carbon films. The relationship between pore structure and adsorption behaviour of carbon sieve materials has been extensively investigated [54,55]. Direct and indirect methods of investigation can both be applied to carbon materials to quantify morphology.

Electron microscopy is the most widely used method of directly observing film morphology. SEM and high resolution transmission electron microscopy (TEM) micrographs provide visual evidence of surface roughness, columnar film growth and the size, shape and distribution of macroscopic voids. This technique is restricted to film surfaces and fracture edges and therefore can not provide much information about the internal features of a film. The quantification of morphological features is therefore limited to visible features and can not be easily generalised to include the entire film.

Sputter deposition can be used to produce a-C:H and metal/carbon cermet films with a range of properties. The key deposition parameters which govern the morphology of sputtered films are the substrate temperature and the pressure of the sputtering gas. Figure 2.10 shows structure zones reflecting the dependence of film structure on these two parameters. Higher substrate temperature and sputtering gas pressure deliver more energy to the growing film resulting in greater atomic mobility, recrystallisation and large grain sizes. As the energy is reduced, grains become smaller and more defined. At low energies films consist of fine porous

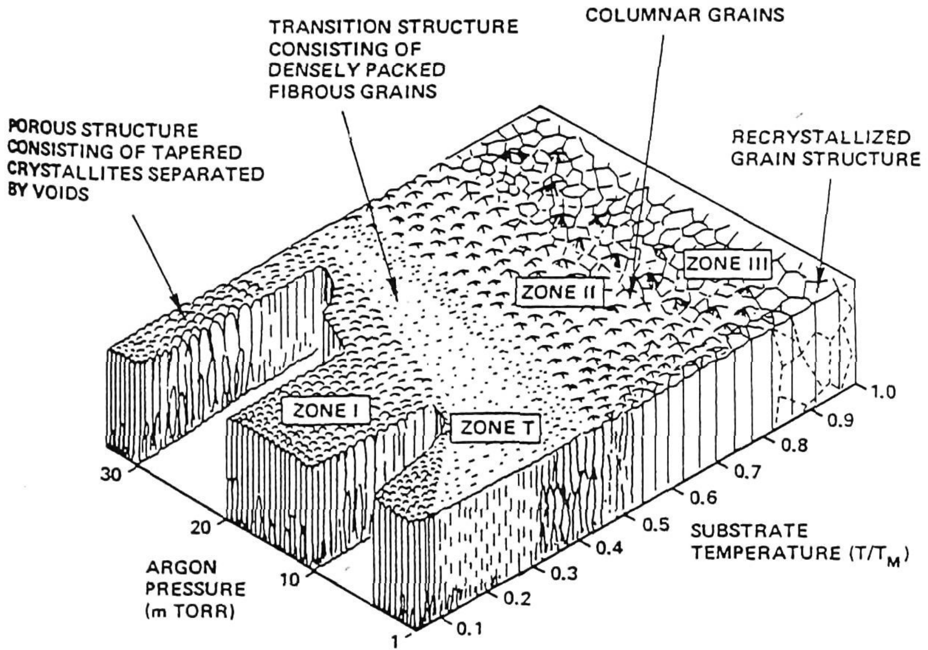

Figure 2.10

Influence of substrate temperature and Ar pressure on the microstructure of sputtered metallic coatings. The numbers refer to Movchan-Demchishin zones, [reprinted from ref. 38].

columns separated by voids. The films used in this study are Zone T films with a transition structure consisting of densely packed fibrous grains without well defined voided boundaries.

Amorphous carbon films of moderate hardness are produced by processes such as sputter deposition using a d.c. cylindrical magnetron apparatus. Figure 2.11 shows the macroscopic features of the a-C:H films used in this work [14]. These a-C:H films show a predominance of sp^2 bonded material and a lesser amount of sp^3 bonded material [14,56]. The upper a-C:H layers of the spectrally selective film have a columnar structure with an approximate column diameter of 20nm [14]. The columnar texturing of the film reduces reflection and is essential for satisfactory gas adsorption behaviour.

Electron diffraction has shown that as - deposited films are primarily constituted of 5 and 7 member ring structures joined by regions of diamond bonded material in a disordered layer structure. Baking the films (770K, 60 minutes) causes increases in both interlayer and intralayer ordering. Following baking the films are composed of regions of six membered graphitic ring structures connected by regions of diamond bonded material [36]. The inherent porosity of the film increases the adsorption capacity at low pressures by around two orders of magnitude with respect to geometrical surface area [57].

Morphological information for amorphous carbon films can be obtained using a number of techniques. Electron microscopy produces images of the film surface with topographic contrast but little elemental information. Scanning tunnelling microscopy (STM) and atomic force microscopy (AFM) are techniques based around scanning a fine tip very close to the film surface and are used with conducting and insulating samples respectively. A fixed electron tunnelling current or tip/sample force is established and used as feedback control to adjust the tip position as it is scanned across the surface. Maps of the film surface are produced with a vertical resolution of about 0.2Å (atomic resolution) [58,59].

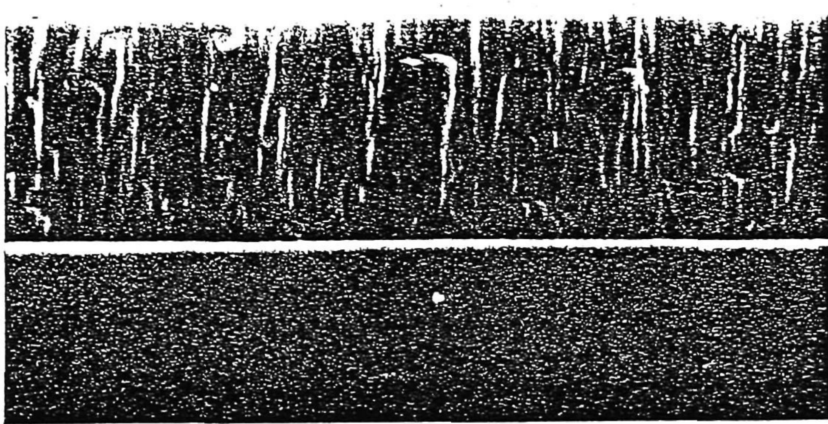

Figure 2.11 Scanning electron micrograph of the fractured edge of an as deposited, 500nm thick film of a-C:H showing pronounced columnar structure. [reprinted from ref. 14]

2.6.2 Physical Adsorption of Gases

Film composition and bonding can be satisfactorily studied using a variety of surface sensitive and structure sensitive spectroscopies. The characterisation of porous films requires a range of indirect experimental techniques. Density can be determined with measurements of film thickness and volume, whereas void fraction is commonly studied using small angle X - ray scattering (SAXS). Gas adsorption is the most common and most useful means of studying pore structure. Film morphology, pore structure and gas adsorption behaviour are interdependent in the context of developing a thermal switching mechanism for ETCs.

The gas adsorption behaviour of carbonaceous materials has been studied for centuries. The extraction of useful information about the pore structure of adsorbents has only been possible with the development of satisfactory methods of presenting adsorption data and models for the behaviour observed. The adsorption isotherm has emerged as the principal method of data presentation. The quantity of material adsorbed by an adsorbent is expressed as a function of the pressure of the adsorptive over the surface at constant temperature. By way of definition, the "adsorbent" is the sieve, porous film or similar material adsorbing atoms or molecules onto its surface or into its pores. The "adsorptive" is the material to be adsorbed, in the gas phase, whereas the "adsorbate" is material adsorbed on the absorbent.

Adsorption isotherms have been classified into six groups, as shown in figure 2.12, corresponding to different types of behaviour and adsorbents [60,61]. The Type I isotherm is characteristic of the physical adsorption of gases by a microporous solid. Similarly, Types II and IV correspond to nonporous and mesoporous solids, respectively. Types III and V are characteristic of weak gas - solid interactions, corresponding to nonporous or macroporous solids and mesoporous or microporous solids, respectively. The Type VI step - like isotherm corresponds to multi - layer adsorption, with each step occurring with the adsorption of successive layers. The branching seen in Types IV and V is characteristic of hysteresis in the adsorption process. The gas is adsorbed along the lower branch and desorbed along the upper branch [61].

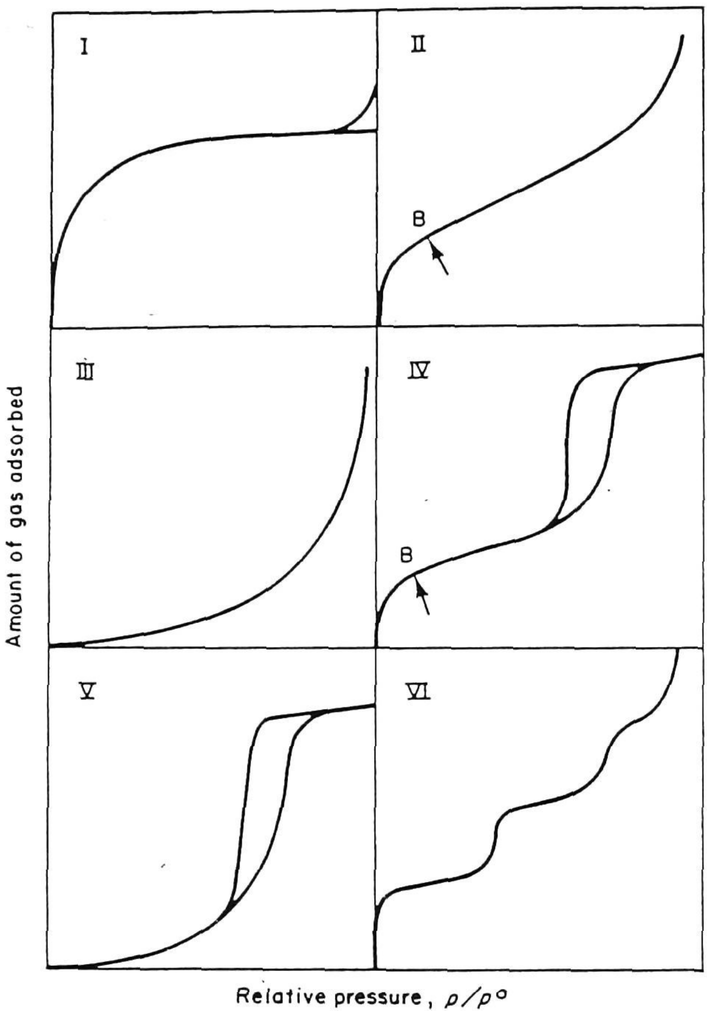

Figure 2.12 The five generic types of adsorption isotherm as classified by Brunauer, Deming, Deming and Teller [60], together with the Type VI stepped isotherm.
[reprinted from ref. 61]

The physical adsorption of gases is driven by dispersion (Van der Waals) forces, short range repulsive forces and electrostatic forces (due to polar molecules) [61]. The potential energy, ε, between two isolated atoms is a function of separation, r, and is generally expressed by the Lennard - Jones potential [62],

$$\varepsilon(r) = -K_1 r^{-6} + K_2 r^{-12} \qquad (2.1)$$

where K_1 and K_2 are constants. The general form of the relationship between potential energy and atomic separation for two isolated atoms is reproduced in figure 2.13. Adsorption occurs when atoms or molecules become trapped in the potential well close to the adsorbent surface.

A number of equations have been devised which model the behaviour observed in adsorption isotherms. The isotherm equations allow parameters characterising various aspects of the adsorption to be extracted from experimental data. While, the greatest area of applicability is in the sub - monolayer regime, progress has also been made in characterising multi - layer adsorption. The amorphous carbon films and graded stainless steel/carbon cermet films are microporous, so the consideration of the model isotherm equations will be restricted to Type I adsorption isotherms.

The Brunauer - Emmett - Teller (BET) equation [63] is derived by assuming that the first layer of adsorbed molecules is bound to a surface with an interaction energy ε_o, and that all subsequent layers are bound with an interaction energy ε_1. The BET equation has the form,

$$\frac{\frac{p}{p_0}}{N\left[1-\frac{p}{p_0}\right]} = \frac{1}{c\,N_m} + \frac{c-1}{c\,N_m}\,\frac{p}{p_0} \qquad (2.2(a))$$

$$c = \exp\left[\frac{\varepsilon_0 - \varepsilon_1}{kT}\right] \qquad (2.2(b))$$

where N is the total number of molecules adsorbed and N_m is the number of molecules adsorbed in one monolayer. The relative pressure, p/p_o, is the ratio of the adsorptive pressure, p, over the adsorbent surface to the saturated vapour pressure of the adsorptive, p_o, at a given temperature. The BET equation is most useful for

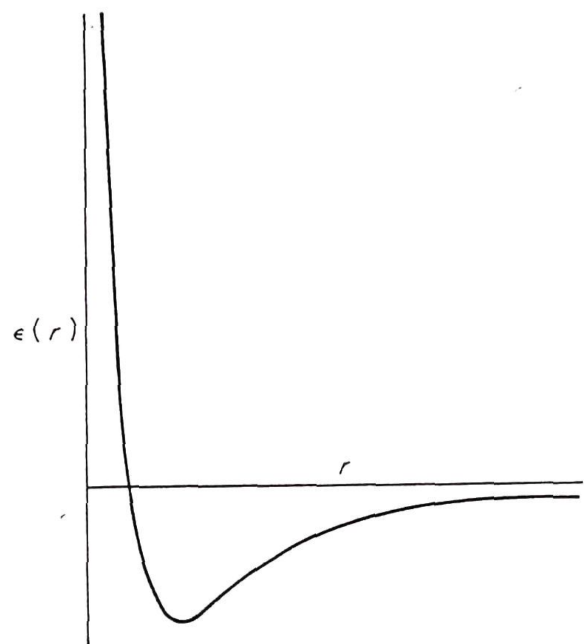

Figure 2.13 The potential energy, ε (r), of two isolated atoms as a function of the distance, r, between their centres. The curve for the potential energy of a molecule as a function of its distance from the surface of a solid has the same general form.
[reprinted from ref.61]

describing multi - layer adsorption on non - porous surfaces, near monolayer coverage. The equation ignores co - operative effects and breaks down at sub - monolayer coverages and coverages greater than 2. Surface area and N_m can be deduced with reasonable accuracy (< 20%) with errors arising from difficulties in assigning a specific molecular area to the adsorbing molecule. It has been shown that the BET approach is still valid for rough surfaces at low values of p/p_o [64,65]

The Dubinin - Radushkevish (DR) equation [66] is particularly useful in the study of microporous materials. This equation linearises adsorption isotherms over a wide range of relative pressures at sub - monolayer coverages and is generally written as:

$$N = N_m \exp - \left[\frac{k}{\beta^2} \varepsilon^2\right] \tag{2.3(a)}$$

$$\varepsilon = - \Delta G = RT \ln \left[\frac{p_0}{p}\right] \tag{2.3(b)}$$

where k is a constant determining the shape of the distribution function of N and ß is a constant which relates each of the adsorbates. The adsorption potential, ε, is expressed thermodynamically where ΔG is the change in free energy associated with adsorption and R is the gas constant. Empirical interpretations of ß and k are required to extract structural information which makes their precise physical meaning unclear [22]. While this is a thermodynamic theory, its generality allows the description of both sub - monolayer and multi - layer adsorption.

The DR equation assumes a gaussian distribution of pore sizes in the adsorbent. An alternative treatment has been suggested which convolutes a fractal pore distribution with the DR equation [67]. The fractal pore distribution is given by:

$$J(x) = bx^{2-D} \tag{2.4}$$

where b is a constant, x is the pore size and D is the fractal dimension.

The resulting isotherm equation has the form:

$$N = N_m \; K(D) \; \ln\left[\frac{p_0}{p}\right]^{-(3-D)} \tag{2.5}$$

where K(D) is a characteristic constant [67,68]. This equation can be used to describe adsorption on fractal surfaces in the form of sequential filling of micropores from small to large [69]. In this interpretation pore filling and surface adsorption are indistinguishable and so the terms monolayer and monolayer capacity, N_m lose their original physical significance [70]. This equation has the same form as the Frenkel - Halsley - Hill (FHH) equation which describes multi - layer adsorption [61].

A modification to the FHH equation has been proposed for adsorption on fractal surfaces to give a more realistic representation of adsorption behaviour [69]. The modified equation is:

$$N + N_c = N_m \; K(D) \; \ln\left[\frac{p_0}{p}\right]^{-(3-D)} \tag{2.6}$$

where N is the experimentally measured number of molecules adsorbed and N_c is a constant including contribution from two different physical effects. The first effect represents the volume of pores that are inaccessible due to small size and geometrical constrictions. The second effect represents the amount of preadsorption due to exposure of the surface before the commencement of the measurement of the adsorption isotherm.

2.6.3 Experimental Studies of Gas Adsorption

Studies of the gas adsorption behaviour of porous materials and thin films are widely reported in the literature. Porous materials are generally investigated using a technique which quantifies the amount of adsorbate for a given adsorptive pressure over the surface. Thin films, on the other hand, are investigated using comparatively minute amounts of adsorbate and techniques which quantify "microscopic", atom - surface interactions rather than collective gas adsorption properties. Few studies are reported which deal with porous thin films. Relatively simple adsorption processes, which are typically studied on single crystal surfaces, are complicated by adsorption in surface pores.

The porosity and roughness of hard carbon films have been investigated using a quartz crystal microbalance (QCM) to quantify nitrogen adsorption [71,72]. Adsorption was studied using relative pressures ranging from < 0.1 to 1 (the saturated vapour pressure of the adsorbate). Adsorption isotherms are constructed using the FHH equation, described above, assuming a perfectly fractal porous surface [72,73]. The effect on adsorption of capillary condensation in surface pores is also incorporated in the model. Estimates of the fractal dimension of the surface, pore size and morphology can be deduced from experimental data using this analysis.

An extension of the QCM technique has been reported [74] in which the solid - liquid interfacial viscosity is deduced from changes in the amplitude of crystal vibration. It is proposed that this behaviour corresponds to slippage of physisorbed monolayers on the film surface. The dynamical behaviour of adsorbates can be studied using this technique as a function of temperature and a variety of surface conditions [74].

Gas adsorption behaviour of amorphous carbon films and graded stainless steel/carbon cermet films has been studied previously in this laboratory using a volumetric adsorption technique [57] and a QCM technique [70]. A range of adsorbates has been used. Most work, however, has concentrated on benzene.

Adsorption is volumetrically quantified by allowing a known quantity of adsorbate to reach adsorption equilibrium with a known surface area in a known experimental volume. The number of molecules introduced into the system coupled with accurate measurements of the equilibrium pressure of adsorbate over the surface can then be used to construct adsorption isotherms. The use of a quartz crystal microbalance to quantify gas adsorption by accurate film mass measurements is a significant extension of the basic technique. The reliance on accurate pressure measurements remains an important aspect of this technique. A typical set of adsorption isotherms obtained using these methods is shown in figure 2.14.

The accuracy of pressure measurements limits the adsorption regime for these experiments to pressures greater than $1x10^{-7}$ torr, the limit of resolution of spinning rotor (gas viscosity) pressure gauges. This corresponds to a relative pressure (p/p_o) of about $1x10^{-9}$, (p_o, the saturated vapour pressure of benzene ≈ 80 torr at 298K). At the lower limit of this pressure regime long times are required to allow the adsorbate and sample to reach equilibrium. The accuracy of these experiments

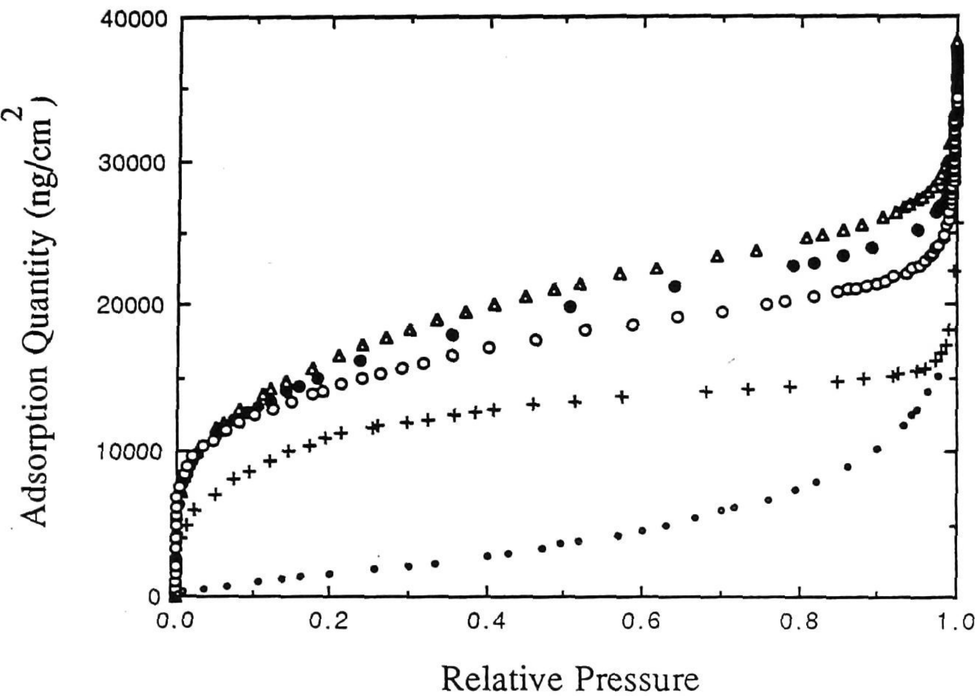

Figure 2.14 A typical set of adsorption isotherms for the amorphous hydrogenated carbon (a-C:H) films used in these experiments. The isotherms cover a relative pressure range from submonolayer coverages (< 0.1) to condensation coverage (1.0) at the saturated vapour pressure of the adsorptive, benzene (80 torr at 298K). The adsorption capacity of the film increases greatly with increased baking temperature and duration. The adsorption experiments described in this thesis were undertaken in a pressure regime located between 5×10^{-10} torr and 1×10^{-4} torr. This corresponds to a relative pressure range of around 10^{-11} to 10^{-6} for a benzene adsorptive or at the left hand axis of the figure above. [redrawn from ref. 70]

decreases as their duration increases. This occurs because of the difficulty in maintaining precisely constant experimental conditions and the uncontrollable influence on the adsorption characteristics of residual background gas. Parameters such as environmental temperature, instrumental temperature and stability of controlling or measuring electronic devices are all subject to change over extended periods.

Gas adsorption occurs throughout the graded stainless steel/carbon region of the spectrally selective film. Adsorbing molecules do not appear to permeate the copper low emittance layer [22,57]. The effective adsorption area has been shown to be proportional to film thickness which indicates a high level of pore connectivity, particularly in baked films [57]. The films are uniformly porous over a wide range of thicknesses, with the whole pore structure accessible to adsorbate [70]. The rate of adsorption and degree of porosity depend on the film annealing conditions. The rate at which adsorbate penetrates into deep pores is dependent on pore constrictions and the film void fraction. Percolation theory suggests a void fraction of 0.25 or greater is required for pores to be just accessible to the gas phase. Films with void fractions of 0.25 or less consequently require very long times to attain equilibrium adsorption [70]. Experimentally, such effects are observed for film annealing temperatures of less than 620K.

There is considerable evidence to suggest that micropores in the film occur in a wide distribution of sizes. Volumetric studies [57] deduced a pore size distribution for the film. It was found that the film contained 65% very narrow slit - like micropores (width < 7Å), approximately 20% wider micropores (7Å < width < 20Å) and approximately 15% mesopores and external surface.

Preadsorption has a marked effect on the gas adsorption behaviour of a-C:H films. A range of very high energy adsorption sites is apparently filled prior to the start of gas dosing by residual gas molecules in the vacuum system [57]. The time required for a-C:H samples to come to adsorption equilibrium increases dramatically as the pressure in the vicinity of the surface is lowered. Preadsorption and low dose gas adsorption are only partially reversible, causing adsorption hysteresis [22,23]. Small doses of n - decane , for example, are tenaciously adsorbed, requiring baking for complete removal [57]. Subsequent and concurrent benzene adsorption is inhibited by preadsorption of water vapour, with hysteresis resulting from pore constriction and a loss of pore connectivity [22]. There are significant implications for the manufacture of gas dosed ETCs as the industrial manufacturing process will

ensure preadsorption with residual gases such as water vapour, carbon monoxide and carbon dioxide.

The current gas adsorption experiments were conducted under ultrahigh vacuum conditions. Lower base pressures in the vacuum chamber allowed previously undetectable adsorption/desorption phenomena to be examined for the first time. The relationship between the bulk adsorption studies undertaken using the spectrally selective film and the current work is indicated in figure 2.14. Although thermal desorption and work function studies have been widely used to study surface behaviour, no reports have been found detailing studies of complex, porous surfaces. The pressure regime used for these experiments is located between 1×10^{-4} to 5×10^{-10} torr.

An alternative method of gas dosing was used in the current work which removes the difficulties of accurate pressure measurement. Further, reduced pressures slow the rate of adsorption of residual gases. Work function studies were undertaken in which the sample films were exposed to a quantified gas dose (pressure, time) rather than a known quantity of gas (number of molecules). Relative pressures ranged from 1×10^{-6} to 1×10^{-11} over time periods of the order of minutes. Pressure measurements were made with an ionisation gauge. The relative amount of adsorbate delivered to the sample in successive experiments can be expressed simply and accurately in terms of exposures. An exposure at a pressure of 1×10^{-6} torr for 1 second is defined as 1 Langmuir (L). While no information can be deduced about the absolute quantity of gas adsorbed, this can often be inferred from other aspects of film behaviour simultaneously recorded.

2.7 Summary

Amorphous carbon films have considerable scientific and technological importance. The utility of these films originates in the unique bonding configurations of the carbon material and the ready control of bonding characteristics available with different deposition methods and post - deposition processing. The microstructural characteristics and macroscopic physical properties of amorphous carbon films are determined by the sp^3/sp^2 bonding ratio, the hydrogen content and post - deposition processes, such as thermal annealing.

The bonding configuration and hydrogen content of amorphous carbon films are dependent on the method of film deposition. Control of deposition parameters varies between techniques. Influential parameters include the starting material or precursor, the energy characteristics of the beam of atoms, ions or particles condensing to form a film and ion assistance. Greater control of the characteristics of ion beams often is offset by a significant reduction in ion flux and hence reduced deposition rates.

Carefully controlled film deposition must be supported by rigorous analysis of the resulting films. Analytical techniques range in complexity and in the nature of the information obtained. Simple methods of film analysis, such as the physical and electrical properties, can provide significant structural information. Advanced analytical techniques provide a more direct probe of film structure and more detailed structural information. While all these techniques are experimentally complex, electron diffraction and electron energy loss spectroscopies are rapidly developing as accessible and interpretable methods of obtaining detailed structural information. A range of other techniques, such as NMR, ESR and other electron spectroscopies, provide complementary and supplementary information.

The spectrally selective films fabricated for use in thermally switching ETCs are required to exhibit appropriate optical performance, gas adsorption/desorption behaviour and structural stability over a lifespan of twenty years. Film structure and morphology are the critical factors ensuring satisfactory overall performance. These factors are determined by the type of deposition process employed and the control of that process. The spectrally selective films used in this study and employed in ETCs are deposited using reactive d.c. magnetron sputtering in a batch coater with a realistic industrial capacity. The batch coater allows a reasonable amount of flexibility in altering or adjusting the deposition parameters.

The gas adsorption behaviour observed for baked a-C:H films is typical of microporous adsorbents. Well defined Type I adsorption isotherms have been obtained using volumetric and QCM measurement techniques. The pressure regime of these techniques is limited by instrumentation and experimental difficulties. Surface sensitive adsorption techniques and modified gas dosing, as developed in this work, will be seen to extend the pressure regime accessible with particular significance for the observation of the effects of contamination and low level adsorption.

References - Chapter 2

[1] P.H. Holloway, K. Shanker, G.A Alexander, L. de Sedas, Thin Solid Films, 177, 95 (1989).

[2] S.E. Horstrom, S.E. Karlsson, A. Ross, B. Westerstrandh and A. Kamf, Sol. Energy Mater., 9, 367 (1984).

[3] G.L. Harding and B. Window, J. Vac. Sci. Technol., 16, 2101 (1979).

[4] G.L. Harding, Sol. Energy Mater., 7, 123 (1982).

[5] J.D. Garrison, J.C. Haiad and A.V. Averett, Proc. SPIE, 823, 225 (1987).

[6] H.R. Wilson, D.R. McKenzie and L.M. Briggs, Thin Solid Films, 91, 123 (1981).

[7] G.L. Harding, Z. Yin, S. Craig and S.P. Chow, Sol. Energy Mater., 10, 187 (1984).

[8] R.D. Patel, M.G. Takwale and V.G. Bhinde, Thin Solid Films, 135, 21 (1986).

[9] G.L. Harding, S. Craig and B. Window, Appl. Surf. Sci., 11/12, 315 (1982).

[10] B. Window and G.L. Harding, Sol. Energy, 32, 609 (1984).

[11] G.L. Harding, Sol. Energy Mater., 2, 469 (1980).

[12] R.E. Collins and R. Schmid, Sol. Energy, 40, 181 (1988).

[13] S. Craig, PhD thesis, Department of Applied Physics, University of Sydney, 1982.

[14] D.R. McKenzie, R.C. McPhedran, N. Savvides and L.C. Botten, Phil. Mag. B, 48, 341 (1983).

[15] J. Robertson, Adv. Phys., 35, 317 (1986).

[16] F. Olcaytug, K. Pirker, R. Schallauer, F. Kohl, G. Urban, A. Jachimowicz, O. Prohaska, W. Fallmann and K. Riedling, Materials Science Forum, 52/53, 671 (1990).

[17] S.D. Berger, D.R. McKenzie and P.J. Martin, Phil. Mag. Lett., 57, 285 (1988).

[18] D.C Green, D.R. McKenzie and P.B. Lukins, Materials Science Forum, 52/53, 103 (1990).

[19] C. Kittel, "Introduction to Solid State Physics", 5th ed., John Wiley, 1976.

[20] G.M. Jenkins and K. Kawamura, "Polymeric Carbons - carbon fibre, glass and char", Cambridge University Press, 1976.

[21] D.R. McKenzie, D. Muller, B.A. Pailthorpe, Z.H. Wang, E. Kravtchinskaia, D. Segal, P.B. Lukins, P.D. Swift, P.J. Martin, G. Amaratunga, P. Gaskell and A. Saeed, Diamond and Related Materials, 1, 51 (1991).

[22] S.J. O'Shea, PhD thesis, Department of Applied Physics, University of Sydney, 1989.

[23] Y. Yin, Personal communication.

[24] G.L Harding and B. Window, Sol. Energy Mater., 7, 101 (1982).

[25] S.P. Chow and G.L. Harding, Sol. Energy Mater., 11, 123 (1984).

[26] D.R. McKenzie, Personal communication

[27] P. Koidl, Ch. Wild, B. Dischler, J. Wagner and M. Ramsteiner, Materials Science Forum, 52/53, 44 (1990).

[28] A.M. Bonnet, Thin Solid Films, 185, 111 (1990).

[29] C.V. Deshpandey and R.F. Bunshah, J. Vac. Sci. Technol. A, 7, 2294 (1989).

[30] S. Aisenberg and F.H Kimock, Materials Science Forum, 52/53, 1 (1990).

[31] M.J. Mirtich, Materials Science Forum, 52/53, 217 (1990).

[32] K - H Muller, J. Vac. Sci. Technol. A, 4, 184 (1986).

[33] Y. Lifshitz, S.R. Kasi and J.W. Rabalais, Materials Science Forum, 52/53, 237 (1990).

[34] D.M. Sanders, J. Vac. Sci. Technol. A, 7, 2339 (1989).

[35] P.D. Swift, D.R. McKenzie, I.S. Falconer and P.J. Martin, J. Appl. Phys., 66, 505 (1989).

[36] D.R.McKenzie, P.J. Martin, S.B. White, Z. Liu, W.G. Sainty, D.J.H. Cockayne and D.M. Dwarte, Proc. E - MRS Meeting, 17, 203 (1987).

[37] J.L. Vossen and J.J. Cuomo, In eds J.L. Vossen and W. Kern, "Thin Film Processes", Academic Press, 1978.

[38] J.A Thornton and A.S. Penfold, In eds J.L. Vossen and W. Kern, "Thin Film Processes", Academic Press, 1978.

[39] W.D. Westwood, In eds M.H. Francombe and J.L. Vossen, Physics of Thin Films - Vol. 14, "Contemporary Preparative Techniques", Academic Press, 1989.

[40] G.L. Harding, B. Window, D.R. McKenzie, A.R. Collins and C.M. Horwitz, J. Vac. Sci. Technol., 16, 2105 (1979).

[41] I. Petrov, I. Ivanov, V. Orlinov, J. Kourtev and J. Jelev, Thin Solid Films, 185, 247 (1990).

[42] Z. Has, S. Mitura, M. Clapa and J. Szmidt, Thin Solid Films, 136, 161 (1986).

[43] J.D Finegan and R.W. Hoffman, 8th Natl Symp. on Vacuum Technology Trans., Pergamon Press, New York, 935 (1961).

[44] D.W Hoffman and J.A. Thornton, Thin Solid Films, 45, 387 (1977).

[45] H.C. Tsai, Materials Science Forum, 52/53, 71 (1990).

[46] P.V. Plunkett, R.M. Johnson and C.D. Wiseman, Thin Solid Films, 64, 121 (1979).

[47] D.J. Miller and D.R. McKenzie, Thin Solid Films, 108, 257 (1983).

[48] A.K Green and V. Rehn, J. Vac, Sci. Technol. A, 1, 1877 (1983).

[49] T.J. Moravec and T.W. Orent, J. Vac, Sci. Technol., 18, 226 (1981).

[50] P. Sander, U. Kaiser, M. Altebockwinkel, L. Wiedmann and A. Benninghoven, J. Vac, Sci. Technol. A, 5, 470 (1987).

[51] P.J. Pigram, R.N. Lamb, B.J. Wood and R.E. Collins, Appl. Phys. A, 52, 145 (1991).

[52] M.A. Petrich, Materials Science Forum, 52/53, 387 (1990).

[53] D.R. McKenzie, R.C. McPhedran, N. Savvides and D.J.H. Cockayne, Thin Solid Films, 108, 247 (1983).

[54] Ed.s S.J. Gregg, K.S.W Sing and H.F. Stoeckli, "Characterisation of Porous Solids", Society of Chemical Industry, London, 1979.

[55] F. Rodriguez - Reinoso and A. Linares - Solano, In ed. P.A. Thrower, Chemistry and Physics of Carbon - Vol.21, "Microporous Structure of Activated Carbons as Revealed by Adsorption Methods", Marcel Dekker, 1989.

[56] L.M. Briggs, D.R. McKenzie and R.C. McPhedran, Sol. Energy Mater., 6, 455 (1982).

[57] S.J. O'Shea, B.A. Pailthorpe, R.E. Collins and D.N. Furlong, Langmuir, submitted October 1990.

[58] G. Binnig and H. Rohrer, Surface Sci., 126, 236 (1983).

[59] See for example the entire contents of the following journal issues: IBM Journal of Research and Development, 30 (No.4 & 5), (1986).

[60] S. Brunauer, L.S. Deming, W.S. Deming and E. Teller, J. Amer. Chem. Soc., 62, 1723 (1940).

[61] S.J. Gregg and K.S.W. Sing, "Adsorption, Surface Area and Porosity", 2nd ed., Academic Press, 1982.

[62] J.E. Lennard - Jones, Physica (Eindhoven), 4, 941 (1937).

[63] S. Brunauer, "The Adsorption of Gases and Vapours", Princeton Univ. Press, Princeton, 1944.

[64] S.M. Cohen, R.A. Guyer and J. Machta, Phys. Rev. B, 34, 6522 (1986).

[65] P. Levitz, H. Van Damme and J.J. Fripiat, Langmuir, 5, 781 (1988).

[66] M.M. Dubinin and L.V. Radushkevich, Russ. J. Phys. Chem., 40, 697 (1965).

[67] D. Avnir and M. Jaroniec, Langmuir, 5, 1431 (1989).

[68] P. Pfeifer, J. Kenntner and M.W. Cole, Proc. Conf. "Fundamentals of Adsorption", Sonthofen 1989.

[69] Y. Yin and R.E. Collins, in preparation.

[70] Y. Yin, R.E. Collins and B.A. Pailthorpe, J. Appl. Phys., submitted December 1990.

[71] C.D. Stockbridge, "Vacuum Microbalance Techniques", Plenum, 1966.

[72] C.L. Wang, J. Krim and M.F. Toney, J. Vac. Sci. Technol. A, 7, 2481 (1989).

[73] P. Pfeifer, Y.J. Wu, M.W. Cole and J. Krim, Phys. Rev. Lett., 62, 1997 (1989).

[74] J. Krim, E.T. Watts and J. Digel, J. Vac. Sci. Technol. A, 8, 3417 (1990).

CHAPTER 3

Structure and Surface Composition of Amorphous Carbon and Graded Stainless Steel/Carbon Cermet Films.

3.1 Introduction

The gas adsorption behaviour of spectrally selective films is dependent on the types of material used and, to a lesser extent, the structure of the film. Bonding structure can be deduced using electron diffraction or X - ray diffraction. Key parameters such as surface composition, layer structure and film purity can, however, only be investigated using surface analytical techniques. The electron spectroscopies used in this work reveal the compositional differences between as - prepared and baked film surfaces. Studies of deposition quality were also undertaken, examining areas where deeper layers are exposed at the surface and where film constituents have diffused through neighbouring layers. Defects or irregularities in the deposition process adversely effect the optical behaviour and adsorption behaviour.

Secondary ion mass spectroscopy (SIMS) and X - ray photoelectron spectroscopy (XPS) have been used to analyse the surface composition of spectrally selective films and amorphous carbon films. Data are presented showing the effects of post - deposition annealing and impurities introduced during the deposition process.

Differences in film structure arising from the method of deposition are well known. In this case, differences in bonding structure at the surface interface are considered. XPS has been used to investigate differences between amorphous carbon films prepared using different techniques. Data are presented showing the surface composition of films produced using sputtering, glow discharge deposition and vacuum arc deposition. The surface layers of each of the films were eroded using argon ion etching to provide a comparison between the surface structure and bulk structure of the films.

3.2 X-ray Photoelectron Spectroscopy

Electron spectroscopies based on electron emission are an important source of information about the electronic properties of a film. The energies and spatial distribution of emitted electrons show features characteristic of the atoms making up the surface layers of the film. Using these techniques the relative concentrations of the surface constituents can be deduced together with depth profile information [1].

Electrons with energies in the range of 10 - 1000eV are ideal for probing the first few atomic layers of a solid surface. The shallow depth from which the electrons emerge is a result of the interaction of electrons with solids. This gives a minimum mean free path (MFP) of around 5Å for a 50eV electron. The "universal curve" showing electron MFP as a function of kinetic energy is shown in figure 3.1 [2]. One of the implications of this curve is that interactions involving electrons with energies in this range occur in the first 5 - 40Å of the film and are therefore considered surface sensitive [2].

The minimum in the universal curve arises from the combination of electron energy loss processes. Core level ionisation, single particle excitation and plasmon excitation are the three main processes. The collective excitation of electrons associated with a material is referred to as a plasmon. A characteristic energy threshold for plasmon creation exists, below which electron energy loss occurs only via single particle processes. Electron energy loss is dominated by plasmon creation above the plasmon energy. The electron MFP resulting from these two processes has a minimum at an energy 2 - 3 times the plasmon energy then gradually increases with energy [3].

X - ray photoelectron spectroscopy (XPS) involves the energy analysis of photoelectrons evolved from samples as a result of X - ray absorption. Core level electrons are ejected when a material is irradiated with sufficiently energetic X - rays. Figure 3.2 gives a schematic illustration of the electronic processes involved in XPS. X - rays are produced by electron bombarding metal targets, generally Mg or Al, held at a potential of 15 - 20kV. A thin foil window (usually Al or Be) separates the X - ray source and sample, preventing electron escape from the source region.

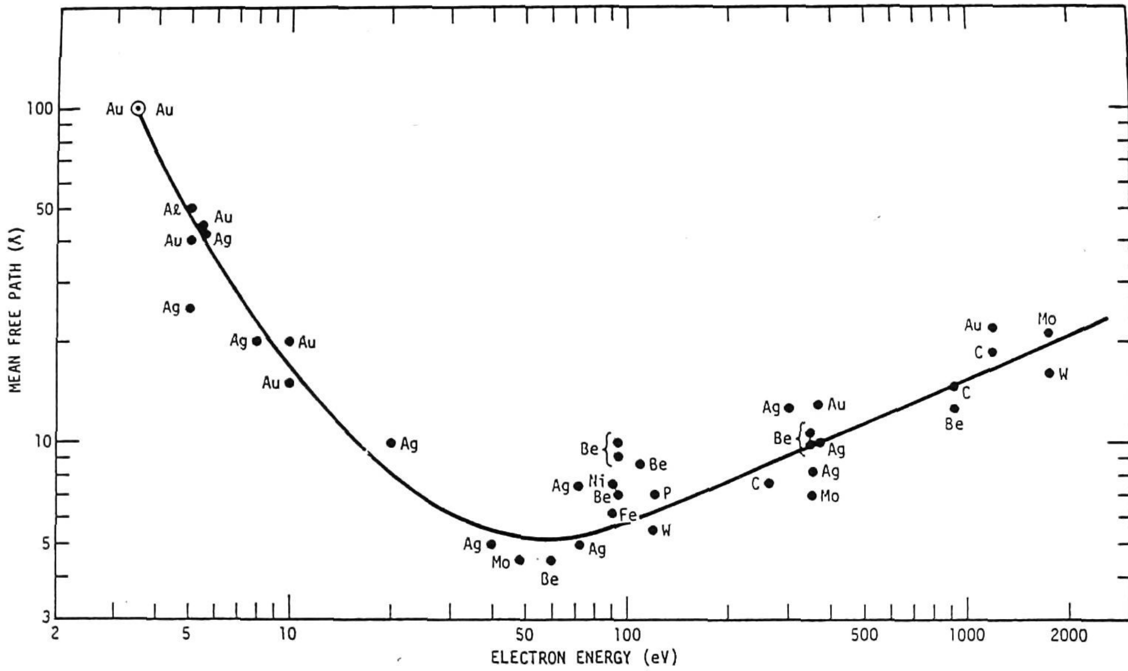

Figure 3.1 A "universal curve" is formed by the relationship between the electron mean free path for inelastic scattering in solids and electron kinetic energy. The minimum in the curve arises from the interaction between single particle and plasmon excitation processes. At low energies the dominant interaction is with single electrons; the mean free path for this process decreases with energy. At high energies, the interaction of the incident electrons is dominated by collective effects; the mean free path for such plasmon excitation processes increases with energy [reprinted from ref. 2].

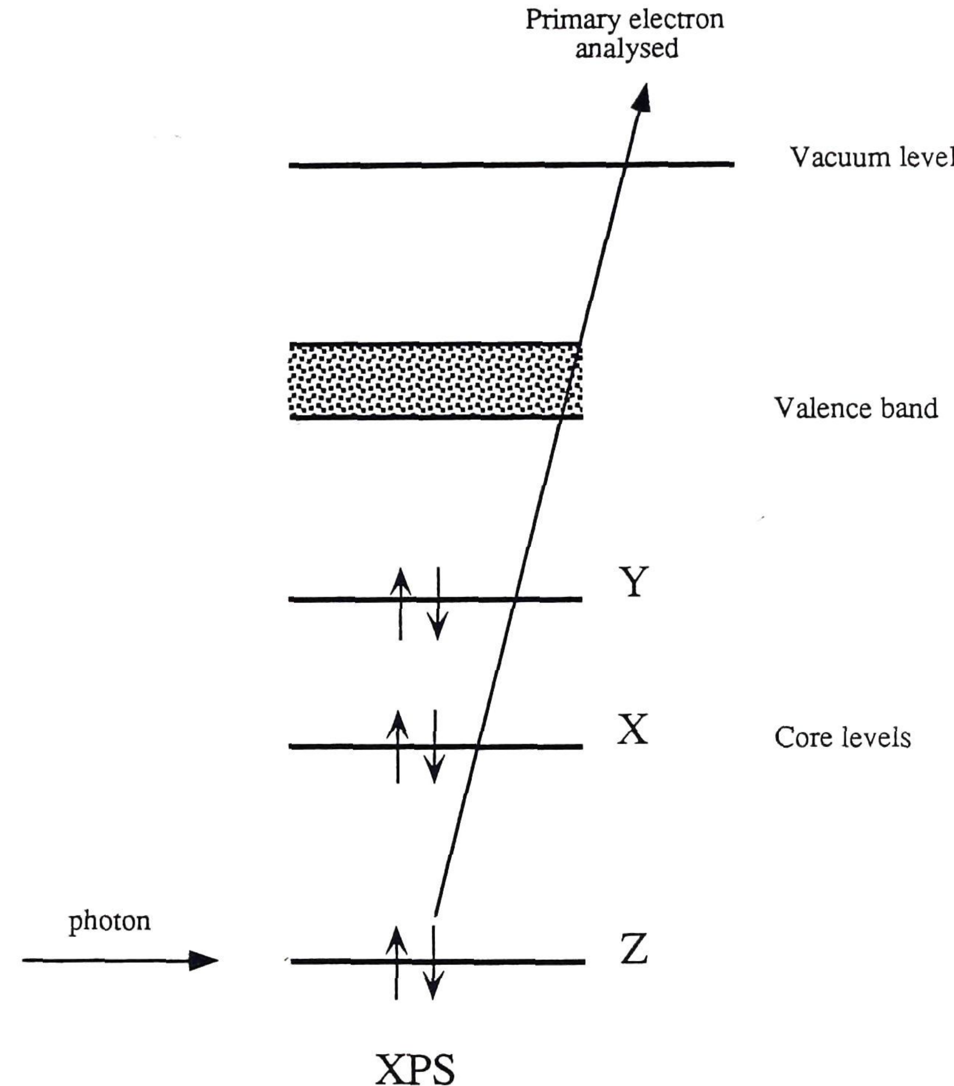

Figure 3.2 Schematic description of the electronic processes forming XPS

The spectrum of the X - rays produced contains bremsstrahlung and characteristic K_α emission components. Bremsstrahlung accounts for around 50% of the observed X - ray intensity, however, does not have a significant effect on photoelectron emission. Bremsstrahlung is distributed over several keV and has a small amplitude in comparison with the K_α emission components. The $K_{\alpha\ 1,2}$ line has a FWHM of around 1eV for Mg and Al sources with greater energy resolution achievable if a monochromated X - ray source is used [4]. Standard unmonochromated X - ray sources are sufficient to determine core level binding energies to within 0.2eV. The electronic transitions and resulting spectral distribution associated with Al $K_{\alpha\ 1,2}$ X - ray emission are shown in figure 3.3. Other metals, such as Cr, Cu and Mo, can be used as X - ray sources. However, the FWHM of the K_α emission in each case is greater than 2 eV [4].

The photoelectrons are energy analysed resulting in a determination of the energy distribution of electron emission. This distribution shows characteristic peaks corresponding to the surface constituents. The kinetic energy of the photoelectrons arising from an atomic species can be written as

$$E_{KE} = h\nu - E_B - e\phi \qquad (3.1)$$

where $h\nu$ is the energy of the incident radiation, E_B is the characteristic atomic binding energy of the ejected electron and $e\phi$ is the work function term. The kinetic energy of the photoelectrons is dependent on the energy of the incident radiation. Using X - rays from Mg (1253.6eV) and Al (1486.6eV) sources in combination provides additional information which is useful for discriminating between photoelectron and Auger electron emission processes and identifying instrumental effects.

The scope of photoelectron spectroscopy is broadening with the availability of synchrotron radiation. Electron synchrotrons provide a source of intense, polarised continuum radiation ranging from the ultraviolet to hard X - rays [3]. The energy of the source radiation is selected using a monochromator, removing the experimental restrictions of a single source energy.

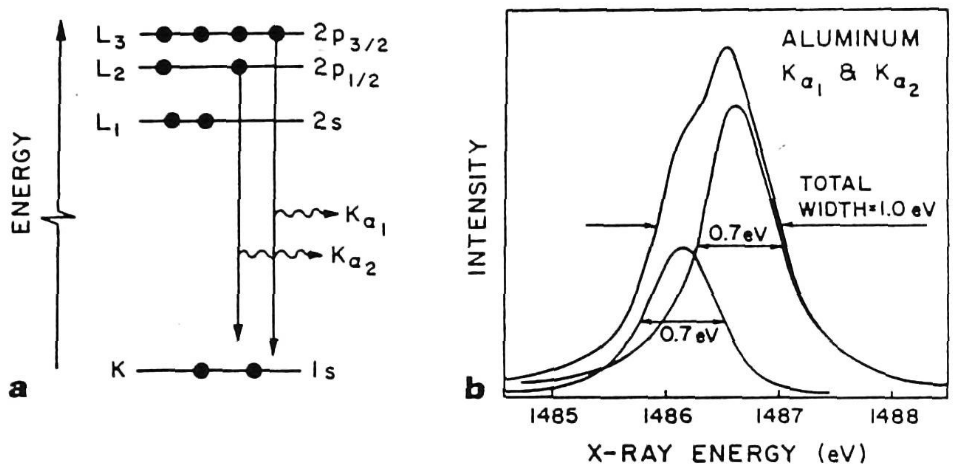

Figure 3.3 An X-ray photon source in common use in XPS spectrometers
(a) the electronic transitions giving rise to Al X-ray emission
(b) the two components which comprise the Al $K_{\alpha1,2}$ X-ray spectrum
[reprinted from ref. 4]

A Perkin Elmer PHI Model 560 surface analysis system located at the University of Queensland and a Kratos XSAM 800pci surface analysis system located at the University of New South Wales were used for the surface studies. XPS and Auger electron spectroscopy (AES) (discussed in the next chapter) both require accurate energy analysis of electrons emerging from a sample material. The Kratos system incorporated a concentric hemispherical analyser (CHA) whereas the Perkin Elmer system incorporated a cylindrical mirror analyser (CMA). Both forms of electron energy analyser are in common use.

Figure 3.4 shows the general layout of an XPS spectrometer incorporating a CHA [5]. Photoelectrons from the sample are collected and focussed by an electron optical system onto the entrance slit of the CHA. The use of an aperture and iris in the electron optics enables the size of the electron collection spot to be restricted to less than 80μm for XPS. The addition of scanning plates enables the effective collection point to be scanned across the sample, creating a compositional map of the surface.

The final electron lens retards the energy of the electrons to a preselected pass energy before they enter the hemisphere. Retardation is used in both CHA and CMA systems to enhance the relative resolution of the analyser. For example, obtaining an absolute energy resolution of 0.5eV for 1000eV electrons requires an analyser capable of achieving relative resolutions of 5×10^{-4}. If a pass energy of 50eV is used the relative resolution required is 1×10^{-2} and more easily achievable [6,7]. This enhancement is of particular importance for XPS.

Potential differences are applied, with respect to earth, to the two concentric sectors of the CHA. The electrons are electrostatically guided through the analyser along equipotentials, ending at the exit slit and electron detector [4]. A complete energy spectrum is obtained by sweeping the retarding field potential and recording the electron counts as a function of kinetic (or binding) energy [8].

Figure 3.5 shows the general layout of an XPS spectrometer incorporating a double pass CMA. Electrons emerging from the sample enter the analyser through two spherical retarding grids. These grids retard the kinetic energy of the electrons entering the CMA to the pass energy. The electrons travel along curved paths, reflected by the potential difference applied between the outer and inner cylinders, ending at the exit slit and electron detector [6-8]. For XPS, the inner cylinder is floating above earth, whereas for AES both the inner cylinder and the retarding grids

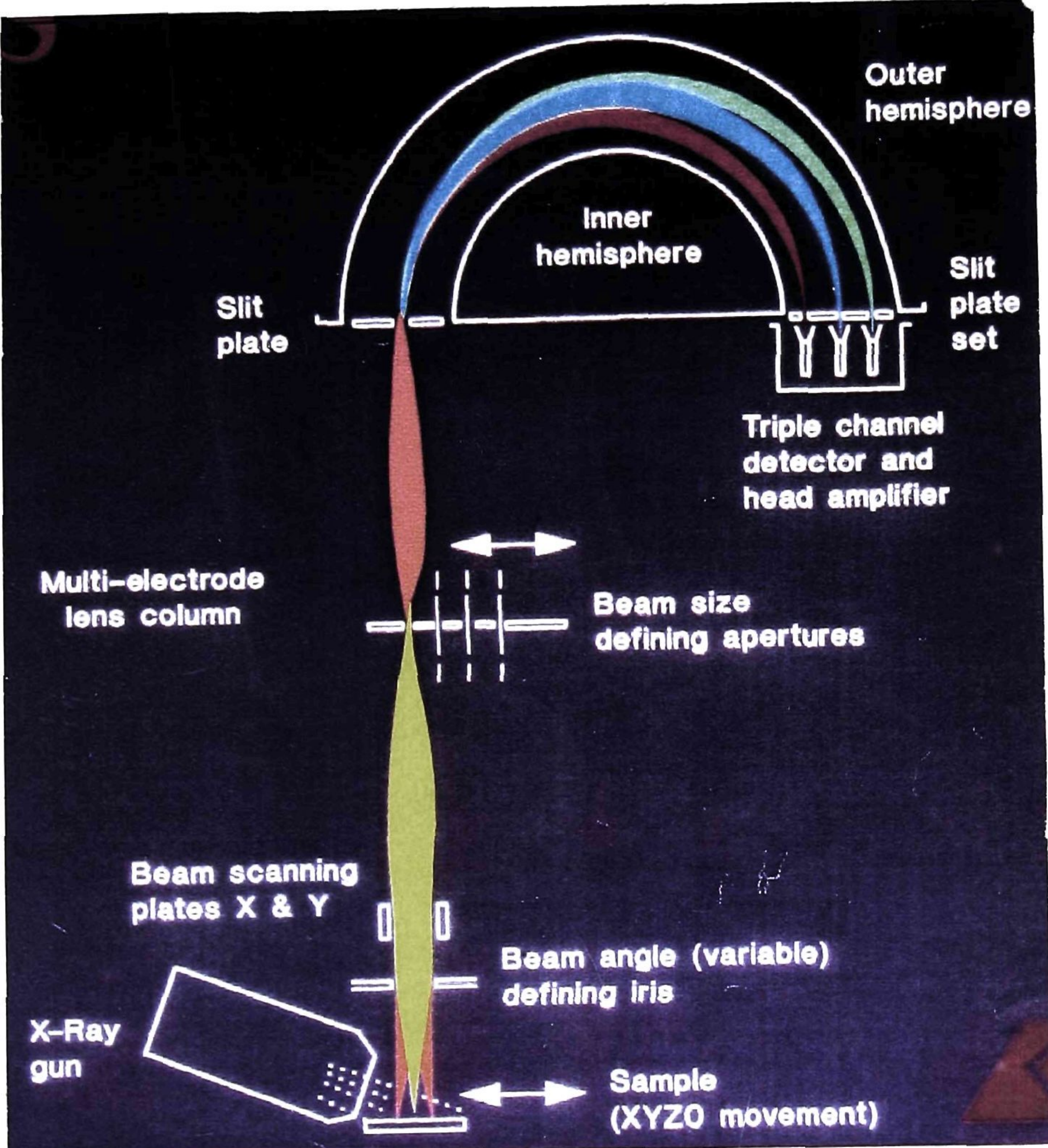

Figure 3.4 Schematic description of an XPS spectrometer incorporating an concentric hemispherical analyser (CHA). X-rays are produced by electron bombarding a metal target (usually Mg or Al) held at 10-20kV with electrons from an adjacent filament. X-ray irradiation of a sample produces photoelectrons which are collected and focussed by the electron optics onto the entrance slit of the hemisphere. The photoelectron energies, measured using the CHA, provide both chemical and elemental information about the sample. [reprinted from ref. 5]

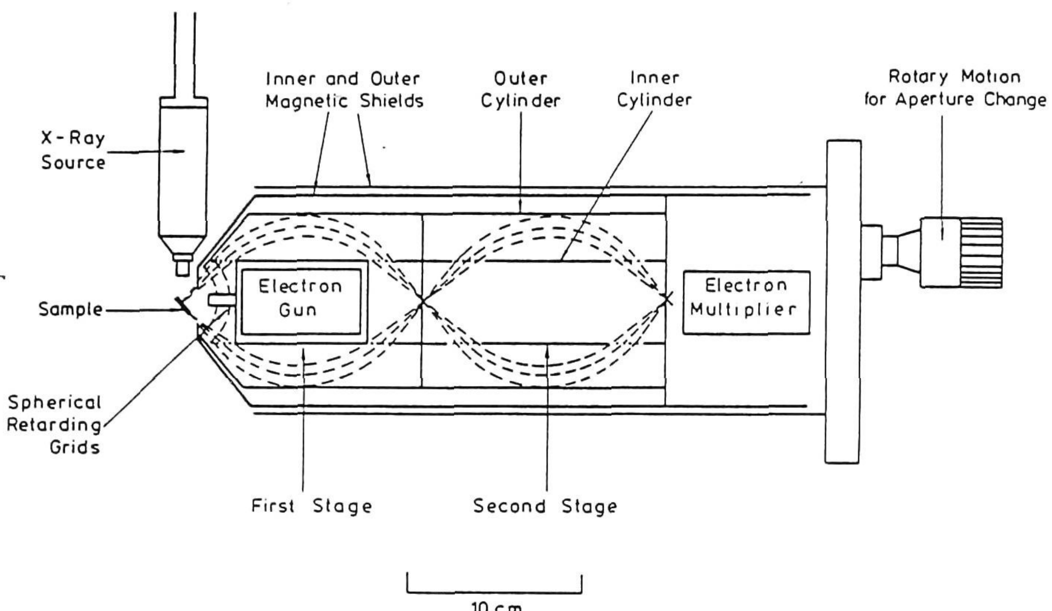

Figure 3.5 Schematic description of an XPS spectrometer incorporating a double pass cylindrical mirror electron energy analyser (CMA) used for both XPS and AES. The electrons entering the CMA are retarded to a constant pass energy using two spherical grids at the entrance. The apertures at the entrance and exit of the second stage of the CMA can be adjusted remotely to alter the function of the analyser. For AES both the inner cylinder and the spherical grids are earthed [reprinted from ref. 6].

are earthed [6,7]. A complete energy spectrum is created by sweeping the retarding field potential and recording electron counts as a function of kinetic (or binding) energy.

Electrons are detected at the output of the analyser by an electron multiplier. The channel electron detector (or channeltron™ [9]) is commonly used for this purpose. The detector, in this case, is a continuous dynode consisting of a curved semiconductor coated glass funnel or tube. A potential difference of several keV is applied between the ends giving a gain of up to 10^6. The walls have high secondary electron coefficients with incident electrons creating a cascade of electrons along the channeltron™ [4,10]. Single electrons are detected and counted as 200mV negative pulses [11]. The surface analysis systems used for this study both incorporated computer controlled data acquisition.

3.3 Film Preparation

One of the primary aims of this study was to investigate film structure and degradation processes in commercially produced ETCs. The deposition apparatus used to produce the films, described in section 2.4.2, was originally constructed as an industrial prototype. Industrial coaters used in Australia and in Japan are based closely on this design. The film preparation methods described in this section were chosen to emulate the commercial deposition process. The results obtained in this study are therefore directly transferable to commercial deposition processes.

Spectrally selective films were deposited according to a standard production method for solar ETCs [12,13]. Pure a-C:H films were deposited using only the final steps of the production method with the correct starting conditions. Films were deposited onto a range of substrates: glass microscope slides, high purity polycrystalline copper (99.9%, Goodfellow Metals), oxygen free, high conductivity (OFHC) polycrystalline copper (ETP - Oxford), and commercial grade polycrystalline copper and aluminium. The substrates were cut to size (square: 10mm x 10mm and 25mm x 25mm) and polished to a mirror finish using a combination of abrasive paper, metal polish and suspended alumina (0.3μm). The substrates were repolished and cleaned with acetone and isopropyl alcohol immediately prior to deposition.

The sputter process involves a series of steps, as shown in Table 3.1. A summary of the deposition conditions used in the sputter process is shown in Table 3.2. The first layer deposited is a stainless steel/carbon mixture. This results from a sputter cleaning operation in argon gas of the stainless steel cathode which had been coated with carbon at the end of the previous deposition cycle. This first layer enhances the adhesion of the spectrally selective film to the glass but otherwise plays no role in determining the properties of the system. The second layer to be deposited is copper which is sputtered from a copper cathode in argon gas. The copper is responsible for the very low emittance of the completed spectrally selective film. The third and final layer is graded stainless steel/carbon cermet which increases the solar absorptance of the surface without substantially increasing the thermal emittance. This layer is produced by sputtering a stainless steel cathode in a mixture of argon and acetylene. The layer is metal rich at the copper interface, grading to pure a-C:H at the film surface. This gradation in composition is achieved by increasing the amount of acetylene in the discharge during the deposition process. Towards the end of the process, the decomposition of acetylene leads to the deposition of carbon onto the surface of the cathode at a greater rate than it is removed by sputtering ("poisoning"). The sputter yield for carbon is significantly lower than that of stainless steel [14] so the cathode rapidly becomes completely covered with carbon and deposition of stainless steel ceases. [15].

The composition and properties of the spectrally selective film depend on the details of the deposition parameters at each step - discharge current and voltage, gas pressure and composition, magnetic field - as well as on the geometry of the magnetron source and substrate location. An optimisation of the film deposition conditions was performed by Harding, Window and Craig [13,16]. Films made according to this optimisation are made commercially by Shiroki Corporation (Japan) and are referred to here as "production" films.

Sample substrates polished
and cleaned

Samples loaded into batch coater
and chamber evacuated to a pressure
of $\approx 5 \times 10^{-6}$ torr

Pressure gauges, power supplies, gas pressures,
flow rates and cooling water checked
before commencement of deposition process

Stainless steel cathode sputtered
in Ar until clean. This process
forms the SS/C adhesion layer

Copper cathode sputtered in Ar
to form the copper low emittance layer

Stainless steel cathode sputtered in Ar with
an increasing concentration of acetylene.
This process forms the graded
stainless steel/carbon cermet layer.

Chamber isolated, cooled and vented with
argon then dry nitrogen. Samples are removed
and stored in a dessicator until analysed

Table 3.1

Flow chart showing the major steps in the fabrication of spectrally selective films in this laboratory.

General Conditions	
System base pressure:	~5 x 10^{-6} torr
Argon pressure:	4 x 10^{-3} torr
Magnetic field:	0.03 T
Cathode current:	8 A

a-C:H deposition	
Argon flow rate:	80 sccm
Acetylene flow rate:	95 sccm
Discharge voltage:	650 - 750 V
Approximate deposition rate:	9 nm/min

Stainless steel/carbon deposition	
Argon flow rate:	90 sccm
Acetylene flow rate:	0 - 250 sccm
Discharge voltage:	600 - 700 V
Approximate deposition rate:	variable

Copper deposition	
Argon flow rate:	90 sccm
Discharge voltage	590 V
Approximate deposition rate:	17 nm/min

Table 3.2 Deposition conditions for the sputtered films. The approximate deposition rates quoted correspond to targets moving in a planetary fashion around the cathode. The cathode to substrate distance is 30 - 100mm. [1 sccm = a flow of $1cm^3$ of gas at STP per minute]

3.4 Experimental Method

The experiments were performed in ultrahigh vacuum using a Perkin Elmer PHI Model 560 surface analysis system and a Kratos XSAM 800pci surface analysis system.

The Perkin Elmer system contained a double pass CMA with a concentrically mounted electron gun for AES and a perpendicularly mounted dual anode (Mg/Al) X - ray source for XPS. The MgK_{α} X - ray source was operated at 400W. The maximum energy resolution of the CMA was 1.2eV operated for XPS analysis in the fixed analyser transmission (FAT) mode with a pass energy of 25eV for the Ag $3d_{5/2}$ emission. The Perkin Elmer system is shown in figure 3.6.

The Kratos system contained a CHA with three channeltron™ detectors. Electrons were collected and focussed onto the entrance slit of the analyser with an electron optical system. An aperture plate and iris were incorporated into the optics to restrict the electron collection spot to a minimum diameter of about 80μm. The aperture plate contained large size (approximately 6mm x 4mm), 600μm, 200μm and 100μm openings. The perpendicularly mounted dual anode (Mg/Al) X - ray source was operated at 150 - 300W. The maximum energy resolution of the CHA was 0.75eV operated for XPS analysis in the fixed analyser transmission (FAT) mode with a pass energy of 5eV for the Ag $3d_{5/2}$ emission. The Kratos system is shown in figures 3.4 and 3.7. The electron binding energies (E_B) for both systems were calibrated against the Au $4f_{7/2}$ emission at E_B = 84eV [17,18].

3.5 Semiquantitative Analysis of XPS Data

The data obtained from XPS experiments can be analysed to give semiquantitative estimates of film thickness, composition and bonding configuration. The existence of photoelectron peaks in an XPS spectrum readily identifies the elements present in the film surface layers. Approximate estimates of stoichiometry can be deduced by comparing the intensities of the peaks against those in samples of known composition. Bonding configurations are investigated by deconvoluting complicated peak line shapes into a series of gaussian components.

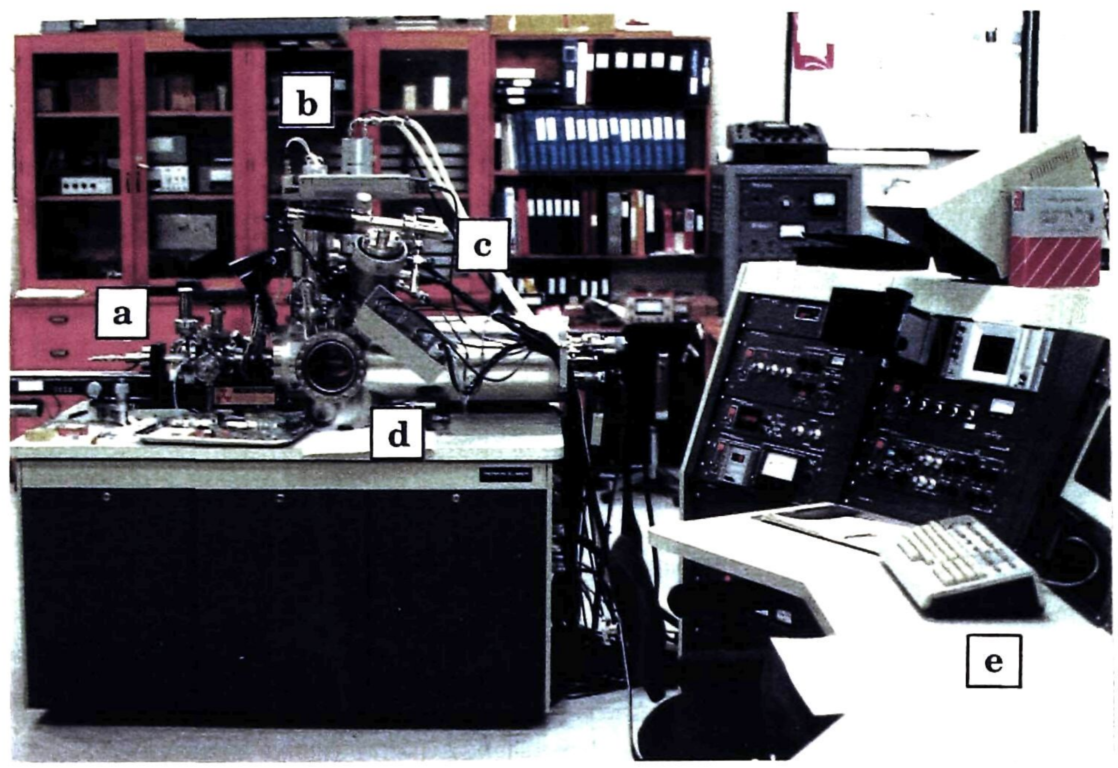

Figure 3.6 The Perkin Elmer 560 surface analysis system.

(a) Sample entry lock

(b) Secondary ion mass spectroscopy (SIMS) and X - ray gun

(c) Ion gun

(d) Main analysis chamber and cylindrical mirror analyser (CMA)

(e) Control instrumentation

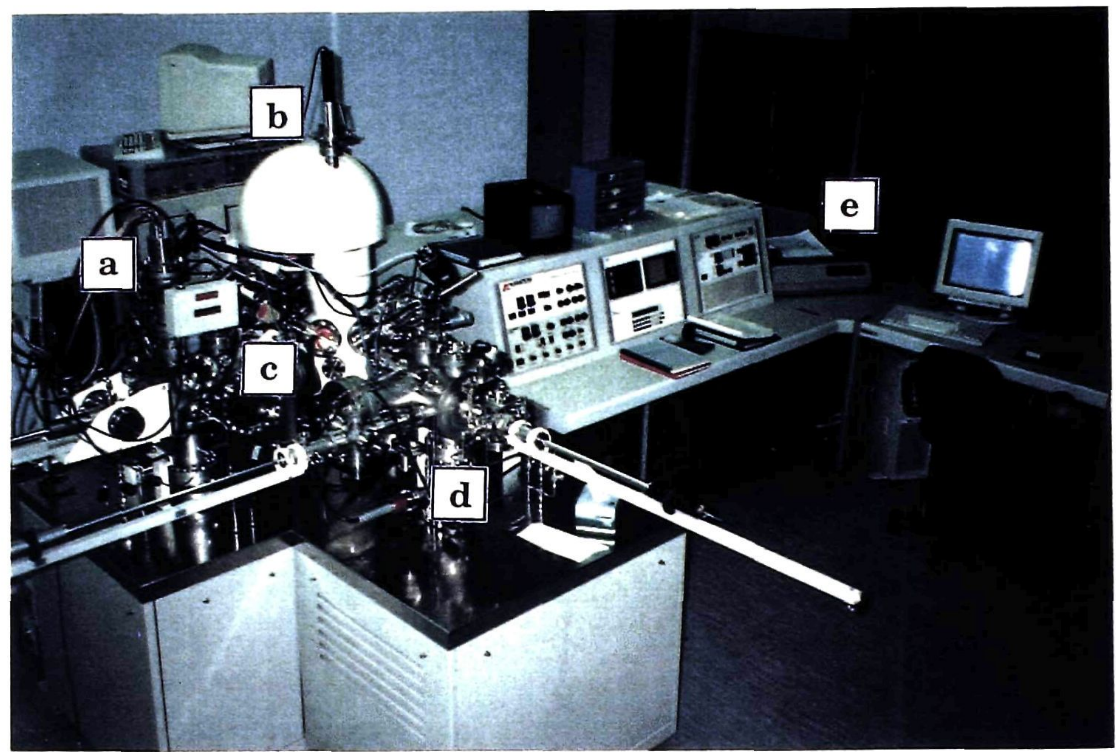

Figure 3.7 The Kratos XSAM800pci surface analysis system

(a) Secondary ion mass spectroscopy (SIMS)

(b) Concentric hemispherical analyser (CHA) and sample alignment laser

(c) Main analysis chamber (white) and ion gun

(d) Sample entry lock and preparation chamber

(e) Control instrumentation

The attenuation of XPS signals originating from the film substrate can be used to quantify film thickness [19].

Photoelectron emission intensity for a surface constituent or adsorbate X is given by

$$I_x \propto \sigma_x N_x \Gamma(E) T(E) \qquad (3.3)$$

where σ_X is the photoelectron excitation cross section, N_X is the number of X atoms per unit area, $\Gamma(E)$ is the MFP of electrons with energy E and T(E) is the transmission function of the analyser at energy E [20]. This relationship only includes contributions from a single atomic species and assumes a homogeneous film of sufficient thickness to screen any contributions from the underlying substrate [19]. The relative concentration of two atomic species, X and Y, can therefore be written as

$$\frac{N_x}{N_y} = \frac{I_x \sigma_y \Gamma_y T_y}{I_y \sigma_x \Gamma_x T_x} \qquad (3.4).$$

If the photoelectron peaks have about the same energy, the MFPs and transmission functions are approximately equal and can be cancelled out [4]. The electron MFPs for very thin films are greater than the thickness of the film and therefore can be neglected. Photoelectron excitation cross sections are generally referenced to the C 1s emission (σ_{C1s} = 1.00) and are widely reported [21,22]. The transmission function is determined by experiment and calculation for each instrument, taking the form

$$T(E) \propto E^{-k_1} \qquad (3.5)$$

where k_1 is a constant (usually ≈ 0.7 - 1.0) [4]. Electron MFP can be deduced from sources such as the universal curve [2] or empirical expressions such as

$$\Gamma = k_2 \frac{E^{k_3}}{\mu} \qquad (3.6)$$

where k_2 and k_3 are constants, μ is the density of the material and E is the electron energy (for E less than 150eV) [19].

Combining equations 3.4, 3.5 and 3.6, the relative concentration of two atomic species can be written as

$$\frac{N_x}{N_y} = \frac{I_x \sigma_y}{I_y \sigma_x}\left[\frac{E_x}{E_y}\right]^{k_3 - k_1} \qquad (3.7)$$

where k_3 equals zero for very thin films [19].

The line shapes of XPS spectra contain information about the bonding environment of the constituents of the film. Several factors contribute to the complicated lines shapes observed in this work. Most peaks are asymmetric with a considerable tail at higher binding energies adjacent to the peak centre. This arises from inelastic scattering of a portion of the photoelectrons emerging from buried regions of the film and is a function of the electron MFP. Multiple plasmon losses are also observed in materials such as Mg, Al and Na. A series of small peaks occurs at higher binding energies, each separated by intervals corresponding to the plasmon energy [3].

Each discrete bonding state present makes a contribution to the total peak for a given emission peak. The different chemical environments of the atoms cause shifts in the central peak energy. If these shifts are sufficiently large then the individual contributions from the various chemical states can be identified. Sophisticated curve fitting software is routinely incorporated in surface analysis systems to facilitate this process. Assigning bonding states to deconvoluted XPS data generally requires additional information. Peak energies for atoms in many different compounds and bonding configurations are tabulated in reference atlases [23]. Sample charging must also be considered as peaks can be shifted towards higher binding energies by several eV. This occurs when the substrate is a poor conductor and cannot maintain electrical neutrality in response to photoelectron emission [24].

XPS can be used to estimate film thickness by quantifying the attenuation of a characteristic substrate peak by a thin uniform overlayer of a known material. The film thickness, d, is given by

$$d = \Gamma \ln\left[\frac{I_0}{I}\right] \qquad (3.8)$$

where Γ is the electron MFP in the overlayer and I and I_o are the intensities of a characteristic peak from a covered substrate and a clean substrate, respectively. The

accuracy of this technique depends on two factors, the accuracy of the electron MFP and the uniformity of the overlayer. A non - uniform overlayer will give substrate peaks dominated by contributions from the thinnest portions of the film due to the exponential thickness/peak intensity relationship [19].

3.6 Results and Discussion

3.6.1 Surface Composition of Stainless Steel/Carbon Cermet Films

The results of XPS surveys of the outermost surface of graded stainless/carbon cermet films on polycrystalline copper substrates are shown in figure 3.8. The method of film preparation is described above in section 3.3. These data are for films as - prepared and after baking for 60 minutes to 670K Note that no corrections for surface charging have been made. There are strong peaks at binding energies, E_B ~ 286eV and E_B ~ 536eV, corresponding to C 1s and O 1s emission respectively. Carbon and oxygen appear to be the main species on the surface of the film. Traces of argon (E_B~ 238eV), the sputtering gas used in the production process, and residual nitrogen (E_B~ 400eV) from the batch sputter coater chamber are also evident in some films. The incorporation of residual gases is common in sputtered carbon films. The dense, tightly packed structure of some carbon films prevents residual gases diffusing out of the structure under normal conditions [25].

Following baking to 670K for 60 minutes in vacuum (~ 10^{-6} torr), there is a decrease in the intensity of O 1s as compared with C 1s and a loss of argon and nitrogen. The former effect may be attributed to formation and desorption of CO and CO_2 during the baking process [26,27]. The major outgassing products, H_2 and CO, have been previously observed at temperatures > 470K with lesser quantities of H_2O and CO_2 being detected at temperatures up to 570K [28].

XPS was used to study the composition a-C:H surface layers of the cermet films. Figure 3.9(a) shows the carbon 1s photoelectron emission peak from such a film. Note that no corrections for surface charging have been made. The broad C 1s emission (FWHM = 2.5eV) indicates the presence of a variety of chemical environments. This is consistent with the fact that amorphous hydrogenated carbon films have been shown previously to exist in a combination of ring structures and

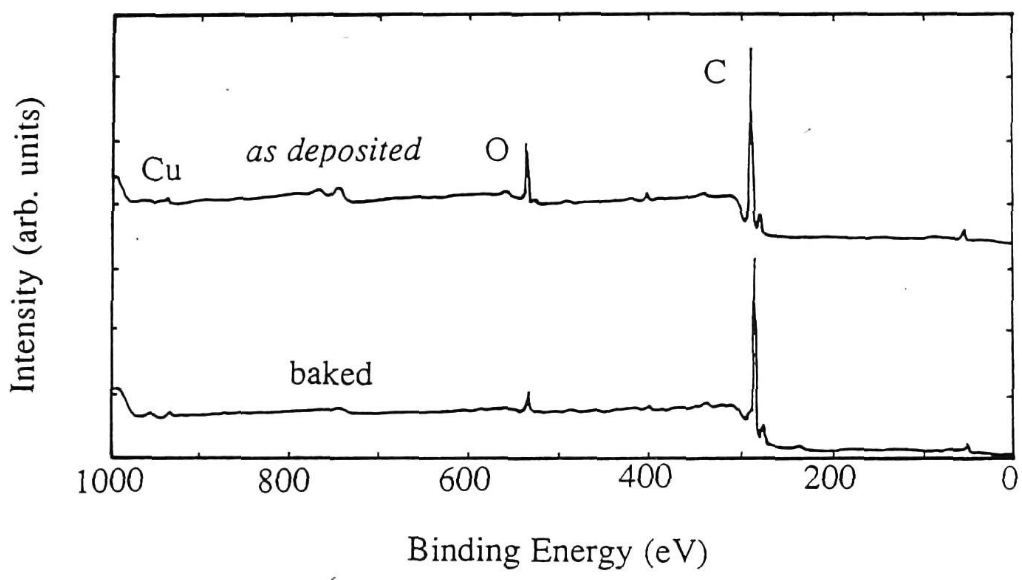

Figure 3.8 XPS surveys (on the same scale) of spectrally selective films deposited on polycrystalline copper as deposited and after baking to 670K for 60 minutes.

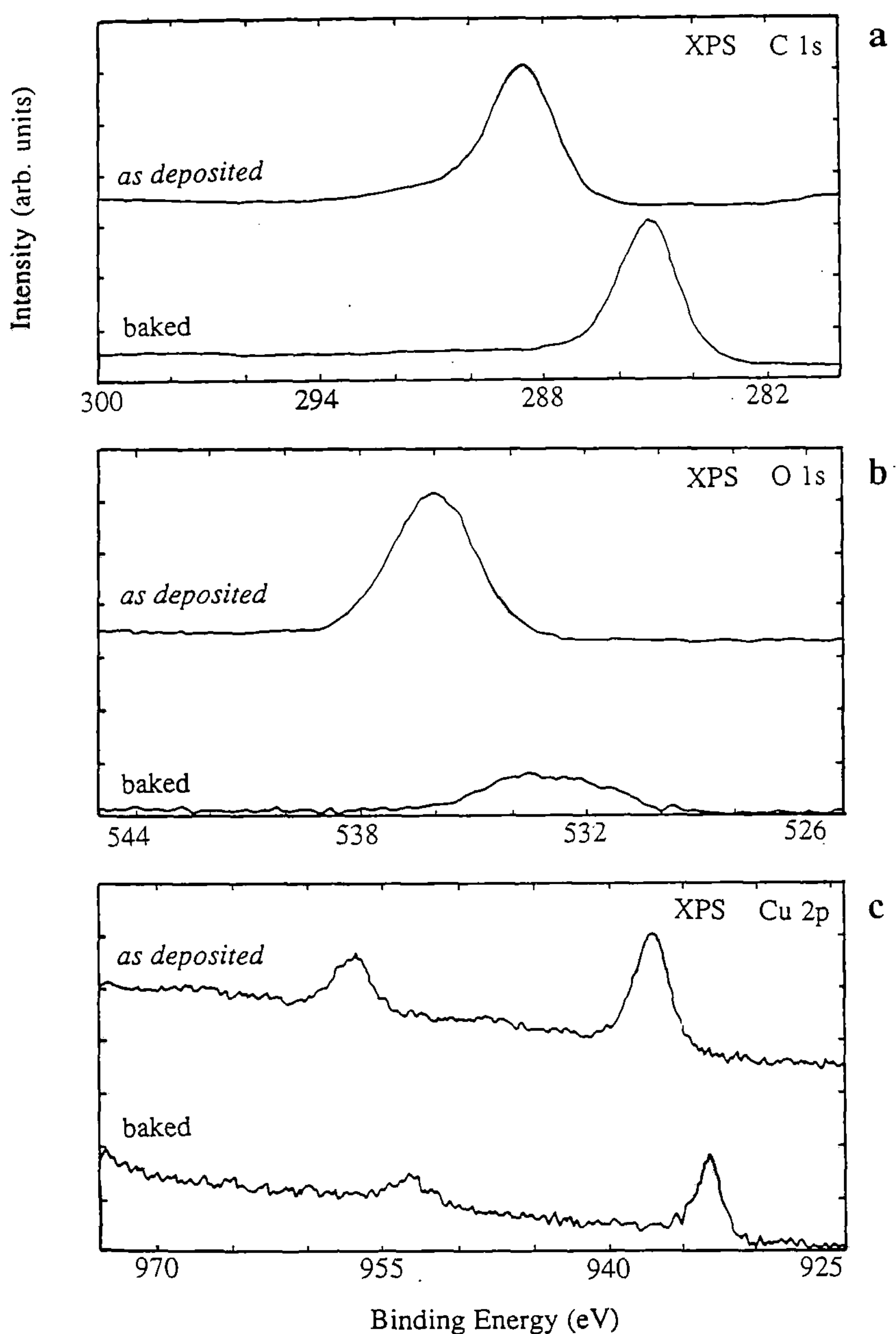

Figure 3.9 XPS spectra (on the same scale) of the surface constituents of the spectrally selective film as deposited and after baking to 670K for 60 minutes: (a) C 1s; (b) O 1s; and (c) Cu 2p.

diamond - like bonding [29]. The 20% decrease in the FWHM of the carbon 1s photoelectron peak after baking (figure 3.9(a)) may be attributed to marked bonding changes in favour of six member, graphitic carbon ring structures, with the liberation of H_2 and CO [30]. Both the interlayer and intralayer ordering are increased [31] while the variety of carbon bonding is reduced.

The intensity of the O 1s emission is significantly reduced as a result of baking, as shown in figure 3.9(b). The lack of change in the FWHM of O 1s after baking, as compared with C 1s, suggests that residual O 1s material in all configurations has been reacted uniformly with C 1s to form CO and CO_2. The results of previous surface degassing studies are consistent with these observations [26,28].

XPS studies of the freshly prepared films on polycrystalline copper substrates (both as - prepared and baked) show no evidence of subsurface layers. Yet, copper is present in the surface of such films stored in air for around 4 months (figure 3.9(c)). This indicates that holes may have formed in the film over a period of months, exposing the copper layer of the film or alternatively substrate imperfections may be protruding through the deposited film. The structural changes observed may be a long term analogue of those occurring as result of baking. When the films are baked, the copper signal is attenuated suggesting that the film is collapsing over the exposed copper regions. This may be due to removal of volatile contaminants from the film or possibly surface oxidation.

The ratio of the intensities of one of the copper peaks before and after baking gives the attenuation of the signal. In this case the Cu $2p_{3/2}$ transition is reduced by a factor of ~ 2.9. The copper peak is centred at E_B~ 934eV and corresponds to a photoelectron kinetic energy of ~ 319eV for a Mg X - ray source. The approximate MFP, with reference to the universal curve (figure 3.1 [2]), is (8.5 ± 0.5) Å. The thickness of the layer formed over the copper regions as a result of baking can therefore be estimated using equation 3.8 as (9.2 ± 1.5) Å.

After the baking of the film the copper signal had two weak satellite peaks. This peak configuration indicates weak oxidation of the copper, probably to a Cu_2O state [32]. This apparent instability in air poses no major problems in the ETCs but limits the potential of the surface in non - vacuum applications on polycrystalline substrates containing oxygen.

The structural changes in the film induced by baking cause changes in film conductivity, dielectric constant and sample charging behaviour in response to X - ray induced photoemission. After baking a shift of about 4eV to lower binding energies is observed in the central energy of photoelectron peaks shown in figures 3.9(a) - (c). The shift in energy is the same for each of the photoelectron peaks. The likely cause of this shift, therefore, is changed sample charging behaviour rather than a chemical shift in any of the peaks.

Baking significantly reduces the quantities of residual argon and nitrogen in the surface structure of the film, as shown in figure 3.10. These materials are incorporated into the film during deposition. While the presence of these contaminants is unlikely to affect significantly either the optical or gas adsorption performance of the film, the concomitant improvement in film purity simplifies the optimisation of film properties.

Secondary ion mass spectroscopy (SIMS) was also used to identify the atomic constituents of the film surface by eroding the surface layers with an argon ion gun and analysing the sputtered material with a quadrupole mass spectrometer coupled to a series of ion lenses and accelerating grids. SIMS provides a qualitative indication of the species present and is particularly sensitive to materials present in small traces. These results are presented to complement the studies of film properties discussed in this chapter and in the subsequent chapters. Detailed consideration of the technical aspects of SIMS is beyond the scope of this work.

Figures 3.11(a) and (b) show the SIMS spectra for positive and negative ions ejected from the film surface. The carbon, hydrogen and oxygen components of the film are featured in figure 3.11(a), along with a wide range of metal ions. The metal atoms are present in the film only in trace quantities and are not observed using XPS. They can, however, be unambiguously identified using SIMS. Similarly, figure 3.11(b) shows the carbon hydrogen and oxygen negative ion components expected along with other species, such as fluorine and chlorine, present in trace quantities.

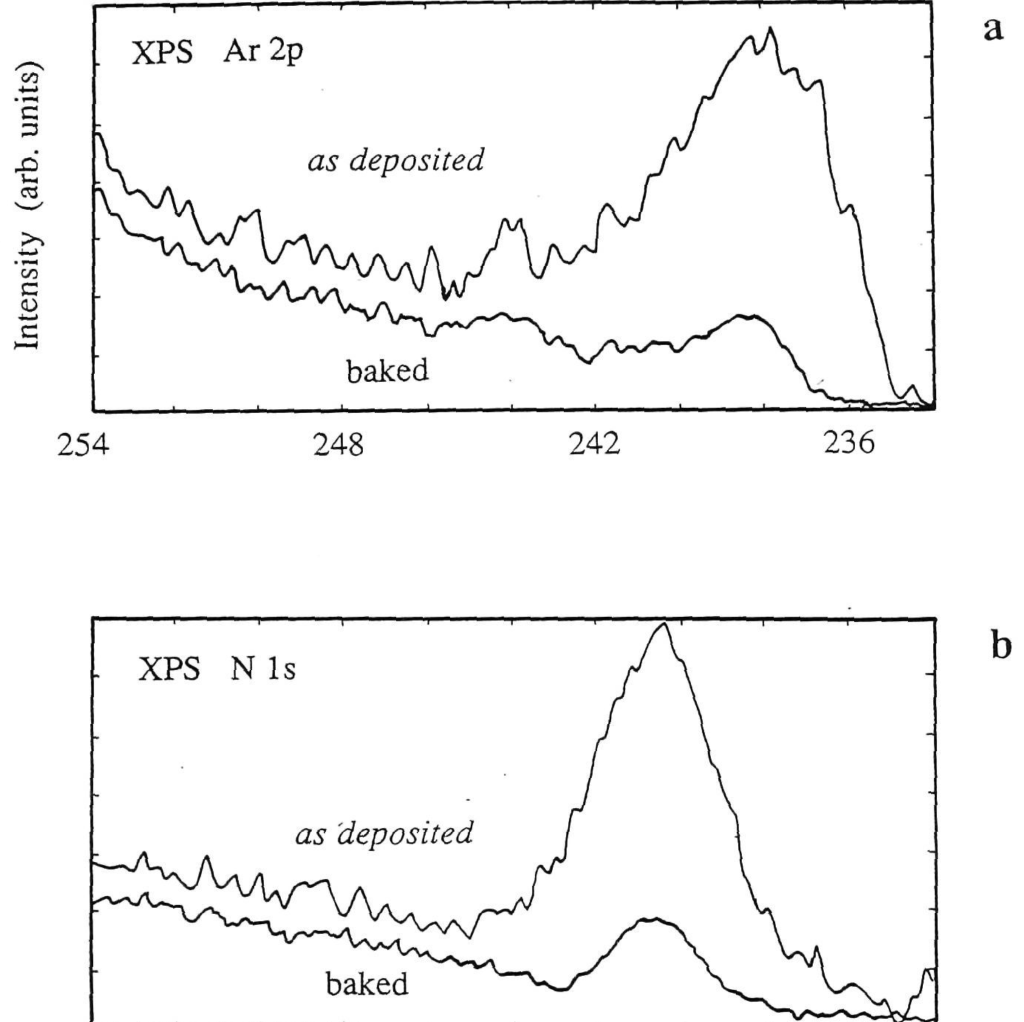

Figure 3.10 XPS spectra (on the same scale) of the (a) Ar 2p and (b) N 1s photoelectron peaks. The spectrally selective film sample was analysed as deposited and after baking to 470K for 60 minutes. The intensity of the photoelectron peaks after baking is attenuated to about 25% of the initial value.

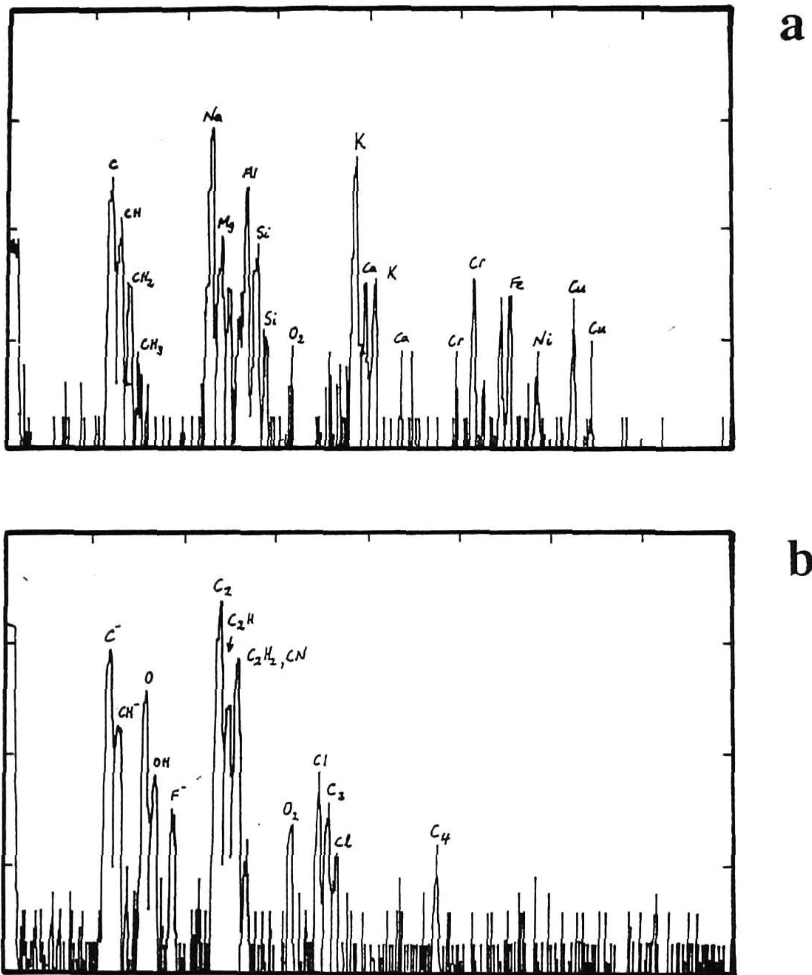

Figure 3.11 (a) Positive ion and (b) negative ion SIMS spectra giving the elemental composition of the outermost layers of the spectrally selective film. The ionic species corresponding to each of the peaks are indicated. SIMS is particularly sensitive to trace impurities, thus, carbon, hydrogen and oxygen species are detected along with a range of other species.

3.6.2 Surface Structure of Amorphous Carbon Films

The method of film preparation has a strong influence on the properties of amorphous carbon and metal/carbon cermet films. XPS was used to investigate the surface structure of three amorphous carbon films fabricated using different methods. Films were produced using reactive d.c. magnetron sputtering, as described in section 3.3, r.f. glow discharge decomposition of methane and in a filtered cathodic vacuum arc system using a graphite target [33].

Figures 3.12(a) - (c) and 3.13(a) - (c) show the C 1s and O 1s XPS spectra, respectively, obtained for each of the three amorphous carbon films. The films were analysed as - prepared, without any additional surface cleaning. The Kratos system was set for analysis with a wide aperture size (6mm x 4mm) and fully open iris setting. Three gaussian components have been optimised to each of the peaks. The optimisation of the fitted components was chosen on the basis of model bonding configurations and associated binding energies.

The carbon spectra obtained in each case are quite complicated. The FWHM of each peak is strongly dependent on the chemical environments present. No single solution can be applied to the data using this scheme so the curve fit depicted is not unique. As a consequence, there are problems with attaching too much emphasis to the peak assignments and characteristics [34].

Surface structure is indicated by various features of the line shapes of the XPS spectra. All of the spectra have comparatively large FWHM. The FWHMs for the C 1s and O 1s spectra are all greater than 1.7eV and 2.1eV, respectively. This indicates that carbon and oxygen are present in a variety of chemical environments, as discussed above. It should be noted that the Kratos system used for this analysis has significantly better resolution than the Perkin Elmer system used to obtain the spectra shown in figure 3.9. The FWHMs obtained for the sputtered film in this case are therefore significantly reduced.

The C 1s peaks are all asymmetric; inelastic emission processes change the line shape at higher binding energies. A shoulder or satellite peak is present at $E_B \sim$ 290eV in the inelastic tail of the C 1s peaks of sputtered films and, in particular, vacuum arc films. This is due to a π bond shake - up originating from aromatically bonded carbon components [3]. The O 1s peaks are more symmetric than the C 1s peaks. However, they are also composed of a number of different contributions.

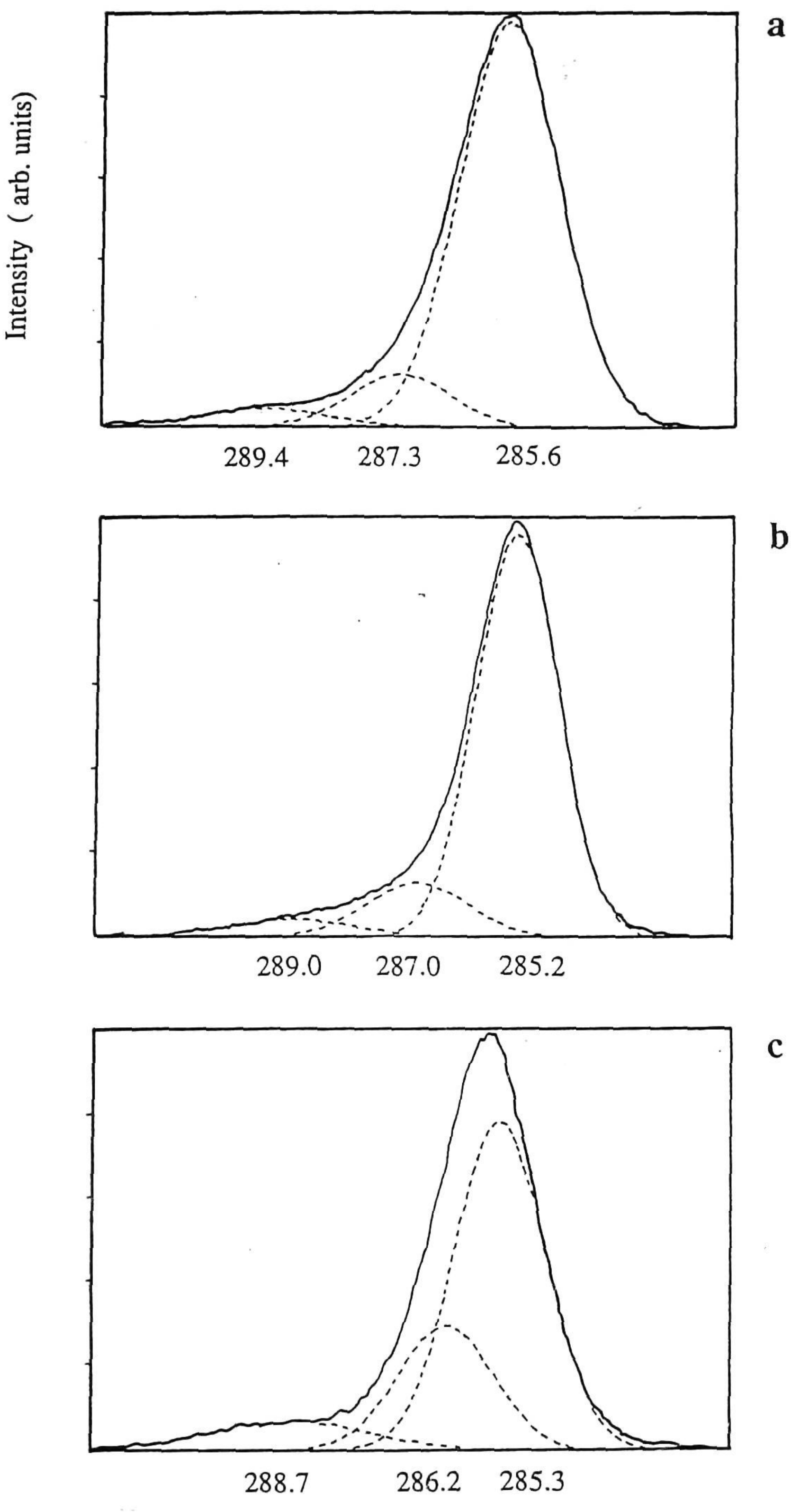

Figure 3.12 Carbon 1s XPS spectra for amorphous carbon films deposited using three different fabrication methods. The peaks have been deconvoluted into a three gaussian components (central energies are shown).
(a) reactive d.c. sputtering using acetylene; (b) r.f. glow discharge deposition using acetylene; and (c) vacuum arc deposition using a graphite target

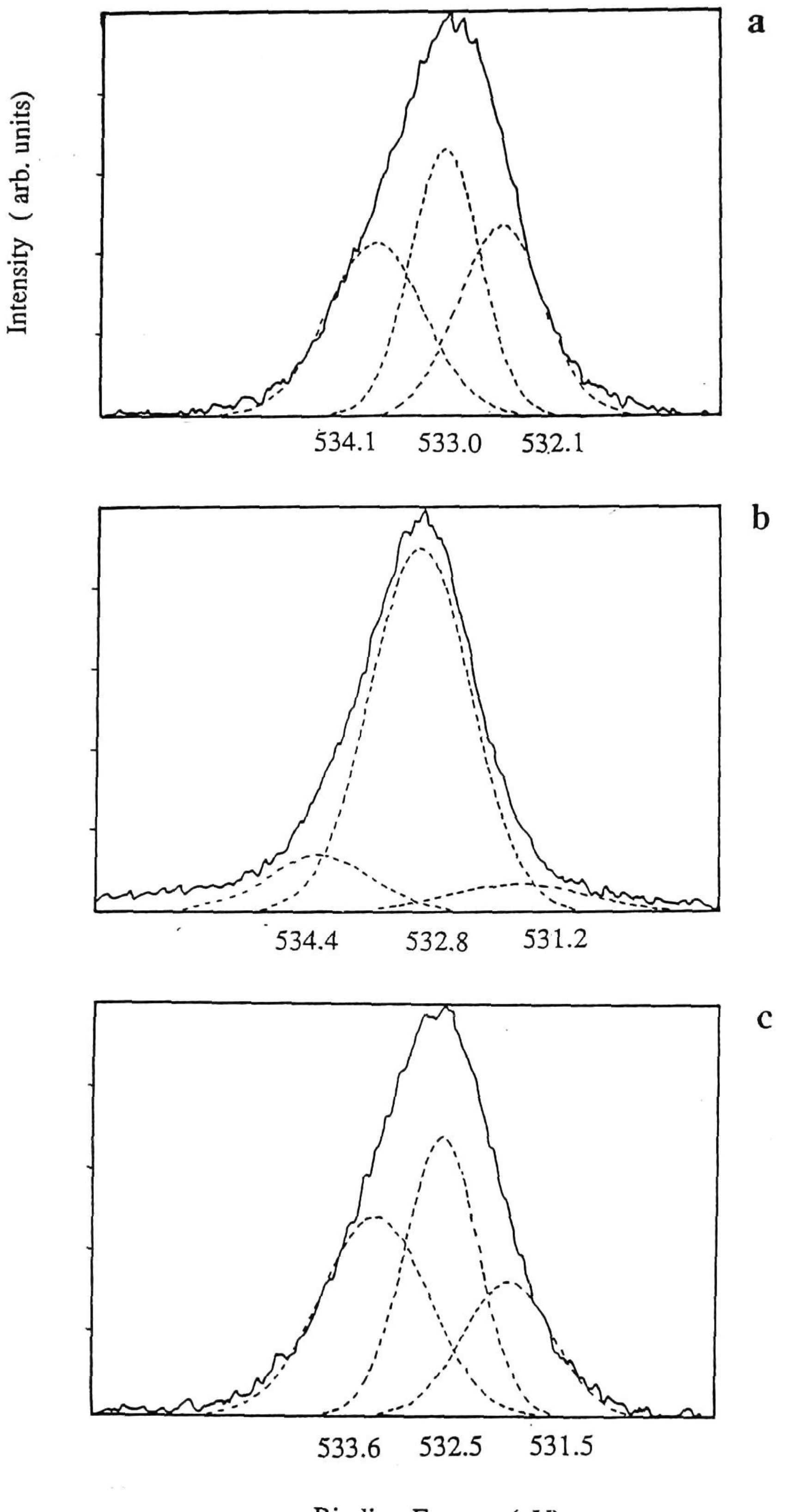

Figure 3.13 Oxygen 1s XPS spectra for amorphous carbon films deposited using three different fabrication methods. The peaks have been deconvoluted into three gaussian components (central energies are shown).
(a) reactive d.c. sputtering using acetylene; (b) r.f. glow discharge deposition using acetylene; and (c) vacuum arc deposition using a graphite target

Previous studies indicate that the sputtered film is composed of a mixture of graphitic and tetrahedral carbon [31]. The glow discharge carbon was deposited using a preferential etching technique. This deposition strategy seeks to increase the proportional of tetrahedral carbon in the mixed graphitic/tetrahedral carbon film composition [35]. The vacuum arc film is a diamond - like carbon film composed of greater than 85% tetrahedral carbon [31,36].

It is proposed that the three components fitted to the C 1s spectra correspond to contributions from material in the following bonding configurations: C - C ($E_B \sim$ 285.2eV), C - O ($E_B \sim$ 287eV) and aromatically bonded carbon ($E_B \sim$ 289eV). The assignment of these components is consistent with the atomic composition of the surface and the degassing studies mentioned above [26,28]. Similarly, it is proposed that the three components fitted to the O 1s spectra correspond to contributions from material in the following bonding configurations: O^{2+} ($E_B \sim$ 531.5eV), OH^- ($E_B \sim$ 532.5eV) and H_2O ($E_B \sim$ 534eV) [37].

The films were analysed using XPS as - prepared and after argon ion etching. Figures 3.14(a) - (c) show the C 1s spectra for the sputtered, glow discharge and vacuum arc films, respectively. The Kratos system was set for analysis with a 600μm aperture size and an iris setting giving a moderately restricted beam. The intensity of the C 1s emission for the glow discharge film was virtually unchanged by etching. The O 1s emission, however, was reduced in intensity by as much as 90%, corresponding to the removal of surface contaminants, as shown in figure 3.15(a) - (c). This coincided with a reduction of the FWHM of the C 1s emission as the variety of chemical environments present was reduced.

Etching removes contaminants from the carbon surface, in particular adsorbed water and CO. Shifts in the central energy of the C 1s photoelectron peaks to lower binding energies after etching can be attributed to changes in the chemical environment of the carbon surface atoms with the removal of C - O bonded species [23,37]. No significant changes in peak position are expected due to changes in sample charging behaviour as the bulk structure of the films is not affected by etching.

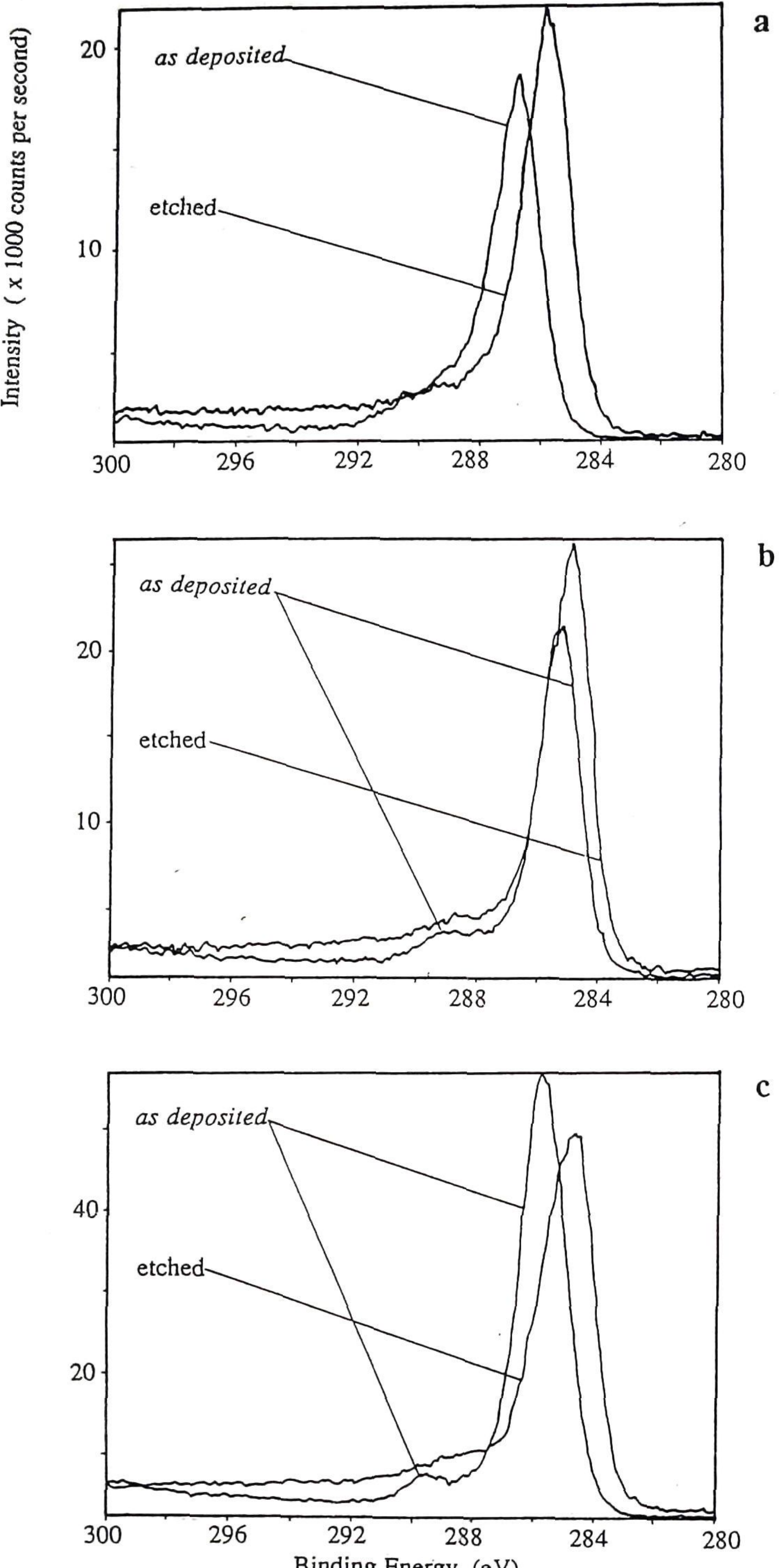

Figure 3.14 Carbon 1s XPS spectra for amorphous carbon films deposited using three different fabrication methods, before and after argon ion etching
(a) reactive d.c. sputtering using acetylene; (b) r.f. glow discharge deposition using acetylene; and (c) vacuum arc deposition using a graphite target

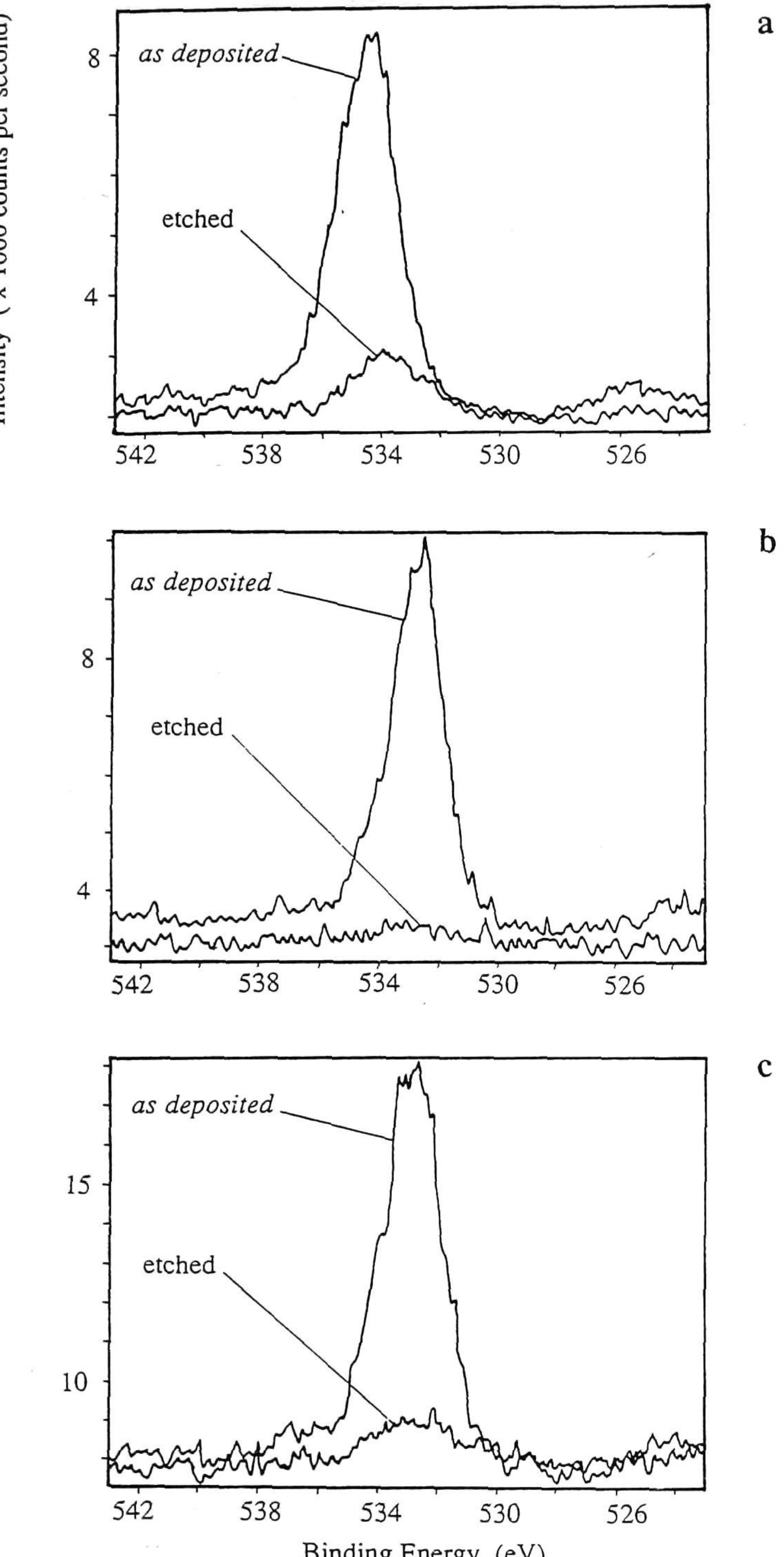

Figure 3.15 Oxygen 1s XPS spectra for amorphous carbon films deposited using three different fabrication methods, before and after argon ion etching
(a) reactive d.c. sputtering using acetylene; (b) r.f. glow discharge deposition using acetylene; and (c) vacuum arc deposition using a graphite target

The line shape of the C 1s emission for the vacuum arc carbon changed significantly with etching. The shoulder, corresponding to an aromatic shake up, was greatly reduced in intensity and the line shape of the main peak was also considerably altered. Possible explanations for this behaviour include the removal of the aromatically bonded carbon by etching or the disruption of aromatically bonded carbon to form an amorphous phase. The carbon surface layers of the vacuum arc carbon are apparently different in structure from the carbon bulk. It is proposed [38] that the vacuum arc carbon film has a tetrahedrally bonded bulk structure, terminated at the surface with a thin layer of graphitically bonded material. This is supported by the behaviour of the C 1s emission in response to etching.

This method of analysis allows surface contamination to be identified and distinguished from the surface structure. Complications arise, however, because both the film surface layers and the greater proportion of the surface contamination are carbonaceous in nature.

Argon was used to sustain a discharge in the case of the films produced using sputtering and glow discharge deposition. It is difficult to avoid the implantation of low levels of argon and any other gaseous species present (nitrogen, for example) in the film surface during these deposition processes. No significant changes in argon and nitrogen photoemission spectra are observed after etching. These results imply that either the argon ion beam was not sufficiently energetic to etch the implanted impurities or the latter were distributed throughout the film in relatively equal concentration. While both these explanations are plausible, depth profile analysis of the films is required to further investigate this area.

It is important to note the role of surface contaminants in this series of analyses. Contamination arising from a number of sources existed on the surfaces of all the films studied before analysis. High vacuum deposition apparatus was used in all cases to fabricate the films resulting in the incorporation of carbonaceous contamination and adsorbed water into the surface layers. Further, exposure to the atmosphere during storage, transport and transfer of the films between the point of fabrication and the point of analysis, inevitably results in atmospheric contamination.

3.7 Summary

XPS and SIMS studies of the surface layers of the spectrally selective film revealed that the principal constituents are carbon and oxygen. There is also surface contamination present as a residual effect of the deposition process in the form of argon and nitrogen. SIMS detected a range of surface contaminants present in trace amounts. While contamination is unlikely to effect the optical performance of the film significantly, gas adsorption is a considerably more surface sensitive process. The changes in the surface structure of the film in response to heating and cooling all must also be carefully considered in the context of long term film stability.

Major changes in the surface composition of the stainless steel/carbon cermet films occurred during film baking. This surface degassing process is an essential phase in the construction of ETCs. It was found that the intensity of the oxygen 1s photoelectron emission was greatly reduced. This corresponds to the removal of surface contaminants such as H_2O and CO. The line shape of the carbon 1s peak also changed as the bonding structure of the film became more ordered. Other effects observed included the appearance of substrate layers at the surface of aged films. Film baking reduced the corresponding peak intensities, suggesting that the regions were covered with a thin film layer.

A comparison was made of the carbon 1s peaks of amorphous carbon films produced using different fabrication methods. A vacuum arc deposited film and a glow discharge deposited film were analysed along with the sputtered films used in this study. The lineshapes of the carbon peaks were all very similar for as prepared films. The FWHM in all cases was large, suggesting that carbon was present in the film surface in a number of bonding configurations.

A significant feature of some the carbon lineshapes was the presence of a shoulder peak at slightly higher binding energy, corresponding to aromatic carbon. The largest shoulder peaks was observed for the vacuum arc deposited carbon. Argon ion etching the surface of each of the films had the effect of removing surface contamination and also removing the upper layers of the film itself. The aromatic shoulder peak in the vacuum arc deposited carbon spectrum was completely removed. The lineshape of the carbon peak was also changed markedly which implies that the carbon surface layers of this film may be significantly different from the carbon in the film bulk.

References - Chapter 3

[1] R.P.H. Gasser, "An introduction to chemisorption and catalysis by metals", Clarendon Press, 1985.

[2] G.A. Somorjai, "Chemistry in Two Dimensions: Surfaces", Cornell University Press, 1981.

[3] D.P. Woodruff and T.A. Delchar, "Modern Techniques in Surface Science", Cambridge University Press, 1986.

[4] L.C. Feldman and J.W. Mayer, "Fundamentals of Surface and Thin Film Analysis", North - Holland, 1986.

[5] Kratos Ltd promotional material.

[6] J.C. Rivière, In ed.s D. Briggs and M. P. Seah, "Practical Surface Analysis", Wiley, 1990.

[7] J.C. Rivière, "Surface Analytical Techniques", Clarendon Press, Oxford, 1990.

[8] J.F. Watts, "An Introduction to Surface Analysis using Electron Spectroscopies", Oxford University Press, 1990.

[9] Channeltron™ is a trade mark of Galileo Corporation.

[10] M. Cardona and L. Ley, In ed.s M. Cardona and L. Ley, Topics in Applied Physics - Vol. 26, "Photoemission in Solids I", Springer - Verlag, 1978.

[11] J.G. Craven, Personal communication

[12] S.J. O'Shea, PhD thesis, Department of Applied Physics, University of Sydney, 1989.

[13] S. Craig, PhD thesis, Department of Applied Physics, University of Sydney, 1982.

[14] H.H. Andersen and H.L. Bay, In ed. R. Behrisch, Topics in Applied Physics - Vol. 47,"Sputtering by Particle Bombardment I", Springer - Verlag 1981.

[15] D.R. McKenzie and L.M. Briggs, Sol. Energy Mater., 6, 97 (1981).

[16] G.L. Harding and B. Window, J. Vac. Sci. Technol., 16, 2101 (1979).

[17] R.J. Bird and T. Swift, J. Electron Spectrosc. and Relat. Phenom., 21, 227 (1980).

[18] M.P. Seah, Surface and Interface Analysis, 14, 488 (1989).

[19] R.N. Lamb, J. Baxter, M. Grunze, C.W. Kong and W.N. Unertl, Langmuir, 4, 249 (1988).

[20] M.P. Seah, In ed.s D. Briggs and M. P. Seah, "Practical Surface Analysis", Wiley, 1990.

[21] V.I. Nefedov, N.P. Sergushin, I.M. Band and M.B. Trzhaskovskaya, J. Electron Spectrosc., 2, 383 (1973).

[22] J.H. Scofield, J. Electron Spectrosc., 8, 129 (1976).

[23] See for example, "Handbook of X - ray Photoelectron Spectroscopy ", Perkin Elmer Corporation, Physical Electronics Division Eden Prairie, MN, 1979.

[24] C.J. Powell and M.P. Seah, J. Vac. Sci. Technol. A, 8, 735 (1990).

[25] S. Aisenberg and F.H Kimock, Materials Science Forum, 52/53, 1 (1990).

[26] S.P. Chow and G.L. Harding, Sol. Energy Mater., 11, 123 (1984).

[27] G.L. Harding, S. Craig and B. Window, Appl. Surf. Sci., 11/12, 315 (1982).

[28] G.L. Harding and B. Window, Sol. Energy Mater., 7, 101 (1982).

[29] J. Robertson, Adv. Phys., 35, 317 (1986).

[30] S Craig and G.L. Harding, Thin Solid Films, 97, 345 (1982).

[31] D.R. McKenzie, P.J. Martin, S.B. White, Z. Liu, W.G. Sainty, D.J.H. Cockayne and D.M. Dwarte, Proc. E-MRS Meeting, 17, 203 (1987).

[32] J.P. Baxter, M. Grunze and C.W. Kong, J. Vac. Sci. Technol. A, 6, 1123 (1988).

[33] Amorphous carbon films prepared in Department of Applied Physics.

[34] J. Schwar, P.W. Jahn, L. Wiedmann and A. Benninghoven, J. Vac. Sci. Technol. A, 9, 39 (1991).

[35] D. McFall, Personal communication.

[36] D.R. McKenzie, D. Muller, B.A. Pailthorpe, Z.H. Wang, E. Kravtchinskaia, D. Segal, P.B. Lukins, P.D. Swift, P.J. Martin, G. Amaratunga, P. Gaskell and A Saeed, Diamonds and Related Materials, 1, 51 (1991).

[37] S. Jin and A. Antrens, Appl. Phys. A, 46, 51 (1988).

[38] D. Muller, Personal communication.

CHAPTER 4

Layer Composition and Depth Profile of Graded Stainless Steel/Carbon Cermet Films.

4.1 *Introduction*

The optical properties of multi - layer, spectrally selective films are determined by the refractive indices and optical absorption behaviour of the individual constituents and by the thicknesses of the various layers. Deposition processes can be calibrated by depositing samples of each of the constituents individually and measuring thickness, composition and optical properties. The composition and layer profile of a multi - layer film is then deduced from these data. Additional spectroscopic information is essential as film deposition and processing can alter the final layer profile substantially.

The optical performance of the completed film indicates film quality and the interaction of the optically active constituents. It provides some information about deficiencies and departures from the intended structure, allowing conclusions to be drawn regarding the possible causes of satisfactory or unsatisfactory behaviour. The gas adsorption behaviour of these films is also sensitive to film structure but is not related to satisfactory optical behaviour.

This chapter examines various parameters and processes which affect the grading profile of the film, including deposition effects, substrate interactions and the effects of film baking. The film properties observed have been correlated to optical measurements. Inferences can be drawn as to the aspects of film structure and deposition technique which give rise to the observed behaviour. Results are presented showing the layer structure of a range of spectrally selective films produced using different pieces of deposition apparatus.

4.2 Auger Electron Spectroscopy

Auger electron spectroscopy (AES) is a surface sensitive electron spectroscopy which can be used to identify atomic species present in the surface layers of a film. In contrast with XPS, it is difficult to extract detailed chemical information using this technique. Significant advantages, however, arise from the use of an electron beam to stimulate Auger electron emission. The electron gun provides a collimated electron beam and can be set to raster scan the sample, producing an elemental map of the surface, or steered to a particular point and set to a particular size.

AES involves reduction of the level of atomic excitation by the emission and energy analysis of secondary electrons. Figure 4.1 gives a schematic illustration of the electronic processes involved in AES. An electron is ejected from a core level (Z) by incident radiation (X-rays or electron beam) and an electron falls from a higher level (X) to fill the core level vacancy created. The energy state of the atom is reduced by the ejection of a second (Auger) electron from a higher level (Y). The kinetic energy of the Auger electron, with reference to figure 4.1, may be written as

$$E_{KE} = E_Z - E_X - E_Y - e\phi \qquad (4.1)$$

where $e\phi$ is the work function term. The kinetic energy is independent of the energy of the incident radiation [1]. Peaks corresponding to Auger transitions are observed in response to both X-ray and electron beam bombardment of a sample. The Auger process produces far fewer electrons than the primary emission process; electron beam bombardment, with beam energies of around 4keV, is commonly used to produce a measurable current of Auger electrons. Auger electron nomenclature takes the form (Z,X,Y), reflecting the many different combinations of atomic levels that may be involved in a single emission process. Emitted electrons are conventionally labelled according to the shell from which they originated, as follows: emissions from the 1s shell are labelled K; the 2s shell are labelled L_1; and the 2p shells are labelled L_2 and L_3. Valence shell electrons are labelled V. The two electrons, emitted from levels X and Y, forming the Auger process may originate from the same level and either or both may originate from the valence levels [1].

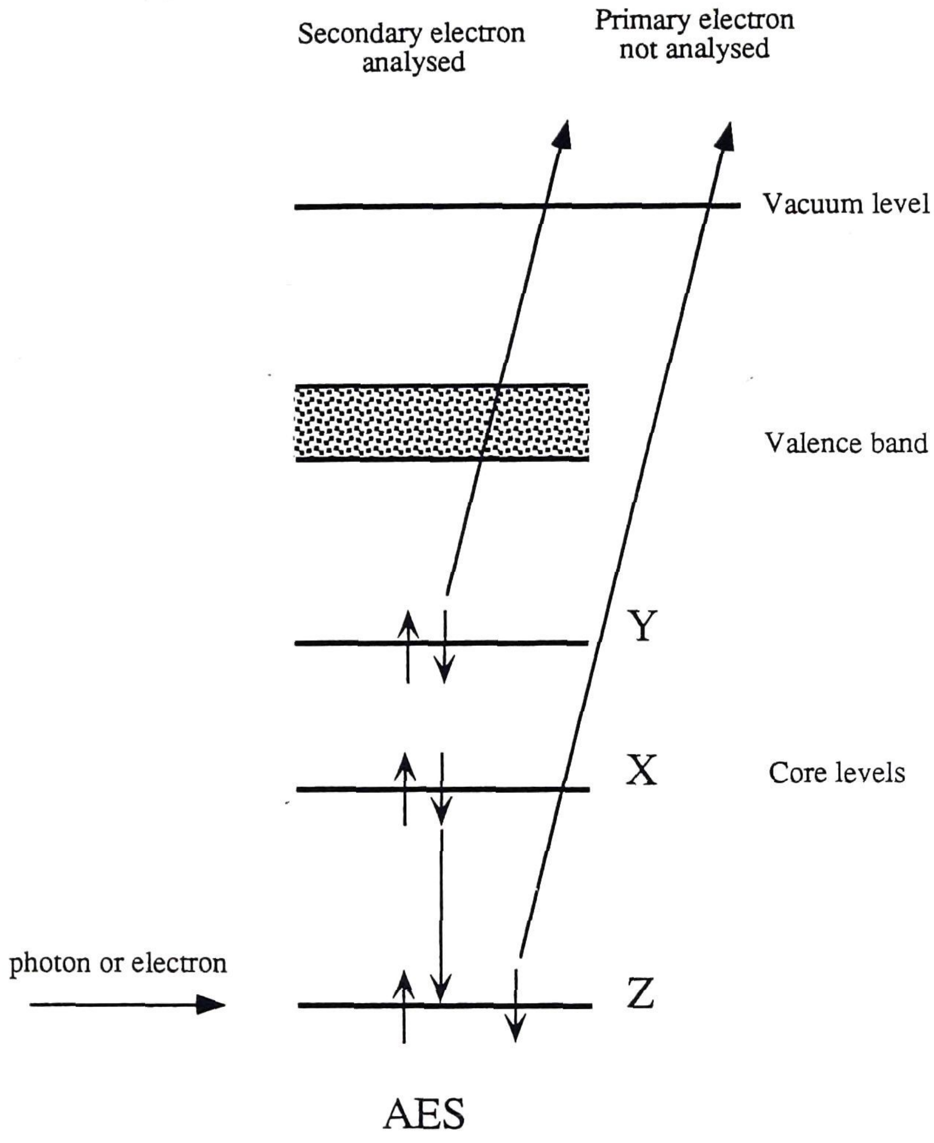

Figure 4.1 Schematic description of the electronic processes forming AES

X-ray fluorescence competes with Auger electron emission during atomic de-excitation. X-ray emission occurs when an electron from level X falls to level Z to fill a core level vacancy. The Auger electron yield and X-ray yield per core level vacancy are dependent on atomic weight. X-ray yield is negligible for atomic weights less than 15, but rises to exceed Auger electron yield for atomic weights greater than 30 [2].

AES identifies the atomic species present in a film surface. In combination with an argon ion gun, the film can be etched away to produce an elemental profile as a function of depth. Auger electrons are detected and energy analysed using a concentric hemispherical analyser (CHA) or cylindrical mirror analyser (CMA). Both these analysers are described in section 3.2, in the previous chapter. Scanning electron microscopy (SEM) facilities are routinely incorporated in AES systems. SEM is commonly used to examine the etch crater and to align the electron beam spot with the centre of the crater.

AES depth profiling offers a wide range of information relating to film bulk as well as interfacial regions. The accuracy of the depth profile is dependent on the quality and uniformity of sample etching and the incident position of the electron beam ejecting Auger electrons. If the area being etched is not sufficiently large, a cup shaped crater results. If the analysing electron beam is not then directed to the flat central portion of the crater, Auger electrons may be ejected from all strata in the crater edge causing serious errors. Surface roughness may also cause similar effects and therefore can not be neglected in depth profiling experiments.

4.3 Experimental Method

The experiments were performed in ultrahigh vacuum using a Perkin Elmer PHI Model 560 surface analysis system. This contained a double pass CMA with a concentrically mounted electron gun for AES. The energy resolution of the CMA was 1.2eV operated for XPS analysis in the fixed analyser transmission (FAT) mode with a pass energy of 25eV for the Ag $3d_{5/2}$ emission. The electron binding energies (E_B) were calibrated against the Au $4f_{7/2}$ emission at E_B = 84eV [3,4]. The composition of the film as a function of depth was determined with AES whilst the surface was being eroded with an argon ion beam. The ion etching beam was set to raster scan an area of about 3mm by 3mm. The ion beam current was adjusted to

2.0μA at an accelerating voltage of 4kV giving an etch rate of 45Å per minute for tantalum pentoxide [5]. The etch rates of each of the film constituents (and hence layer thicknesses) are discussed in section 4.4. An SEM image was used to position the electron beam with a rastered area of 0.2mm x 0.2mm used for analysis.

4.4 Determination of Depth Profile and Film Thickness

The depth profile of the film was determined using AES to monitor the atomic concentration of the film surface as a function of argon ion sputter time. Sputter time was transformed into a depth scale using previously reported sputtering characteristics of the individual elemental constituents [6-8]. In this process it is important to note that the estimates of depth profile may be significantly in error if large differences exist in the sputtering rates of the constituent components of the film. An extreme case would occur, for example, if the sputtering rate of one component was very small compared with that of the layer immediately below it. Below monolayer coverage the constituent with low sputtering rate would remain on the surface whilst the underlying atoms were preferentially removed. The AES data would indicate an appropriate amount of this constituent provided that the correct sputtering yields were used. However, this material would appear to be distributed over a much greater thickness than actually occurred in the original material.

The sputtering rate of each elemental component of the film can be deduced in the following way [6]. Sputter yields for various elements and compounds have been tabulated in a range of reference materials [6,8]. The sputter yield for a material is the number of atoms sputtered by a single incident ion of a given energy. The sputter yield Y may be written as

$$Y = \frac{\Delta m}{M n} N_A \qquad (4.2)$$

where n is the number of incoming projectile ions, N_A is Avogadro's number (6.02×10^{23}) and Δm and M are the mass change and the molecular weight of the sputtered material respectively. This approximation of sputter yield assumes that atoms are sputtered individually and that the sputtering ions are not trapped in the film [6].

The amount of material removed, Δm, is given by the product of the volume etched and the film density so the equation above can be rewritten as

$$Y = \frac{Z A \rho}{M n} N_A \tag{4.3}$$

where Z is the etch depth, A is the etch area and ρ is the film density. The sputter rate $\dot{Z}$ (m s^{-1}) is therefore

$$\dot{Z} = \frac{M}{N_A} \frac{Y}{\rho} \frac{\dot{n}}{A} \tag{4.4}$$

where $\dot{n}$ is the sputtering flux. The sputtering ion current density j_p can be written as

$$j_p = \frac{\dot{n}\, e}{A} \tag{4.5}$$

where e is the electronic charge (1.6 x 10^{-19}C). So

$$\dot{Z} = \frac{M\ Y\ j_p}{N_A\ \rho\ e} \tag{4.6}$$

This leads to

$$\dot{Z} = 2.3 \times 10^{-6}\ \frac{M\ Y}{\rho} \tag{4.7}$$

with the sputter conditions used in this study (ie. $j_p = 0.22$ A m^{-2}). The sputtering rates of the constituent parts of the spectrally selective film have been estimated using published values for sputter yield [6-8]. The sputtering rates of the three parts: amorphous hydrogenated carbon, stainless steel and copper, are roughly in the ratio 1:2:4. The loss of depth resolution which results from widely differing sputter rates, discussed above, is therefore not expected to be severe in this case. A sharp interface between stainless steel and copper, for example, would be spread by about 1nm. In the data presented here, therefore, argon ion etching time can be converted directly to an estimate of depth using a weighting factor proportional to the sputtering rate in nm s^{-1}. The AES depth profile results, weighted in this way, may be used to obtain an estimate of the overall thickness of the composite.

4.5 Results and Discussion

4.5.1 Comparison of Spectrally Selective Films

The structure of the spectrally selective films developed at the University of Sydney has been described in the preceding chapters (see in particular section 2.1 and figure 2.1). AES depth profiling was carried out on the production film, as originally devised, during development [9]. Figure 4.2 shows the layer profile of the production film as prepared and after baking (670K, 60 minutes).

The grading profile was originally devised by investigating the optical properties of the various film layers in homogeneous form and modelling their optical interaction in a multi - layer stack. Using this method the thickness of the various layers giving optimal performance was established [9]. Spectrally selective, rather than black body, optical characteristics are observed. The layer profile of the production film has smooth transitions between the carbon and stainless steel regions and is virtually unaffected by baking. The stainless steel region of the film extends almost to the film surface and is specifically designed to maximise absorptance in the visible region of the spectrum. A visible absorptance of ≈ 0.93 (reflectance ≈ 0.07) is reported for films produced in this way [9].

The copper layer is also shown in figure 4.2, again with smooth interfacial regions. This layer is designed to minimise radiative losses by providing a low emittance and high reflectance in the near infrared region of the spectrum [10]. Values of less than 0.04 reported for the emittance at low temperatures [9]. The emittance of the spectrally selective film is dependent on absorptance in the thermal IR spectrum. Transparency can be maximised by using a semiconducting material with an optical gap in the near infrared (NIR) so that photons in this region do not have sufficient energy to cause electronic transitions [11].

Figure 4.3(a) shows the AES depth profile of the spectrally selective film as currently produced in the laboratory. The film was produced using the same deposition apparatus as for the film shown in figure 4.2, but using a different production schedule. The film was analysed as prepared, without baking. The four elements selected for the AES depth profile were carbon, iron, oxygen, and copper. The stainless steel component of the film is composed principally of iron, chromium, and nickel.

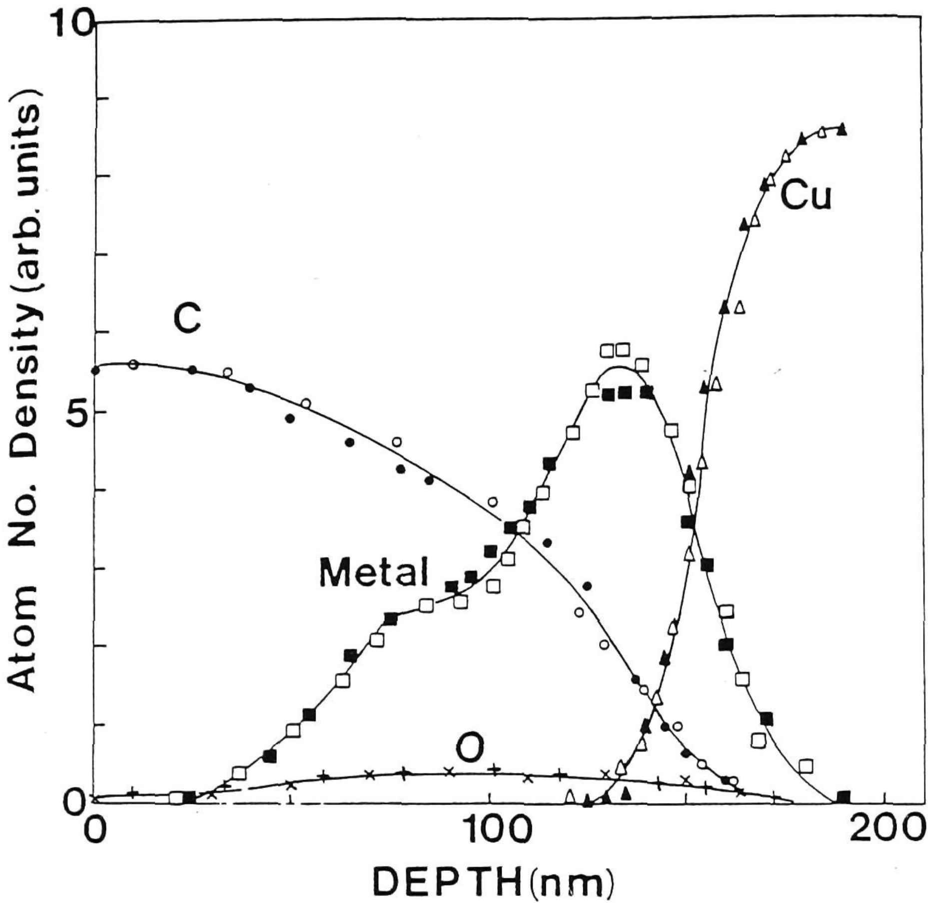

Figure 4.2 Depth profiles of the as prepared and heat treated production spectrally selective films as determined by AES and simultaneous argon ion milling of the film surface. Relative atomic number densities were calculated using standard elemental sensitivity factors, (metal = Fe + Cr + Ni). The etch rates of the a-C:H and stainless steel layers of the film were estimated to be 3.9nm/min and 4.3nm/min, respectively, for the etching conditions used. The method used to arrive at these values for the etch rates was not recorded in any detail in ref. 9.

Solid symbols: As prepared film.

Open symbols: Heat treated film.

[reprinted from ref. 9]

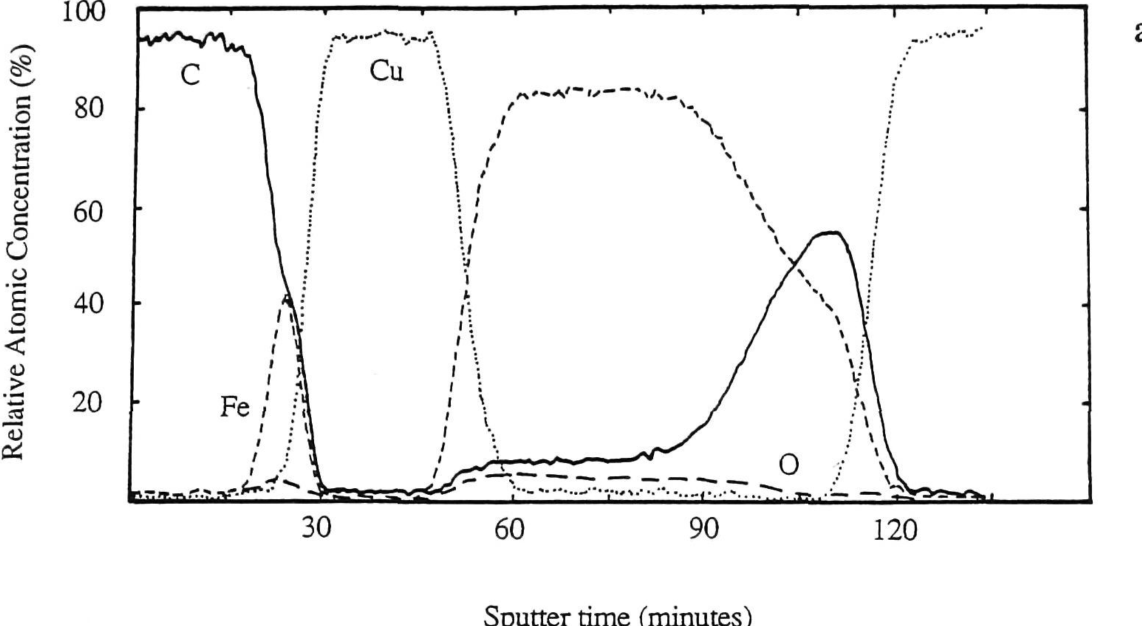

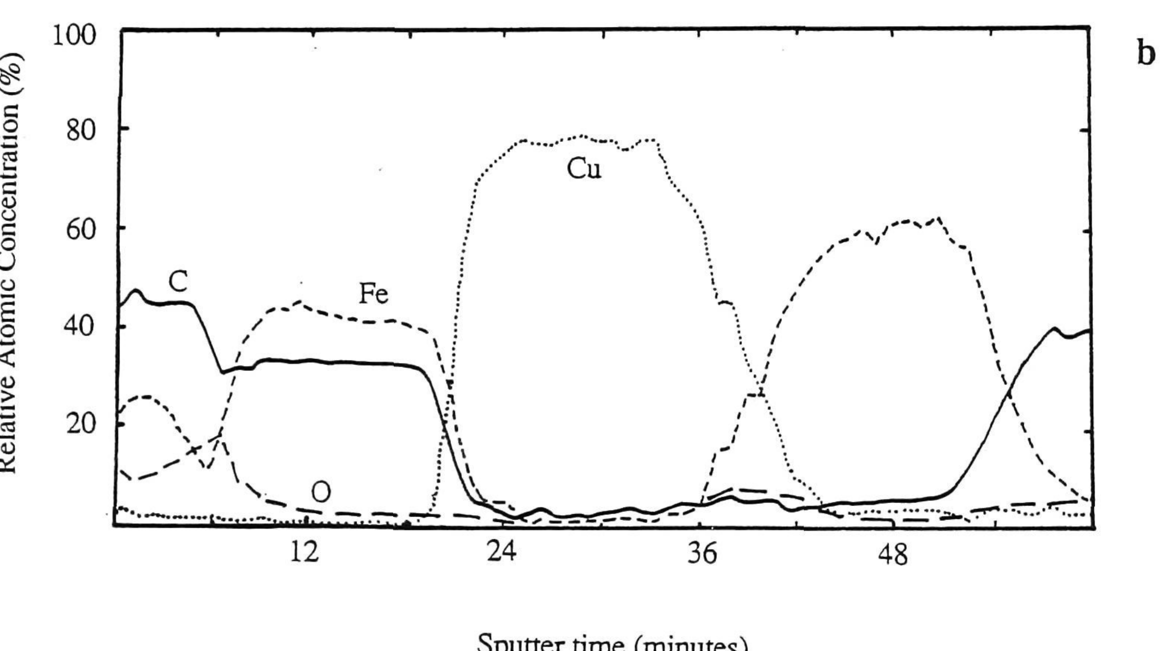

Figure 4.3 AES depth profiles of spectrally selective films: (a) the current, laboratory prepared film ; and (b) the current, commercially produced film [13]. These profiles are presented to show the qualitative differences between the layer structures of the two films. Layer thicknesses can not be directly compared as the conditions used to analyse each of the films are different. This results in different sputter times and etch rates.

Table 4.1 gives estimates of the thicknesses of the individual layers, and of the overall film obtained using published values for sputter yield and the analysis presented in the previous section. The overall thickness of the film calculated in this way (351nm) is in excellent agreement with the thickness obtained from stylus measurements (340nm). The various film layers are visible in this film. However, there are quantitative differences between the layer profiles of these films and the films originally produced.

The present film is significantly thinner overall than the production film. Only the outermost carbon layers are of comparable thickness (35nm). These differences are a direct result of different deposition conditions in the two investigations. Sputtering times, gas pressures and magnetron geometry are the same in both cases. The most significant change in the deposition parameters is that the present films are formed at a lower discharge current density when the cathode is in a non-poisoned state which reduces the sputtering rate. Under poisoned conditions, the discharge current densities in the two studies are comparable, resulting in similar thickness for the outermost layer of the deposited film.

The graded metal - carbon layer of this film is only 55nm thick, compared with about 140nm in the production film, and the low emittance copper layer is 162nm compared with 300nm for production films, due to differences in sputter deposition conditions [9]. The films currently being produced are approximately half as thick as those of the production spectrally selective film [9].

The interfacial regions being of the order of 15nm showed smooth transitions with some evidence of metal interdiffusion between the layers of films deposited on metal oxide substrates in response to baking [12]. Depth profiling of a baked spectrally selective film subjected to a slower etch rate confirmed that stepping the acetylene flow into the sputtering chamber during deposition translated to a smooth transition in the relative quantities of stainless steel and carbon.

Figure 4.3(b) shows AES depth profiles of spectrally selective films produced using a batch coater operated commercially by Shiroki Corporation in Japan. The films produced were black in colour and non - reflective, suggesting a satisfactory layer profile. The stainless steel/carbon cermet region of the film, however, is incorrectly graded. The homogeneous structure of this layer degrades the absorptance in the visible region to a value of about 0.8 [9]. A structure such as this

FILM LAYER	Top layer a-C:H	Stainless Steel	Copper	Adhesion Layer
Molecular weight M (x 10^{-3}kg)	12	55.9	63.6	55.9
Density ρ (x 10^{3}kg m^{-3})	1.25	7.5	9.0	7.5
Sputter yield Y (atoms/ion)	1.2	2.5	5.25	2.5
Sputter time (min)	22	7.5	26	63
Etch rate Z (nm/min)	1.6	2.6	5.1	2.6
Calculated layer thickness (nm)	35	19	133	164

TOTAL FILM THICKNESS = 351nm

Table 4.1 Calculations of film layer thicknesses from elemental sputter yields. Layer thicknesses are calculated using equation 4.7 and the tabulated data. The first two layers calculated together make up the graded stainless steel carbon cermet, while the adhesion layer is treated as a stainless steel layer for convenience. Layers were taken to be bounded by the mid point of the adjoining interfacial regions

would function as a solar absorbing surface when incorporated in an ETC. However, overall efficiency, particularly at lower light levels would be impaired. The copper low emittance layer has a simple structure and has been correctly fabricated.

The main cause of poor layer definition and incorrect grading profiles is probably poor control of the gas flows in the deposition chamber and inaccurate measurements of pressure. Coating conditions require regular recalibration to account for changes in the behaviour of the coating system. Measurements of the optical properties of the films produced are generally insufficient to identify specific faults in deposition. Spectroscopic techniques such as AES provide a broader range of information and expedite fault analysis.

4.5.2 Effect of Annealing Conditions on Optical Properties and Layer Profile

AES depth profiling was carried out on a number of solar selective films deposited on different substrates. Freshly prepared films showed similar layer profiles independent of the substrate on which they were deposited. Films deposited on glass, OFHC copper, polycrystalline copper and polycrystalline aluminium substrates were analysed as - prepared (figure 4.3(a); in this case the substrate was polycrystalline copper) and after baking to 670K for 60 minutes (figure 4.4).

The optical reflectance of selected films in the range of 200 - 2500nm was measured using a Cary 2300 UV - NIR spectrophotometer. The reflectance of the spectrally selective films was measured as - prepared and after baking (670K, 60 minutes). Figure 4.5 shows the reflectance of the spectrally selective films as a function of wavelength in comparison with the production film.

The amorphous carbon - stainless steel top layer of the film plays a critical role in determining the spectral selectivity of the film. Production films, with a larger proportion of stainless steel through their structure, have achieved better optical performance [9]. The films used in this study have a larger proportion of higher resistivity a-C:H in the outer layer than the production films (see figures 4.2 and 4.3(a)). Annealing of the film has been predicted to convert the non - optimal refractive index profile to a better performing profile [14]. The reflectance of the baked film (see figure 4.5) is around 0.12 in the visible spectrum, compared with 0.22 for the as - prepared film. In addition, baking sharpened the reflectance edge in the NIR region of the spectrum.

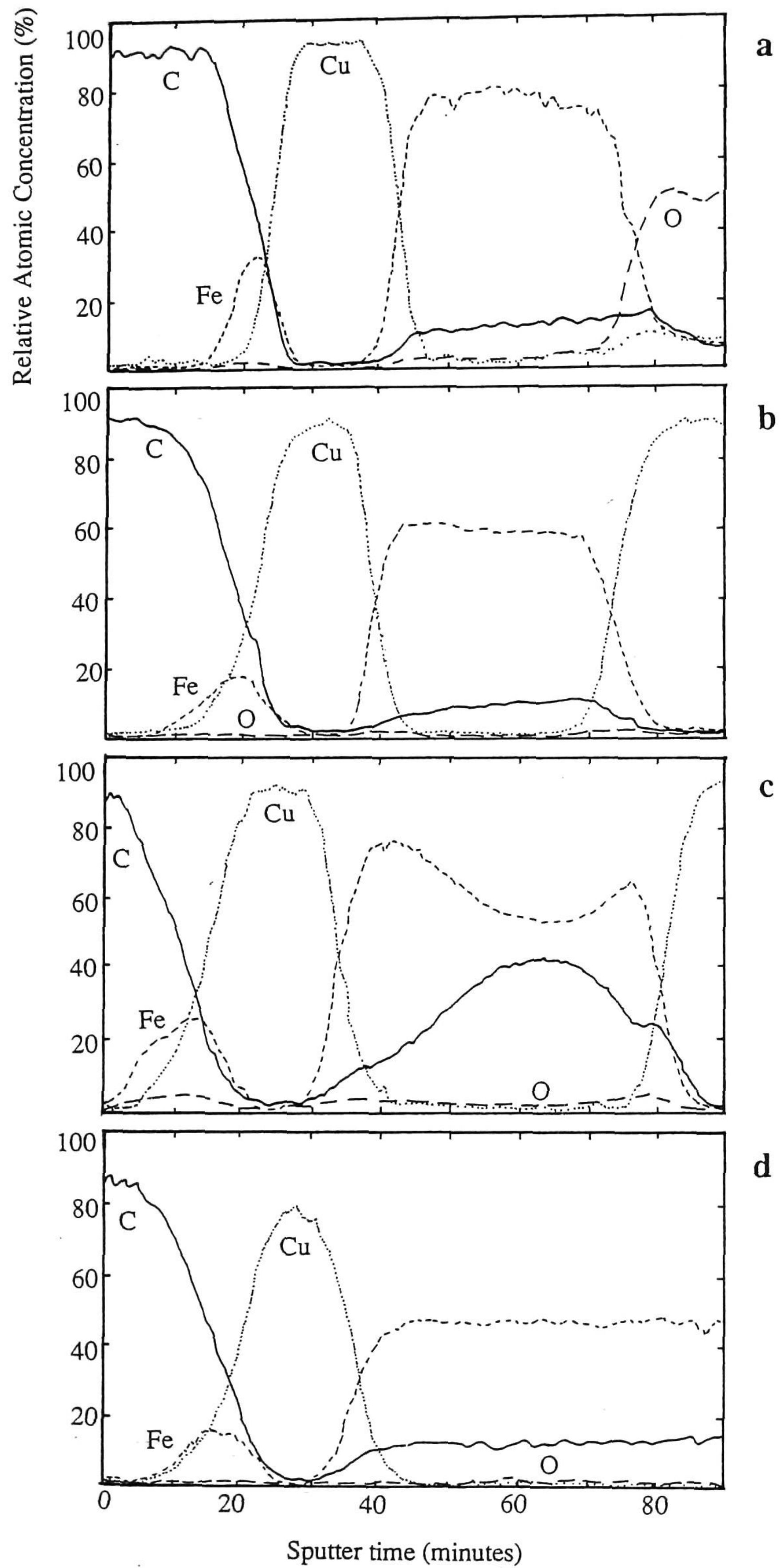

Figure 4.4 AES depth profiles of freshly prepared spectrally selective films baked to 670K for 60 minutes, deposited on: (a) microscope slide glass; (b) OFHC copper; (c) polycrystalline copper; and (d) polycrystalline aluminium.

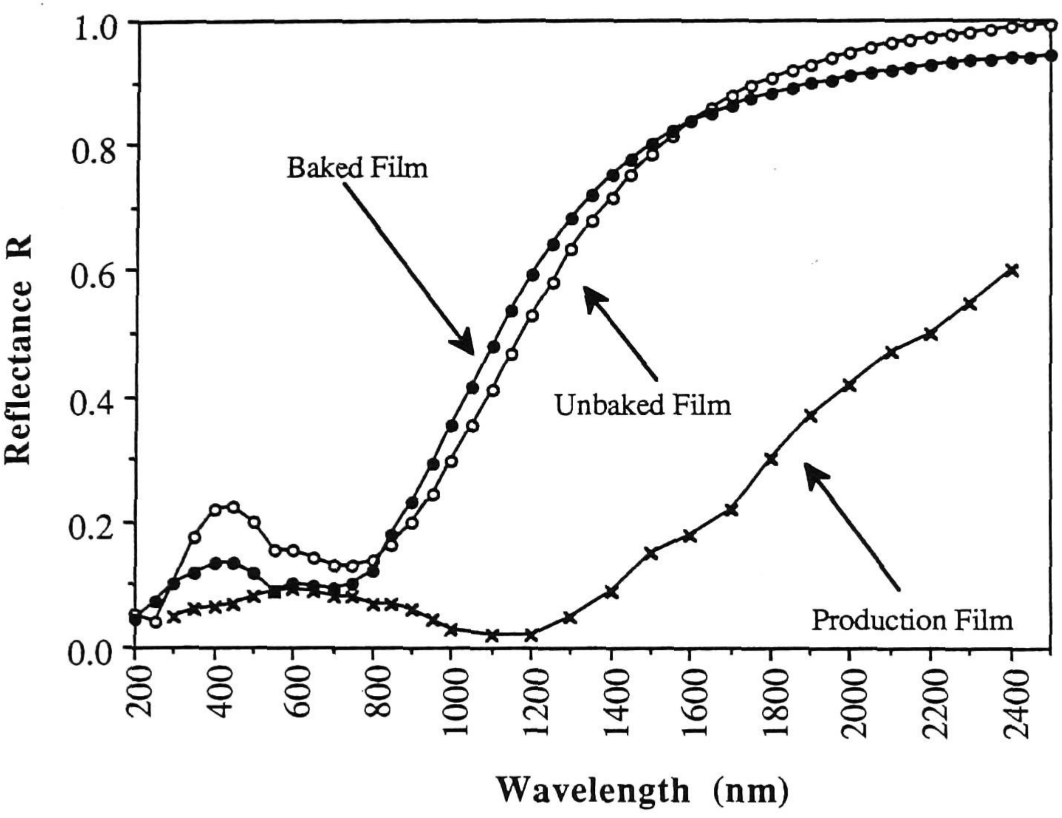

Figure 4.5 Reflectance spectra for the production selective film (x) and the selective films used in this study (unbaked (o), baked (•)). The production film has a reflectance of < 0.1 in the visible spectrum whereas the films currently being produced have a reflectance of ~ 0.22 as prepared and ~ 0.12 after baking. The change in reflectance with baking of the latter films corresponds to a colour change from a dark metallic to an opaque black.
[Data for production film reproduced from ref. 9]

Films deposited on glass (figure 4.4 (a)) and OFHC copper (figure 4.4(b)) substrates show little change in response to baking. Depth profiles show a clearly defined layer structure and a slight reduction in film thickness as a result of outgassing and layer compaction [9,15]. The optical properties of this type of graded selective film improve after baking [14,16]. The film colour visibly changed from a dark metallic to a opaque black.

Films deposited on metal substrates containing oxygen show significant changes in structure in response to baking. Films deposited onto polycrystalline copper change colour from a dark metallic to a semi - transparent sepia colour after baking. Figure 4.4(c) shows that after baking the stainless steel layer of the film has diffused into the neighbouring layers and extends almost to the film surface. The film has been thinned by the removal of surface carbon and by layer compaction. Depth profiles of films deposited onto polycrystalline aluminium substrates (figure 4.4(d)) showed major structural changes during the heating process which resulted in the baked film delaminating from its substrate. The breakdown of film/substrate adhesion may arise from differences in the structure and bonding behaviour of the aluminium and copper materials

These results show that film structural changes and optical degradation appear to depend on the nature of the underlying substrate and do not occur with substrate materials, such as OFHC copper and glass, with little or no surface oxygen. Oxygen in the surface of the as - prepared film oxidises the surface carbon layers with each successive heating forming CO, which is liberated from the surface thereby reducing the overall thickness of the carbon layers.

A mechanism for the thermal degradation observed necessarily involves substrate oxygen diffusing through the film bulk and if the film temperature is sufficiently high, activating a process forming CO and other degradation products. XPS results reported in the previous chapter show significant quantities of oxygen (~ 10 atom %) present at the surface of as - prepared films. Baking results in the removal of most of this oxygen by the formation and desorption of CO in a process similar to that proposed here.

Figure 4.4(b) shows that surface oxides on an OFHC substrate will induce limited oxidation of the carbon film surface. Degradation stops in films with oxygen free metal substrates once surface oxygen has been exhausted. There is no evidence to suggest that oxygen arising from the metal interlayers is contributing significantly to structural changes in the film. Oxygen at the surface of a film may be continuously replenished by oxygen diffusion from a polycrystalline metal substrate.

4.5.3 Interlayer Diffusion

Diffusion of the metal components of the selective film has been observed in the presence of oxygen during baking [12]. More striking, however, is the diffusion of carbon in the adhesion layer of the films deposited on polycrystalline copper (figure 4.6). This behaviour was not observed on other substrates because the stainless steel cathode was cleaned prior to the film deposition (removing most of the contaminating carbon) to enhance the characteristics of the completed films.

In a freshly prepared film deposited on polycrystalline copper, the carbon is predominantly located at the film/substrate interface. This is expected as it is the first material to be sputtered from the stainless steel cathode during the deposition process. The carbon layer extends into a stainless steel region as the cathode is gradually sputtered clean. When the selective film is baked to 470K (figure 4.6(b)), some of the carbon residing at the film/substrate interface diffuses into the bulk of the stainless steel adhesion layer. Baking to 670K (figure 4.6(c)) results in carbon diffusing into the middle of the stainless steel layer; some of the carbon starts to merge into the interface region between the adhesion layer and the low emittance copper layer. The carbon is contained in this region by the copper layers on either side.

The behaviour of the copper regions of the film, in some respects, is in parallel with inferences drawn from previous gas adsorption studies [17]. Film morphology and pore structure has a greater influence on adsorption behaviour than the properties of the individual film constituents. These spectrally selective films adsorb gases through the entire thickness of the microporous metal/carbon cermet layer. The underlying copper layer is non - porous and hence non - adsorbent. There is what might be termed a morphological mismatch between the layers. Similarly, in this case the same mismatch is precluding significant diffusion between the metal/carbon cermet regions and copper regions of the film.

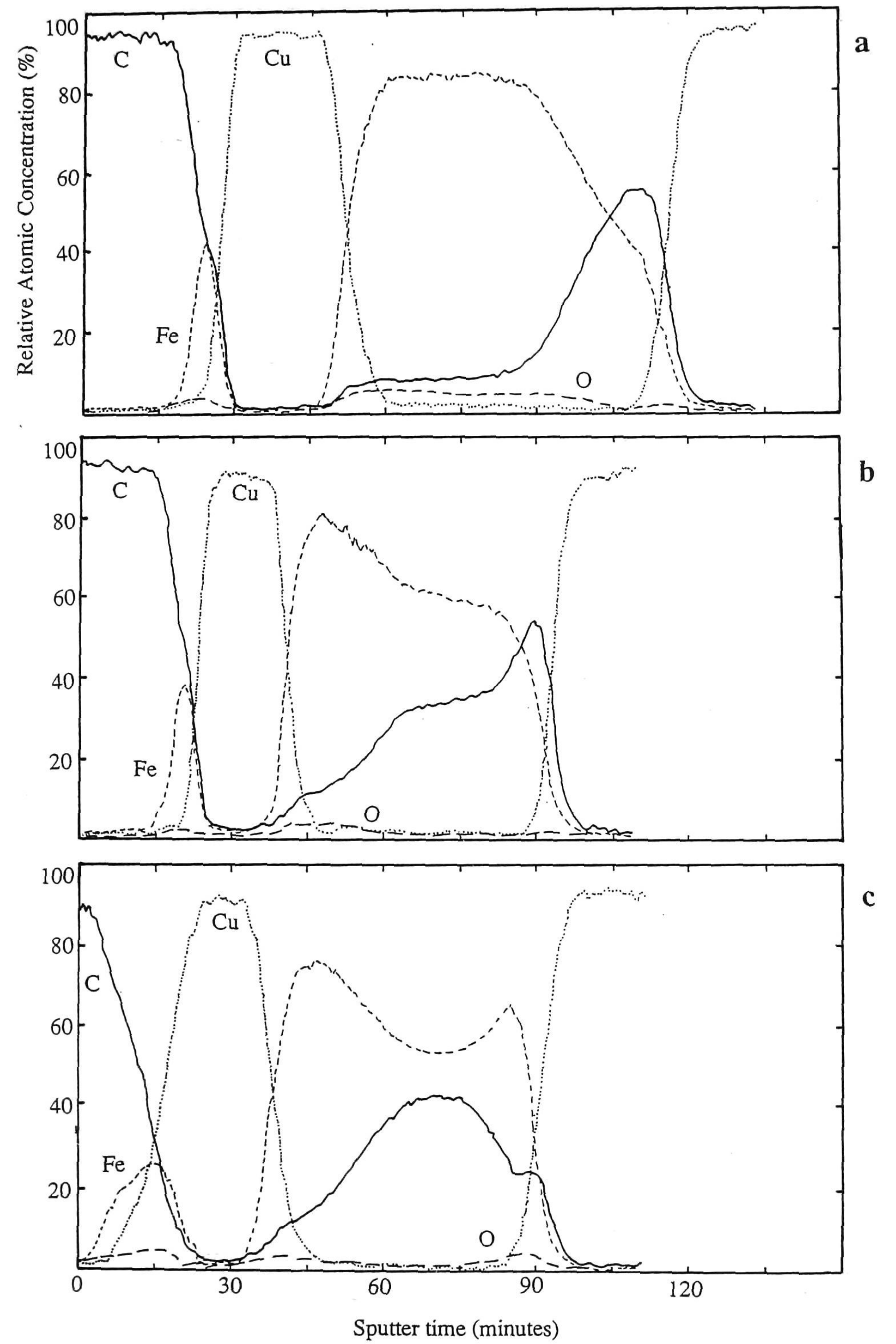

Figure 4.6 AES depth profiles of freshly prepared spectrally selective films deposited on polycrystalline copper: (a) as deposited; and after baking for 60 minutes to (b) 470K and (c) 670K.

Visible pinholes are formed in the surface after baking, indicating that interlayer adhesion has been adversely affected. Some of the carbon has started to diffuse into the low emittance copper layer of the film. This diffusion behaviour may therefore have serious implications for film stability and interlayer adhesion. Film oxidation has been identified as a potential source of degradation in all - glass ETCs over long periods of time [12,18]. This can be avoided if a getter is incorporated into the ETC and the spectrally selective film and glass envelope are satisfactorily outgassed before final vacuum sealing [12].

4.6 Summary

The films prepared for these experiments were fabricated according to procedures laid down for the production film. Studies of the optical properties of the films reveal deficiencies in the optical performance but do not provide sufficient information about the structural causes of the deficiency. The layer profile of the films produced, however, is markedly different from that reported for the production films when originally developed. This is concomitant with observations and measurements of degraded optical performance. The unwanted homogeneity of the metal/carbon cermet layer of the commercially produced films arises, in all probability, from poor control of gas flows into the coater vessel. Inadequate characterisation of the batch coating system and poor control of deposition parameters could result in the production conditions not being satisfactorily attained or reproduced.

The optical characteristics of spectrally selective films are integrally dependent on layer structure of the film. An important optical effect observed in this study was the darkening of the layered films in response to baking. The departure of the optical properties of the spectrally selective films currently produced from those of the film originally devised has been traced to significant differences in layer profile. The overall thickness of the film currently produced has been reduced and the relative proportion of a-C:H in the outer metal/carbon cermet layer is much higher.

Many of the long term problems associated with ETCs identified in this study would appear to originate with the choice of substrate material for the spectrally selective film. Depth profiling of identical films subjected to different heat treatments has shown the effect of film baking on layer structure. Film stability can be significantly degraded with the application of heat in films deposited on substrates containing significant amounts of oxygen. The implications of this behaviour are that spectrally selective films with a metal/carbon cermet structure should ideally be deposited onto glass substrates. This is the current industrial practice.

There are advantages in using metal substrates in metal - in - glass ETCs. Collectors with a metal - in - glass configuration, employing a metal/carbon cermet film are susceptible to loss of performance over long periods. It is, therefore, necessary to use high purity oxygen free metals to retain film stability. This significantly adds to the production cost of ETCs of this design. The amount of oxygen in metal substrates is the key to the speed and extent of structural change due to baking. The films deposited on OFHC copper and glass do not show significant degradation of optical performance with baking indicating that oxygen free metals and glass are the only satisfactory types of substrate materials for ETCs.

References - Chapter 4

[1] R.P.H. Gasser, "An introduction to chemisorption and catalysis by metals", Clarendon Press, 1985.

[2] L.C. Feldman and J.W. Mayer, "Fundamentals of Surface and Thin Film Analysis", North - Holland, 1986.

[3] R.J. Bird and T. Swift, J. Electron Spectrosc. and Relat. Phenom., 21, 227 (1980).

[4] M.P. Seah, Surface and Interface Analysis, 14, 488 (1989).

[5] G.C Morris and B.J. Wood, Materials Science Forum., in press (1990)

[6] H.H. Andersen and H.L. Bay, In ed. R. Behrisch, Topics in Applied Physics - Vol. 47,"Sputtering by Particle Bombardment I", Springer - Verlag, 1981.

[7] N. Veisfeld and J.D. Geller, J. Vac. Sci. Technol. A, 6, 2077 (1988).

[8] G. Betz and G.K. Wehner, In ed. R. Behrisch, Topics in Applied Physics - Vol. 52,"Sputtering by Particle Bombardment II", Springer - Verlag, 1983.

[9] S. Craig, PhD thesis, Department of Applied Physics, University of Sydney, 1982.

[10] B. Window and G.L. Harding, Sol. Energy, 32, 609 (1984).

[11] D.R McKenzie, N. Savvides, D.R. Mills, R.C. McPhedran and L.C. Botten, Sol.Energy Mater., 9, 113 (1983).

[12] G.L. Harding, S. Craig and B. Window, Appl. Surf. Sci., 11/12, 315 (1982).

[13] Produced by Shiroki Corporation, Japan.

[14] D.R. McKenzie, R.C. McPhedran and L.M. Briggs, Sol. Energy Mater., 7, 75 (1982).

[15] G.L. Harding and B. Window, Sol. Energy Mater., 7, 101 (1982).

[16] L.M. Briggs, D.R. McKenzie and R.C. McPhedran, Sol. Energy Mater., 6, 455 (1982).

[17] S.J. O'Shea, PhD Thesis, Department of Applied Physics, University of Sydney, 1989.

[18] G.L. Harding and S. Craig, Sol. Energy Materials, 4, 413 (1981).

CHAPTER 5

Thermal Desorption Behaviour of Amorphous Carbon Films

5.1 Introduction

This chapter incorporates a discussion of measurements of gas desorption from a-C:H films under the influence of changing temperature. This technique is called thermal desorption spectroscopy (TDS). It is one of a class of spectroscopies which can be categorised in terms of thermally stimulated desorption behaviour. TDS is a useful technique for studying adsorption/desorption systems because complicated desorption spectra can be reduced to a series of simple desorption peaks, each associated with a binding site or state with a different activation energy. Coupling these results with another analytical technique, such as work function measurements, can allow the adsorbate/film interaction underlying a particular desorption peak to be identified.

TDS measurements of benzene desorption from a-C:H films reflect, in part, a microscopic view of the adsorption/desorption mechanism of the proposed thermal switch for ETCs. At temperatures around 300K benzene is adsorbed on the a-C:H film. When the film temperature is increased, the benzene desorbs. TDS measures the rate at which the benzene desorbs from the surface. This contrasts with the volumetric and quartz crystal microbalance studies of gas adsorption using this system in which the total amount of material adsorbed is quantified. TDS provides additional insights into the adsorption/desorption process. For example, using TDS, it is possible to estimate directly the activation energy of desorption processes.

Previous studies of hydrocarbon adsorption on metal carbide films suggest that very little adsorption occurs in low pressure regimes ($< 10^{-6}$ torr) [1,2]. Arrhenius analysis of the thermal desorption data has been used to give estimates of the activation energies of desorption of the various binding states observed. The temperature position of the desorption peaks and the rate at which adsorbate is liberated from the surface determines the threshold switching temperature, (ideally

around 350K), and the temperature range over which the switching action occurs. These are important issues in designing and incorporating a commercial thermal switch mechanism in ETCs.

5.2 Thermal Desorption Spectroscopy

Desorption spectroscopies rely on relating the partial pressure of desorbing species (or the total pressure) to an external parameter controlling the energetic state of the sample such as temperature, electron beam energy, electric field etc. In this way the properties of the various desorption states can be quantified in terms of rate and energy subject to experiment limitations. Information gathered principally concerns the state of adsorbate/substrate bonding with incidental details relating to surface composition and surface coverage [3]. A mass spectrometer detects the partial pressure of each desorbing species as a function of the changing state of the parameter causing desorption. Alternatively, rudimentary information about the desorption rate of all species can be obtained from measurements of chamber pressure. This method is limited by the effects of extraneous desorption from the chamber walls and sample supports.

The most common desorption spectroscopy is thermally activated desorption which will be discussed below. Other methods include electron stimulated desorption (ESD) and ion impact desorption (IID). ESD methods rely on electron impact to cause adsorbate transitions to excited, ionised states. If the potential energy of these states exceeds that of an equivalent free particle then desorption can occur [4]. Similarly, desorption using IID arises from adsorbate excitation by bombardment. The distinction between desorption and etching resulting from sputtering is not clear cut resulting in an overlap between the areas [4]. In photodesorption experiments, the energy required to induce desorption is supplied by an intense, well characterised and controllable laser beam [4]. Very high electric fields can also be used to induce desorption. This process is observed in field ion microscopy where it is used for imaging purposes [3].

Thermal desorption spectroscopy (TDS) is a general description for a range of experimental techniques in which the partial pressure of gaseous species desorbing from a sample surface, in response to heating, is recorded as a function of time and sample temperature. Partial pressures are detected with a mass spectrometer by rapid

or continuous sampling of the mass channels corresponding to the species of interest. Absolute evaluation of partial pressures is not generally possible as conductances in the vicinity of the mass spectrometer head can not easily be measured. Calibration, however, gives satisfactory relative measurements which can be compared with results from other experimental techniques.

Significant thermal desorption spectra are dependent on accurate measurements of sample temperature. The most common method of measuring temperature is with a thermocouple. Difficulties can arise with this method if the point of measurement is not in good thermal contact with the sample face. An offset can be introduced into temperature measurements if the sample is biased or not adequately earthed.

A number of distinct experimental methods are employed in TDS experiments. Flash desorption and temperature programmed desorption are two common variations of TDS. Flash desorption involves heating a sample over a few seconds so that the rate at which gas enters the system due to desorption exceeds the rate at which it is pumped out of the system. These experiments are carried out in closed systems or systems with restricted pumping capacity. The effect of the fast desorption rate is to integrate the data giving a total quantity of gas evolved [3]. Temperature programmed desorption was used in the current work and involves heating a sample over a period of a few minutes. Gas evolved from different binding states is detected as a series of plateaus in the pressure - temperature curve for flash desorption and as a series of peaks for temperature programmed desorption [3]. Desorption rates and pumping rates must be optimised to give the clearest thermal desorption spectra. Plateaus and peaks corresponding to different binding states can be identified from pressure - temperature data. Curve fitting and mathematical analysis are, however, required to deduce rate information and activation energies.

Studies of stainless steel/carbon cermet films have been undertaken previously using thermomanometric analysis which has some features in common with TDS [5-7]. Pressure - temperature curves are generated for gas evolved from a sample in response to heating. The temperature ramp typically extends from 300 - 1100K with a duration of the order of hours. Gases evolved are sampled and analysed during the course of the experiment [6]. These experiments investigated degassing and thermal decomposition of graded stainless steel/carbon films rather than gas adsorption/desorption behaviour. The degassing behaviour of production films is shown in figure 5.1. The major products are CO and H_2 which are evolved in significant quantities at temperatures greater than 400K. Lesser quantities of CO_2

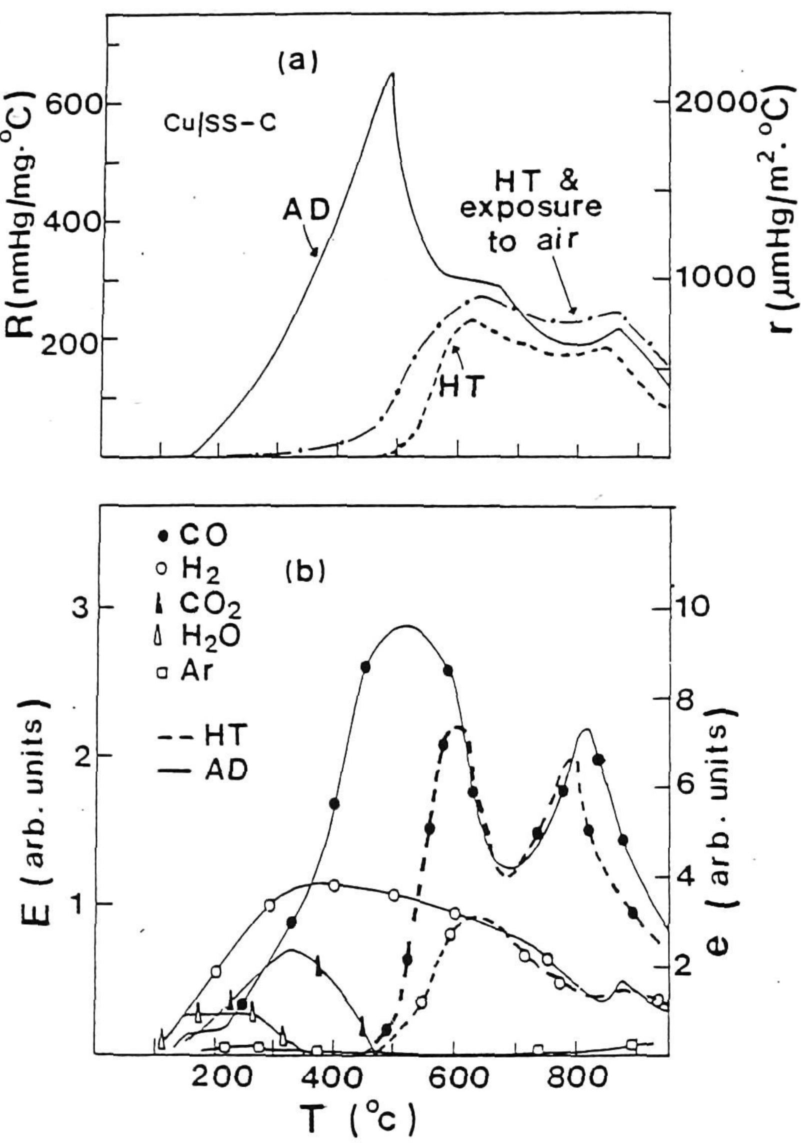

Figure 5.1

(a) Degassing rates R (nmHg/mg.^{o}C) and r (µgHg/m^{2}.^{o}C) as a function of temperature T (^{o}C) for as - deposited (AD) and heat treated (HT) (500°C) spectrally selective films. Degassing rates for a heat treated sample, exposed to air, are also shown.

(b) Evolution rate/mg (E) and the evolution rate/m^{2} (e) of various gases for as - deposited (AD) and heat treated (HT) (500°C) spectrally selective films.

[reprinted from ref. 7]

and H_2O are evolved in the temperature range of 400 - 700K. Heat treated films (770K, 60 minutes) show significantly reduced gas evolution in subsequent thermomanometric analysis below this temperature [6]. Similar degassing behaviour was observed in the current experiments. Amorphous carbon films were heated adjacent to a mass spectrometer and the partial pressures of CO, CO_2, H_2 and H_2O were observed as a function of temperature. Heating rates, however, were not sufficiently constant to record significant results. Heat treated films showed little gas evolution upon reheating apart from the effects of residual gas adsorption.

5.3 Ultrahigh Vacuum System

5.3.1 Design and Construction

The investigation of the gas adsorption/desorption behaviour of amorphous carbon and metal/carbide films requires the creation of an experimental environment in which atmospheric contaminants can be reduced to a minimum and the effect of different adsorbates studied independently. An ultrahigh vacuum (UHV) chamber was used for these experiments which had a base pressure of 5×10^{-10} torr.

The chamber is based on a 6 - way cross (Varian) with 200mm Conflat flanges. The chamber is pumped with a 300 litre per second turbomolecular pump (Varian V300) and is backed by a two stage rotary pump (Leybold Trivac). The chamber can be isolated from the pumping system and the pumping speed adjusted during adsorption experiments using an all - metal plate valve (Varian). Chamber pressures (10^{-3} torr - 10^{-10} torr) are measured using nude ionisation gauge and controller (Varian 580 head/880RS controller).

The layout of the experimental equipment is shown in figure 5.2. The sample is located centrally in the chamber using a custom designed sample mounting fitted to a XYZθ manipulator (Varian) mounted from a side flange. A Kelvin probe and ionisation gauge are mounted from the flange opposite the sample. A shielded mass spectrometer head is mounted adjacent to the sample, opposite the gas dosing line. Alignments are made by viewing through a window located on the top of the chamber. Rotating the sample from the Kelvin probe and gas doser across to the mass spectrometer allows sequential adsorption and desorption experiments.

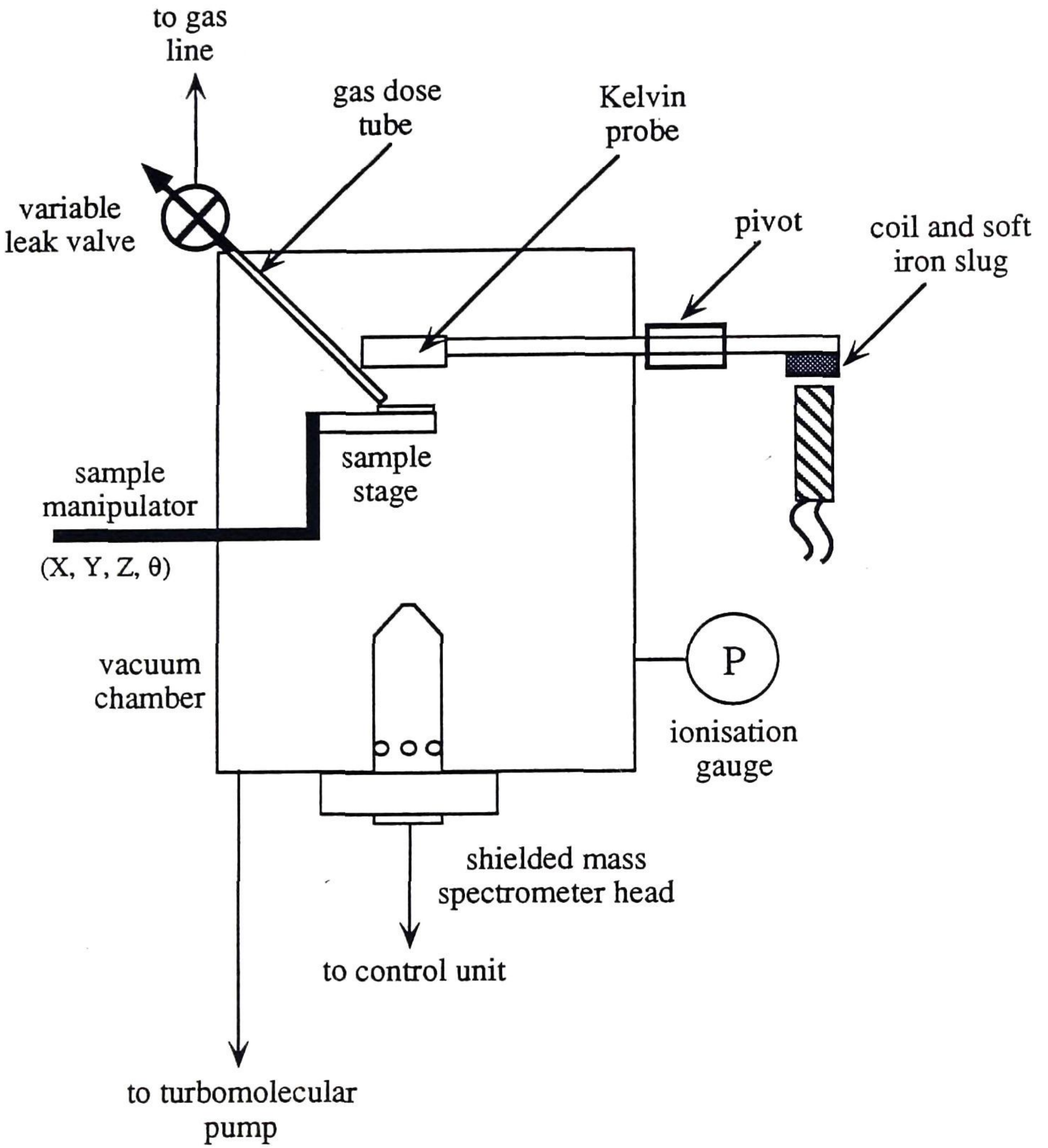

Figure 5.2 Schematic description of experimental apparatus used for thermal desorption and work function studies

5.3.2 Sample Mounting and Manipulation

Several sample mountings were constructed to allow the manipulation of the sample, the control and measurement of sample temperature and the control of sample bias voltage during CPD experiments.

In earlier versions of the sample mounting, 10mm square substrates were placed in a copper foil envelope which was suspended between two copper support rods with 280µm diameter tungsten wire. Figure 5.3(a) shows the layout of the sample mounting. The copper support rods were insulated from the sample manipulator using a machined ceramic block (Macor, Corning Glass). The temperature of the sample was measured using a Type K thermocouple resting in a small hole drilled through the corner of the substrate. The sample was heated resistively by passing a current through the tungsten sample support wires. The same heating circuit was used to bias the substrate during CPD experiments.

A number of problems were experienced using this sample mounting. The sample could not be heated and biased simultaneously as the sample was in direct electrical contact with the sample mounting. The application of a current to heat the sample produced significant interference with thermocouple measurements. The sample heating rate was difficult to control and not sufficiently even across the face of the sample. It was suspected that most heating occurred due to conduction from the exposed wires between the sample and the support. The sections of wire in close electrical contact with the sample carried a reduced current and therefore did not contribute significantly to sample heating.

An improved sample mounting is shown in figure 5.3(b). The body of the mounting is a machined ceramic block which supports and insulates the sample. The sample was fastened to the mounting using screws at each corner. A heating element was constructed from 280µm diameter tungsten wire in a zig - zag configuration using holes and slots in the ceramic mounting. Heating rates of 0.2-2K per second were obtained by passing currents of 2 - 7A through the wire. Temperature was measured using two Type K thermocouples located at the corners of the sample. The sample was biased using an additional electrical connection.

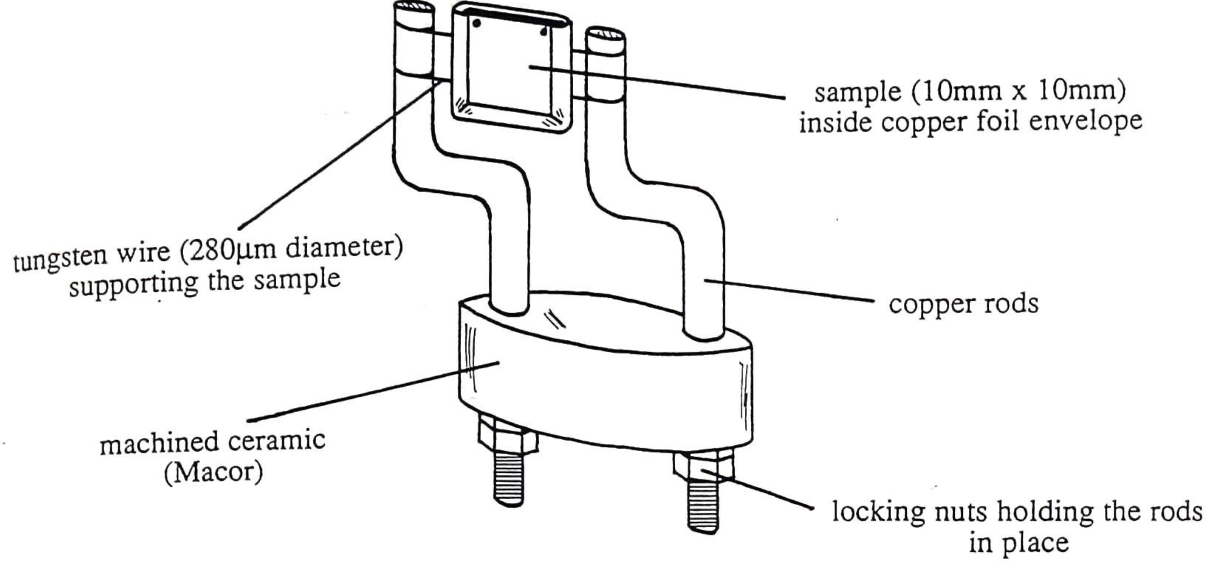

Figure 5.3(a) Sample holder for 10mm x 10mm substrates

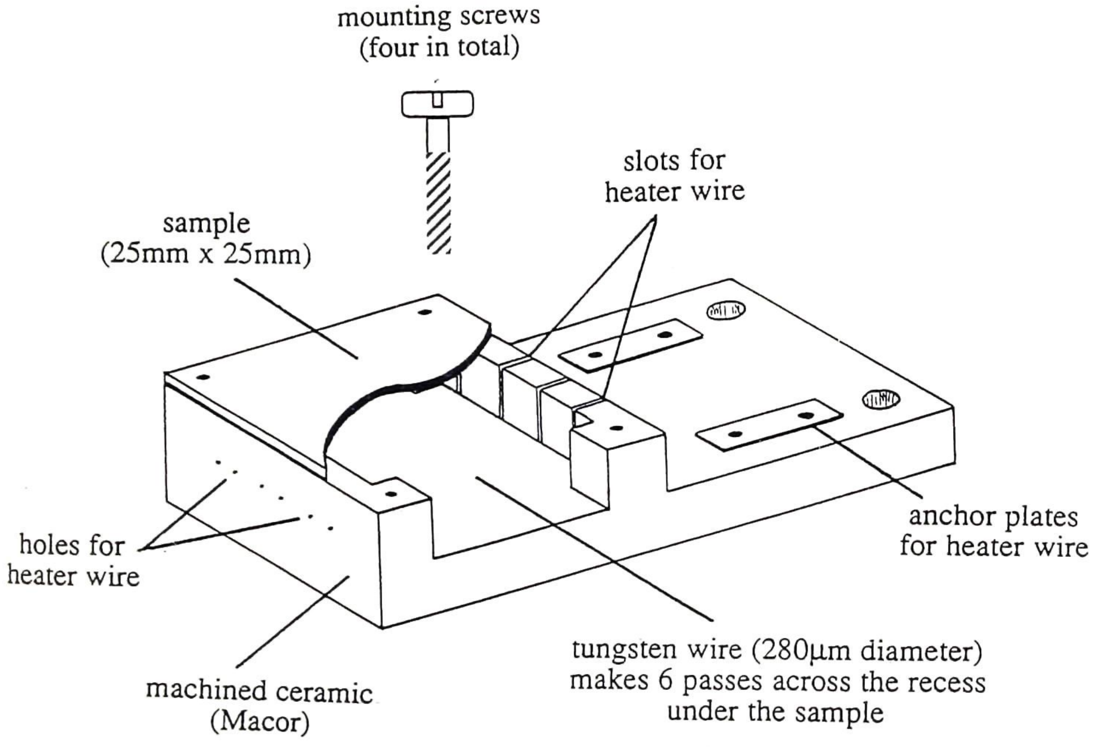

Figure 5.3(b) Sample holder for 25mm x 25mm substrates

The performance of the revised sample mounting was satisfactory for TDS experiments. The following comments are relevant to future modifications. The ceramic sample body provides a useful mounting platform. It has been noted that after about 200 heating cycles (670K) cracks are visible in the ceramic bulk. Some evaporation of the tungsten wires has taken place with leakage currents detectable across evaporated material on the surface of the ceramic during heating. The use of stainless steel structural parts and small ceramic insulators will improve the mechanical properties and strength of the sample holder and potentially eliminate current leakage from the heating circuit. A smaller sample size and sample mounting will facilitate sample manipulation.

5.3.3 Gas Dosing Facilities

Adsorbates used for adsorption/desorption experiments are introduced into the main vacuum chamber via a gas dosing line. The gas dosing line is shown schematically in figure 5.4. It consists of a small vacuum chamber pumped with a 50 litre per second turbomolecular pump (Leybold). This chamber is connected to the main chamber by a variable leak valve (Varian). Two adsorbate reservoirs are connected to the system with shut off valves (Nupro SS - 4H). The arrangement of the valves allows for the liquid adsorbates to be freeze - degassed individually before dosing, for the adsorbates to be dosed individually, simultaneously or consecutively and for the gas dosing line to be pumped clean after dosing.

The dose rate of the adsorbates into the main chamber is controlled with the leak valve and monitored using the ionisation gauge and mass spectrometer in the main chamber. The adsorbates are delivered to the vicinity of the sample surface via a 5mm internal diameter stainless steel dosing tube extending from the leak valve outlet. The sample is positioned adjacent to the end of this tube when gases are being adsorbed. The pumping speed in the main chamber is regulated with the plate valve at the entrance to the turbomolecular pump.

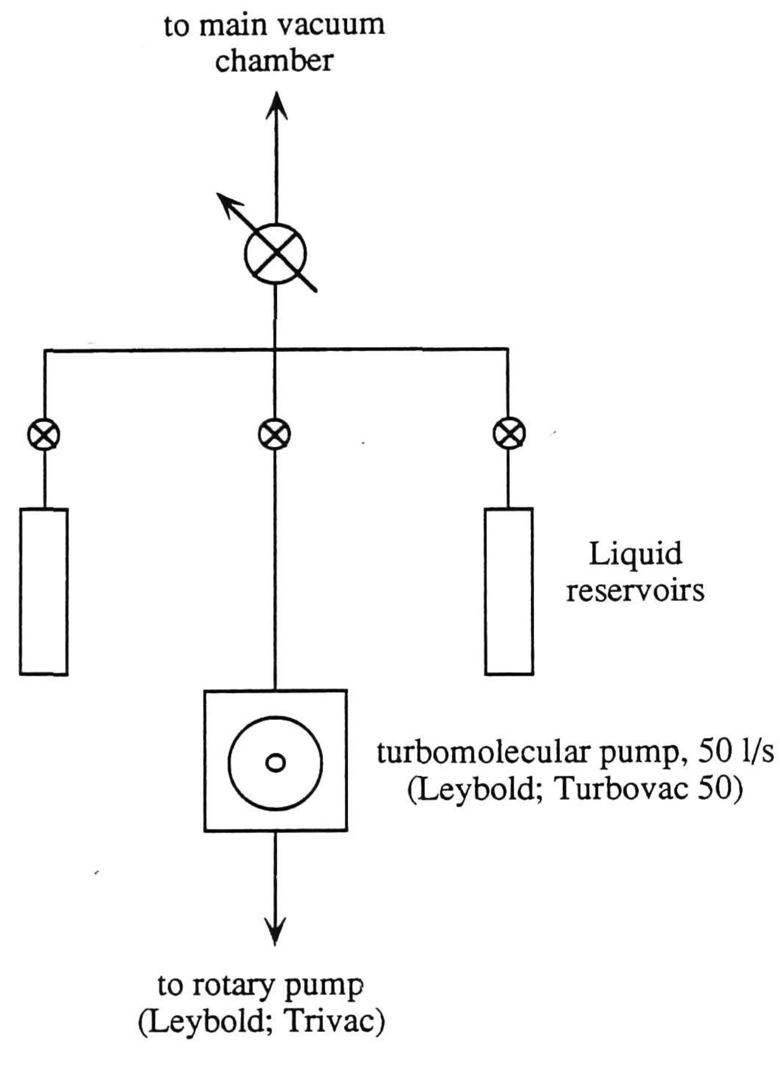

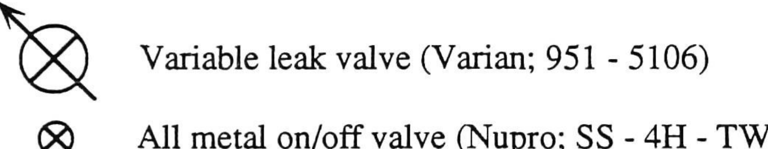

Figure 5.4 Schematic description of the gas dosing line connected to the main vacuum chamber.

5.4 Design and Construction of Thermal Desorption System

5.4.1 Design and Construction

TDS experiments were carried out using a mass spectrometer (Spectramass Dataquad 200) to monitor the partial pressure of gaseous species as a function of sample temperature. Several partial pressures could be monitored simultaneously but with a loss in instrument sensitivity.

It was found in these experiments that adsorbates liberated from the sample surface by heating were most successfully detected using the most sensitive detection ranges of the mass spectrometer. This creates the problem of avoiding the detection of adsorbates desorbing from the chamber walls and sample supports. The detection of spurious signals can be minimised by shielding the mass spectrometer head.

A number of methods of shielding and differentially pumping the quadrupole head of mass spectrometer systems have been developed [8-10]. Reference [10] lists more than one hundred implementations of mass spectrometer - based desorption spectrometers which incorporate shielding. The quadrupole head is shielded from all gas sources except those coming from the immediate vicinity of the heated sample and a differential pumping action is provided to pump the desorption products through the quadruple head, promoting greater gas detection sensitivity [9].

The sample shielding and pumping adopted for these experiments is shown schematically in figure 5.5. The quadrupole head is entirely encapsulated in a cylindrical stainless steel case with a conical endpiece. The endpiece has a 4mm diameter hole in it which is positioned as close as possible to the sample surface during thermal desorption experiments. The differential pumping action is achieved using a series on 10mm diameter holes in the opposite end of the cylindrical cover. This arrangement encourages the movement of desorbed gases through the small aperture into the shielded area, across the accelerating grids of the quadrupole head, and out of the shielded area via the larger holes at the other end. It was found that these measures sufficiently increased the sensitivity of the mass spectrometer system to allow meaningful thermal desorption experiments to be undertaken.

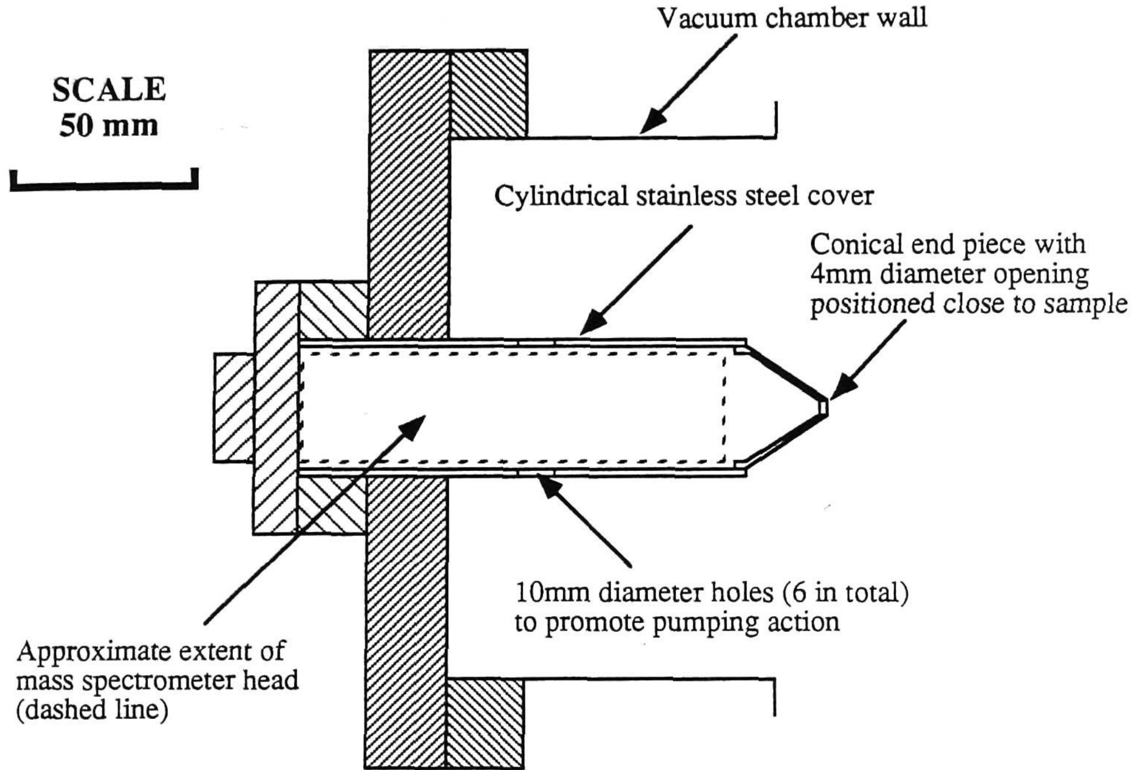

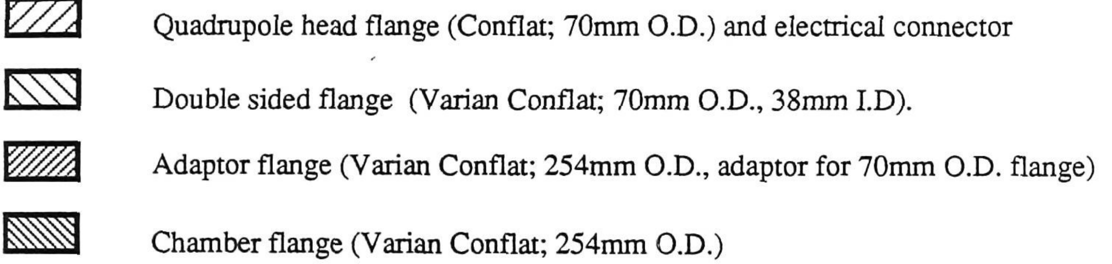

Figure 5.5 Schematic description of the shielding cone constructed for the mass spectrometer head.

5.4.2 Data Acquisition and Testing

The collection of thermal desorption spectra required the careful adjustment of a number of the operating parameters of the mass spectrometer and data recording system. The mass spectrometer "precision" setting was adjusted to give readings every 0.5 seconds. The dwell time of the digitally based mass spectrometer is determined by the combination of precision and the selected gain range. The mass spectrometer also incorporated a hard - wired calibration routine which adjusted the instrument output between its different functions. The mass spectrometer output and sample temperature were simultaneously logged at a rate of around three readings per second using a computer controlled datalogger (Data Electronics DT100 Datataker) during TDS experiments.

A number of tests was carried out on the system to optimise performance. Trial desorption runs were undertaken to set gain levels and dwell times correctly and to test the number of mass channels that could be effectively recorded. The effect of heating rate and pump throttling were also investigated to maximise sensitivity. It was found that gas evolution rates increased with higher heating rates. However, as gas evolution rates approached the chamber pumping speed, desorption features became broadened.

5.5 Experimental Method

Amorphous hydrogenated carbon (a-C:H) films were deposited on oxygen free high conductivity (OFHC) polycrystalline copper substrates (Goodfellow Metals, 99.99% purity). The substrates were cut (25mm square) and polished to a mirror finish using a combination of abrasive paper, metal polish and suspended alumina (0.3μm). Substrates were stored in a dessicator until required, then cleaned with reagent grade acetone and isopropyl alcohol immediately prior to deposition. Films were deposited with the dual cathode, cylindrical magnetron batch sputter coater described in section 3.3.

The samples were exposed to a range of dose pressures of benzene, then heated adjacent to the mass spectrometer. The resistive heating rate of the samples ranged from 0.25 - 2K per second. Adsorbates used in these experiments included reagent grade benzene and spectrophotometric grade benzene (99+%). Adsorbates

were freeze degassed before being admitted to the main chamber [1]. The adsorption behaviour of a-C:H films of different thicknesses was studied by adsorbing benzene in increasing doses and observing changes in the line shape of the thermal desorption spectra. The position and relative intensity of peaks in a series of thermal desorption spectra provide information about adsorption energetics and film structure. The effect of different heating rates during thermal desorption was also investigated. Arrhenius analysis of the resulting thermal desorption spectra was used to estimate the activation energies of desorption for the various binding states observed.

A mixture of benzene and air was accidentally dosed onto the a-C:H films during one series of experiments. This resulted from an air leak in the gas dosing line of the experimental apparatus. The composition of this mixture was not carefully determined. Mass spectral data at the time suggested that approximately equal parts of benzene and air were present in the adsorptive. This misadventure provided TDS results (discussed in section 5.7) and work function results (discussed in chapter 6) which were significantly different from those obtained using pure adsorptives. Contrasting the results facilitated interpretation of adsorption behaviour.

A number of experimental conditions affected thermal desorption behaviour. These included heating rates, mass spectrometer settings, sample positioning and gas dosing procedures. A protocol was devised to minimise variations in the experimental conditions. The sample was left in position, adjacent to the mass spectrometer cone opening, for the duration of each set of thermal desorption experiments. The gas dosing method was also standardised. A series of preliminary experiments was undertaken for each of the sets of thermal desorption data to optimise the settings of the mass spectrometer. The mass spectrometer did not have any provision for rescaling between detection ranges. Best results were obtained if exposures were selected which allowed the use of a single detection range.

5.6 Semiquantitative Analysis of TDS Data

5.6.1 Arrhenius - Redhead Analysis

Thermal desorption phenomena are the result of removing adsorbed particles from a surface by thermally breaking the adsorption bond. Thermal desorption may therefore be described as a reaction where physisorbed or chemisorbed species (A) are removed from surface adsorption sites (B) resulting in the evolution of A_{gas} and empty surface sites:

$$\underset{\text{before heating}}{A - B} \leftrightarrow \underset{\text{after heating}}{A_{gas} + B} \tag{5.1}$$

The kinetic order indicates the complexity of the adsorption/desorption process. First and second order processes are most commonly observed and are identified by the behaviour of peak positions in response to increasing coverage [4,11].

In first order processes, peak position remains unchanged when coverage is increased. A typical process is the desorption of non - dissociatively adsorbed molecules for which the gas evolution rate is linearly dependent on the number of adsorbed molecules. The desorption peak is asymmetric, rapidly falling immediately past the peak centre [11].

In second order processes, peaks move to lower energies (desorption temperatures) in response to increases in coverage. A typical second order process occurs when dissociated adsorbates recombine to form polyatomic molecules in the gas phase as a result of desorption. The inference in this case is that two suitable molecules must be located adjacent to one another for desorption to occur [3]. Second order desorption peaks can be identified by their symmetry about the peak centre. Integrating the area under the curve confirms that the coverage at the peak centre is half the initial coverage [12].

Using standard chemical kinetics [4], the rate of desorption,

$$R_d = -\frac{dn}{dt} = f(n,T) \qquad (5.2(a))$$

may be analysed in terms of an Arrhenius equation of the form

$$R_d = k\,n^a = \nu_a n^a \exp\left[\frac{-E_d}{RT}\right] \qquad (5.2(b))$$

where n is the surface concentration or coverage of adsorbed particles per unit area,
T is the absolute temperature (K),
k is the rate constant,
a is the order of the desorption reaction,
ν_a is the pre - exponential factor (s^{-1}),
E_d is the activation energy of desorption (J mol^{-1}),
and R is the gas constant (J K^{-1} mol^{-1}) [3,4,11,12].

The simple Arrhenius equation used for this analysis provides a macroscopic description of a complicated sequence of microscopic processes. The rationale for applying this equation is that the desorption process can be treated as a series of interacting elements, each represented by a separate term [4]. The equation may be considered to be composed of three terms: the coverage term, the pre - exponential term and the exponential term. It is assumed that the coverage term, n^a, wholly describes film coverage and that the exponential term wholly describes the temperature dependence of the system. Menzel [4] gives the following descriptions of each of the terms:

(i) The coverage term represents the number of particles taking part in the critical step in the desorption process;

(ii) the pre - exponential term represents the frequency of attempts of the system to move in the direction of reaction; and

(iii) the exponential term represents the number of attempts having the necessary minimum energy for this to occur.

The desorption experiments discussed in this chapter were carried out using a linear temperature ramp of the form

$$T = T_0 + \beta t \qquad (5.3(a))$$

$$\beta = \frac{dT}{dt} \qquad (5.3(b))$$

where T is the temperature (K) at time t (s), T_o is the initial temperature (K) and β is the heating rate (K s^{-1}). The pressure - temperature data collected with the mass spectrometer during a temperature ramp is dependent on the relationship between the desorption rate and the pumping rate of the chamber. In these experiments the pumping rate was significantly greater than the desorption rate; desorption events, therefore, appear as peaks rather than plateaus in the pressure - temperature curves. The desorption rate under these conditions is directly proportional to pressure as measured by the mass spectrometer [11].

A desorption peak corresponds to a local maximum rate of desorption. Therefore, at the peak temperature, T_p, $d^2n/dt^2 = d^2n/dT^2 = 0$. Differentiating equation 5.2 with respect to temperature and setting $d^2n/dT^2 = 0$ gives

$$\frac{E_d}{RT_p^2} = \frac{\nu_a}{\beta} \, a n^{a-1} \exp\left[\frac{-E_d}{RT_p}\right] \qquad (5.4(a)).$$

For first order processes a = 1 and therefore

$$\frac{E_d}{RT_p^2} = \frac{\nu_1}{\beta} \exp\left[\frac{-E_d}{RT_p}\right] \qquad (5.4(b)),$$

similarly, for second order processes a = 2, and

$$\frac{E_d}{RT_p^2} = 2n \frac{\nu_2}{\beta} \exp\left[\frac{-E_d}{RT_p}\right] \qquad (5.4(c)).$$

For first order processes the activation energy can be obtained directly from equation 5.4(b) if a suitable value for the pre - exponential factor, ν_1, is assumed. A value of 10^{13} s^{-1} is widely used [11-14], and is justified on the grounds that pre - exponential factors in chemical reactions and vibrational frequencies of surface bonds are of the same order [11]. Activation energy is plotted as a function of peak

temperature for the heating rates used in these experiments in figure 5.6. The relationship between E_d and T_p is approximately linear (± 1.5%) for $10^{13} < (\nu_1/\beta) < 10^8$. Redhead [12] expresses equation 5.4(b) empirically as

$$E_d = R\,T_p\left[\ln\left[\frac{\nu_1 T_p}{\beta}\right] - 3.64\right] \qquad (5.5).$$

While this method of obtaining activation energies is straightforward, significant errors may be encountered as the pre - exponential factor can differ from the ideal value by several orders of magnitude in some circumstances [15,16]. Errors can also be introduced if desorption is not first order or is mixed order [3,13].

The activation energy can be deduced without assuming a value for the pre - exponential factor if peak temperature is measured as a function of the heating rate, β [13]. Values for β should vary over two orders of magnitude to ensure reasonable accuracy [12]. The activation energy for an arbitrary order process can be deduced [13] by rewriting equation 5.4(a) as

$$\ln\left[\frac{T_p^2}{\beta}\right] = \frac{E_d}{RT_p} + \ln\left[\frac{E_d}{\nu_a R}\right] + (\text{"order dependence"}) \qquad (5.6)$$

and plotting $\ln\left[\frac{T_p^2}{\beta}\right]$ as a function of $\frac{1}{T_p}$. The slope of the plot is given by

$$\frac{d\left(\ln\left[\frac{T_p^2}{\beta}\right]\right)}{d\left(\frac{1}{T_p}\right)} = \frac{E_d}{R} \qquad (5.7).$$

For first order processes, equation 5.4(b) can be rewritten as

$$\frac{d(\log\beta)}{d(\log T_p)} = \frac{E_d}{RT_p} + 2 \qquad (5.8)$$

where E_d can be deduced from the slope of a plot of log T_p against log β. The pre - exponential factor can be obtained from equation 5.4(b) using the value for E_d.

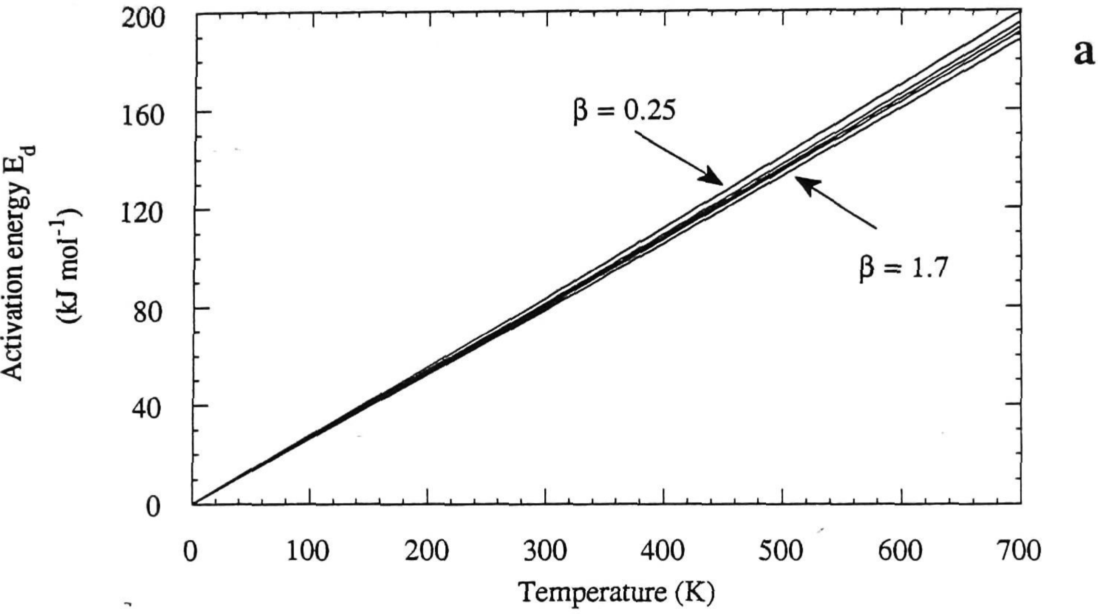

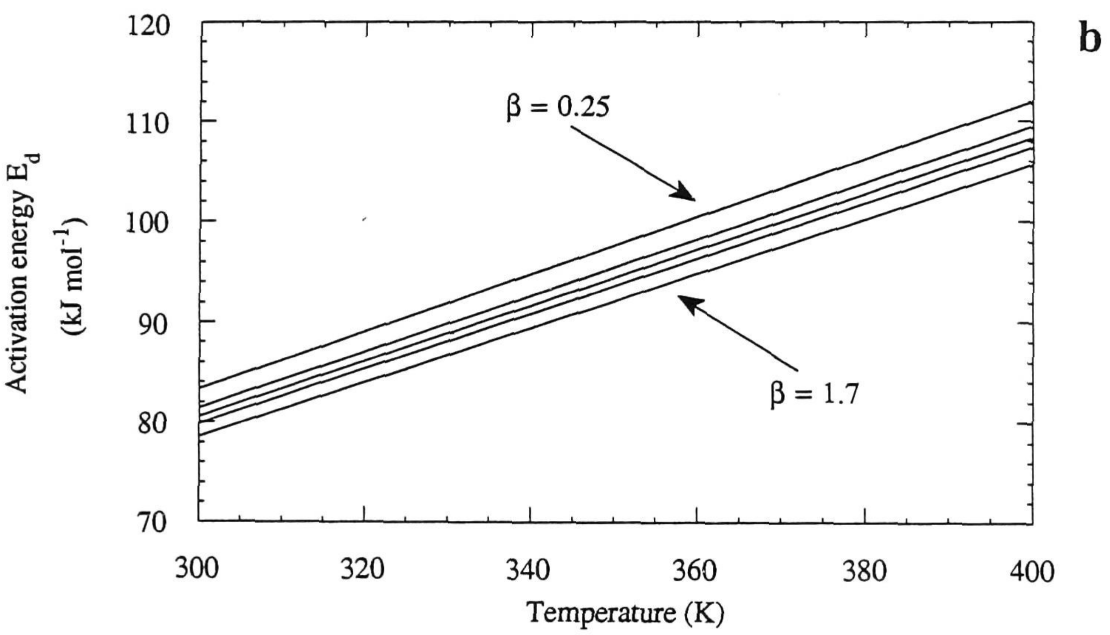

Figure 5.6 Activation energy of desorption (E_d) as a function of peak temperature T_p for a first order reaction and a linear temperature sweep ($T = T_0 + \beta t$). The pre - exponential factor ν_1 was assumed to be 10^{13} s^{-1}. The heating rates (K s^{-1}) used in these experiments were 0.25, 0.53, 0.75, 1.0, 1.7. The curves on the plots, moving from top to bottom, correspond to increasing heating rates. Plot (b) is an expanded region of plot (a)

[adapted from ref. 12]

Second order processes can be analysed using equation 5.4(c). Since coverage at the centre of a second order peak, n, is equal to half the initial coverage, n_o, equation 5.4(c) can be rewritten as

$$\ln\left[n_0 T_p^2\right] = \frac{E_d}{RT_p} - \ln\left[\frac{\nu_2 R}{\beta E_d}\right] \qquad (5.9).$$

If the desorption process is genuinely second order, then a plot of $\ln\left[n_0 T_p^2\right]$ against $1/T_p$ will be linear with a slope of E_d/R [11,12]. The pre - exponential factor can be found by substituting the value for E_d into equation 5.4(c).

5.6.2 Modelling Thermal Desorption Behaviour

Line shape analysis of multiple peak thermal desorption spectra allows the modelling of separate desorption processes. The most commonly used method involves deconvoluting spectra into a series of curves on the basis of structural features [14]. The activation energy for each of the processes can be estimated using the variants of the Arrhenius equation outlined in the previous section.

These methods only take account peak position in determining the energetic characteristics of the desorption processes. It is generally assumed that desorption processes are either first or second order, depending on changes in peak position with coverage and whether peak line shape is symmetric or asymmetric. In reality desorption processes may be of mixed order; this difficulty is not addressed in the simple formulations discussed above [4,11,13].

An alternative approach involves explicitly incorporating contributions from different elements of a complex desorption process. Analysis of the rates of desorption from individual binding states can be used to take account of readsorption, the sticking probability for each binding state and interconversion between states during a thermal desorption process [14].

For example, the rate of desorption from the ith binding state may be expressed as follows

$$\frac{dn_i}{dt} = \nu_i n^{a_i} \exp\left[\frac{-E_{d_i}}{R T_p}\right] + s_i P [2\pi m k T_g]^{-\frac{1}{2}} + F_i \qquad (5.10(a))$$

such that

$$\frac{dn}{dt} = \sum_i \frac{dn_i}{dt} \qquad (5.10(b))$$

where s_i is the sticking probability of the ith state, P is pressure, m is adsorbate mass, k is Boltzmann's constant, T_g is the gas phase temperature and F_i is the net interconversion of other binding states to the ith state [17]. This approach to desorption analysis takes account of interactions between different binding states.

A simple model has been developed for the thermal desorption behaviour of the porous a-C:H films used in this study [18,19]. Knowledge of the structure of the porous surface obtained from other experimental techniques has been incorporated into the model system to provide a degree of physical reality. The key elements of the model are set out below; the results of the modelling are discussed in section 5.7.2.

The model system consists of a cylindrical pore of radius r and depth l, opening into a pumped volume with a pressure P, which is monitored with a mass spectrometer. At the beginning of a model experiment, (time = 0), the pore is filled with an amount, n_l^0, of benzene which is given by pore volume and coverage. A variable temperature is applied to the pore; the temperature and the mass spectrometer signal are measured at discrete times. Benzene evaporates from the pore into the gas phase leaving behind an increasing area of adsorbed benzene. The benzene is more strongly bound and desorbs at a higher temperature. The system can be analysed in terms of rate equations describing the behaviour of the three phases involved. The number of molecules in each phase are denoted as: liquid molecules, n_l; adsorbed molecules, n_p; and gas phase molecules, n_g.

Evaporation processes are characterised by an enthalpy of vaporisation, ΔH_v. Assuming ideal gas behaviour and that ΔH_v is constant over the temperature range of interest, the vapour pressure, P_j, of a material j can be written as

$$P_j = \exp\left[\frac{-\Delta H_v}{RT} + A_1\right] \tag{5.11}$$

where A_1 is a constant [20]. The surface tension, γ, of a liquid when it is in the form of a droplet or bubble modifies the vapour pressure and hence evaporation behaviour. Similarly, when a liquid is contained in a cylindrical enclosure or pore, the surface tension of the meniscus formed reduces the vapour pressure, making it more difficult for the liquid to evaporate. The Kelvin equation gives a quantitative estimation of changes in vapour pressure arising from surface tension and interface curvature effects. The Kelvin equation can be written as

$$P_j^* = P_j \exp\left[-\frac{2\gamma}{r}\frac{V_m}{RT}\right] \tag{5.12}$$

where P_j^* is the reduced vapour pressure for the material j, $-\frac{1}{r}$ is the curvature of the meniscus and V_m is the molar volume of the adsorbate [20]. Combining equations 5.11 and 5.12 gives a reduced vapour pressure of

$$P_j^* = A_2 \exp\left[\frac{-\left[\Delta H_v + \frac{2\gamma V_m}{r}\right]}{RT}\right] \tag{5.13}$$

where A_2 is a constant. The adsorbate used in these experiments was benzene. At 293K benzene has a surface tension of 28.85×10^3 N m^{-1} and a molar volume of 8.89×10^{-5} m^3 [21].

The rate of evaporation or, equivalently, the rate of change of the number of molecules in the liquid phase, $\frac{dn_l}{dt}$, is proportional to the surface area of the pore, r^2, and P_j^* and can be written as

$$\frac{dn_l}{dt} = -k_1 r^2 \exp\left[\frac{-\left[\Delta H_v + \frac{2\gamma V_m}{r}\right]}{RT}\right] \qquad n_l^0 \geq n_l > 0 \tag{5.14(a)}$$

$$= 0 \qquad n_l = 0 \tag{5.14(b)}$$

where k_l is a constant. A fixed pore volume constrains n_l to values greater than or equal to zero.

The rate of desorption of material adsorbed on the pore walls, $\frac{dn_p}{dt}$, is characterised by two competing processes and may be expressed as

$$\frac{dn_p}{dt} = -\frac{\delta}{r}\frac{dn_l}{dt} - k_2 n_p \exp\left[\frac{-E_d}{RT}\right] \qquad (5.15)$$

where δ is thickness of the adsorbed layer and k_2 corresponds to the pre - exponential factor used in the Arrhenius analysis discussed in section 5.6.1. The first term corresponds to interconversion of material between the liquid and physisorbed states as the pore walls are exposed by evaporation. The evaporation process removes a volume of liquid to expose an area of surface covered by an adsorbed layer at a rate proportional to $\frac{1}{r}$. The second term describes the competing, first order desorption process using an Arrhenius equation of the form described in equation 5.2(b).

The number of molecules in the gas phase is augmented by evaporation of liquid in the pore and desorption from the pore walls and depleted by pumping. The rate of change of the number of molecules in the gas phase, $\frac{dn_g}{dt}$, is given by

$$\frac{dn_g}{dt} = -\frac{dn_l}{dt} + k_2 n_p \exp\left[\frac{-E_d}{RT}\right] - k_3 n_g \qquad (5.16)$$

where k_3 is the pumping constant. The three terms correspond to evaporation, desorption and pumping, respectively. Initial conditions are assumed to be $n_g = 0$, $n_p = 0$ and n_l,= n_l^0. A constant of proportionality is taken up in the value assigned to n_0^l. The mass spectrometer signal is proportional to the number of benzene molecules in the gas phase, n_g.

Solutions for the set of three differential equations discussed above may be found numerically. An optimisation was undertaken in which a computer generated mass spectrometer signal was compared with an experimentally derived mass spectrometer signal. There are eight adjustable parameters used in the optimisation: k_1, k_2, k_3, ΔH_v, E_d, r, δ, and n_0^l. Modified Runge - Kutta integration was used to

evaluate the differential equations in which the temperature at any time was determined from a cubic spine fit to the experimental data. The optimisation is a steepest descent (Powell) method [22].

The numerical evaluation of this set of differential equations was conducted by establishing reasonable starting values for each of the adjustable parameters and holding each value constant, in turn, while the others are optimised to fit the experimentally derived data. This process creates a matrix of values for all variables. This matrix can then solved to provide values for each of the parameters [18,19]. Knowledge of the experimental system can be introduced into the optimisation in the selection of the starting values. Parameter values were constrained to physically reasonable values, incorporating, where appropriate, experimentally derived characteristics of the desorption system.

Peak positions (or peak energies) were established in the initial stages of the optimisation to provide a basis for fitting peak shapes. The remaining parameter values were determined using both the peak position and the line shape of the peak. The latter, arguably, contains most of the information about the desorption processes underlying each thermal desorption spectrum. Evaluation of peak energies was undertaken using the thermal desorption data corresponding to a benzene exposure of 4700L (see figure 5.9 in the next section). The peaks in this spectrum are more clearly defined than those in the three accompanying spectra (1900L, 180L and 50L) and therefore more suitable for optimisation. The energy values deduced for the two peaks were then applied to each of the remaining spectra in turn. Changes in peak energy with coverage are neglected. It is assumed, however, that these changes are small in comparison with changes in peak shape with coverage.

A difficulty encountered with optimisations such as the one under consideration is compensatory adjustment of parameters. This occurs when one parameter is changed and the optimisation process automatically introduces a correction to another parameter to balance the change. Two pairs of parameters are linked in this way in this model: the parameter, k_1, and the enthalpy of evaporation, ΔH_v, (see equation 5.14(a)); and the pre - exponential factor, k_2, and desorption activation energy, E_d, (see equation 5.15). The desorption activation energy can take on any value provided that the pre - exponential factor can be adjusted to compensate for the change. In this sense, these pairs of parameters are not independent variables.

Compensatory adjustment of parameters is caused by local minima in the rate equations being optimised. The optimisation may commence with an arbitrary value for the pre - exponential factor and an energy value which puts the peak in the correct position. A series of values for this pair of parameters exists, however, which provide a better curve fit; each of these pairs represents a local minima. Peak shape changes for each pair of parameters while peak position is unchanged. The best fit can only be found if the optimisation process can move between these local minima. The parameter changes required for this to occur can result in a rapid increase in the function being optimised and a return to the original local minimum. The values returned by the optimisation are therefore largely determined by the starting values for the parameters. Sensitivity of the optimisation process to increases in the function value must be balanced against the need to efficiently locate minima.

This difficulty can be resolved by creating a linear relationship between the pre - exponential and energy parameters, resulting in a single independent variable. Equations 5.14(a) and 5.15 can be rewritten so that the exponential terms incorporate the respective energy parameters and the logarithms of the pre - exponential parameters (expressed as linear functions of the former). A linear relationship was established between the parameters by identifying energy values corresponding to a series starting values for the pre - exponential parameter. Slope and intercept constants are assigned to constrain the energy parameter to this set of values. The rate of evaporation can be expressed as

$$\frac{dn_l}{dt} = -r^2 \exp\left[\ln k_l - \frac{\left[\Delta H_v + \frac{2\gamma V_m}{r}\right]}{RT} \right] \qquad (5.17(a))$$

$$= -r^2 \exp\left[\left[4.07 \times 10^{-4} \Delta H_v + 40.96 + \varepsilon\right] - \frac{\left[\Delta H_v + \frac{2\gamma V_m}{r}\right]}{RT} \right]$$

$$n_l^0 \geq n_l > 0 \qquad (5.17(b))$$

where $\ln k_l$ has been replaced with a function of ΔH_v.

Similarly, the rate of desorption can be expressed as

$$\frac{dn_p}{dt} = -\frac{\delta}{r}\frac{dn_l}{dt} - n_p \exp\left[\ln k_2 - \frac{E_d}{RT}\right] \qquad (5.18(a))$$

$$= -\frac{\delta}{r}\frac{dn_l}{dt} - n_p \exp\left[\left[3.58 \times 10^{-4} E_d - 3.54 + \varepsilon\right] - \frac{E_d}{RT}\right] \qquad (5.18(b))$$

where ln k_2 has been replaced by a function of E_d. As the energy parameter is changed by the optimisation routine, peak position will always remain approximately correct as a result of the linear relationship discussed above. An additional independent parameter, ε, is included in each of the exponential terms to allow small adjustments of the energy parameter. This effectively creates a narrow band of suitable energies.

With such a large number of adjustable parameters, the validity of the results obtained using these methods depends on the accuracy of the parameter values used. In particular, care must be taken in arriving at values for the pre - exponential factors and energies, as discussed above. If values are arbitrarily assumed then precise curve fits can be obtained which contain no physical information at all 14,23].

5.7 Results and Discussion

5.7.1 Determination of Activation Energies using Arrhenius Analysis

The desorption behaviour of the amorphous hydrogenated carbon (a-C:H) films was studied using a range of dosing and heating conditions. Benzene and a mixture of benzene and air were the adsorptives used for the experiments. The thermal desorption spectra shown in figures 5.7, 5.8 and 5.9 were obtained for a range of benzene exposures using a-C:H films of different thicknesses (figure 5.7, 48nm film; figure 5.8, 83nm film; figure 5.9, 190nm film). Note that an exposure at a pressure of 1×10^{-6} torr for 1 second is defined as 1 Langmuir (L). The spectra are characterised by two coverage - dependent peaks corresponding to different binding states and energies. The ratio of the intensities of the two peaks changes with exposure.

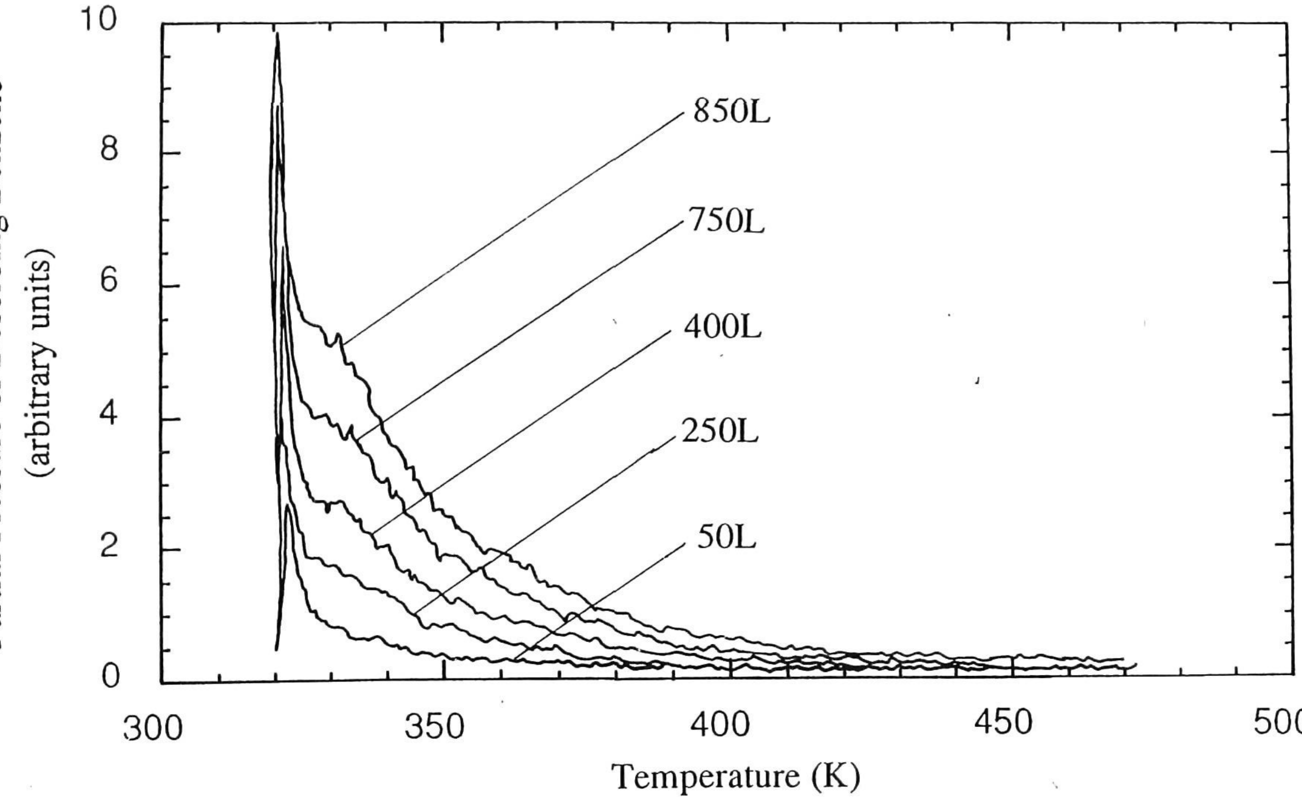

Figure 5.7 Thermal desorption spectra for range of exposures of benzene obtained using a 48nm thick a-C:H film.

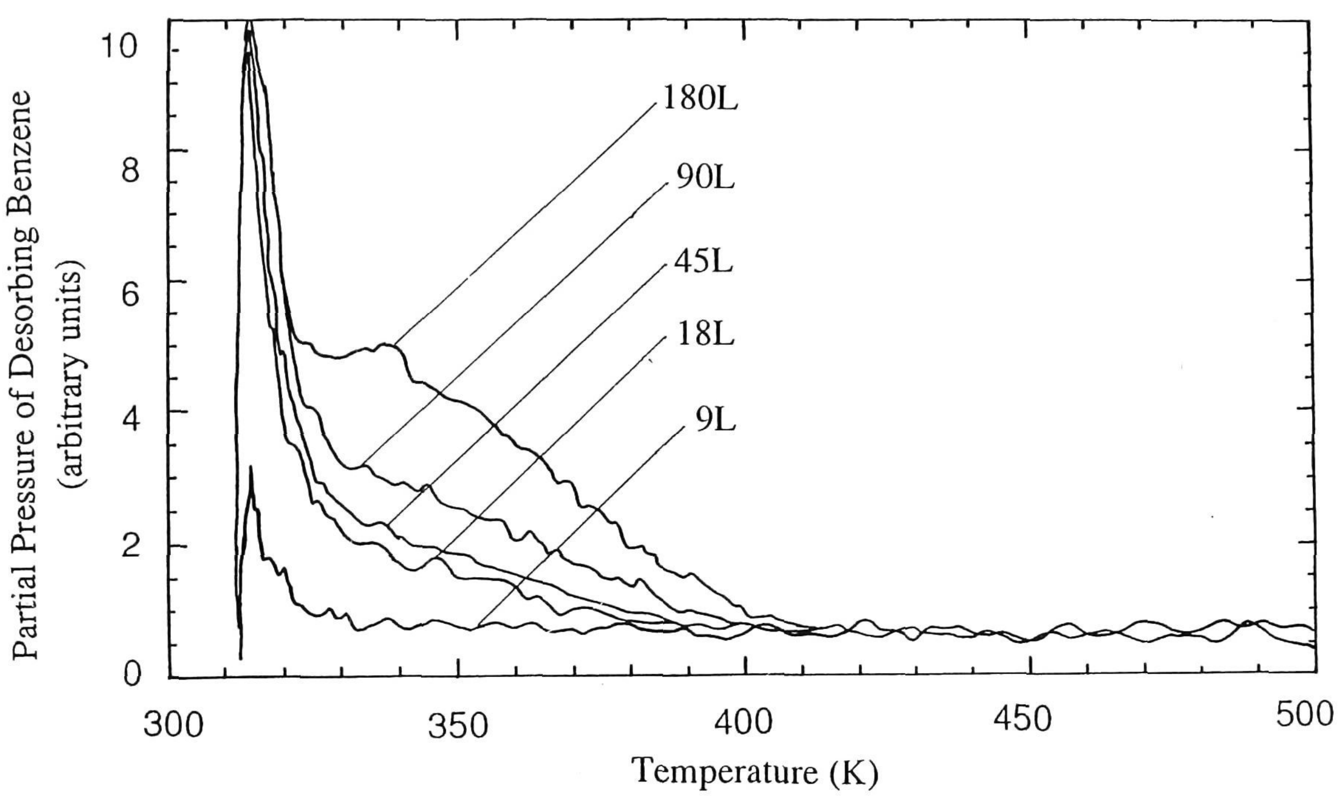

Figure 5.8 Thermal desorption spectra for range of exposures of benzene obtained using a 83nm thick a-C:H film.

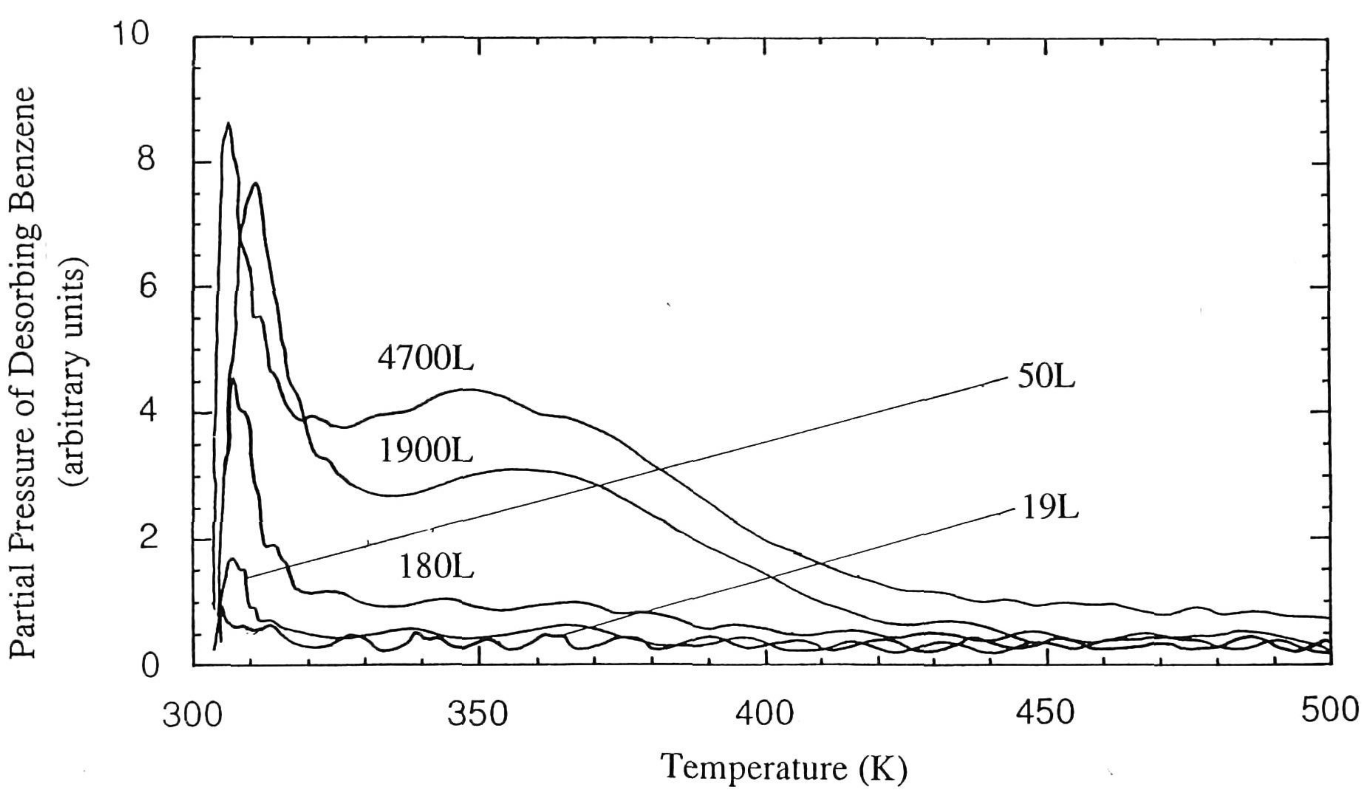

Figure 5.9 Thermal desorption spectra for range of exposures of benzene obtained using a 190nm thick a-C:H film.

Arrhenius analysis, as discussed in section 5.6.1, was used to obtain the activation energies for the two binding states observed as peaks in the thermal desorption data. The empirical expression derived by Redhead [12] and shown as equation (5.5), was used for the analysis. A value of 10^{13} s^{-1} was assumed for the pre - exponential factor. The gas constant R was taken to be 8.314 J mol^{-1} K^{-1}. Table 5.1 shows the calculated activation energies for the thermal desorption curves shown in figures 5.7, 5.8 and 5.9. The approximate, mean activation energies for the two binding states identified were: (a) 85kJ mol^{-1} and 88kJ mol^{-1} for the 48nm a-C:H film; (b) 83kJ mol^{-1} and 90kJ mol^{-1} for the 83nm film; and (c) 81kJ mol^{-1} and 95kJ mol^{-1} for the 190nm film. The heating rates used to obtain these thermal desorption spectra ranged from 1.1 - 1.3K s^{-1}, as indicated in the table.

Figure 5.10 shows the thermal desorption behaviour of a 190nm a-C:H film in response to various exposures of a mixture of benzene and air. This adsorbate was used as a result of an experimental misadventure rather than by design; the desorption behaviour of oxygen and nitrogen was not investigated using TDS. The results for the adsorption of benzene and air, however, illustrate a number of aspects of this adsorption/desorption system and have been retained in this discussion.

The spectra show the partial pressure of benzene evolved from the film as a function of temperature. As before, two coverage dependent peaks are observed, corresponding to desorption from binding sites of different energy. The intensity of peaks is reduced in comparison with those observed for a pure benzene adsorptive (figure 5.9). Benzene adsorption is apparently inhibited either by preferential adsorption or by pore blocking effects. The activation energies for the thermal desorption spectra shown in figure 5.10 are recorded in table 5.2(a). The energies for the two peaks are approximately 82kJ mol^{-1} and 99kJ mol^{-1}. The higher energy peak had a large FWHM and reduced intensity, making the assignment of a centre temperature difficult. Co - adsorption of benzene and contaminant gases is an issue in the design of an industrial production process for temperature limited ETCs. The incorporation of contaminants such as air and water vapour is unavoidable in such a process.

There are a number of shortfalls with Redhead's method, in particular, the estimate of the pre - exponential factor. If, for example, a value of 10^{12} s^{-1} is assumed for the pre - exponential factor, the values for the activation energy are reduced by around 7%. Experimental uncertainties also have a significant effect on estimates of activation energy. Measurements of temperature in the these

(a) Adsorbate = benzene, film thickness = 48nm, heating rate = 1.1 K s^{-1}

Exposure (L)	T_{p1} (K)	E_{p1}(kJ mol^{-1})	T_{p2} (K)	E_{p2}(kJ mol^{-1})
50	322	85.6	330	87.8
250	321	85.3	330.5	87.9
400	321.5	85.5	331	88.1
750	320.5	85.2	330.5	87.9
850	320.5	85.2	330	87.8

(b) Adsorbate = benzene, film thickness = 83nm, heating rate = 1.15 K s^{-1}

Exposure (L)	T_{p1} (K)	E_{p1}(kJ mol^{-1})	T_{p2} (K)	E_{p2}(kJ mol^{-1})
9	314	83.3	-	-
18	314	83.3	340	90.4
45	315	83.6	340	90.4
90	315	83.6	338	89.9
180	315.5	83.7	335	89.0

(c) Adsorbate = benzene, film thickness = 190nm, heating rate = 1.3 K s^{-1}

Exposure (L)	T_{p1} (K)	E_{p1}(kJ mol^{-1})	T_{p2} (K)	E_{p2}(kJ mol^{-1})
19	308	81.3	-	-
50	306.7	81.0	359	95.3
180	307.1	81.1	358	95.0
1900	310.4	82.0	356.6	94.6
4700	306.7	81.0	351.2	93.1

Table 5.1 Activation energies of desorption peaks for a range of film thicknesses and adsorbate exposures, calculated using Redhead's empirical method [12]. T_{p1}, T_{p2}, E_{p1} and E_{p2} correspond to the centre temperatures and calculated activation energies, respectively, of the two binding states identified in the thermal desorption spectra.

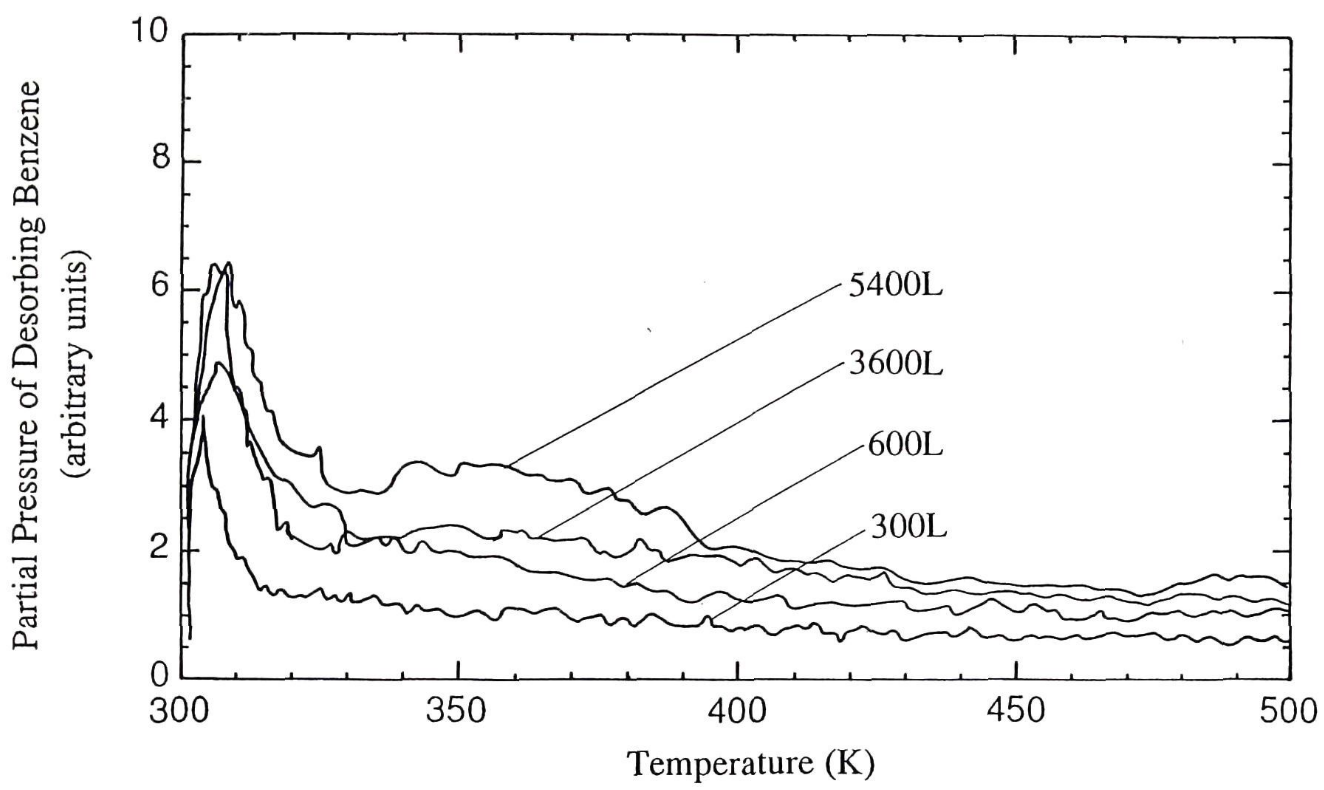

Figure 5.10 Thermal desorption spectra for range of exposures of a mixture of benzene and air obtained using a 190nm thick a-C:H film.

(a) Adsorbate = benzene + air, film thickness = 190nm, heating rate = 0.7 K s^{-1}

Exposure (L)	T_{p1} (K)	E_{p1}(kJ mol^{-1})	T_{p2} (K)	E_{p2}(kJ mol^{-1})
300	304.8	82.0	-	-
600	305.5	82.2	365	98.8
3600	307.5	82.8	365	98.8
5450	307.8	82.9	365	98.8

(b) Adsorbate = benzene, film thickness = 48nm, exposure = 300L

Heat rate (K s^{-1})	T_{p1} (K)	E_{p1}(kJ mol^{-1})	T_{p2} (K)	E_{p2}(kJ mol^{-1})
0.25	319.7	88.9	326	90.7
0.53	319.7	86.9	327.4	89.1
0.75	322.1	86.6	330	88.8
1.0	320.7	85.5	330.4	88.2
1.7	319.2	83.7	333.2	87.5

Table 5.2 Activation energies of desorption peaks calculated using Redhead's empirical method [12]. T_{p1}, T_{p2}, E_{p1} and E_{p2} correspond to the centre temperatures and calculated activation energies, respectively, of the two binding states identified in the thermal desorption spectra.

(a) Adsorbate used was a mixture of benzene and air.

(b) Constant exposure (300L), heating rate ranged from 0.25 to 1.7K s^{-1}.

experiments were made using type K thermocouples attached to the corner of the sample. The opening of the mass spectrometer cone was positioned in the centre of the sample. Temperature offsets between the sample centre and edge can be caused by different heating rates and conduction rates or by the heat sinking effect of the sample supports. Uncertainty in temperature measurement can also occur due to spurious offsets in the thermocouple circuit. The uncertainty in the measurement of temperature at the centre of the sample, taking into account all sources of error, was estimated to be less than ±10K. This corresponds to an error of about 4% in the energy calculation. The total uncertainty in the energy calculation is expected to be less than ±15%.

A number of potentially more reliable methods for deducing activation energies exist using thermal desorption spectra obtained with a range of heating rates. Activation energies are given by the slope of various functions of peak temperature and heating rate. Table 5.2(b) shows the heating rates and centre temperatures of a series of thermal desorption experiments. An exposure of 300L of benzene was desorbed from a 48nm a-C:H film using heating rates ranging from 0.25 to 1.7K s^{-1}. The activation energies of the two peaks calculated using the Redhead analysis described above are also included (approximately 86kJ mol^{-1} and 89kJ mol^{-1}). The rate of evolution of benzene increases with heating rate and the peak centres are shifted to marginally higher temperatures.

Figure 5.11(a) shows a plot of $\ln\left[\frac{T_p^2}{\beta}\right]$ as a function of $\frac{1}{T_p}$ for the higher energy desorption peak (T_{p2}, E_{p2}). The slope of the plot is given by equation 5.7. The activation energy calculated for the peak using this method is approximately 220kJ mol^{-1}. Figure 5.11(b) shows a plot of log β as a function of log T_p for the higher energy desorption peak (T_{p2}, E_{p2}). The slope of the plot is given by equation 5.8. The activation energy calculated for the peak using this method is also approximately 220kJ mol^{-1}.

These results are inconsistent with the activation energies calculated using the Redhead method, even allowing for errors in the assumption of the pre - exponential factor and temperature measurements. Reasonable results are expected only if the heating rate is varied over two orders of magnitude. The apparatus used for these experiments, however, was not designed to accommodate this requirement so the heating rate could only be varied over less than an order of magnitude. These results

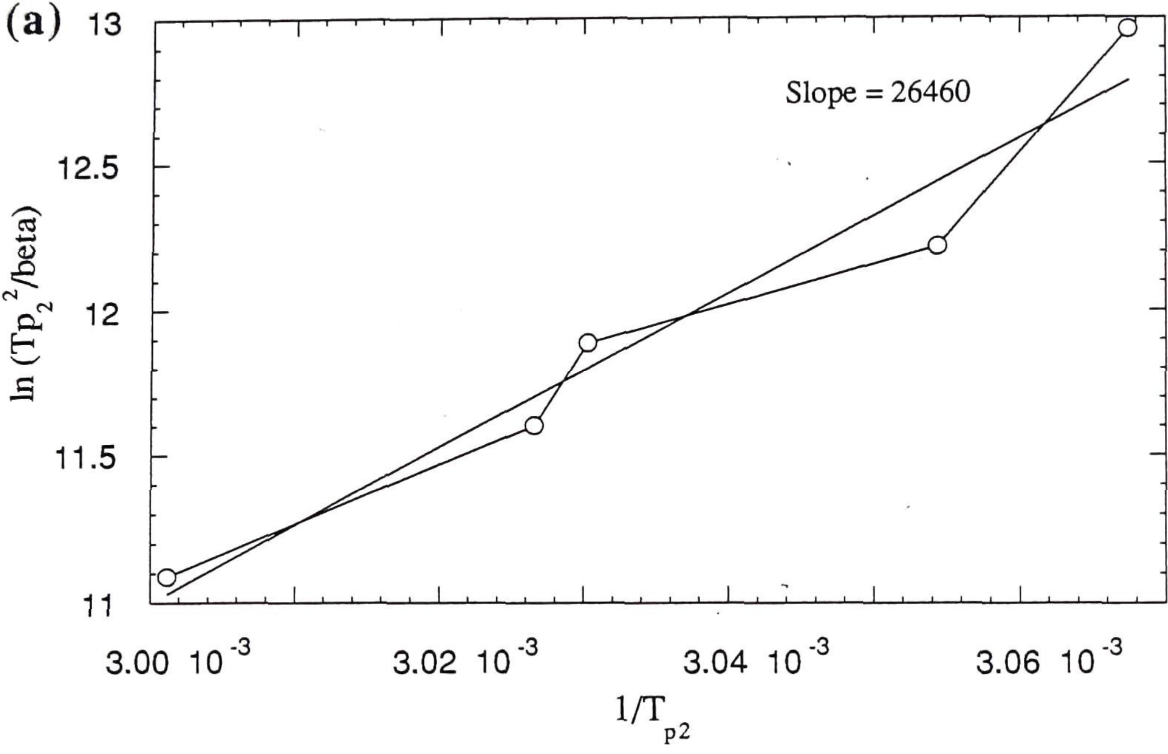

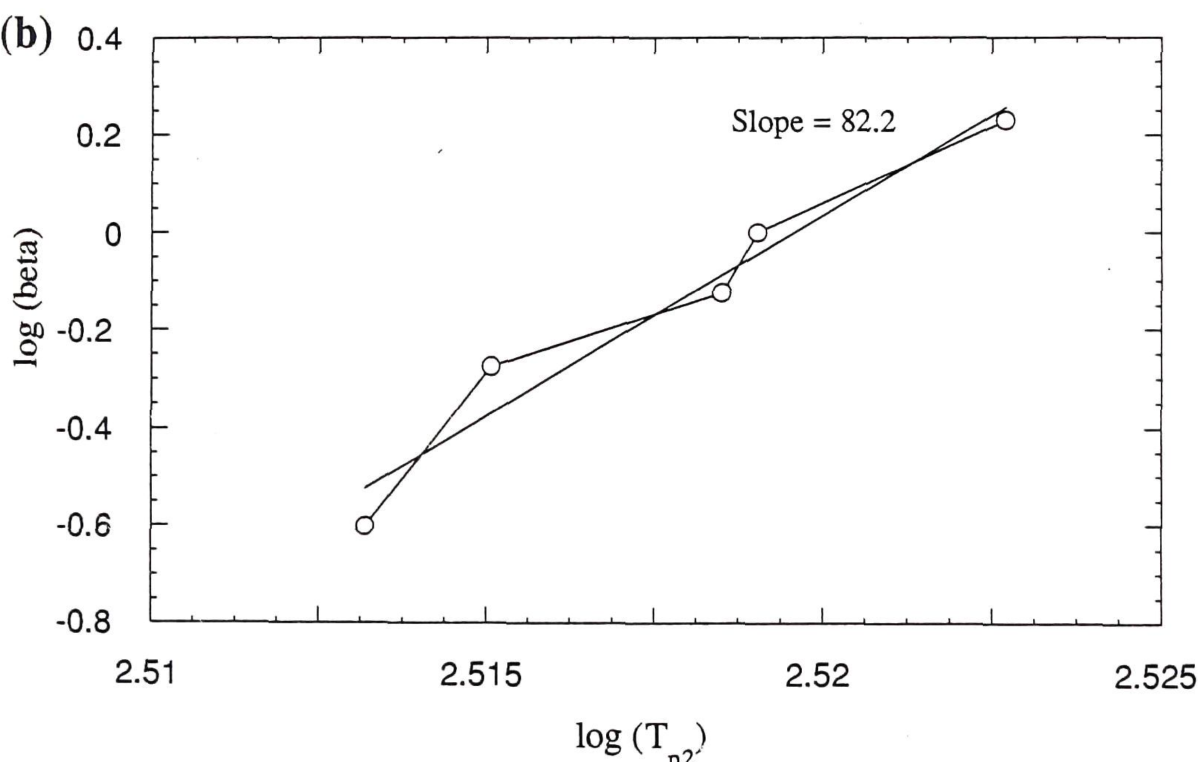

Figure 5.11

(a) Plot of $\ln(T_{p2}^2/\beta)$ as a function of $1/T_{p2}$. The slope is equivalent to E_d/R.

(b) Plot of $\log(\beta)$ as a function of $\log(T_{p2})$. The slope is equivalent to $E_d/RT_p + 2$.

can be discarded on the grounds that the range of heating rates achievable was far too small to obtain realistic results.

5.7.2 Discussion of Desorption Modelling

The desorption model described in section 5.6.2 was applied to the thermal desorption data shown in figure 5.9. A curve fit of a thermal desorption spectrum (4700L benzene exposure) is shown in figure 5.12, accompanied by the experimental data points and heating rate. A precise curve fit has been obtained for both of the desorption peaks using the simple evaporation/desorption model for a single pore of fixed radius. Table 5.3 shows the values for the activation energies, initial coverage and model pore dimensions for the desorption spectra shown in figure 5.9.

The accuracy of the model and the optimisation process can be measured by the combination of the closeness of the fit and whether or not the parameter values are physically reasonable. The optimisation process returned a value of 63.2kJ mol^{-1} for the higher energy desorption peak in comparison with an Arrhenius value of 93.1kJ mol^{-1}. While these values differ by about 30%, the result is satisfactory given the simple single pore model used. The optimisation process returned a value of 33.0kJ mol^{-1} for the lower energy desorption peak in comparison with a significantly different Arrhenius value of 81.0kJ mol^{-1}. Approximating lower energy gas evolution from the surface by evaporation is apparently unsatisfactory. The current model, for example, takes no account of the known distribution of pore sizes in these films or the possibility of percolation effects [1,24].

The exposure (L) is proportional to the number of molecules hitting the sample surface. The initial coverage, n_0^1, is proportional to the number of molecules sticking to the film surface. Comparison of the corresponding values for exposure and coverage gives information about variations in the surface sticking coefficient with increasing coverage.

The pore radius, r, in this model represents some form of weighted average of all the pores and the pore length, l, is proportional to the film thickness. The values calculated by the model for pore radius and pumping constant should remain constant as the same film was used for all experiments; only the exposure and heating rate vary between experiments. This is observed for the three higher exposure experiments. The model breaks down for the 50L experiment, probably

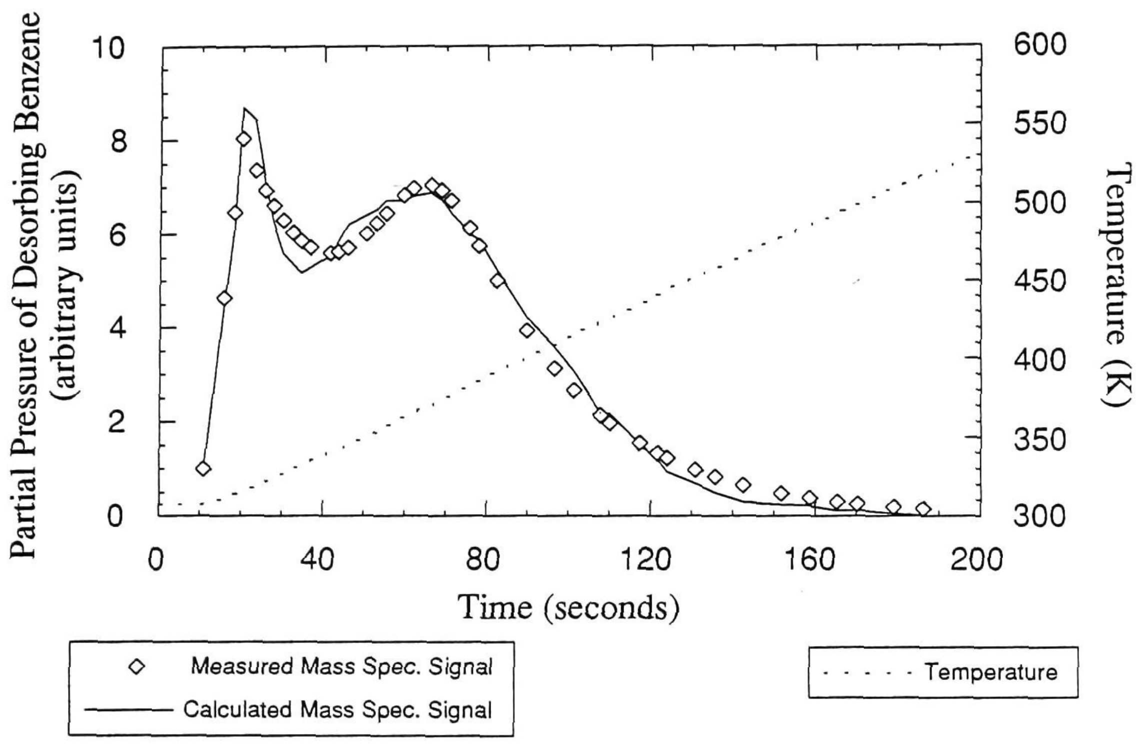

Figure 5.12 Thermal desorption spectrum for a 4700L benzene exposure and a corresponding model desorption curve calculated using the methods described in section 5.6.2. The thermal desorption temperature ramp, used in the modelling process, is also shown.

Exposure (L)	E_{p1} (ΔH_v) (kJ mol^{-1})		E_{p2} (E_d) (kJ mol^{-1})		Coverage n_l^0 (arb. units)	Pore radius r (x10^{-9}m)	Thickness δ (x10^{-9}m)	Pump const. k_3
	Arrhenius	Model	Arrhenius	Model				
50	81.0	33.0	95.3	63.2	1.45	3.73	1.56	0.0276
180	81.1	33.0	95.0	63.2	3.76	1.53	1.48	0.0335
1900	82.0	33.0	94.6	63.2	5.11	1.53	1.47	0.0336
4700	81.0	33.0	93.1	63.2	8.23	1.20	1.60	0.0340

Table 5.3 Activation energies of desorption peaks for a range of adsorbate exposures calculated using the model discussed in section 5.6.2. The data used for the modelling correspond to the thermal desorption spectra and data shown in figure 5.9 and table 5.1(c). The peak energies were calculated for the 4700L desorption spectrum. The values for coverage, pore radius, thickness and the pumping constant were optimised for all exposures for the calculated peak energies.

because the shapes of the desorption peaks are not clearly defined and curve fitting is considerably more difficult.

Pore radius must be always greater than or equal to the thickness of the adsorbed layer, δ, within the pore for a physically reasonable result. The 180L and 1900L experiments returned approximately equal δ values which suggests that after evaporation, the pore still remains almost completely filled. The 4700L experiment, however, returned a pore radius which is slightly smaller than the thickness of the adsorbed layer (a non - physical result). The pore radius determined in the optimisation ($\sim 1.5 \times 10^{-9}$m) is in good agreement with micropore radii deduced in previous benzene adsorption studies using these a-C:H films (0.4 - 1.0×10^{-9}m) [1].

These results demonstrate that a useful analysis of the thermal desorption behaviour of a porous material can be undertaken using a simple model. However, a number of improvements to the model used in this study have been identified. Interrelated parameters, such as pore radius and adsorbed film thickness, should have explicit constraints placed on the range of permissible values. Similarly, constraints should be applied to parameters which remain constant for all experiments, such as pore radius and pumping constant. Simultaneously optimising parameter values for a number of desorption spectra may not be feasible due to long computing times. Applying these constraints improves the accuracy of the optimisation process by incorporating known properties of the system.

The "single pore" model used in this study should be extended to take account of the distribution of pore sizes observed in these amorphous carbon films. Ideally, an expression for the pore radius distribution is required which includes micropores, mesopores and macroscopic surface roughness. The desorption behaviour approximated by evaporation in the current model may then be more accurately expressed as desorption from lower energy mesoporous sites. Convoluting the pore radius distribution with an expression for desorption again will require considerable computer time.

5.7.3 Discussion of Thermal Desorption Behaviour

The thermal switch proposed for ETCs requires that over a narrow temperature range, in the vicinity of 350K, a sufficient quantity of gas is released from the a-C:H film to provide a conductive heat loss path to the surroundings. The activation energy for desorption (or desorption temperature) and the quantity of gas evolved

are linked by the temperature dependence of gas sticking coefficient and by changes in heats of adsorption with film coverage. The effect of film thickness on adsorption behaviour is also an issue in optimising switching behaviour. The following discussion relates phenomena observed in the ultrahigh vacuum regime used for these experiments to similar behaviour studied using a much higher pressure regime.

Isosteric heats of adsorption (q_{st}) for benzene adsorbed on a-C:H films have been determined experimentally and theoretically by S.J. O'Shea [1]. The isosteric heat, by definition, is the heat liberated per mole by the reversible adsorption of an infinitesimal amount of gas at constant temperature and pressure [1]. The adsorption potential, ε, is related to the isosteric heat by

$$\varepsilon = -\Delta H = q_{st} - q_0 \qquad (5.19)$$

where $-\Delta H$ is the change in enthalpy and q_0 is the heat of vaporisation. The isosteric heat was evaluated using the DR equation (see section 2.6.2) as follows

$$q_{st}(DR) = q_0 + \sqrt{\frac{-\beta^2}{k} \ln \theta} \qquad (5.20)$$

where β and k are constants and θ is the fractional surface coverage. Figure 5.13 shows the isosteric heat as a function of adsorbate relative pressure. Experimental data are presented for benzene adsorption on films baked to 770K (500°C) and 570K (300°C), together with corresponding values for q_{st} calculated using equation 5.20.

The thermal desorption experiments discussed in this chapter were undertaken using benzene pressures of around 10^{-6} torr (or a relative pressure of $\sim 10^{-8}$ at 298K). This pressure regime corresponds to the left hand edge of the plot shown in figure 5.13. The isosteric heat of adsorption of benzene at a relative pressure of $\sim 10^{-8}$ at 298K on an a-C:H film baked to 670K should be approximately 90kJ mol^{-1}. This is in excellent agreement with the values for the desorption activation energy E_d deduced using Arrhenius analysis for the higher energy thermal desorption peak. Adsorption reversibility implies that the heat of adsorption and the activation energy for desorption should be equal in magnitude. It is to be noted that irreversible adsorption has been observed for some films baked at lower temperatures (~570K) and for shorter periods of time. The comparison of these energy values (E_d and q_{st}), calculated using separate experimental data and

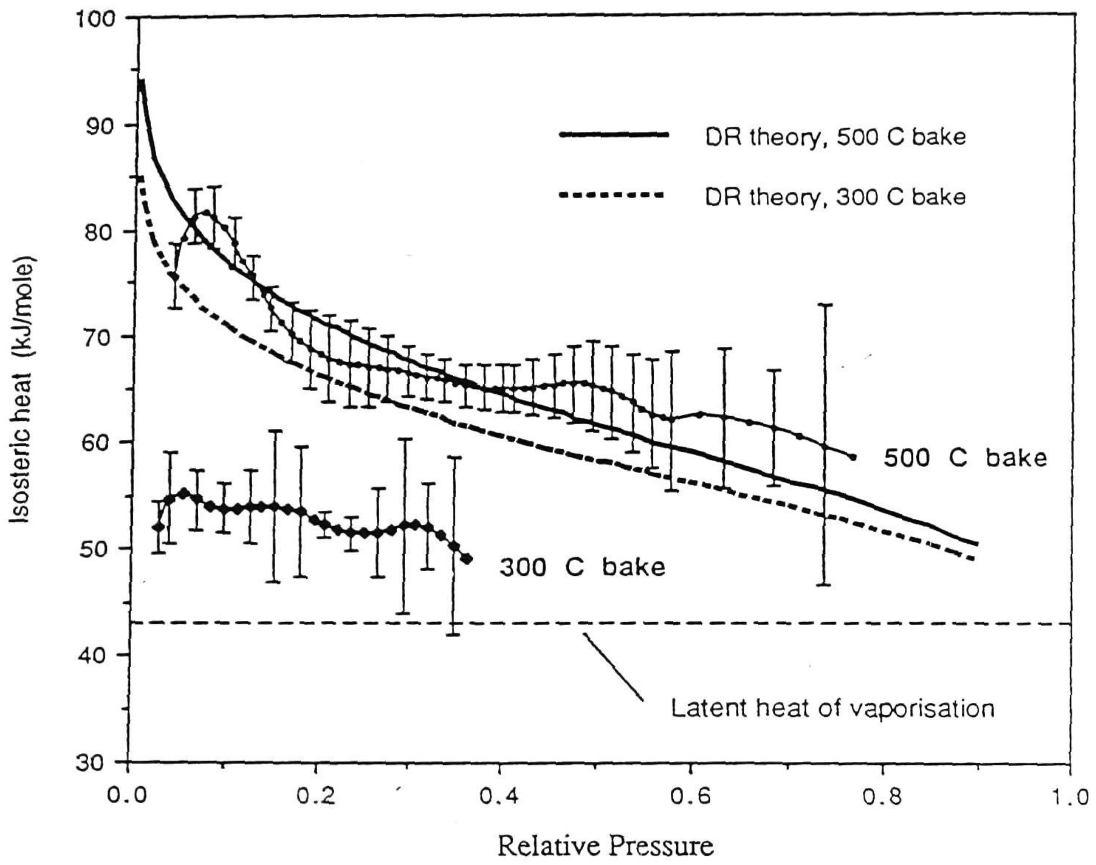

Figure 5.13 Isosteric heat of adsorption of benzene on baked (570K, 770K) spectrally selective films on the type used in this study, calculated at 303.5K. The latent heat of vaporisation for benzene and isosteric heats of adsorption calculated using the DR equation (equation 5.18) are also shown. The adsorption experiments described in this thesis were undertaken in a pressure regime located between 5×10^{-10} torr and 1×10^{-4} torr. This corresponds to a relative pressure range of around 10^{-11} to 10^{-6} for a benzene adsorptive or at the left hand axis of the figure above. [reprinted from ref. 1]

techniques, provides a link between the ultrahigh vacuum and high vacuum pressure regimes used for adsorption studies of a-C:H films. These results confirm that the broad higher energy peak observed using thermal desorption methods can be attributed to microporous adsorption sites.

A comparison of figures 5.7, 5.8 and 5.9 shows that the peak shape and the area under the curves change for the films of different thickness. As film thickness increases, the lower energy peak is shifted to lower values and the FWHM of the peak is increased significantly. It is proposed that this peak corresponds to desorption from mesoporous regions of the film. These regions are immediately or readily accessible to the film surface. Larger pore sizes act to reduce the energy with which adsorbed species are bound to the surface. Rapid desorption over a relatively small temperature results in a narrow, intense desorption peak. Decreases in peak energy with increases in film thickness may reflect variations in the overall pore structure of the film

As film thickness increases, the FWHM of the higher energy peak increases. The centre temperature (and hence energy) of the peak is also shifted to higher values. It is proposed that the broader higher energy peak corresponds to desorption from the microporous region of the film. A distribution of pore sizes exists and therefore surface/adsorbate binding energies are spread over a wider range with a higher mean value. The changes in peak shape suggest that, on average, increased energies and increased times are required to eject adsorbed material from the internal adsorption sites of thicker films. While overall pore connectivity is high, pore accessibility is apparently diminished in thicker films. The percolation threshold of the film will determine the extent to which rapid desorption is inhibited by pore size. The rate of temperature change also varied slightly between experiments and may affect peak shape. Observations, however, suggest that this is a secondary effect in comparison with those discussed above.

The desorption phenomena evaluated in this study have been treated as first order processes for simplicity. Evidence to date suggests that benzene is physisorbed to the a-C:H film and desorbs via a first order process. Second order processes generally involve intermediate states or co - operative desorption. Restricted pore accessibility and percolation in porous films may result in a desorption process being more accurately described as a mixed order process. Desorption order requires more thorough consideration in any future desorption studies of this system.

In these thermal desorption experiments, the rate of pumping exceeded the rate of gas evolution from the film. The desorption rate (or number of molecules leaving the surface per unit time) is directly proportional to pressure [11]. Therefore, the total number of molecules desorbed during an experiment is proportional to the area under the thermal desorption (pressure vs time) curve. Figures 5.14(a) - (c) show the areas under the TDS curves as a function of exposure for three films of different thickness. The total area under each curve was calculated with no distinction made between the two desorption peaks; uncertainty in the area values was estimated to be less than 10%. A similar increase in area with increased exposure is observed for each film thickness. This reflects a reduction in the sticking coefficient as film coverage is increased. The activation energies of the higher energy peak also moved to lower energies with increased coverage for the 83nm and 190nm films. The magnitude of the energy change was about 2kJ mol^{-1}. Adsorption sites are filled sequentially starting with the highest energy sites. Molecules adsorbed at higher coverages are therefore necessarily bound with a lower energy for a surface with a distribution of pore sizes.

Previous studies of these a-C:H films at higher pressures [1,24] have shown that the adsorption capacity is proportional to the film thickness. This relationship between film thickness and adsorption capacity implies that the film is uniformly porous and that the entire pore volume is accessible to the adsorptive when the films are completely degassed. The areas under the TDS curves for the films used in this study are not proportional to film thickness as expected. Various factors may have contributed to this inconsistency. The repeatability of thermal desorption experiments was an aspect of the experimental work that required considerable attention. Experimental conditions are consistent within each of the sets of thermal desorption spectra. Differences between the sets of spectra arise from unavoidable differences in experimental conditions. Differences in film preparation may also be a factor, although considerable care was taken to standardise preparation techniques. The adsorption capacity of these films, for example, is strongly dependent on the type of heat treatment applied to the film during preparation [1]. Freshly prepared, unbaked films show very little adsorption, whereas baked films (670K, 60 minutes) show greatly enhanced desorption peaks. Adsorption isotherms of as - prepared films show mesoporous characteristics [24].

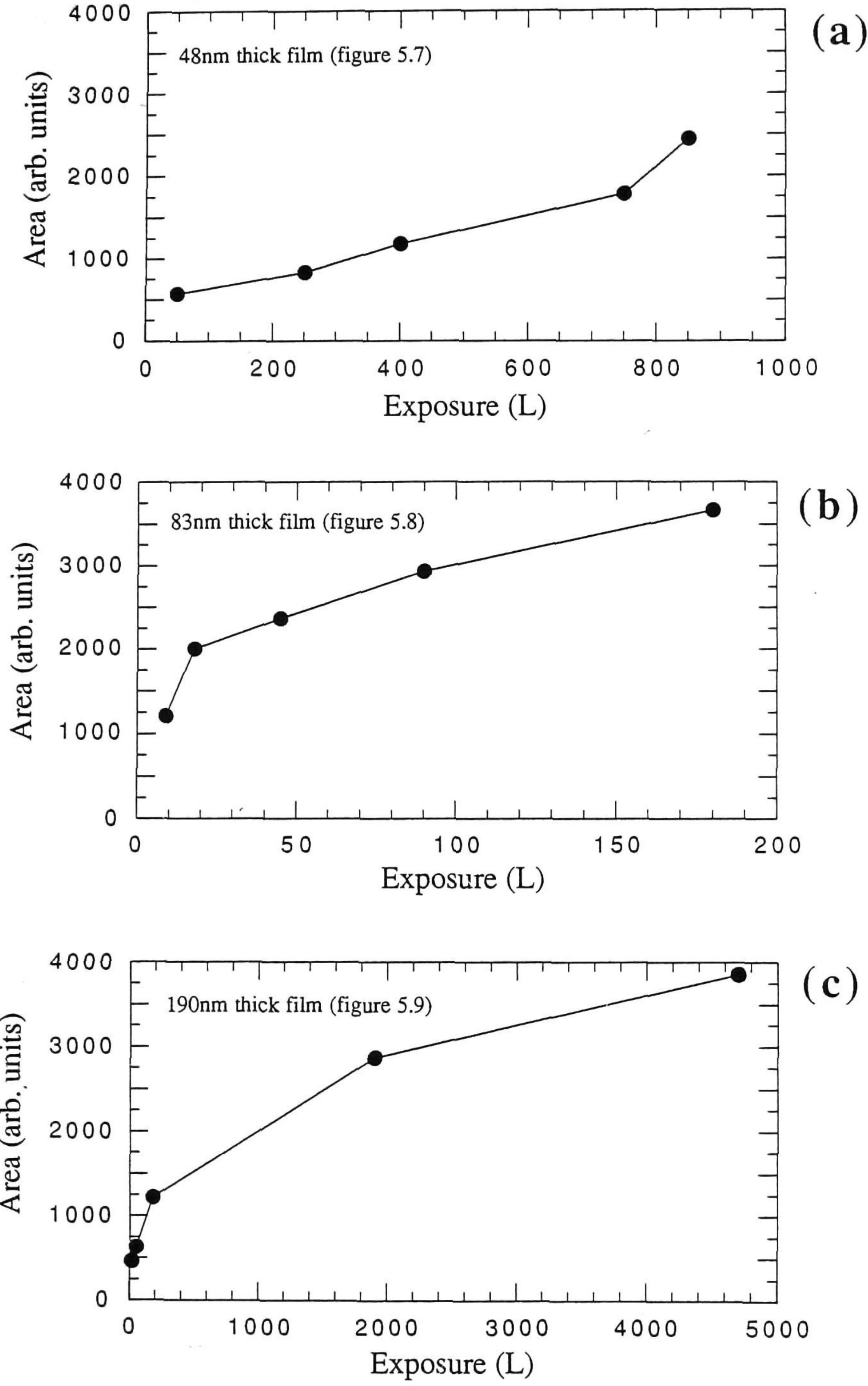

Figure 5.14 Area under pressure - time thermal desorption curves as a function of benzene exposure for three a-C:H films of different thickness. The area is proportional to the number of molecules evolved during the desorption process.

These thermal desorption experiments have revealed two important aspects of the adsorption/desorption mechanism under investigation. Firstly, the activation energies for desorption deduced using these methods are in agreement with energies calculated using a much higher pressure regime. A complete description of the mechanism can be developed over a pressure regime extending from the ultrahigh vacuum region to atmospheric pressure using this link between thermal desorption and volumetric adsorption methods. Secondly, thermal desorption has been used to reveal the constituent parts of a complicated desorption process. Significant changes in desorption behaviour are revealed as a result of changes in exposure and film thickness. The line shape of desorption peaks, for example, is very sensitive to film thickness. The activation energy for the peaks, however, only changes by around 10% between a 48nm thick film and a 190nm thick film. TDS also allows the use of more convenient experimental techniques and methods of measurement at low pressures. The combination of the experimental results obtained in this study and in the previous studies provides the basis of a very thorough understanding of a complicated adsorption system. This understanding is directly applicable to the adsorption behaviour occurring in thermal switching ETCs.

5.8 Summary

An ultrahigh vacuum system has been designed and constructed to provide a clean environment for gas adsorption and desorption experiments. A range of sample mounting devices and gas dosing facilities have also been designed to facilitate the experiments. This type of vacuum system was used to extend the pressure range accessible for experiments and to increase the sensitivity with which low level adsorption processes could be investigated.

Apparatus for thermal desorption spectroscopy (TDS) and work function studies (discussed in the next chapter) were incorporated in the vacuum chamber. The TDS system consisted of a sample mounting incorporating a 2K per second heater and a shielded mass spectrometer. The output from the system was recorded using a computer controller datalogger.

TDS has been used to study the benzene adsorption behaviour of a-C:H films. This material is identical to the surface layer of the spectrally selective films employed in ETCs. It was found that peaks corresponding to two discrete types of binding site could be identified. The peak intensity was dependent on coverage while peak position was dependent on both coverage and film thickness. A narrow desorption peak was observed with an activation energy in the range of 81 - 86kJ mol^{-1}. This peak is thought to arise from desorption from the mesoporous region of the film surface. A second, broader desorption peak was observed with an activation energy in the range of 87 - 95kJ mol^{-1}. The position and FWHM maximum of this peak were dependent on film thickness and coverage. This peak is thought to arise from desorption from the microporous region of the film surface. Changes in the line shape of the higher energy desorption peak suggest that pore accessibility and the time required for the adsorbate to reach the film surface are dependent on film thickness.

Arrhenius analysis was used to estimate the activation energies of the desorption processes observed. Best results were obtained using Redhead's empirical formulation [12] and assuming a value of $10^{13}s^{-1}$ for the pre - exponential factor. Attempts were made to calculate activation energies without such an assumption by varying the heating rate used in the thermal desorption experiments. However, the range of heating rates available using the apparatus in its current form was insufficient to allow accurate results. A simple model for the desorption system was also devised based around the processes of evaporation and desorption from the pores and pumping of the evolved material out of the experimental vessel. The desorption activation energies for the two desorption peaks in a 190nm thick film were calculated to be 33.0kJ mol^{-1} and 63.2kJ mol^{-1}. The average pore radius was calculated to be $\sim 1.5 \times 10^{-9}$m which is consistent with estimates of micropore radii made in previous studies of these films [1].

The adsorption capacity of the films, approximated by the area under the desorption curves, was determined as a function of exposure for films of different thickness. The proportionality between film thickness and adsorption capacity previously observed could not be demonstrated due differences in experimental conditions. Consistent variations in area were observed indicating reductions in sticking coefficient with increased exposure and that the pore structure of the film is well connected and accessible to the adsorbing species.

The desorption peak energies calculated in this study have been shown to be consistent with energy values calculated using higher pressure adsorption experiments and the DR equation in a previous study [1]. This provides the basis of a very thorough understanding of the adsorption/desorption mechanism under investigation over a pressure regime extending from the ultrahigh vacuum region to atmospheric pressure.

Current laboratory work indicates that the thermal switch will operate with benzene partial pressures of the order of 10^{-1} to 10^{-4} torr. The adsorption sites of importance in this higher pressure regime are not filled and therefore unobservable in an ultrahigh vacuum pressure regime used in this study. Thermal desorption spectroscopy, however, provides an understanding of the relationship between adsorption, film structure and morphology. The existence of a range of micropores provides further evidence of the complexity of the film structure. In addition, these sites may have important technological implications if they acted to adsorb impurities which then blocked off parts of the film from the desired adsorbate.

References - Chapter 5

[1] S.J. O'Shea, PhD thesis, Department of Applied Physics, University of Sydney, 1989.

[2] Y. Yin, Personal communication.

[3] D.P. Woodruff and T.A. Delchar, "Modern Techniques in Surface Science", Cambridge University Press, 1986.

[4] D. Menzel, In ed. R. Gomer, Topics in Applied Physics - Vol.4, "Interactions on Metal Surfaces", Springer - Verlag, 1975.

[5] G.L. Harding and B. Window, Sol. Energy Mater., 7, 101 (1982).

[6] S.P. Chow and G.L. Harding, Sol. Energy Mater., 11, 123 (1984).

[7] S.P. Chow, PhD thesis, Department of Applied Physics, University of Sydney, 1984.

[8] P. Feulner and D. Menzel, J. Vac. Sci. Technol., 17, 662 (1980).

[9] S.M. Gates, J.N. Russell, Jr. & J.T. Yates, Jr., Surface Science, 146, 199 (1984).

[10] V.S. Smentkowski and J.R. Yates Jr., J. Vac. Sci. Technol.A, 7, 3325 (1989).

[11] R.P.H. Gasser, "An introduction to chemisorption and catalysis by metals", Clarendon Press, 1985.

[12] P.A. Redhead, Vacuum, 12, 203 (1962).

[13] D. Menzel, In ed. R. Vanselow and R Howe, Springer Series in Chemical Physics - Vol. 20 "Chemistry and Physics of Solid Surfaces IV", Springer - Verlag, 1982.

[14] D.A. King, Surface Sci., 47, 384 (1975).

[15] J. Falconer and R.J. Madix, Surface Science, 48, 393 (1975).

[16] J.G. McCarty, and R.J. Madix, Surface Science, 54, 121 (1976).

[17] W.L. Winterbottom, J. Vac. Sci., 9, 936 (1972).

[18] D.B. Hibbert and R.H. Campbell, Appl. Catal., 41, 273 (1988).

[19] D.B. Hibbert, Personal communication.

[20] See for example:
W.J. Moore, "Basic Physical Chemistry", Prentice - Hall International, 1983.

[21] R.C. Weast (ed.), "Handbook of Chemistry and Physics" - 66th ed., CRC Press, 1985.

[22] The optimisation routine was written using Turbo Pascal and routines from W.H. Press, B.P. Flannery, S.A. Teukolsky and W.T. Vetterling, "Numerical Recipes - The Art of Scientific Computing", Cambridge University Press, 1986.

[23] C. Pisani, G. Rabino and F. Ricca, Surface Science, 41, 277 (1974).

[24] Y. Yin, R.E. Collins and B.A. Pailthorpe, J. Appl. Phys., submitted December 1990.

CHAPTER 6

Work Function Studies of Gas Adsorption Behaviour of Amorphous Carbon Films

6.1 Introduction

6.1.1 Introduction

A major goal of this study was to develop experimental techniques which discriminate between surface and bulk gas adsorption. Adsorption behaviour observed in amorphous carbon films reflects both the surface and the subsurface aspects of the interaction. Work function studies of gas adsorption are very sensitive to surface processes and are not influenced by material adsorbed within the film bulk. A Kelvin probe was designed and constructed to measure small changes in the work function of the surface The thermal desorption studies discussed in the previous chapter, by comparison, were used to investigate desorption from the pores of the amorphous carbon films. TDS can discriminate between desorption processes with different activation energies but it not surface sensitive. Combining the results obtained using both these techniques allows information to be extracted which differentiates between surface and bulk adsorption/desorption interactions. Optimisation of thermal switching behaviour is dependent on establishing the interrelationship between film morphology and gas adsorption behaviour. An a-C:H film forms the outermost layer of the spectrally selective film employed in the ETC. It has a dominant effect on overall adsorption/desorption behaviour [1].

In this chapter, a discussion is presented of the design, construction and operation of the Kelvin probe. A number of modifications were made to the Kelvin probe and a variety of performance tests undertaken during the process of optimisation. Gas adsorption results obtained using the Kelvin probe are presented which show work function response of a-C:H films to a variety of adsorbates. The irreversibility of some adsorption processes and the adsorption of residual gases from the vacuum chamber are also discussed. A comparison of results obtained

using thermal desorption spectroscopy and work function studies allows a number of conclusions to be made about the gas adsorption processes observed.

6.1.2 Work Function

The electron distribution at the surface of a solid is continuous, falling off over a short distance into the vacuum. The fixed atomic centres are surrounded by an electron cloud resulting in a separation of charge [2], as shown in figure 6.1. The work function (WF) or the amount of energy required to remove one electron from the surface [3] can be defined as the difference between the electrochemical potential μ of electrons inside the surface and the electrostatic potential Φ of electrons just outside the surface [4]. Equivalently, WF may be expressed as the difference between the Fermi level and the vacuum level in the case of both metals and semiconductors. The photoelectric threshold for metals is equal to the work function, whereas in semiconductors it is given by the energy difference between the top of the valence band and the vacuum level [5]. The a-C:H films used in this study are classed as semiconductors.

Measurements of WF can be used to monitor the state of a surface. Gas adsorption and desorption, contamination and decontamination and any reaction or change of state of adsorbed material produce measurable changes (of the order of volts) in CPD [4]. Sensitive measurement techniques allow very low levels of adsorption to be detected in contrast with many other measures of adsorption which are only reliable in the monolayer coverage regime.

The electronic surface state of a material is determined primarily by the outer atomic layers which shield the lattice bulk. The response to adsorption arises from differences in the electron distribution of adsorbed molecules and the surface atoms bound into a lattice structure. The chemical potential of a crystalline surface can be changed by the application of stress. Elastic deformations of the lattice volume cause changes of the order of 100μV [3,6]. Changes in temperature and the application of electric fields are also sources of WF change [3].

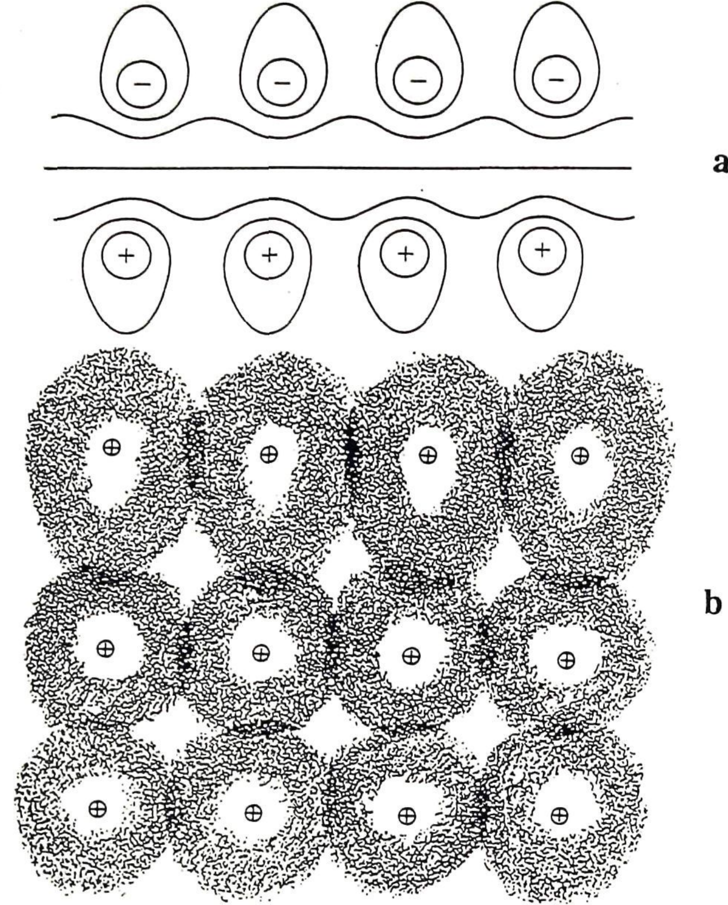

Figure 6.1 Charge distribution at a film surface showing the separation of charge arising from fixed atomic centres and their surrounding electron clouds.

(a) Equipotential lines at an electric double layer. A potential step is formed if the centre of this layer corresponds to a surface plane.

(b) Charge distribution for a fixed lattice of positive ions surrounded by a distorted electron cloud. Double layers can be formed with either a positive or negative net charge outside the surface. [reprinted from ref. 7].

6.2 Methods of Measuring Work Function

6.2.1 Absolute Methods

A range of experimental techniques exists for making absolute measurement of WF. All are based on the stimulation and quantification of electron emission from the sample material. The absolute measurement of WF is made experimentally difficult by phenomena associated with sample charging, high temperatures and high fields.

Thermionic emission can be used to measure absolute WF of surfaces. The thermionic emission saturation current density J_{TE} of electrons emerging from a surface is given by

$$J_{TE} \propto T^2 \exp\left[\frac{-\phi}{kT}\right] \qquad (6.1)$$

(from the Richardson - Dushmann equation), where T is the absolute temperature, ϕ is the WF and k is Boltzmann's constant [3]. Applying an electric field to the system effectively lowers the WF of the material resulting in an emission current which is dependent on both sample temperature and applied field. An appropriate value for ϕ can be extracted from measurements of such emission, although the situation is complicated by the temperature dependence of ϕ [3].

Photoelectric measurements are a more versatile means of determining the absolute WF of a sample. The total photoelectron current increases with the energy of the incident radiation when $h\nu$ is greater than the photoelectric threshold. Only thermionic emission is observed below the photoelectric threshold. Most metals have thresholds of a few electron volts so ultraviolet radiation is commonly used to study work function [7]. Information is extracted by determining the photoelectric current as a function of the wavelength of the incident light. These experiments can be performed using a variant of ultraviolet photoelectron spectroscopy (UPS). The principal instrumental requirements are a tunable ultraviolet source and an electron energy analyser with satisfactory low energy resolution, such as a retarding field analyser (RFA) or a cylindrical mirror analyser (CMA).

Work functions can be absolutely determined using electron spectroscopies such as XPS and AES. The ability to measure electron current from a sample as a function of energy allows the photoelectric threshold to be determined in a single process. The energetic onset of secondary electron emission gives the work function subject to the effects of sample charging [8]. Polycrystalline surfaces consist of patches with significantly different WFs. Combining WF measurements with scanning AES allows maps of work function topography to be created [8]. The spatial resolution is determined by the electron beam spot size and the accuracy of beam scanning. This contrasts with other methods where average WFs are measured or where patch detection depends on the applied field or energy of the incident radiation [3].

As expected from the previous discussion, work function varies between crystal faces. For example, the (111) crystal face of tungsten has a WF of 4.39eV whereas the (112) crystal face has a WF of 4.69 eV [7]. A field emission microscope (FEM) can be used to observe these WF differences if a strong accelerating field is applied to a finely pointed crystal tip. A measurable electron current results from electron tunnelling. Electrons arising from the various crystal faces appear as fluorescent spots on a nearby phosphor screen. The incorporation of a moveable Faraday cup allows the individual WFs to be measured rather than just the average value [3].

The scanning tunnelling microscope (STM) operates in a similar mode to the FEM with an applied field causing electrons to tunnel out of a sample to a finely pointed tip. The very small tip - to - surface distance and radius of curvature of the tip reduce the required magnitude of the applied field to the order of a few volts. The WF at a single point can be deduced by fixing the tip position and measuring the I - V characteristic, that is, the change in tunnelling probability with applied field.

6.2.2 Relative Methods

Relative methods of determining WF rely on measuring changes in the contact potential difference (CPD) between a sample and reference surface. The CPD is equal to the difference in WFs of the sample and reference electrodes for zero applied potential difference [4]. The problems associated with the absolute methods discussed above are generally avoided as experimental conditions can be more carefully controlled. These techniques are useful for studying gas adsorption where changes in WF in response to adsorption mirror various aspects of the process itself.

Changes in CPD are commonly studied using either diode or condensor methods. The former method relies on the characteristics of the thermionic diode. The flow of electrons from a hot wire cathode to some remote anode depends on the applied potential between the two points. Changes in the I - V characteristic of a diode system will occur if the surface potential of the anode is changed by adsorption. The change in CPD is given by any shift in the potential required to maintain a constant current [4]. Diode systems can be operated in either retarding field or space charge limited modes where the diode anode is slightly negative or positive compared with the cathode, respectively [4].

The CPD between a sample and reference electrode can be measured by sensing the electric field existing between the two electrodes as a result of the difference in surface potentials. These experiments are collectively referred to as condensor methods of measuring CPD. All variations are contactless and hence the surface condition of the sample is not changed by the measurement process [3]. Experiments are generally undertaken at room temperature, with low applied potentials and without electron or proton bombardment. These favourable experimental conditions render condensor methods extremely versatile for studying the effects of gas adsorption and changes in temperature.

Several static capacitor and field effect probe techniques have been devised which preserve contactless measurement and also eliminate interference associated with vibrating capacitors (the latter are discussed in the next section).

The static capacitor method detects a flow of charge between the sample and reference electrodes when the CPD is changed by gas adsorption or temperature change [4]. Only changes in CPD can be detected using this technique. The main difference between the dynamic and static methods is in the application of nulling voltages. The electric field between the plates of the vibrated capacitor is maintained at zero by a constantly applied nulling voltage. In the static case, a nulling voltage is rapidly applied to reduce charge flow to zero in a time much smaller than the time constant of the capacitor/reference electrode circuit [9].

The field - effect probe (FEP) provides a static, non - intrusive means of measuring CPD. The FEP consists of a modified MOSFET device, as shown in figure 6.2. The sample acts as the MOSFET gate with the electric field between the sample and probe inducing a charge in the substrate, therefore, determining the

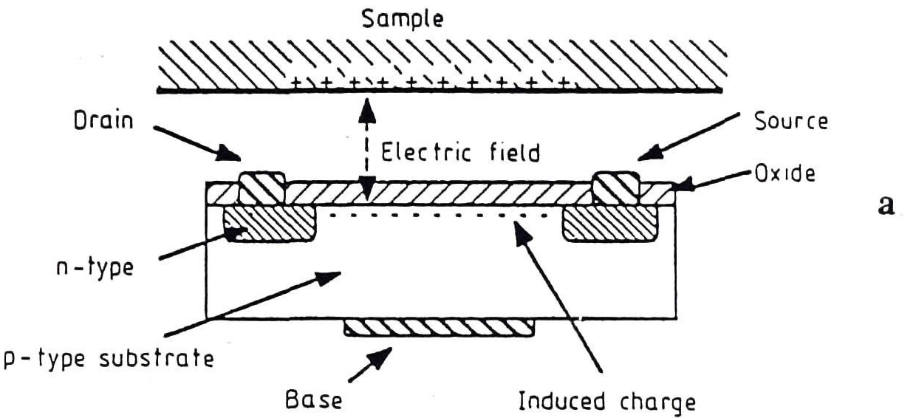

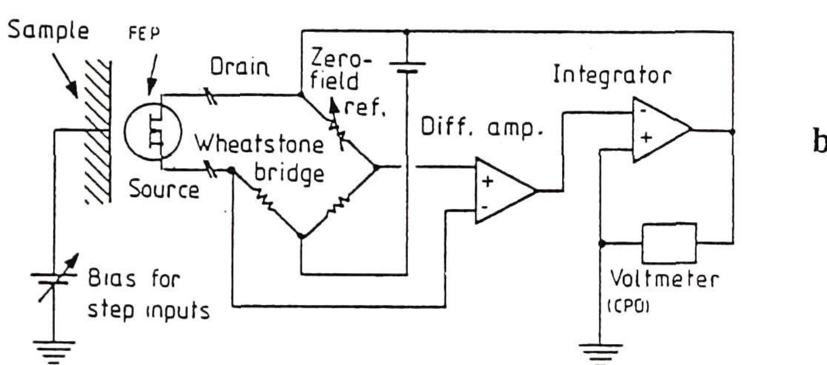

Figure 6.2 The Field Effect Probe (FEP).

(a) Cross section of the probe and sample surface. The gate is formed by the sample electrode, with the conductivity of the source/drain path modulated by the electric field induced by any contact potential difference existing between the probe and the sample.

(b) Schematic description of the probe and associated instrumentation.

[reprinted from ref.10]

source/drain conductivity. If an enhancement/depletion type device is used then both positive and negative fields can be detected.and used to control a nulling circuit. A shortcoming of this device is the temperature dependence of the source/drain conductivity. Temperature compensation can be achieved either by the incorporation of an additional *n - p - n junction in the probe construction* or by immersing the probe and sample in a constant temperature bath. In the latter case, instrument resolution has been optimised to 1mV. This is a very versatile technique, finding application in both surface science and electrochemistry, in air, vacuum and liquid environments [10].

Other condensor methods reported include an electron interferometer system and a ribbon/sample system in which an a.c. and d.c. signal is applied between the electrodes and the CPD deduced using a bridge arrangement [3].

6.3 The Kelvin Method

6.3.1 Implementations of the Kelvin Method

The most widely used condensor technique is the Kelvin method. This vibrating capacitor technique is based on the original work of Lord Kelvin (1898) [11] and developed by W.A. Zisman (1932) [12]. The Kelvin method is a contactless, non - intrusive method of measuring changes in CPD between a sample and a closely spaced parallel reference electrode, forming a parallel plate capacitor [11]. The surface potential of the sample and reference electrodes is related to the respective Fermi levels by WF. If the WFs of the two electrodes are unequal then a non - zero electric field will exist between them at zero applied voltage. Vibration of the reference electrode with respect to the sample changes the capacitance of the system and produces an a.c. signal at the same frequency as the vibration.

A nulling voltage can be applied between the electrodes to reduce the electric field in the gap to zero. Under zero - field conditions no charge flows between the equipotential electrodes as a result of the movement of the electrodes, hence, no signal is detected in the external circuit. The Kelvin method is a null technique with results independent of the gap between the surfaces to first order.

Gas adsorption, changes in temperature and other external influences can change the surface potential of the sample. A corresponding change in the CPD between the sample and reference electrode occurs if the latter is suitably inert. An adjustment of the nulling voltage is required to restore the null state as the electric field between the electrodes is no longer zero. Changes in CPD are measured by recording changes in the nulling voltage in response to experimental conditions.

The original vibrating capacitor instrument devised by Zisman [12] has been adapted for many different applications. Kelvin probes vary in size, methods of vibration and shielding. Figure 6.3 describes a commercially available instrument (KFA) consisting of a vibrating metal reed driven by piezoelectric ceramic foil. The end of the reed is formed into the reference electrode. All electrical connections are made to the sample. No measures for reducing stray signals detected by the probe have been implemented in this design. A resolution of 100 μV for 10 second signal averages is reported [13]. Reference electrodes for this type of Kelvin probe range from thin reeds to wire loops and grids.

Another widely used variation of the Kelvin probe consists of a reference electrode attached to an electromagnetically driven, resonant mounting bar. Drive mechanisms operate in a push - pull fashion as in a loudspeaker or from side - to - side with the mounting bar supported at a suitable pivot point. Drive mechanisms can be located inside or outside the vacuum chamber. Such systems are considerably more bulky than the piezoelectric devices.

The use of a guard ring around the reference electrode in a Kelvin probe system provides enhanced shielding of the electrode and also ensures approximately plane parallel geometry by reducing fringing fields at the electrode edges [14]. The guarded electrodes designed and constructed for this work will be discussed in section 6.5.1. Apparatus incorporating a large diameter Kelvin probe can be configured to integrate WF information over large areas, giving average values. Alternatively, small diameter probes can be used to scan very small areas, producing WF maps [15]. The spatial resolution of the measurements is determined by the reference electrode diameter. This in turn affects the voltage sensitivity since the reduced signal from a fine electrode can give rise to signal - to - noise difficulties [16].

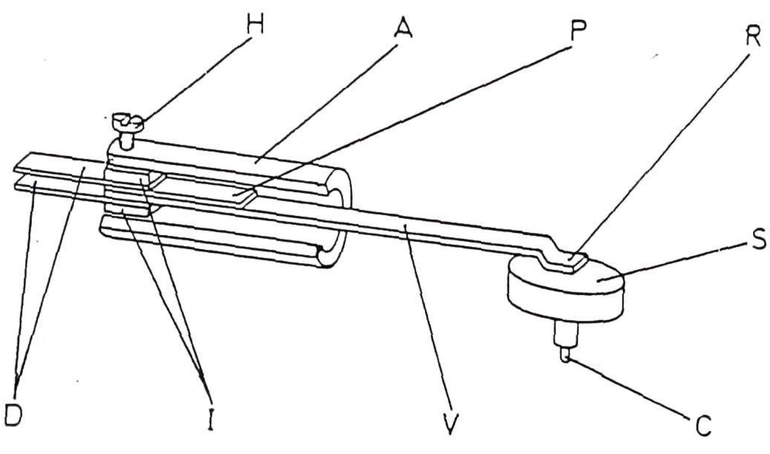

Figure 6.3 KFA Kelvin Probe.

This commercially available instrument consists of a specially shaped, vibrating reed (V,R) which is driven by piezoceramic foil (P) attached along the midsection. The reed is supported and anchored with a holding screw (H) in a cylindrical shield housing (A). All electrical connections (C) are made to the specimen (S). No measures for reducing stray capacitance detected by the probe have been implemented in this design, however, a resolution of 0.1mV for 10s signal averages is reported. [reprinted from ref. 13].

Changes in the work function of the sample are measured relative to the work function of the "reference" electrode. It is essential, therefore, that the work function of the reference electrode maintains a constant absolute value at all times during experiments. For this reason, reference electrodes are formed from or coated with materials which minimise gas adsorption. Reference electrode inertness can be tested by selecting experimental conditions (elevated sample temperature, for example) which minimise gas adsorption by the sample. Alternative methods include the use of TDS and QCM to quantify adsorption.

The discussion of the Kelvin probe has been confined, thusfar, to vibrating electrode devices. The only essential feature of a Kelvin probe is movement. Kelvin's original system, for example, was a non - periodic device, based around a gold leaf electrometer [11]. Other implementations of the Kelvin probe include a fine vibrating wire, used to investigate spatial variations in WF arising from adsorption. Spatial resolutions of 50µm are obtained by moving the wire reference electrode parallel to the sample surface [3]. Changes in WF in response to atomic bombardment can be observed using a Kelvin probe operating in a pendulum mode. The reference electrode moves from side to side, parallel to the sample surface, leaving the sample and guard ring exposed to a flux of atoms for a significant portion of the operating cycle [3]. These Kelvin probe variants trade - off unique operating features with the design simplicity and superior signal - to - noise characteristics of vibrating electrode devices.

6.3.2 Theoretical Description of the Kelvin Method

In this section a simple analysis is presented of a periodically excited Kelvin probe of the type used in this study. The reader is also referred to a number of analyses presented in the literature [17-23].

The Kelvin probe (or reference electrode) and the sample form a parallel plate capacitor. For the stationary case, capacitance is given by

$$C_{stat} = \frac{\varepsilon A}{d_{stat}} \tag{6.2}$$

where ε is the permittivity of the material between the electrodes, A is the surface area of the probe, and d_{stat} is the stationary probe - sample separation. Zisman [12] first proposed that the reference electrode be vibrated with respect to the sample.

A sinusoidally varying electrode spacing can be described by

$$d = d_0 + d_1 \sin(\omega t) \qquad (6.3(a))$$

$$= d_0 [1 + \gamma \sin(\omega t)] \qquad (6.3(b))$$

where d_0 is the mean probe - sample spacing, d_1 is the vibration amplitude, ω is the angular frequency of vibration and γ equals d_1 / d_0. Capacitance can be rewritten [17,19,24] as

$$C = \frac{\varepsilon A}{d} \qquad (6.4(a))$$

$$= \frac{\varepsilon A}{d_0 [1 + \gamma \sin(\omega t)]} \qquad (6.4(b))$$

The signal which arises due to the variations in the geometry of the capacitor under open circuit (constant charge) conditions may be written as

$$V = \frac{Q}{C} = \frac{Q d}{\varepsilon A} \qquad (6.5)$$

where Q is the charge residing on the reference electrode and C is given by equation 6.4(b).

The Kelvin probe is not a truly isolated system. It is capacitively coupled to the walls of the vacuum chamber containing it, as well as to the other components within the vacuum system. Microphonic signals can be generated by the vibration of signal carrying leads with respect to the chamber and the surrounding shielding. The signal produced at the probe output, therefore, includes components due to these pick up signals with the same frequency and in a constant phase relationship with the true signal [20,21]. Stray capacitances can also be a significant problem in Kelvin probe systems. Sources include capacitive coupling between the edges of the Kelvin electrode and the adjacent guard ring and casing and the capacitance of signal carrying leads within metallic shields. A simple equivalent circuit for the Kelvin probe and associated pick up and stray signals is shown in figure 6.4.

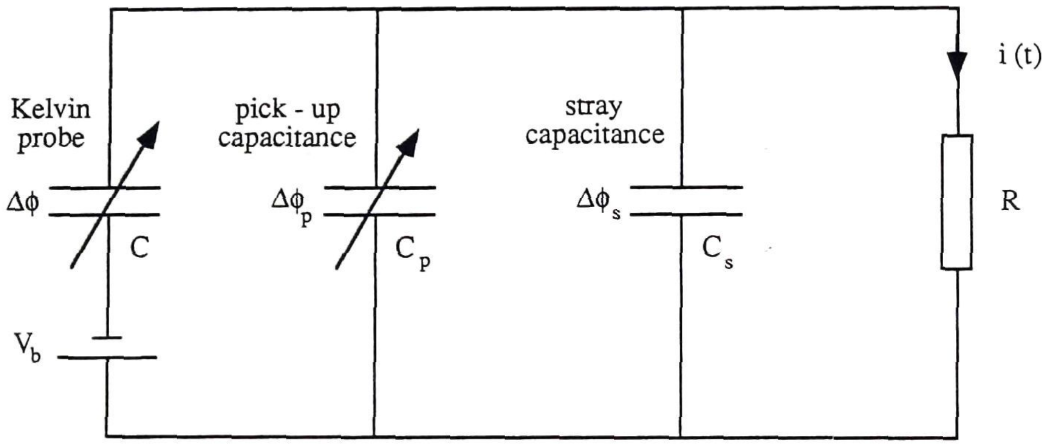

Figure 6.4 Equivalent circuit for the Kelvin probe comprising parallel capacitances C, due to the Kelvin probe, C_p, due to pick - up arising from microphonic signals and capacitive coupling between the Kelvin probe and the walls of the vacuum system and C_s due to stray signals arising from sources such as the connection leads. The contact potentials $V_b + \Delta\phi$, $\Delta\phi_p$ and $\Delta\phi_s$ are acting at these capacitances, respectively. The current i(t) caused by changes in the capacitances flows through the load R, which represent the input of a current sensitive preamplifier and lock - in amplifier in combination. The output voltage V_b of the detection system is shown, applied to the sample.

The Kelvin method is a null technique. The condition for the null state is that the electric field in the gap between the probe and the sample is zero. The potential difference across the Kelvin capacitor at any time is given by the sum of the CPD ($\Delta\phi$), and the applied bias voltage, V_b so in the null state

$$\Delta\phi + V_b = 0 \tag{6.6}$$

Changes in CPD in response to gas adsorption are deduced by recording adjustments of V_b required to restore and maintain the null state. The pick up capacitance (C_p) and the stray capacitance (C_s) act in parallel with the Kelvin probe and represent the sum of all individual pick up and stray capacitances, respectively. These capacitances reduce the true signal by the capacitive division. The total charge on the reference electrode, taking into account pick up and stray signals [20], is given by

$$Q = C\,(\Delta\phi + V_b) + C_p\,\Delta\phi_p + C_s\,\Delta\phi_s \tag{6.7}$$

The stray capacitance is time invariant and has no effect on the true signal other than capacitive division. The pick up capacitance can produce a signal at the same frequency as the true signal and with a constant phase relationship, as mentioned above. While phase sensitive detection minimises the effect of the pick up signal, the null point of the probe and the required bias voltage can be affected if the phases of two signals are similar. Changes in work function can be measured satisfactorily provided the pick up signal remains constant.

The Kelvin capacitance is given by equation 6.4(b). For small values of γ, the probe - sample separation is large with respect to the vibrational amplitude of the probe and the capacitance varies sinusoidally around a value given by $\frac{\varepsilon A}{d_0}$. The output signal under these conditions is also approximately sinusoidal. A distortion of the output signal can be expected as γ becomes larger because probe vibration can no longer be considered as a perturbation of the probe - sample separation. Distortion of the output signal at small separations has been observed in small area Kelvin probes in the laboratory. In practice, the factor limiting the smallest probe - sample separation is the non - parallelism of the electrode surfaces. No distortion of output signal was observed in the current experiments due to the use of band pass filtering.

A great deal of effort was invested in Kelvin probe design and optimisation to reduce or eliminate unwanted signal detection. Capacitive coupling can be reduced by careful shielding and by maximising the distance between the probe and the chamber walls. The Kelvin probe design adopted (discussed in section 6.4.1) incorporates a earthed guard electrode surrounding the Kelvin electrode. The guard electrode is stationary with respect to the Kelvin electrode. Microphonic signals can be reduced or eliminated by careful anchoring of leads and preamplifier components so that they remain stationary with respect to the surrounding earthed shielding. The effect of stray capacitances can be minimised by positioning the preamplifier as close as possible to the Kelvin electrode. While some signal loss was unavoidable in this Kelvin probe system, no in - phase pick up was detected from this source during performance testing. A fuller discussion of shielding and filtering techniques is presented in section 6.5.1.

6.4 Design and Construction of Kelvin Probe

6.4.1 Guarded Electrode Design

The Kelvin probes used in this work were designed using a guarded electrode configuration. Figure 6.5 shows the two versions of the Kelvin probe constructed for use with different size samples. The design features a circular electrode disc with a threaded mounting post incorporated in the centre of the rear surface. The electrode was located very close to a guard ring formed by the probe casing (a gap of around 0.2mm was achieved), but electrically insulated from it using two ceramic spacing washers. The edge of the electrode disc was recessed to form a thin lip which minimises capacitive coupling between the electrode and the probe casing. The probe casing was closed at the top using a snugly fitting lid to complete the shielding.

The Kelvin probe was manufactured using UHV compatible materials (stainless steel (316 type) and machinable ceramic (Macor, Corning Glass)) to permit bakeability, and to achieve minimum outgassing levels in the vacuum chamber. The face of the electrode and the guard ring were ground flat using abrasive papers (silicon carbide, grades 400, 600 and 1200). A mirror finish was imparted using a fine abrasive metal polish. On completion of fabrication the probe was disassembled and cleaned using a vapour degreaser and acid bath electropolishing.

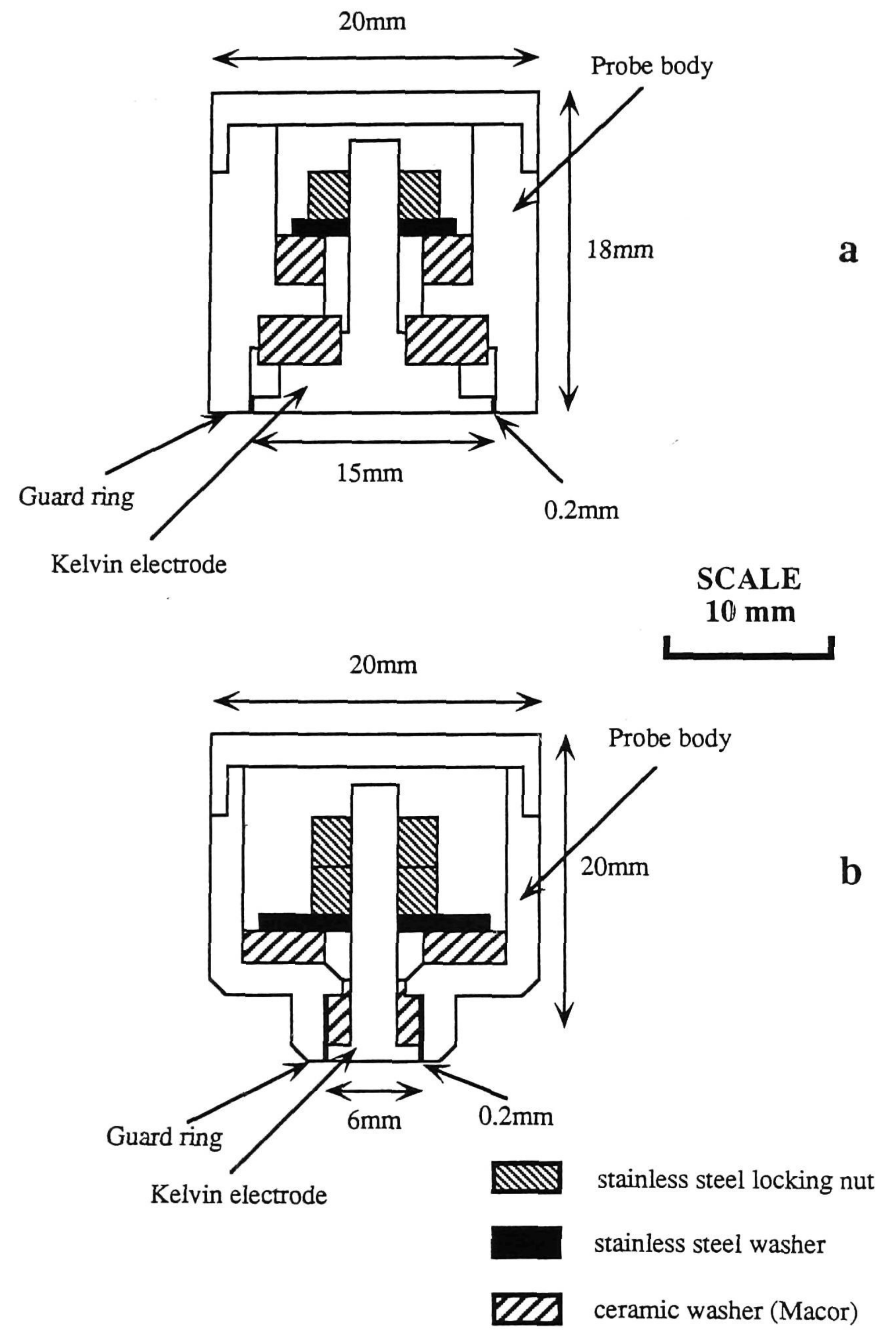

Figure 6.5 Cross sectional views (to scale) of the guarded Kelvin probes used in this study, (a) probe with 15mm diameter electrode face; and (b) probe with 6mm diameter electrode face. There is a 0.2mm gap between the electrode disk and the guard ring in each case. Electrical connection is made via 5mm diameter hole in the probe body

Measurements of CPD require an inert reference electrode so that only the adsorptive behaviour of the sample contributes to experimental results. Kelvin electrodes are commonly faced with a material such as gold [4,19,21,25] or tin oxide [4,9,17,21] to minimise adsorption. A reasonably robust film was required to avoid the need for regular recoating. The adhesion of gold films on the stainless steel electrodes used in this study was unsatisfactory. Consequently, the face of the electrode disc was coated with a 400Å layer of tin oxide. The film was deposited by electron beam evaporation using a vacuum coating system (Airco Temescal). The electrode was heated to approximately 500K during deposition to promote adhesion. The inertness of the reference electrode was confirmed by a number of gas adsorption experiments. The work function behaviour of the reference electrode is discussed in more detail in section 6.7.

A number of Kelvin probe mountings were tested for mechanical stability and satisfactory vibratory characteristics. Various resonant bar mountings were constructed using a tube welded into a recessed vacuum flange. The tube protruded from either side of the flange supporting the Kelvin probe inside the vacuum chamber. This flange also provided a connection point for a vibratory drive outside the vacuum chamber. A number of different wall thicknesses and recessing profiles were tested. The advantages of this design are good mechanical stability and the isolation of the electromagnetic drive coil from the probe. It was found, however, that all the mountings tested resonated at much higher frequencies than desired (thousands of Hz rather than hundreds of Hz) and with a small vibrational amplitude. The welded construction of these mountings prevents subsequent adjustments and lengthens any optimisation process.

A pivotting Kelvin probe mounting was eventually adopted for use (see figure 6.6). The mounting consisted of a stainless steel tube, sealed at the vacuum end using an insulated electrical feedthrough [26]. The feedthrough was used to carry the probe signal to a preamplifier inside the tube. A stainless steel collar was brazed onto the tube at a position which would locate the Kelvin probe centrally in the vacuum chamber. A stainless steel bellows was brazed to the collar and to a Conflat flange, completing the vacuum feedthrough. The mounting tube was supported by two stainless steel pins resting in recesses in the collar. These pins in turn were attached to a frame extending from the vacuum flange.

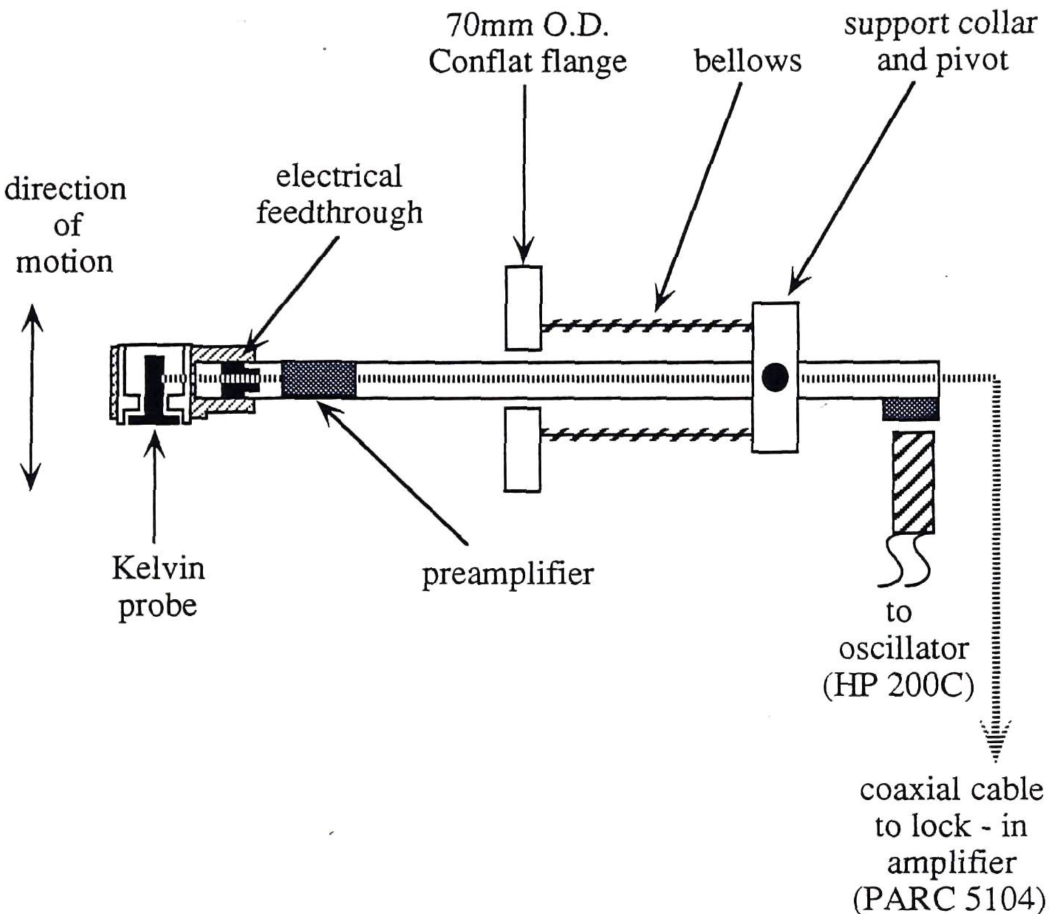

Figure 6.6 Kelvin probe and the associated pivoting feedthrough. The feedthrough consists of a pivoted collar electron beam brazed to the probe mounting tube and a stainless steel bellows. The other end of the bellows is welded, via an adapter, to a Conflat flange.

Electron beam brazing was employed during the construction of the pivotting mounting. The brazing was performed under a vacuum bell jar and in clean conditions. The work piece was placed on a platform which could be raised to a potential of 1000 - 1500V. A tungsten filament was formed around the work piece at a distance of about 2mm and fired before use. A high current was passed through the filament (~ 20A), inducing electron current from the filament to the work piece (up to 2A depending on the size of the work piece). The work piece was heated by electron bombardment, melting a silver copper eutectic braze ring placed at the joining site. This method of brazing is completely flux free and clean. Three electron beam brazes were required in the construction of the pivotting feedthrough to join a number of pieces with vastly different thermal masses.

The bellows provided the flexibility for the vibration of the probe. The probe was vibrated at one of the resonant frequencies of the mounting during work function experiments By adjusting pivot stiffness the resonant frequency of the probe could be changed by 5 to 10Hz. This design provided adequate vibratory motion, but fairly poor mechanical stability. The Kelvin probe showed some susceptibility to laboratory vibrations. The problem was significantly reduced when the rotary pumps associated with the vacuum chamber were moved to a remote location.

The oscillatory force on the probe was provided using a soft iron slug and coil in combination. The soft iron slug was clamped to the top of the mounting tube, with the coil mounted adjacent to the slug with an adjustable bracket. A light compression spring was used between the tube and the bracket to adjust the resting position of the probe and the stiffness of the vibrating assembly. The frequency of probe oscillation was twice the coil driving frequency which reduced interference of the drive signal with the probe output signal.

6.4.2 Signal Detection and Data Acquisition

Optimal system performance depends on efficient signal generation and low noise signal detection. The signal from the Kelvin probe was detected using a low noise preamplifier and lock - in amplifier. The preamplifier circuit designed for the Kelvin probe is shown in figure 6.7. A low noise, high input impedance ($10^{12}\Omega$) JFET operational amplifier (LF411CH) was used with 56MΩ input resistance and 36MΩ feedback resistance. The input resistance was included to provide better amplifier stability. The amplifier operates as a current - to - voltage converter. In this

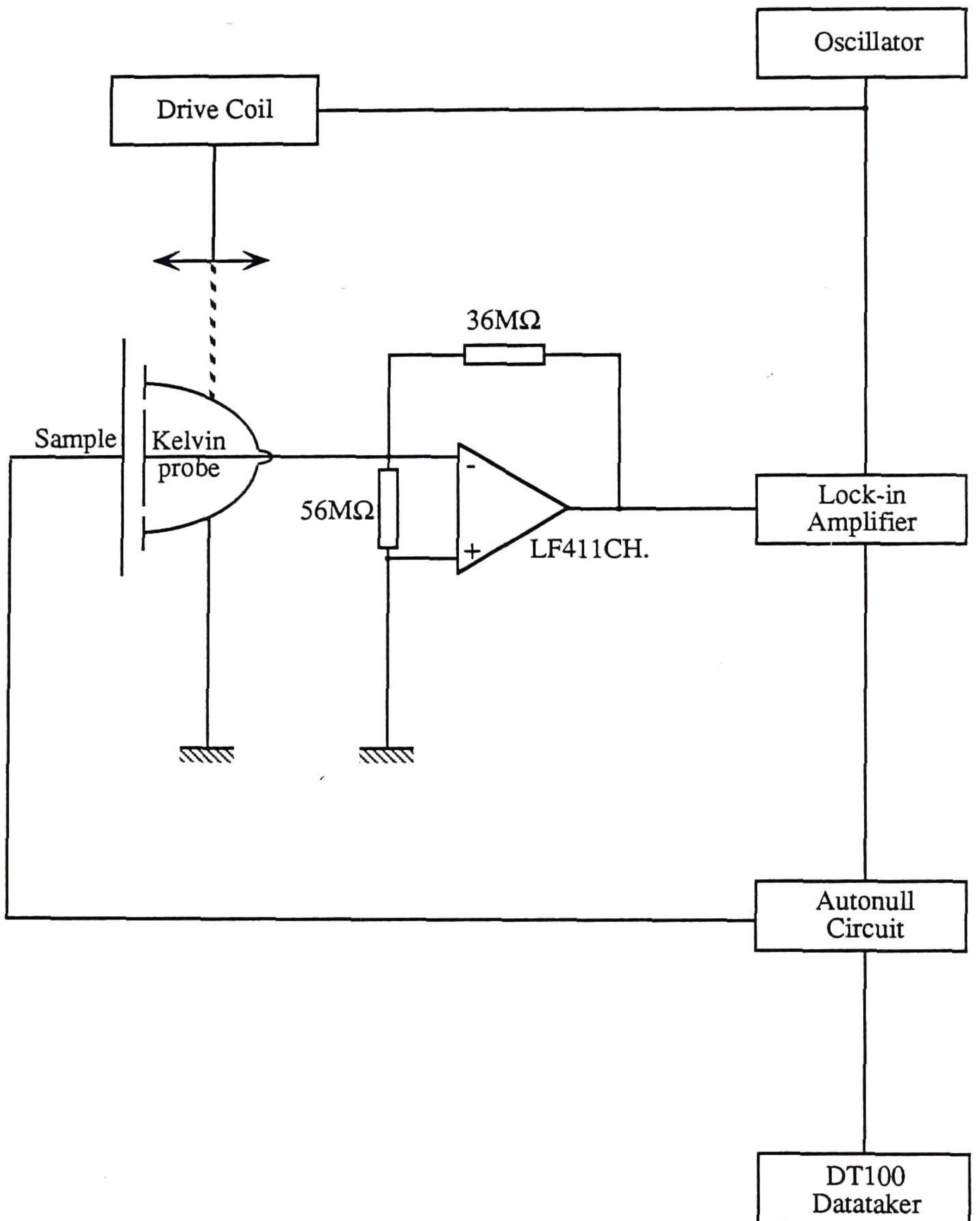

Figure 6.7 Kelvin probe preamplifier circuit

configuration, the Kelvin electrode is virtually grounded and therefore the inverting input of the operational amplifier is effectively at ground potential. Virtually none of the signal current flows through the 56MΩ input resistor; it is all channelled through the 36MΩ feedback resistor to give a voltage output.

An amplifier housed in a metal can was used with components being soldered directly to its legs, avoiding the need for a bulky circuit board. The miniaturised device was inserted into the probe mounting tube to make an electrical connection with the Kelvin electrode via the electrical feedthrough. The preamplifier was located as close as possible to the Kelvin probe to minimise signal losses by capacitive division. The detected voltage is reduced by the divider effect of the capacitance of the Kelvin probe (≈ 10pF) and the capacitance of the electrical connections (≈ 12pF) and the input capacitance of the preamplifier (≈ 2pF). The amount of stray capacitance introduced is reduced by minimising the length of the connections. Noise levels on the Kelvin probe output are also reduced. Changes in the experimental apparatus during the course of the study necessitated an extension of the probe mounting tube. This unavoidably increased the effect of stray capacitance.

The preamplifier was carefully shielded and grounded to minimise pick up of 50Hz noise from the power mains. A lock - in amplifier (PARC 5104) (LIA) was used in the second harmonic mode with the driving signal as the reference frequency. This converted the a.c. Kelvin probe signal into a d.c. output.

Automatic adjustment of the nulling voltage (NV) is a desirable operating feature of a Kelvin probe system. A mechanical device based around a motor driven potentiometer was constructed to control the NV applied to the sample electrode. The LIA output was amplified with an operational amplifier and used to switch one of two relays depending on the sense of the signal. The relays controlled a d.c. motor, which in turn made mechanical adjustments to the setting of a ten - turn potentiometer. The NV was controlled directly by the potentiometer. While the probe output and NV were electrically isolated using this device, the mechanical nature of the device increased the response time compared with electronic circuits and was a source of electromagnetic noise [27].

An electronic autonull circuit was devised and adopted for use with the Kelvin probe. The d.c. output of the LIA was inverted, amplified and regulated, then applied to the sample. The autonull circuit used a low noise, low offset, low drift, high gain operational amplifier (OPA111AM) and a standard operational amplifier

(LM11CN), in combination, to supply the NV to the sample. Figure 6.8 shows the circuit design for the autonull circuit [28]. The circuit had a time constant of around 8 seconds.

Changes in CPD were recorded as a function of temperature and gas dose duration. Data were recorded using a computer controlled datalogger (Data Electronics DT100 Datataker), programmed for a variety of recording and signal averaging tasks. It was found that using 0.1 - 1 second LIA time constants and time averaging NVs over 10 - 30 second intervals for each data point eliminated most of the spurious fluctuations. These fluctuations originated from the autonull "hunting" for a NV in response to a small change in the LIA output. Adjustments to the NV using the autonull circuit were limited only by the interaction between the time constants of the autonull circuit and the LIA. At no stage was the resolution of NV adjustments affected by noise, instabilities or other flaws in the autonull circuit

6.5 Optimising Kelvin Probe Performance

6.5.1 Shielding and Filtering

The Kelvin probe is a highly sensitive means of detecting changes in WF. A consequence of this sensitivity is a high susceptibility to the detection of noise. Optimal Kelvin probe performance is requires rigorous shielding of all noise sensitive components, maximising the signal - to - noise ratio. Types of interference which must be taken into account include external electromagnetic noise arising from power mains and laboratory instrumentation, external vibration, capacitive pick - up and stray capacitances.

Electromagnetic noise was detected from several large d.c. and r.f. power supplies in the laboratory. Additional high frequency noise was observed, probably originating from the two turbomolecular pumps connected to the vacuum chamber. The reduction of external electromagnetic noise from the Kelvin probe output was achieved by shielding and filtering. All signal carrying leads were constructed from coaxial cables with BNC type connectors. Cable lengths were kept as short as possible to minimise the detection of 50Hz mains noise and spurious r.f. signals. All shields and instrument earth points were connected together in such a way as to avoid the creation of earth loops. The preamplifier power source was found to

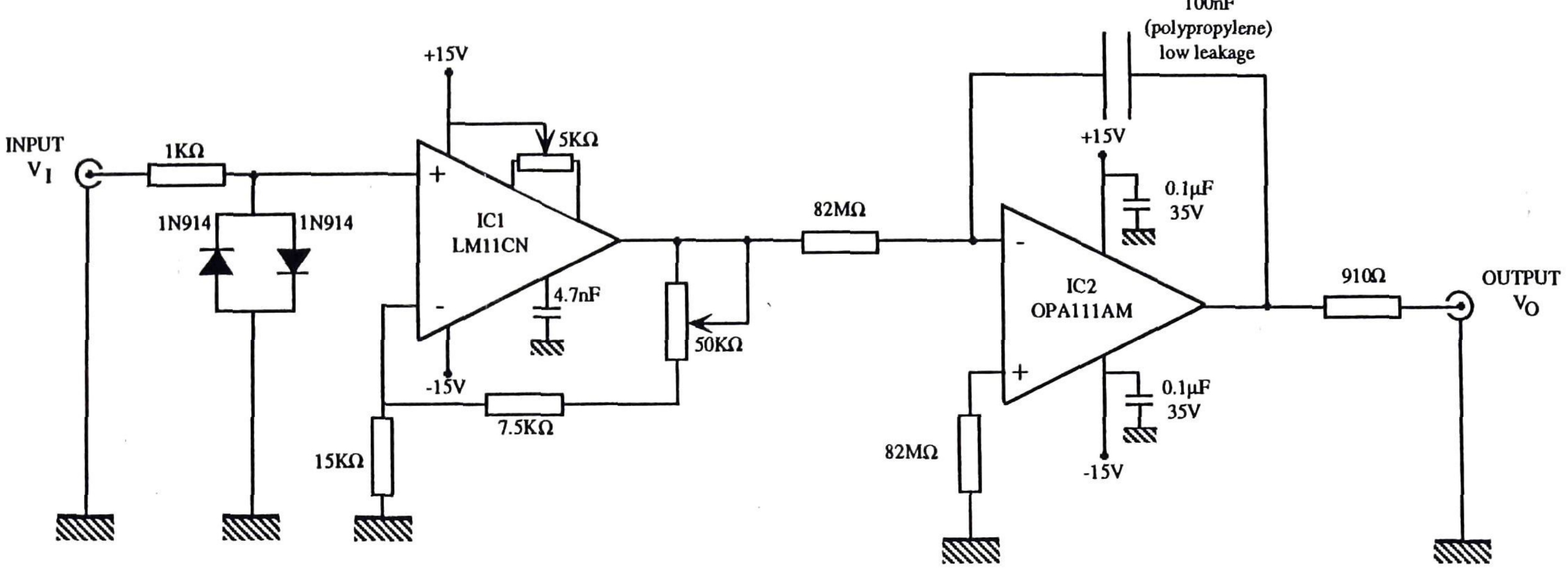

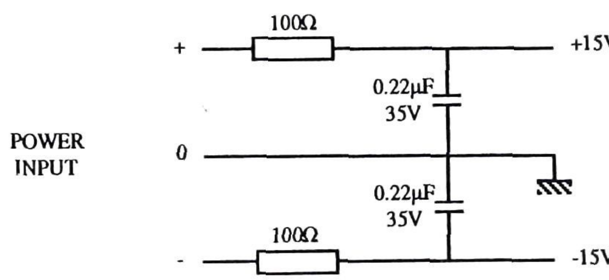

Figure 6.8 Electronic autonull circuit

contribute to noise in the Kelvin probe output. Two 9V batteries, connected in series and tied to the instrument earth, were substituted for a mains driven power supply. Coaxial cable was used for each of the power input leads to the preamplifier.

Detection of the Kelvin probe signal was facilitated with use of phase sensitive detection. Signals at frequencies other than the desired frequency were eliminated using the LIA. Adjustments were made to the LIA gain to give maximum signal response and to the LIA time constant to eliminate the effect of high speed transient events. The time constants used in these experiments (0.1 to 1 second) were much shorter than the time constants of the gas adsorption behaviour (of the order of hours) being studied so no information was lost due to signal averaging effects. The LIA incorporates a line filter which eliminates 50Hz noise and a tracking filter which exhibits a fundamental (sine wave) response. The filtering passband is centred at the reference frequency or the second harmonic of the reference frequency, depending on the mode of LIA operation. This form of filtering rejected a large proportion of the noise passed by the Kelvin probe shielding.

The Kelvin probe system is susceptible to mechanical vibrations arising from poor stability of the mounting. The requirements for the vacuum chamber changed as the experimental programme evolved resulting in several modifications and extensions of the mounting arm. The arm is pivotted outside the vacuum chamber by two lubricated stainless steel pins. The relatively large mass of the probe and mounting arm and a lack of stiffness readily transmits external vibrations along the mounting arm in a lever fashion. Pivot stiffness could not be greatly increased without reducing the amplitude of vibration or causing galling of the stainless steel pins in their locating holes, which resulted in irregular vibration.

A variety of measures were taken to reduce the effect of vibration including removing the rotary pumps to a remote location, optimising pivot adjustment and controlling movement around the apparatus. Vibration from the turbomolecular pumps did not affect the system principally because the resonant frequency of the Kelvin probe is several orders of magnitude below the operating frequency of the pumps. Further development of this Kelvin probe system should directed towards improving mechanical stability. Current designs for compact STMs, for example, are light - weight, small in size and have resonant frequencies of the order of MHz. This results in superior mechanical stability by reducing susceptibility to laboratory vibrations.

Microphonic signals are caused by the vibration of signal carrying components with respect to shields and other chamber hardware. In this experiment, for example, microphonic signals may arise from vibration of the leads in the oscillating mounting tube even though they are snugly fitted. A simple means of reducing the effect of microphonic signals is to place an earthed, conducting metal shield around suspect components. If this shield is stationary relative to the leads then the earthing will act to eliminate microphonics.

The Kelvin probe is designed to reduce the detection of unwanted signals and to present a flat and plane parallel electrode surface to the sample. The probe case forms an earthed guard ring around the detection electrode, maintaining a plane parallel electric field between the probe and the sample [14]. Its function is to avoid fringing of the electric field at the edges of the detection electrode thereby reducing the detection of signals due to pick up and stray capacitance [6]. It also serves to shield all the other surfaces of the electrode. The probe could have been designed to include a driven guard. A driven guard ring is similar in form to an earthed guard ring; an example is shown in figure 6.9. The probe signal is fed back onto the guard ring, eliminating the parallel capacitance effects of the guard. As the probe displayed a high sensitivity a driven guard was deemed to be unnecessary.

The effects of stray capacitance can be reduced by connecting the vibrating Kelvin electrode to earth and monitoring the electrical output of a stationary, guarded sample electrode. Connecting the chamber and the Kelvin probe to earth removes capacitive coupling likely to produce a signal that will affect the output [20]. Capacitive coupling of hardware to the vacuum chamber is another source of stray capacitance. The signal carrying cables and components give rise to a stray capacitance which is independent of the Kelvin capacitor. There are several ways of reducing this type of pick up signal including maximising the distance between the chamber walls and the detection electrode and other hardware, using earthed shields around noise sensitive components, and using conducting screens on the inner walls of the chamber which can be set at appropriate potentials [17,22,23].

Another source of error arises from the Kelvin electrode and the sample electrode not being precisely parallel. The electrodes are positioned by sight, which limits the accuracy of their alignment. The design of the vacuum system does not allow the angular orientation of the Kelvin electrode to be adjusted once in position. The effect of the non - parallelism is to cause different parts of the surface to contribute to the signal by different amounts. Non - parallelism, thus, gives a

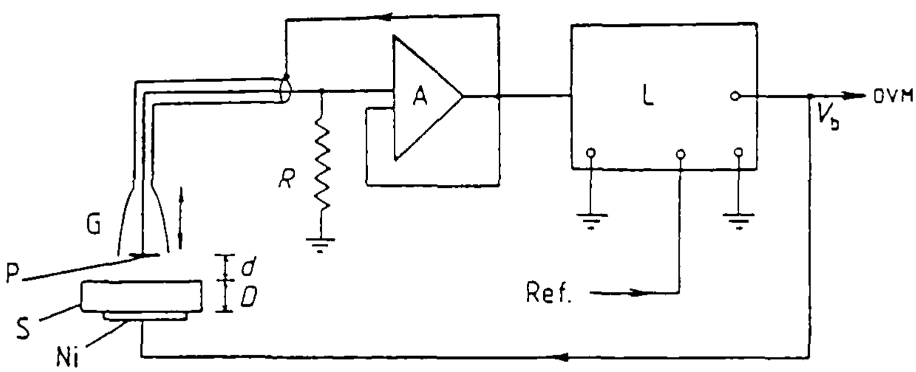

Figure 6.9 Kelvin probe incorporating a driven guard ring
The probe (P) vibrates with respect to the sample (S). The resulting signal is amplified by the voltage-follower preamplifier (A), then fed to the lock-in amplifier (L) and also fed back onto the guard (G).
[reprinted from ref. 25]

spatially weighted average of work function changes. This would become important if, for example, the weighting was changed by variations in parallelism or changes in the size of the gap. The magnitude of this effect falls off rapidly as the probe - sample separation is increased and the weighting of the non - uniform separation diminishes. The problem can be minimised by selecting larger probe - sample separations.

6.5.2 Setting Up the Kelvin Probe

The method used for setting up the Kelvin probe has a significant impact on the level of noise detected and on the accuracy and reproducibility of work function measurements. Two procedures were developed for setting up the Kelvin probe before each experiment to obtain optimal signal quality: a standard method and a reduced pick - up (RPU) method. The standard method maximises the amplitude of the "true" Kelvin signal. Pick - up signals will be detected only if the phases of the true signal and pick - up signal are similar. It is assumed that pick up signals maintain a constant phase relationship with the true signal and will be substantially eliminated using phase sensitive detection and band pass filtering. The RPU method is designed to eliminate pick - up signals. Phase sensitive detection ensures that the true signal will not be completely attenuated while a constant phase relationship exists. The steps constituting each method are set out below. The RPU method is the same as the standard method with the exception of step (iii).

(i) All equipment is switched on and allowed to stabilise for about 15 minutes; this includes the probe preamplifier, the oscillator which drives the probe coil, the autonull circuit, the LIA, the oscilloscope and the datalogger. During this period, communication between the computer and datalogger is established. The oscillator signal and probe signal are both displayed simultaneously on an oscilloscope to assist in probe adjustments.

(ii) The autonull circuit output is disconnected from the sample and replaced by a stabilised power supply. A bias voltage of about 3 - 5Vd.c. is applied to the sample. The probe signal is monitored on the oscilloscope while the sample is moved up as close as possible to the probe (the frequency of the probe signal is twice the oscillator frequency). The oscillator frequency is adjusted to obtain a suitable resonant frequency and a stable, high amplitude probe signal. The bias voltage is varied to confirm that the probe signal varies simultaneously and that a true signal has been obtained.

(iii) <u>Standard Method</u> — <u>Initial settings for the LIA:</u>

second harmonic (2F) mode
line filter and tracking filter activated

sensitivity	1 - 3mV
time constant	1 - 3 seconds

Sensitivity and time constant are chosen to maximise signal amplitude and minimise signal noise and drift. The LIA phase setting is varied until the LIA d.c. output reads zero. The phase is then advanced by 90° to obtain maximum d.c. output.

(iii) <u>RPU Method</u> — <u>Initial settings for the LIA:</u>

second harmonic (2F) mode
line filter and tracking filter activated

sensitivity	1 - 3mV
time constant	1 - 3 seconds

Sensitivity and time constant are chosen to maximise signal amplitude and minimise signal noise and drift. The LIA phase setting is varied until the LIA d.c. output reads zero. The phase is then advanced by 90° to obtain maximum d.c. output.

The Kelvin probe is carefully withdrawn from the sample, causing a decrease in the amplitude of the detected signal. The probe - sample separation is increased until the bias voltage applied to the sample has no effect on the detected signal. The remaining signal is due to pick - up effects alone. The LIA phase is readjusted until the LIA d.c. output reads zero. The probe is then advanced towards the sample, causing an increase in the signal detected. The d.c. output of the LIA now is wholly due to the true Kelvin signal.

(iv) The stabilised power supply is disconnected from the sample and replaced by the output of the autonull circuit. The Kelvin probe system is allowed to stabilise and establish a null (~ 1 minute).

(v) Adsorption experiments are performed using the computer and datalogger to record the d.c. output of the autonull circuit as a function of time while gas dosing is in progress.

Both methods were tested during the Kelvin probe optimisation process. The standard method method was adopted for use as it reliably provided a stable, low noise probe signal. Little interference from pick - up signals was detected after probe shielding had been optimised. Pick up signals which are constant with time will not affect measurements of changes in work function. The RPU method reduced the detection of spurious signals but also significantly attenuated the Kelvin signal in most circumstances. The phase relationship between the pick - up signal and the true signal was found to vary between experiments.

6.5.3 Kelvin Probe Performance Tests

A series of tests was undertaken to assess the performance of the Kelvin probe and to determine the most stable, low noise operating configuration. Many parameters associated with probe operation were adjusted to improve performance including, for example, the particular resonant frequency used to produce oscillation. The probe was found to have a number of resonant frequencies in the range of 100 - 300Hz. The settings of the LIA were also adjusted to maximise noise filtering while retaining signal quality. Kelvin probe resolution was determined be to $< 500\mu V$ for 10 second signal averages, under ideal conditions. Resolutions of $< 300\mu V$ were achievable using 60 second time averages. This level of performance was not deemed to be necessary for the current experiments. Figure 6.10 shows the noise levels on the output signal.

The output signal from the Kelvin probe was frequency analysed in the range of 0 to 500Hz (using an HP Dynamic Signal Analyser). Figure 6.11 shows the power spectrum of the probe output and the amplitudes of the various frequency components. The peaks marked with an arrow and "V"s represent the fundamental frequency of probe oscillation and its harmonics respectively. The peaks marked with "DF" correspond to the probe driving frequency ($\approx$ 68Hz).

Figure 6.11(a) shows the relative amplitudes of the harmonic components and noise components of the output signal. The probe power output at the fundamental frequency at resonance is three orders on magnitude greater than the next largest component. High signal - to - noise ratios, therefore, are achievable if the fundamental frequency is used. The coil/soft iron slug combination used to drive the probe at twice the input oscillator frequency significantly reduces the driving frequency component (68Hz) of the output signal. The noise component of the fully

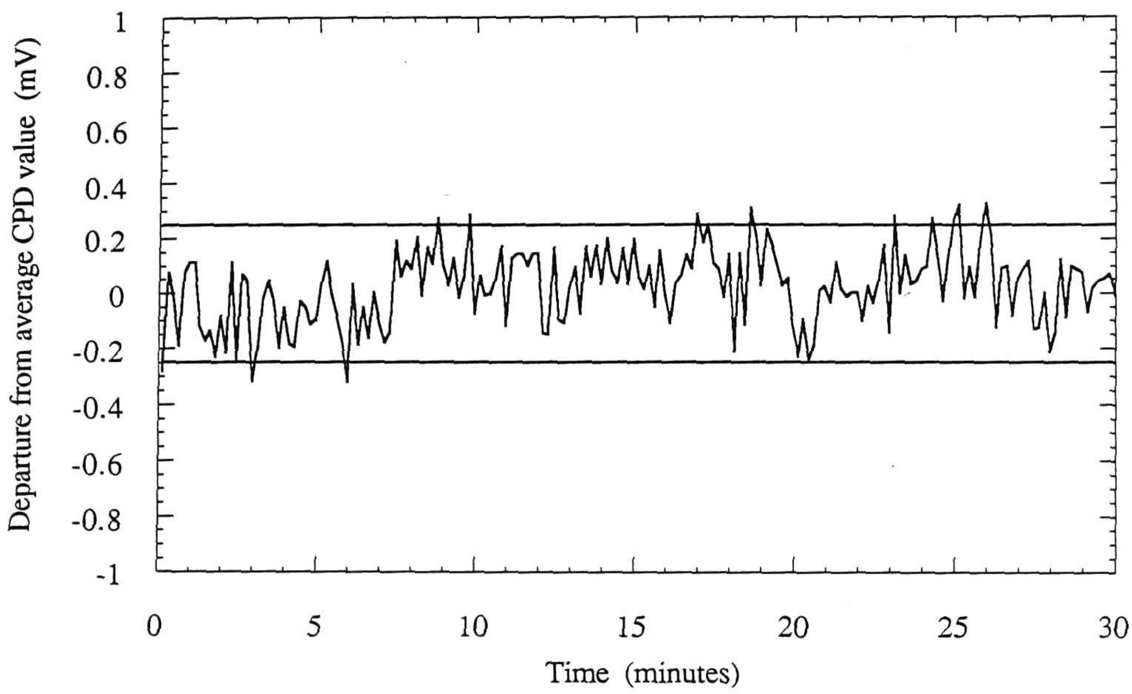

Figure 6.10 Output from the Kelvin probe system operating under best experimental conditions. The horizontal lines on the plot are separated by 500µV. Noise levels are less than 500µV with some signal drift about the mean value. The nulling voltage is sampled approximately 4 times per second by the datalogger and averaged over 10 second time intervals.

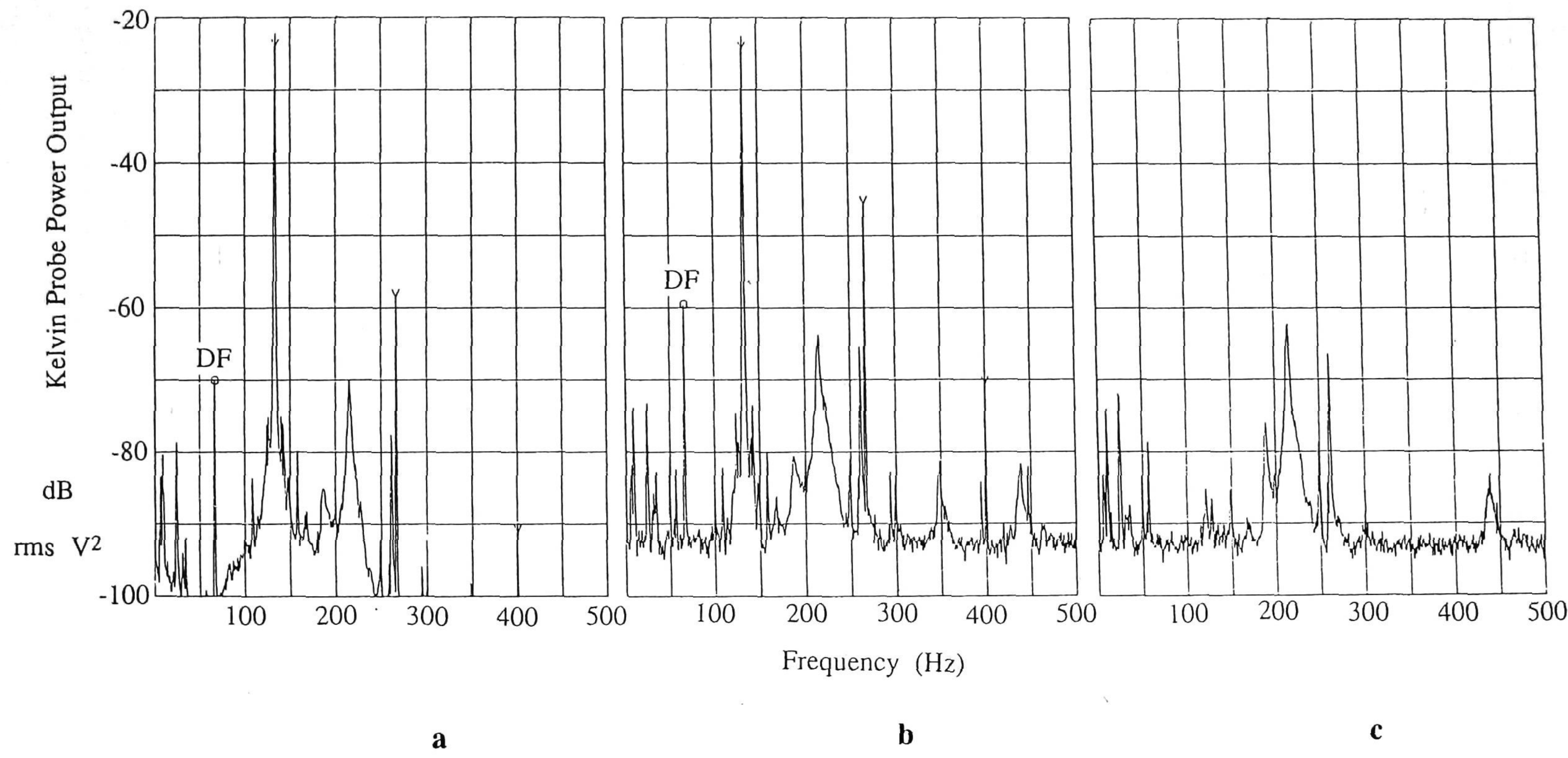

Figure 6.11 Kelvin probe power output: (a) filtered lock-in amplifier output; (b) unfiltered lock-in amplifier output; and (c) unfiltered lock-in amplifier output, no driving frequency applied to the probe. The driving frequency is indicated in (a) and (b) by "DF".

filtered probe output is not broadband but restricted to definite frequency ranges. Figure 6.11(b) shows the unfiltered LIA output. A comparison with figure 6.11(a) gives a measure of the effectiveness of the LIA tracking filter in reducing the level and range of noise components of the probe output.

Figure 6.11(c) shows the unfiltered output from the LIA when no driving frequency is applied to the Kelvin probe. Most of the unwanted signal components are independent of probe oscillation. The 50Hz mains pick up and its harmonics are eliminated by the line filter of the LIA in normal operation. The other pick up signals originate from vibrational or electromagnetic noise from equipment in the laboratory and the signal detection circuitry. The amplitudes of all unwanted signals are more than four orders of magnitude less that of the fundamental frequency.

A number of calibration tests of Kelvin probe performance have been reported [22,23,25,29] which test the linearity of the Kelvin probe response and the effect of probe - sample separation on probe output and nulling voltage. A selection of these tests were performed to assess the performance of the Kelvin probe system constructed for these experiments.

Figure 6.12 shows the relative probe output as a function of the voltage applied to the sample for a range of probe - sample separations. The relative probe output is defined as the output voltage of the LIA and is proportional to the output voltage of the probe. The probe output is linear over the range of voltages used in this test for each of the probe - sample separations. Harris and Fiasson [25] carried out a similar calibration for a guarded Kelvin electrode and also found a linear relationship between the applied voltage and the probe output voltage. Significantly, all the calibration curves intersect at one particular point. The value of the applied voltage at this point represents the CPD between the surfaces. The probe - sample separations quoted neglect probe vibration. The vibrational amplitude of the probe was estimated to be about 0.1mm, increasing the actual separation by 0.05mm.

Figure 6.13(a) shows a log - log plot of the relative probe output as a function of probe - sample separation. As before, the plot does not take account of the vibrational amplitude of the probe. Lines with slopes of -1.5 and -2 are also shown. Equation 6.6 requires that the probe output should fall off as the inverse square of the probe - sample separation. For separations in the range of 0.1 to 0.8mm, the change in probe output with separation is best approximated by a slope of -1.5. For separations approaching 1mm, a line of slope -2 can be fitted. It has been suggested

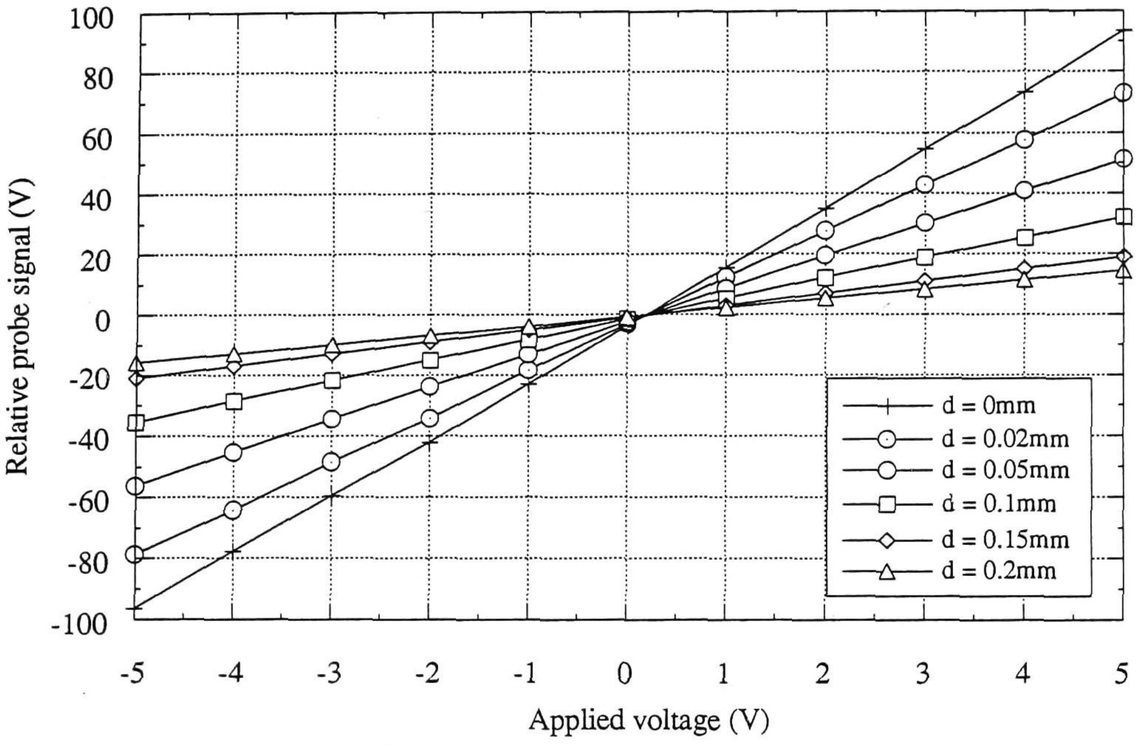

Figure 6.12 Output response of the Kelvin probe for a range of voltages applied to the sample and a range of probe - sample separations. The probe response is linear beyond the range of measurement. The probe - sample separations quoted neglect probe vibration. This adds approximately 0.05mm to each of the quoted separations. For small closest separations (d $\leq$ 0.02mm) a non - linear output response is expected because the probe vibration (~0.1mm) is too large to be considered a perturbation of the probe - sample separation. Non - linearities are not observed because the narrow band filter incorporated in the LIA eliminates any higher order effects.

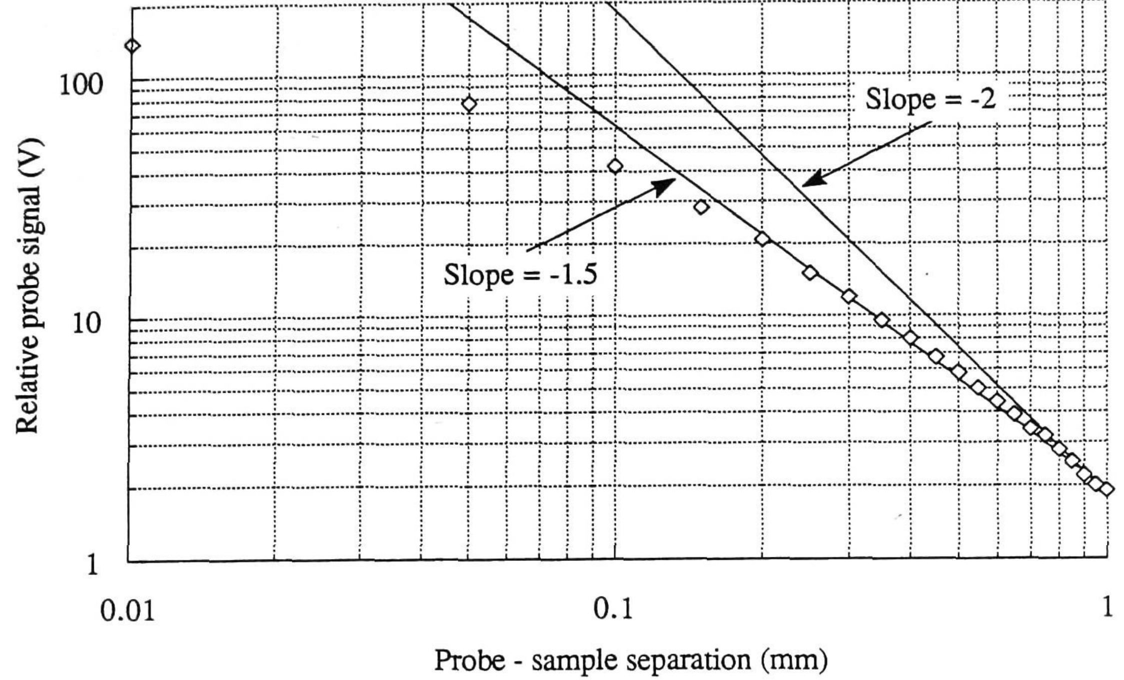

Figure 6.13(a)

Log - log plot of relative probe output as a function of probe - sample separation.

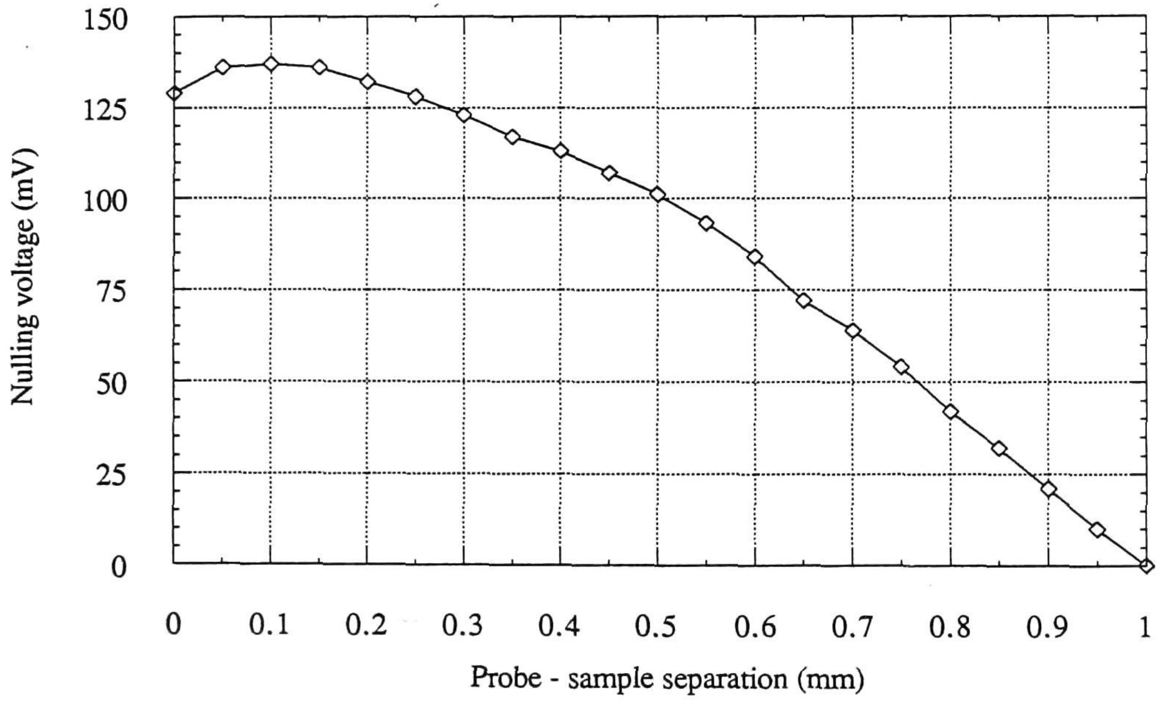

Figure 6.13(b)

Plot of nulling voltage applied to sample as a function of probe - sample separation.

that the behaviour of the probe output is influenced at smaller separations by the probe vibration. In particular, linear variation in the change in capacitance caused by probe vibration is only possible if the probe - sample separation is sufficiently large that it can be considered constant [25].

Figure 6.13(b) shows the change in nulling voltage as the probe sample separation is increased. The nulling voltage required to maintain a null state is reduced as the probe - sample separation is increased to 1mm. The Kelvin method is a null technique and, in principle, the nulling voltage should be independent of probe - sample separation. In practice, the voltage required to maintain a null changes, and is less well determined as the separation increases. The autonull circuit follows the lower edge of the range of values so the nulling voltage appears to be reduced [25]. The experiments discussed in section 6.7 were undertaken using the minimum possible separation at which a stable signal could be obtained from the Kelvin probe. Separations found to be suitable for these experiments were estimated to be in the range of 0.05mm to 0.1mm.

6.6 Experimental Method

The Kelvin probe system described in section 6.4 was used to investigate the gas adsorption behaviour of amorphous hydrogenated carbon (a-C:H) films. The layout of the experimental apparatus is shown schematically in Chapter 5, figure 5.2. The base pressure of the chamber was 5×10^{-10} torr.

The Kelvin probe was operated at frequencies of 130 - 150Hz and 220 - 240Hz. These ranges correspond to two of the resonant frequencies of the probe. The precise position of the resonance can be altered slightly be varying the stiffness of the pivotting feedthrough. Best results were obtained using a frequency of about 136Hz. Driving frequencies were half these values because of the frequency doubling effect of the soft iron drive. The vibrational amplitude of the probe for the adsorption experiments was estimated to be about 0.1mm, with a mean probe - sample separation of 0.05 - 0.1mm.

Signal output from the Kelvin probe was detected with a low noise preamplifier circuit and LIA, in combination. An autonull circuit was used to automatically adjust the NV applied to the sample to maintain the null state. The NV was recorded as a function of time and sample temperature using a computer controlled datalogger. The experimental error associated with the work function results incorporated uncertainties from electronic circuitry (~5%) and signal noise detected by the Kelvin probe. The resolution of the CPD measurements ranged from 0.5 - 10mV, depending on probe set up and success with signal optimisation. This is equivalent to about 1 - 10% of the total change in CPD in any of the experiments reported. Combined experimental error is estimated to be less than 20%.

The a-C:H films were sputter deposited onto polished, high purity copper substrates (Goodfellow, 99.99%) in a cylindrical magnetron sputter coater, as described in Chapter 2. Films with a range of thicknesses were used to investigate the thickness dependence of gas adsorption. Several series of gas adsorption experiments were carried out. Adsorptives were introduced into the chamber using a leak valve. Films were dosed whilst being monitored with the Kelvin probe. An exposure at a pressure of 1×10^{-6} torr for 1 second is defined as 1 Langmuir (L). Liquid adsorbates were freeze degassed before being admitted to the main chamber [30]. Adsorptives used during the course of the experiments included benzene (99+%), water (double distilled), ultrahigh purity (99.999%) nitrogen and ultrahigh purity (99.99%) oxygen. A mixture of benzene and air was also used as a result of misadventure. The composition of this mixture was not accurately determined but estimated to be approximately equal parts of benzene and air.

Experiments are described in section 6.7.2 in which the benzene adsorptives have differing purity. The highest adsorptive purity was achieved using a quantity of molecular sieve (4A type, 1.6mm pellets, Linde, Union Carbide) to adsorb any water remaining in the benzene. The sieve material was baked at 450K for about 70 hours before use. In addition, the gas dosing line was baked to 450K for about 24 hours to remove any residual contamination from previous experiments.

6.7 Results and Discussion

6.7.1 Preliminary Adsorption Studies

A number of preliminary adsorption studies of a-C:H were undertaken to establish the broad parameters of adsorption behaviour. Benzene and a mixture of benzene and air were adsorbed onto a baked film (670K, 60 minutes). The as deposited film was measured to be 190nm thick before baking. A mixture of benzene and air was used as the result of an experimental misadventure rather than by design, as discussed in the previous chapter. The work function results have been included in this discussion as they demonstrate some remarkable adsorption behaviour and form the basis of a continuing study of the adsorption behaviour of a-C:H films.

Figure 6.14(a) shows rapid and immediate changes in the work function of an a-C:H film resulting from dosing with a mixture of benzene and air. Previous adsorption studies [1,30,31] indicate that benzene adsorption on an a-C:H film surface under ultrahigh vacuum conditions is thermodynamically unlikely. One can, therefore, conclude that one or more components of air, assumed to be primarily nitrogen, oxygen and water vapour, are readily adsorbed by the film surface. This behaviour is considered in detail in the next section.

Figure 6.14(b) shows the change in work function of a baked a-C:H film (670K, 60 minutes) in response to the adsorption of benzene and a mixture of benzene and air. Dosing the film with benzene does not produce any change in work function which is consistent with previous studies [30,31].This behaviour suggests that no benzene is adsorbed at or near the film surface.

For exposures of less than $5x10^4$L, the adsorption of benzene and air appears to be irreversible. Partial reversibility in adsorption has been observed for exposures of $2x10^5$L (see figure 6.15). This adsorption is similar to that observed for higher exposures of similar films. This behaviour represents the lower limit of the behaviour measurable in volumetric [30] and QCM studies [31]. Some hysteresis (irreversible adsorption) has been observed in volumetric studies at low pressures for both baked films (670K, 60 minutes) and films preadsorbed with air [30].

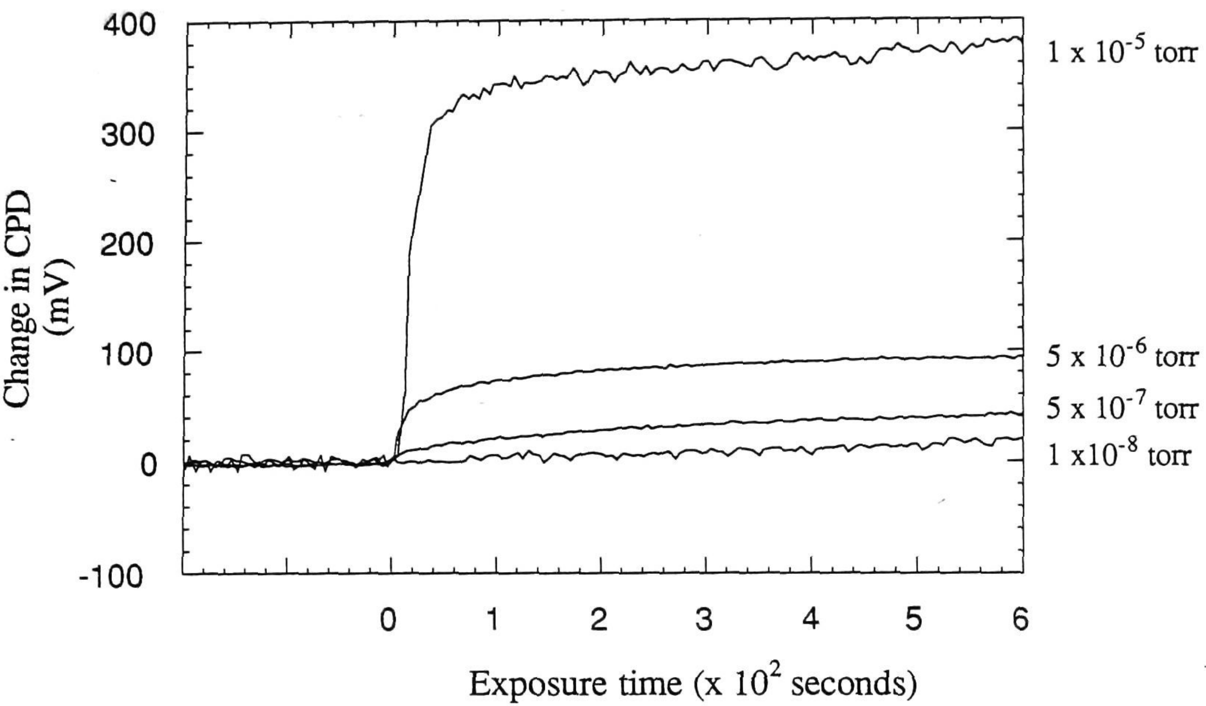

Figure 6.14(a) Changes in CPD in response to different exposures of a mixture of benzene and air. Dose pressure is indicated at the right edge of each plot.

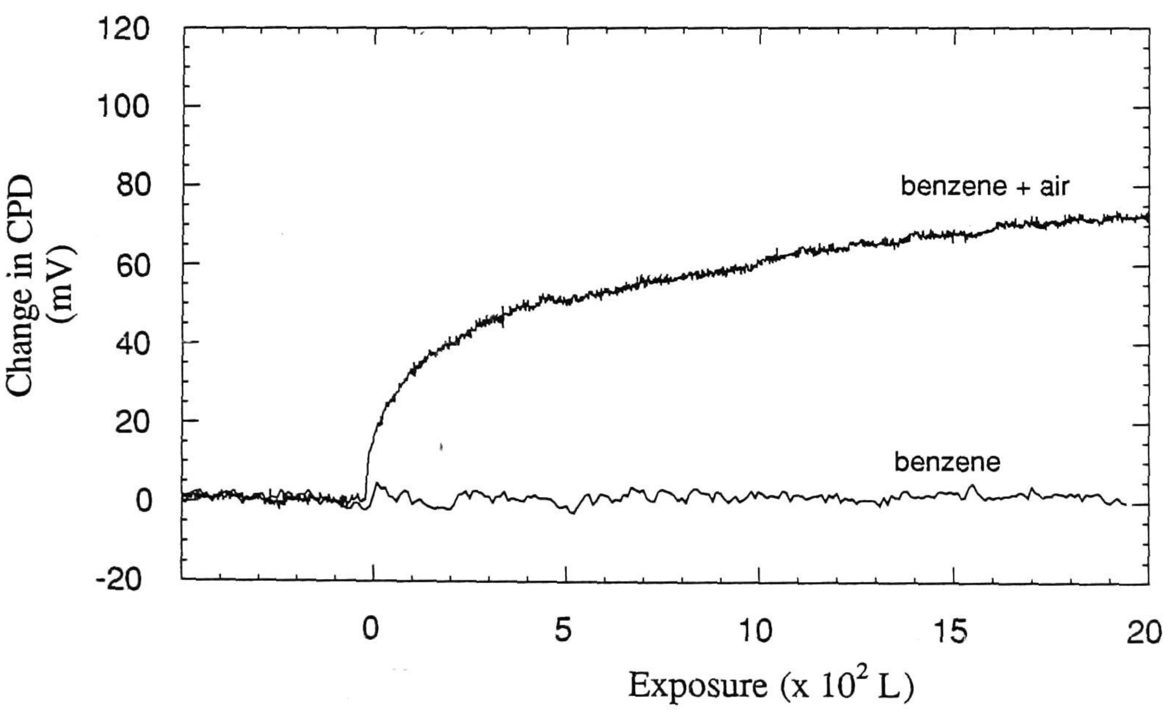

Figure 6.14(b) Comparison of the effect on CPD of identical exposures of benzene and a mixture of benzene and air.

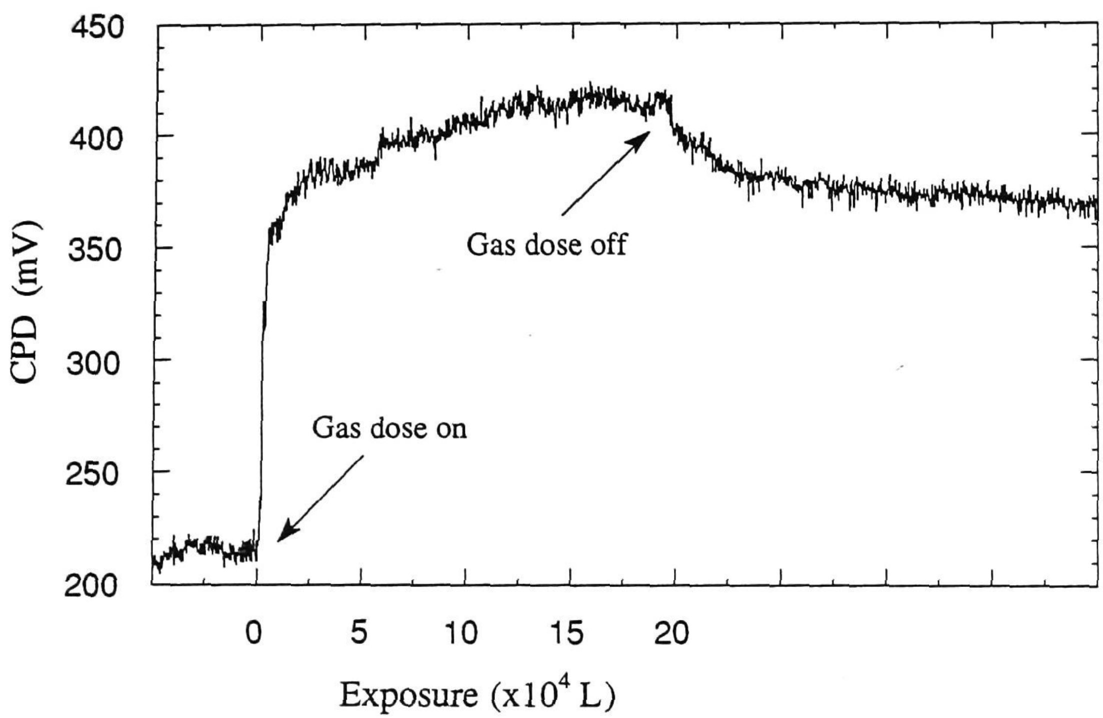

Figure 6.15 Changes in the CPD in response to the adsorption of a mixture of benzene and air were found to be partially reversible for exposures of 2 x 10^5 L. No reversibility in adsorption behaviour was observed for exposures less than 5 x 10^4 L. This behaviour is consistent with the adsorption hysteresis observed in higher pressure regimes.

Work function changes of around 10 - 20mV were observed in all experiments over the last few degrees of sample cooling following baking of the sample. This behaviour is consistent with the adsorption of residual gases in the vacuum system by the degassed sample. Identical behaviour has been observed in QCM studies of this film at pressures around 10^{-8} torr [32]. Surface production and ETC handling pressures are of the order of 10^{-7} torr and the pressure in the vacuum space of the ETC is of the order of 10^{-4} torr. It is assumed therefore that adsorption of residual gases in evacuated tubular collectors is unavoidable.

The effect of adsorbed molecules on the further adsorption characteristics of the film is important and warrants consideration as part of the overall adsorption mechanism. In previous studies, tenacious adsorption of air has been observed for baked films (770K, 60 minutes), requiring extended baking for full removal [30]. The adsorption of air affects benzene adsorption causing pore blocking and a decrease in pore connectivity. This has implications for higher pressure adsorption studies [30,31] as adsorption is found to be proportional to film thickness suggesting that pore accessibility and connectivity are not greatly affected by film thickness.

6.7.2 Work Function Response of a-C:H Films to Different Adsorptives

A series of adsorption experiments was undertaken to identify the species participating in the adsorption processes discussed in the previous section. The adsorptives used for these experiments were nitrogen, oxygen, water and benzene.

Figure 6.16 shows increases in CPD in response to exposure to ultrahigh purity nitrogen (99.999%). The changes in CPD are qualitatively similar to the behaviour observed for the adsorption of a mixture of benzene and air. The rate of change, however, is significantly smaller in this case. The inference that can be drawn from these data is that nitrogen adsorption may be a component of the overall adsorption process. The difference in the rates of change of CPD between the two experiments indicates that other species are also contributing to the benzene and air adsorption process. Increases in CPD were observed throughout the course of the adsorption experiments. This surface adsorption behaviour is consistent with nitrogen adsorption results obtained using the QCM technique. Coverages of around 0.3 - 0.5 monolayers have been observed for nitrogen partial pressures over the a-C:H adsorbing surface approaching 1 atm [32].

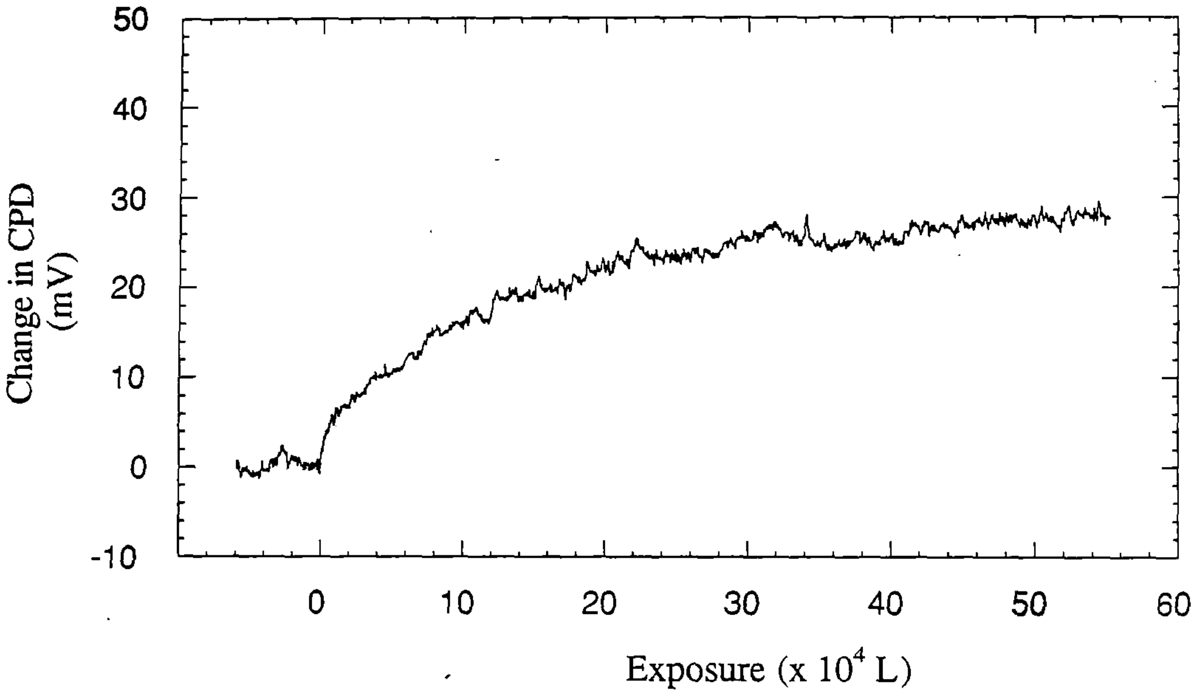

Figure 6.16 Changes in CPD in response to the adsorption of ultrahigh purity nitrogen on an a-C:H film surface. Kelvin probe resolution at the time of this experiment had been optimised to about 1 - 2mV. Subsequent adjustments to the apparatus improved the resolution by a factor of two.

Figure 6.17(a) shows increases in CPD in response to different exposures of ultrahigh purity oxygen (99.99%). The changes in CPD are also qualitatively similar to those observed for the adsorption of a mixture of benzene and air. The rate of change of CPD for oxygen adsorption is considerably greater than that for nitrogen. Figure 6.17(b) shows the changes in CPD in response to identical exposures of oxygen, nitrogen and the benzene and air mixture. Oxygen is clearly the greatest contributor to the changes in CPD observed for the benzene and air adsorption process discussed above.

The strong adsorption behaviour observed is caused by the interaction of oxygen with the a-C:H film surface. Adsorption temperature dependence was assessed by exposing an a-C:H film to equal amounts of oxygen at different temperatures. Figures 6.18 shows changes in CPD in response to the adsorption at temperatures of approximately 314K and 338K. The dose pressure in both cases was equal to 5×10^{-6} torr. Behaviour in each case is virtually identical which infers that in this temperature range the adsorption process is temperature independent.

It is proposed that the oxygen adsorption observed is connected with the formation of carbon monoxide on carbon surfaces at elevated temperatures. One of the principal film degassing processes observed during post - deposition baking and annealing of these spectrally selective films involves the removal of carbonaceous material from surface pores in the form of carbon monoxide (CO) [33-35]. The degassing behaviour of as - prepared films (as shown in figure 5.1(b)) indicates that CO is evolved from the film from temperatures of 500K, with a peak at about 770K. Films baked to 770K do not evolve significant amounts of CO during subsequent heating below this temperature. Further, the temperature required for the formation of CO from the reaction of gaseous oxygen with carbidic and graphitic monolayers on metal substrates is reported to be of the order of 500K [36,37].

It is plausible, therefore, that the oxygen molecules are strongly physisorbed or chemisorbed to the a-C:H surface in a precursor state to the formation of CO at sufficiently high temperatures. The temperature required to form or release CO is significantly in excess of the substrate temperatures used for these experiments. Oxygen adsorption is thermodynamically favoured and remains unaffected by small increases in temperature.

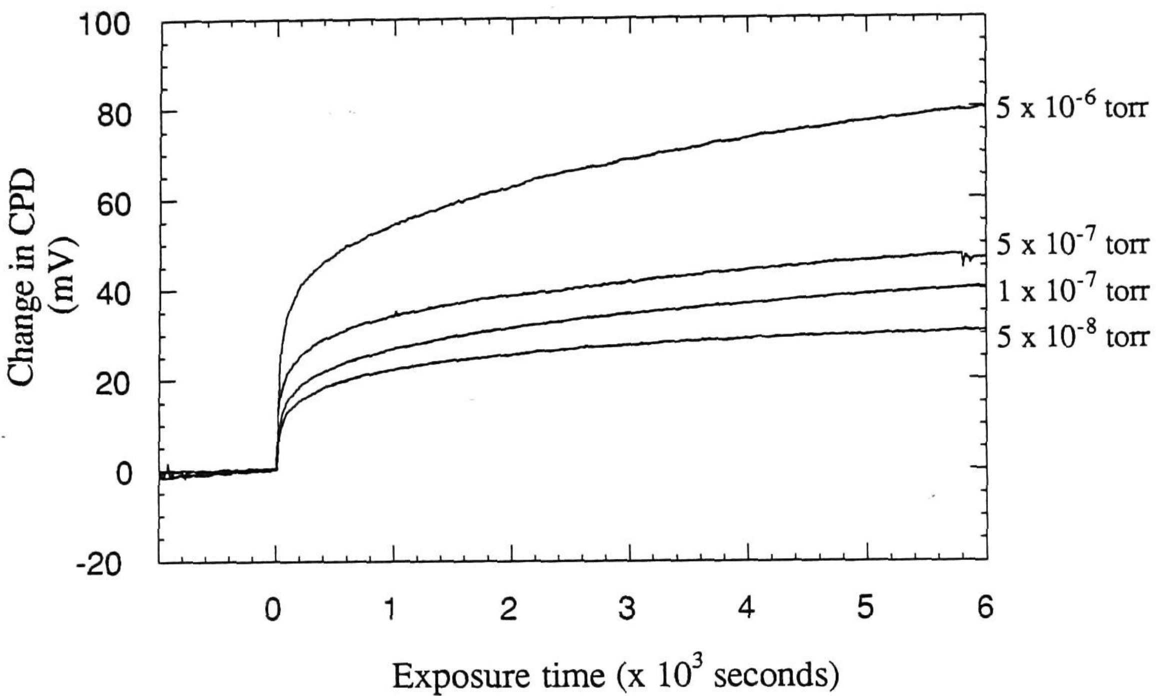

Figure 6.17(a) Changes in CPD in response to the adsorption of ultrahigh purity oxygen. (dose pressures indicated at the right hand edge of the figure)

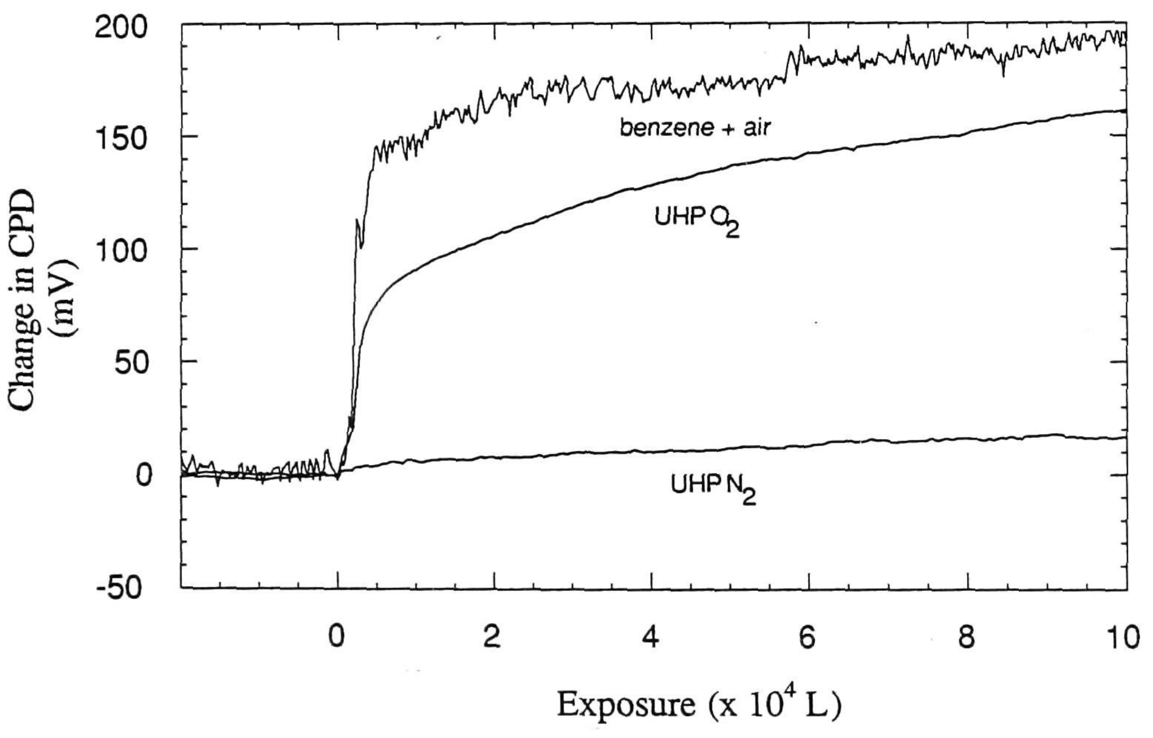

Figure 6.17(b) Changes in CPD in response to different adsorbates: a mixture of benzene and air; ultrahigh purity oxygen; and ultrahigh purity nitrogen. Noise levels on the benzene and air data arise from different Kelvin probe resolution.

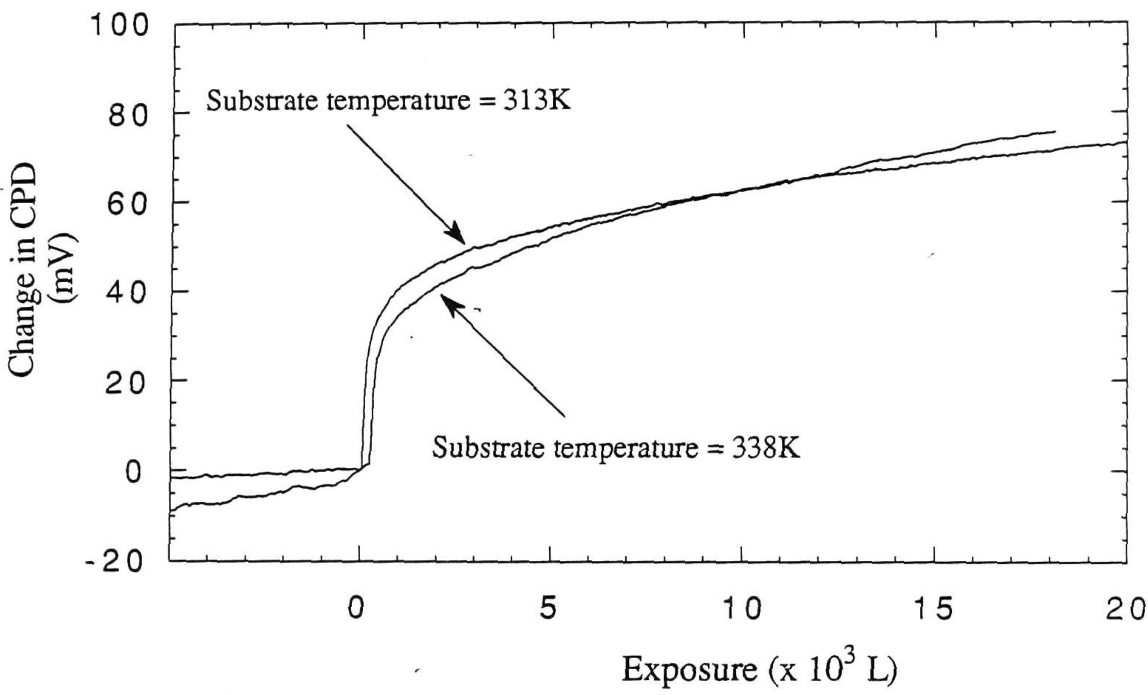

Figure 6.18 Changes in CPD in response to the adsorption of ultrahigh purity oxygen at different sample temperatures (313K and 338K). The CPD response is almost identical, indicating that the oxygen adsorption process is temperature independent at these temperatures. The experimental error associated with the work function results incorporated uncertainties from electronic circuitry (~5%) and signal noise detected by the Kelvin probe (1 - 10%). Combined experimental error is estimated to be less than 20%.

Figure 6.19 shows changes in CPD in response to exposure to water vapour (double distilled). The CPD falls rapidly in the initial stages of adsorption, then rises almost linearly with time, exceeding the starting value. This CPD behaviour strongly suggests two or more competing adsorption processes, some of which are apparently different in nature to those discussed above. It is proposed that the adsorption behaviour results from two discrete adsorption processes. The initial rapid fall in CPD is consistent with an adsorptive/Kelvin probe interaction. The subsequent steady increase in CPD corresponds to adsorption on the surface of the a-C:H film. This experiment extended over a period of 12 hours.

The Kelvin electrode face is coated with a 400Å layer of tin oxide. This material is commonly used to coat Kelvin probes to reduce or eliminate adsorption [4,9,17,21]. The oxide surface will not readily physisorb or chemisorb organic vapours or other gases such as nitrogen and oxygen. Polar molecules, such as water, can be physisorbed to such surfaces. The results suggest that all the surface adsorption sites are filled after an exposure of about 1×10^4 L.

The a-C:H film has a composite structure and is comparatively unreactive in the presence of water. Dangling bonds are passivated by hydrogen incorporation in the film formation process. Water molecules are physisorbed to the a-C:H surface. The rate of adsorption is approximately linear with time but is considerably less than that for the adsorptive/Kelvin probe interaction. The rate of change of CPD over the latter stages of this experiment was constant, indicating a considerable adsorption capacity for water vapour. Water vapour interacts in a physically and chemically different way with the a-C:H film which gives rise to the unusual adsorption behaviour observed.

Figure 6.20 shows the changes in CPD in response to adsorption of benzene. The results show adsorption behaviour which is strongly dependent on the purity of the benzene adsorptive. The CPD in all cases falls in a similar manner to the behaviour observed in response to the adsorption of water. The rate of fall in CPD is reduced if the partial pressure of water in the gaseous adsorptive is reduced. Figure 6.20(a) and (b) show adsorption behaviour and corresponding mass spectral data for benzene adsorptives of differing purity. The rate of fall in CPD is directly proportional to the magnitude of the partial pressure mass channel (18), corresponding to water. The inference is that the changes in CPD observed are primarily the result of the adsorption of water.

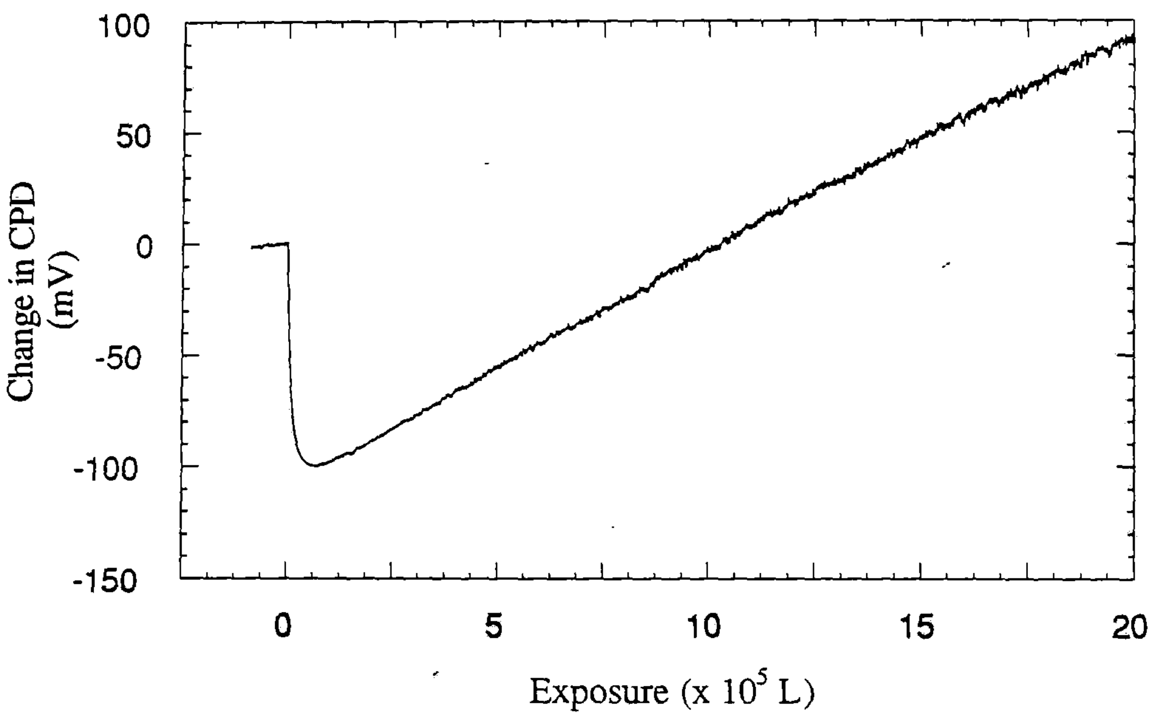

Figure 6.19 Changes in CPD in response to the adsorption of double distilled water. It is proposed that an adsorptive/Kelvin probe interaction causes the fall in CPD and that a competing a-C:H adsorption process causes the steady rise in CPD.

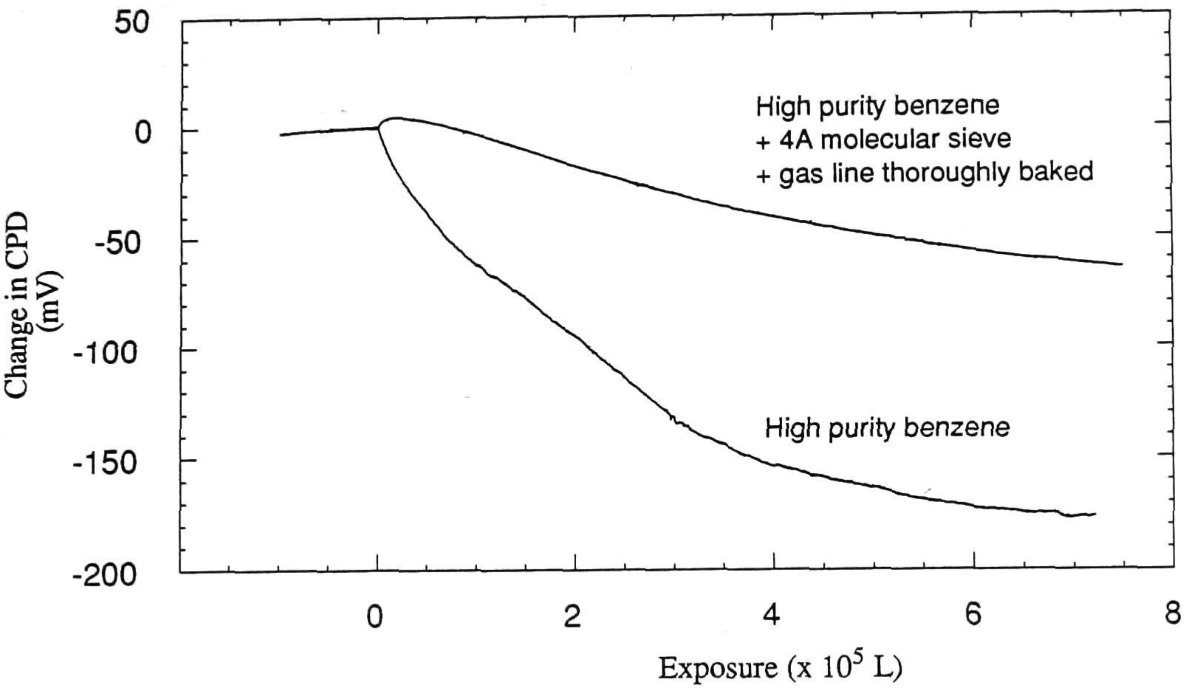

Figure 6.20(a) Changes in CPD in response to the adsorption of benzene. Results were strongly dependent on adsorptive purity. The rate of change of CPD decreased proportionally with the amount of water present in the adsorptive.

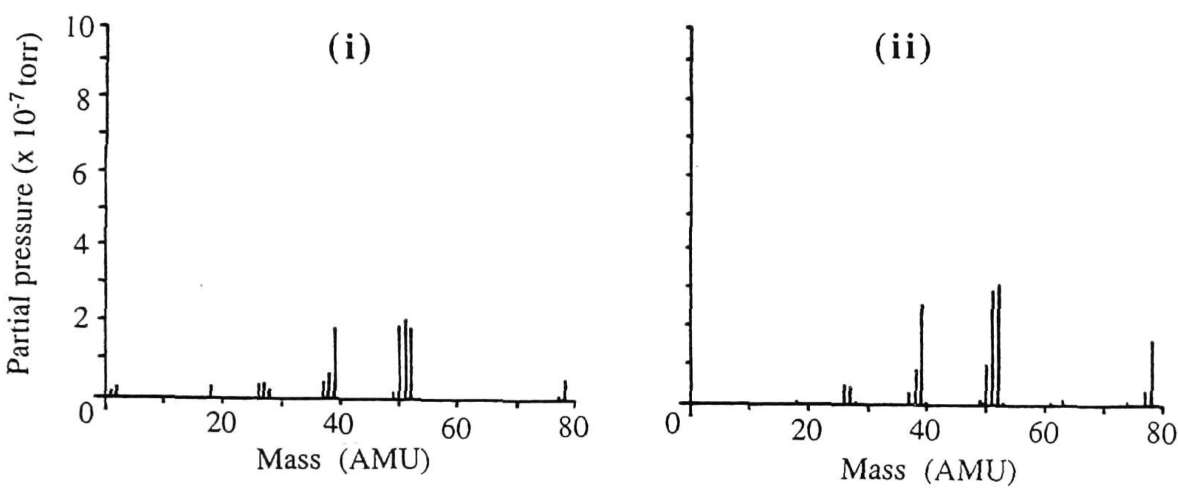

Figure 6.20(b) Mass spectra of the adsorptives used in the experiment described in figure 6.20(a) above: (i) corresponds to the lower curve and (ii) corresponds to the upper curve. Note the peak height of mass 18, (water), in each case.

Figure 6.20(b) shows behaviour resulting from adsorption of benzene with the lowest water impurity level which was attainable in the present apparatus. The initial rise in CPD is probably due to either the adsorption of benzene or the adsorption of residual oxygen and CO in the vacuum chamber. While the magnitude of this effect is insignificant in comparison with the major adsorption process, it does indicate a small amount of surface adsorption of benzene may be occurring in competition with the other processes.

This behaviour was not observed in the preliminary benzene adsorption experiments, described in section 6.7.1, for a number of reasons. Factors affecting the results include purity of the adsorbates and sample preparation. The most significant difference, however, between the experimental conditions is the resolution of the Kelvin probe. The preliminary experiments were undertaken when the Kelvin probe system routinely had a resolution of 5 - 10mV. A continuous process of optimisation of the Kelvin probe was maintained during the experiments. As a result, the resolution of the Kelvin probe for the later experiments was less than 500μV. The improved resolution reveals the underlying adsorption processes, previously obscured by noise.

The results of the adsorption experiments indicate that the magnitude of surface adsorption of benzene detected using the Kelvin probe is insignificant in comparison with the adsorption behaviour of other adsorbates. A probable cause of this behaviour is that the energy of adsorption for benzene is much greater in the film bulk in comparison with the film surface. Further, the surface area of the porous film bulk is much greater than the geometric area of the surface. Previous adsorption studies indicate that the geometric surface area of the film represents, at most, 1% of the total surface area [30].

The strong interaction of oxygen and water vapour with the a-C:H film surface has implications for the proposed gas adsorption/desorption switching mechanism. It has been shown in this work, in Chapter 5, and in other studies [30] that co - adsorption of benzene and other adsorbates significantly changes the adsorption behaviour of the a-C:H films. The surface interactions described here may well be representative of the inhibitory adsorption processes taking place on the surfaces of the pores in the film.

6.7.3 Comparison of Thermal Desorption and Work Function Results

Thermal desorption spectroscopy and work function studies provide sufficient information to discriminate between surface and bulk adsorption processes. TDS measures the amount of gas evolved from the film as a function of temperature and reveals the components of a desorption process which arise from binding sites with different energies. This amount gas evolved is proportional to adsorption capacity and surface area of the film. The geometric surface area of a baked a-C:H film has been shown to constitute as little as 1% of the total surface area [30,31]. The bulk of the gas evolved in a thermal desorption experiment originates from the internal surface area of the film. TDS is, therefore, relatively insensitive to surface adsorbed species. In contrast, work function measurements are highly surface sensitive. The conductivity and dielectric constant of the a-C:H films used in these experiments is such that they act to shield the molecules adsorbed in the pores from the Kelvin probe. The dipole moments (if any) of the adsorbate molecules deep in the pores have no effect on the electric field at the surface and consequently, no measurable effect on the CPD [21]. Changes in CPD originate exclusively from the effects of surface adsorbed species. Combining information from these two techniques provides an insight into the adsorption processes taking place on the porous films. Observed behaviour can be categorised as arising from global, surface or bulk adsorption processes.

Figure 6.21(a) shows the work function behaviour of a baked a-C:H film (670K, 60 minutes) during the adsorption of benzene. Figure 6.21(b) shows the thermal desorption spectrum resulting from a subsequent temperature ramp applied to the film. There is no evidence for adsorption of benzene on the film surface in the work function behaviour. The thermal desorption spectrum, however, shows a well defined two peak desorption process, as discussed in chapter 5. This indicates a relatively complex adsorption process taking place in the film bulk. It is proposed that the higher and lower energy peaks correspond to microporous and mesoporous adsorption respectively.

Figure 6.22(a) shows the work function behaviour of a baked a-C:H film (670K, 60 minutes) during the adsorption of a mixture of benzene and air. Figure 6.22(b) shows the thermal desorption spectrum resulting from a subsequent temperature ramp applied to the film. The work function behaviour indicates strong surface adsorption of one or more of the components (shown above to be oxygen and nitrogen) of the adsorptive mixture. The thermal desorption spectrum for

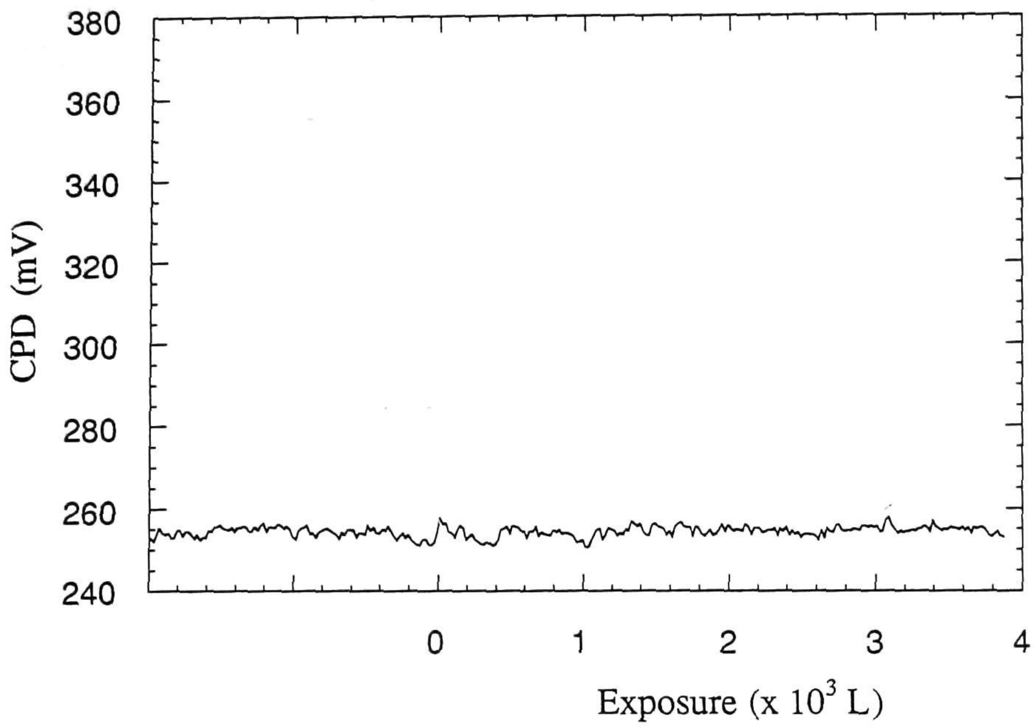

Figure 6.21(a) No changes are apparent in CPD in response to benzene adsorption. Note that optimal Kelvin probe sensitivity had not been achieved.

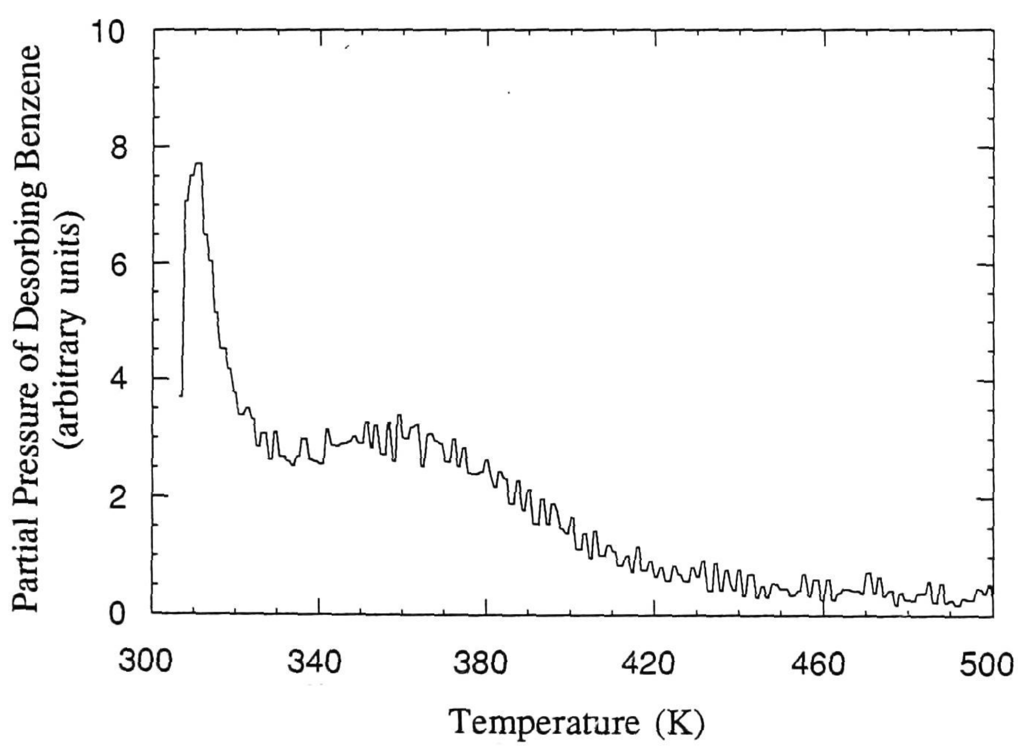

Figure 6.21(b) Thermal desorption spectrum resulting from sweeping sample temperature after the adsorption experiment shown in part (a) above.

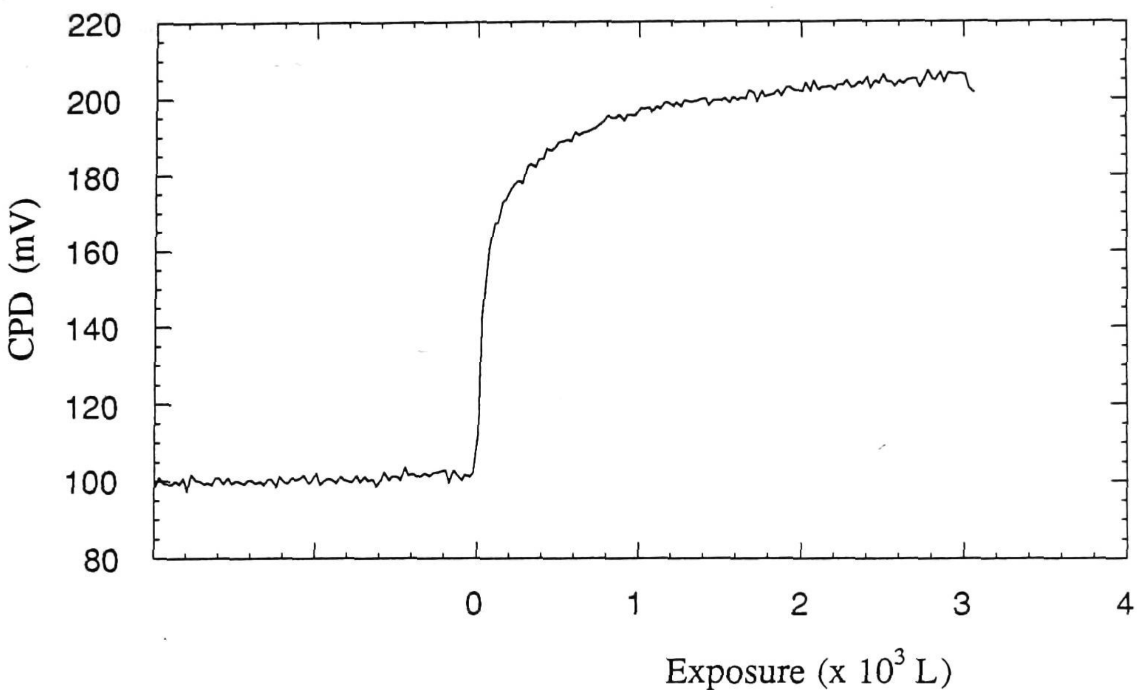

Figure 6.22(a)

Changes in CPD in response to the adsorption of a mixture of benzene and air.

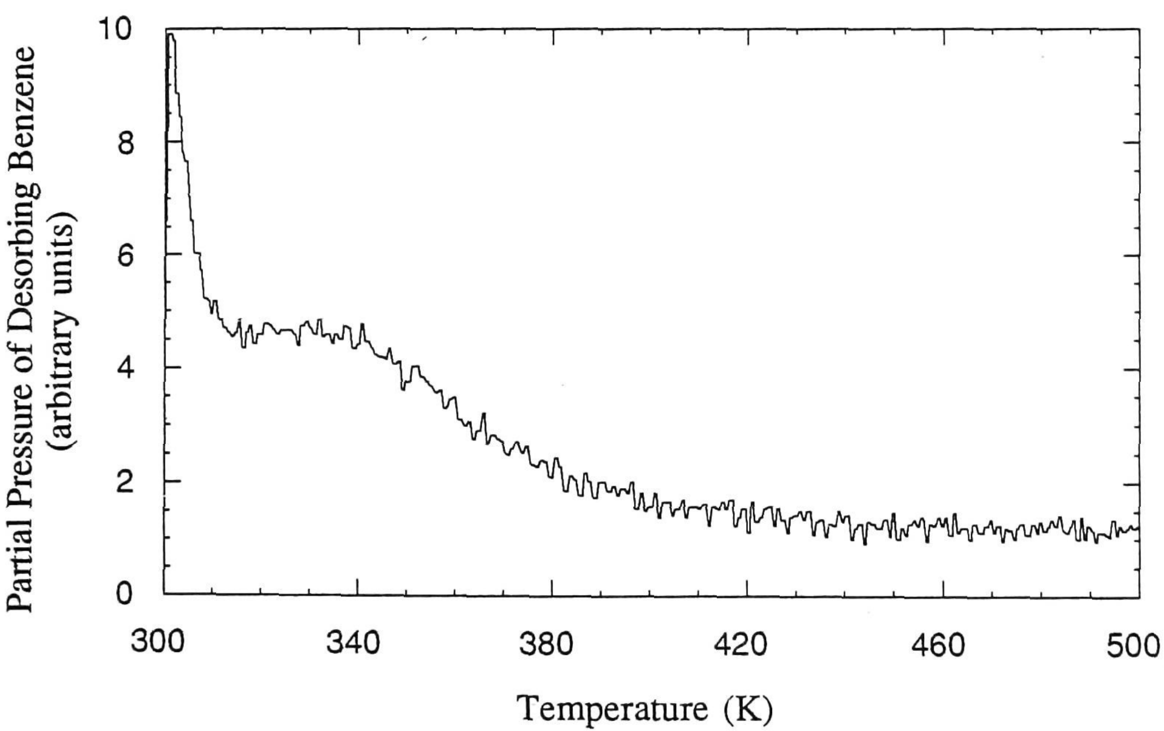

Figure 6.22(b) Thermal desorption spectrum resulting from sweeping sample temperature after the adsorption experiment shown in part (a) above.

benzene shows two coverage dependent peaks, centred at around 310K and 360K. These again are interpreted as arising from benzene adsorption at binding sites of different energies. The shift in centre temperature of the lower temperature peak of the two experiments arises in all probability from differences in experimental conditions.

One can deduce that benzene adsorption occurs in pores, internal to the film and is not observed from the film surface. Further, reduced effects observed with mixtures of benzene and air indicate that co - adsorption can inhibit the adsorption of benzene in the pores either by preferential adsorption or by pore blocking effects. Work function results indicate that oxygen and nitrogen are adsorbed on the film surface. Benzene, by comparison, shows no significant surface adsorption. It is proposed that the energy of adsorption for benzene on the surface is much less than that in the porous film bulk. Furthermore, it seems clear that oxygen and, to a lesser extent nitrogen, are much more strongly adsorbed on the a-C:H films than benzene.

The current understanding of the structure of this type of baked a-C:H film is that it is a microporous absorbent, characterised by a fractally rough surface forming a well connected pore network extending through the entire film thickness. Electron microscopy shows a columnar structure with a high degree of surface roughness [38] and small angle X - ray scattering (SAXS) reveals a considerable microvoid density within the film bulk with fractal characteristics [30]. The combination of thermal desorption and work function allow a range of discrete adsorption processes to be identified.

Changes in CPD are rapid and immediate which suggests surface adsorption. A time delay between the introduction of adsorbate and changes in work function would suggest that initial adsorption occurs exclusively within the porous bulk of the film. In all probability, adsorption is occurring at all surfaces, regardless of location, but at differing rates. Irreversible adsorption and measurable adsorption of residual gases from the vacuum chamber at ultrahigh vacuum has been observed throughout the experimental programme. This is consistent with the existence of very high energy adsorption sites on the a-C:H film surface and pore surfaces.

6.8 Summary

Changes in the work function of amorphous hydrogenated carbon (a-C:H) films in response to gas adsorption were investigated using the Kelvin method. Several versions of a guarded Kelvin electrode were constructed for use with different sized samples. A current sensitive preamplifier and automatic compensation circuit were designed and constructed for use with the Kelvin probe. The probe was electromagnetically driven using a coil and soft iron slug, in combination. The probe oscillated at twice the frequency applied to the coil providing significant noise reduction. The operation of the Kelvin probe system was optimised with adjustments of both mechanical and electronic components. The resolution of the instrument was determined to be $< 500\mu V$ using 10 second signal averages. This resolution was sufficient for the gas adsorption studies undertaken as changes in work function were of the order of tens to hundreds of mV.

While the Kelvin probe system in its final form performed satisfactorily for the purposes of these experiments, there are a number of avenues of improvement. Issues to be addressed include the following:

(i) the addition of a capacitance manometer pressure sensor to the ultrahigh vacuum chamber used for these experiments. This will increase the range of measurable pressures to 10^2 torr - 5×10^{-10} torr and allow direct comparisons to be made with quartz crystal microbalance experiments;

(ii) a better, although more complex alternative would be to combine the Kelvin probe, thermal desorption and quartz crystal microbalance techniques in a single vacuum chamber; and

(iii) the provision of controlled sample heating and cooling. Better control over heating rates and the ability to cool samples below ambient temperature will considerably extend the scope of the existing experimental techniques and will make analysis of results more straightforward.

The surface adsorption behaviour of the a-C:H films used in these experiments was characterised using work function measurements. It was found that exposure to nitrogen, oxygen and a mixture of benzene and air produced qualitatively similar increases in CPD. The rate of adsorption was limited by the adsorptive pressure over

the surface. The adsorption of water caused a complicated response in CPD changes. Work function measurements were characterised by an initial strong fall in CPD, then a steady rise in CPD, beyond the starting point. This behaviour was interpreted as arising from a chemisorption interaction with the Kelvin electrode and a competing physisorption interaction with the a-C:H film.

The adsorption of benzene caused a decrease in CPD. It was shown, however, that the quantity of water present in the benzene adsorptive was directly proportional to the downward rate of change of the CPD. This corresponds to bonding of the polar water molecules to the oxide face of the Kelvin electrode. The relatively small partial pressure of water ensures that the adsorptive/Kelvin probe interaction dominates over the time scale of the experiment. The competing physisorption process is taking place at a much slower rate and is not observed. Highest purity benzene caused an initial, small rise in CPD. This was followed by a downward movement, characteristic of an adsorptive/Kelvin probe interaction. The small rise in CPD observed may originate from the adsorption benzene or possibly residual gases in the vacuum system. In any case, the magnitude of the effect is insignificant in comparison with CPD changes caused by oxygen adsorption.

The main purpose of these experiments was to confirm that adsorption of benzene on these a-C:H films occurred primarily in the film bulk. The thermal desorption and work function results clearly show this to be the case. A comparison of work function and thermal desorption studies shows the complementary nature of the analytical techniques and the different depths of analysis. The Kelvin probe readily detects surface adsorbed gases but is unable to detect benzene located in the film pores. No compelling evidence for the surface adsorption of benzene was obtained. In contrast, a well defined benzene desorption process has been observed using thermal desorption spectroscopy. The two discrete peaks observed in the spectra have been attributed to desorption from mesoporous sites and a range of microporous sites. The intensity of the thermal desorption peaks was observed to be impaired by preadsorption and the co - adsorption of contaminant gases such as air.

References - Chapter 6

[1] S.J. O'Shea, B.A. Pailthorpe, R.E. Collins and D.N. Furlong, Langmuir, submitted October 1990.

[2] R.P.H. Gasser, "An introduction to chemisorption and catalysis by metals", Clarendon Press, Oxford 1985.

[3] J. Hölzl and F.K. Schulte, Solid Surface Physics - Vol. 85, "Workfunction of Metals", Springer - Verlag, 1979.

[4] D.P. Woodruff and T.A. Delchar, "Modern Techniques in Surface Science", Cambridge University Press, 1986.

[5] J.R. Smith, In ed. R. Gomer, Topics in Applied Physics - Vol. 4, "Interactions on Metal Surfaces", Springer - Verlag, 1975.

[6] P.P. Craig and V. Radeka, Rev. Sci. Instrum., 41, 258 (1970).

[7] M. Prutton, "Surface Physics", 2nd ed., Clarendon Press, Oxford 1983.

[8] G. Bachmann, W. Berthold and H. Oechsner, Thin Solid Films, 174, 149 (1989).

[9] T.A. Delchar, A. Eberhagen and F.C. Tompkins, J. Sci. Instrum., 40, 105 (1963).

[10] M.S. Wilson and S. Ichikawa, J. Phys. E: Sci. Instrum., 22, 886 (1989).

[11] Kelvin (Lord) Phil. Mag., 46, 82 (1898).

[12] W.A. Zisman, Rev. Sci. Instrum., 3, 367 (1932).

[13] K. Besocke and S. Berger, Rev. Sci. Instrum., 47, 840 (1976).

[14] R.E. Collins and O.R. French, Rev. Sci. Instrum., 51, 547 (1980).

[15] T.R. Foord, J. Sci. Instrum., 2, 411 (1969).

[16] H. Baumgärtner and H.D. Leiss, Rev. Sci. Instrum., 59, 802 (1988).

[17] H.A. Engelhardt, P. Feulner, H. Pfnür, and D. Menzel, J. Phys. E, 10, 1133 (1977).

[18] A. Noblet, H. Ridelaire and G. Sylin, J. Phys. E, 17, 234 (1984).

[19] M. Wolff, A.E. Guile and D.G. Bell, J. Phys. E, 2, 921 (1969).

[20] R. J. D'Arcy and N.A. Surplice, J. Phys. D, 3, 482 (1970).

[21] N.A. Surplice and R.J. D'Arcy, J. Phys. E, 3, 477 (1970).

[22] B. Ritty, F. Watchel, R Manquenouille, F. Ott and J.B. Donnet, J. Phys. E: Sci. Instrum., 15, 310 (1982).

[23] J.S.W. de Boer, H.J. Krusemeyer and H.J. Burhoven Jaspers, Rev. Sci. Instrum., 44, 1003 (1973).

[24] P.M. Gundry and F.C. Tompkins, In ed. R.B. Anderson, "Experimental Methods in Catalytic Research", Academic Press, 1968.

[25] L.B. Harris and J. Fiasson, J Phys E: Sci. Instrum, 17, 788 (1984).

[26] The insulated electrical feedthrough used was a cathode pedestal assembly (AWA, Code No. 98881).
The feedthrough was constructed by AWA Special Valves Section.

[27] Mechanical autonull system constructed by Martin O'Connor and Julian Magarey

[28] Electronic autonull circuit was designed and constructed by Dr. Phillip Lukins.

[29] E. Weissmann, Ch. Petrescu and D Tarina, J. Phys. E, 1, 426 (1968).

[30] S.J. O'Shea, PhD thesis, Department of Applied Physics, University of Sydney, 1989.

[31] Y. Yin, R.E. Collins and B.A. Pailthorpe, J. Appl. Phys., submitted December 1990.

[32] Y. Yin, Personal communication.

[33] G.L. Harding and B. Window, Sol. Energy Mater., 7, 101 (1982).

[34] S.P. Chow and G.L. Harding, Sol. Energy Mater., 11, 123 (1984).

[35] S.P. Chow, PhD thesis, Department of Applied Physics, University of Sydney, 1984.

[36] R. Sau and J.B. Hudson, Surface Sci.,102, 239 (1981).

[37] R. Sau and J.B. Hudson, Surface Sci.,95, 465 (1980).

[38] D.R. McKenzie, R.C. McPhedran, N. Savvides and L.C. Botten, Phil. Mag. B, 48, 341 (1983).

CHAPTER 7

Conclusions

The research discussed in this thesis is directed towards improving the understanding of the physical processes which determine the operation of temperature limited evacuated tubular collectors. It was previously established that the apparent area for adsorption was much greater than the geometric area, but the nature of the film morphology had not been elucidated. A principal motivation for the current study was to seek experimental evidence, through measurements of changes in work function, that the dominant adsorption mechanism, indeed, occurs in the body of the film rather than on the film surface.

This study has proceeded in parallel with two other investigations of gas adsorption; one using a volumetric technique and the other a quartz crystal microbalance. This study is part of a very broad basic and applied research programme with the goal of better understanding the physics of the thermal switch process in gas - loaded evacuated tubular collectors. In addition to surface potential measurements, the thermally stimulated desorption experiments were undertaken which aimed to obtain information on adsorption energetics from a different perspective and in a much lower pressure regime than had previously been studied. The film composition work sought to build on earlier research by S. Craig and G.L Harding and to seek more details about internal elemental distribution in the materials. The justification for this line of research was that the spatial relationship between the adsorbate and the constituents of the film, principally carbon and metals, could have an influence on the adsorption characteristics. As it turned out, much more was learned about the degradation modes in the film than about adsorption properties in this part of the study.

The main aspects of the gas adsorption behaviour of amorphous hydrogenated carbon films and their relationship to temperature limited ETCs are now understood. This information has been used to identify the key design parameters for a gas adsorption/desorption thermal switch in evacuated tubular collectors. A series of prototype switching collectors is currently under construction and testing. Collectors have been constructed which show non - linear heat loss characteristics. The

stagnation temperature of the test models has been reduced to around 370K. The abruptness of the thermal switching action can be altered by varying the adsorption capacity of the film or by employing different desorbable gases. Field testing of temperature limited ETCs will reveal how readily small scale experimental investigations of thermal switching behaviour can be applied to a commercial product. Similarly, an opportunity exists for comparing computer modelling of ETCs with experimental data gathered over extended periods of field testing.

Additional technological problems must be addressed after satisfactory designs for commercially produced temperature limited ETCs have been established. A major issue is establishing a satisfactory level of uniformity in ETC performance with the use of reproducible manufacturing techniques and good quality control. Adsorbate purity had already been identified as a crucial factor in this area [1] at the commencement of this study. This was further confirmed in this work. Changes in the structure of the spectrally selective film also have a significant impact on the lifetime of temperature limited ETCs.

Considerable evidence has been revealed by this study and quartz crystal microbalance experiments [2,3] for the existence of very high energy adsorption sites on the surface of the film and in the pores. Behaviour attributed to adsorption of residual gases in the vacuum chamber has been observed at pressures below 1×10^{-9} torr. A reliable thermal switch mechanism requires the use of high purity adsorbates to minimise changes in adsorption capacity with time. Since the pressure regime in which the thermal switch operates is of the order of 10^{-1} - 10^{-4} torr these effects will not directly influence the practical performance of the adsorption/desorption system. It has been observed [3] that film adsorption capacity is reduced by this (irreversible) adsorption of contaminant gases.

As stated, the purpose of this study was to investigate aspects of film behaviour associated with the operation of the thermal switch mechanism. The findings of the study encompass a range of scientific as well as practical aspects of the mechanism. Gas adsorption studies have consistently shown that the spectrally selective films and amorphous hydrogenated carbon (a-C:H) films have a microporous structure which adsorbs gases via a physisorption process [1]. The thermal desorption studies reported in Chapter 5 show benzene adsorption which is consistent with the prior work. Two binding states can be identified, the ratio of the intensities of which is dependent on exposure. There is not, as yet, any evidence

linking these observations to specific aspects of the adsorption behaviour observed using the quartz crystal microbalance.

Changes in the contact potential difference (CPD) between a-C:H films and a Kelvin probe provided a means of investigating changes in the surface state of the films in response to gas adsorption. The Kelvin probe senses changes in work function and is highly surface sensitive. In this way the effects of surface and bulk adsorption can be studied independently. The work function studies produced some unexpected results. Little evidence was obtained for adsorption of benzene on the outer surface which was consistent with the current understanding of the benzene/a-C:H adsorption system. Large changes, however, were observed in response to the adsorption of oxygen, air and, to a lesser extent, nitrogen. Quartz crystal microbalance studies [3] also show strong oxygen physisorption or chemisorption on a-C:H films.

The Kelvin (reference) electrode used in this study was coated with a layer of tin oxide to minimise adsorption. The adsorption of water produced significant changes in CPD which may indicate an adsorbate/probe interaction. It is proposed that the polar water molecules are adsorbed on the oxide surface of the probe as part of a complex adsorption process. There is no evidence that the oxide surface adsorbs benzene, oxygen or nitrogen.

It is proposed that the changes in work function observed in response to gas adsorption are associated with physisorption at very high energy surface sites. Oxygen induces the largest changes in work function, possibly in the formation of a precursor state in the production of oxidised carbon species. The latter is one of the largest gaseous outgassing products observed in the film annealing process. At ambient temperatures insufficient energy is available to overcome the activation energy for this process.

Several degradation mechanisms were investigated in this study including progressive thinning of the carbon surface layers of spectrally selective films deposited on certain metal substrates and the removal of contaminants introduced during deposition, such as argon and nitrogen, by post - deposition annealing. If the pore structure of the film changes over time in response to thermal cycling or other influences then significant changes in gas adsorption behaviour can be expected. Some specific aspects of the composition and structural behaviour of spectrally selective films obtained is this study are set out below.

(i) Major elemental surface constituents of the spectrally selective film are carbon and oxygen. Nitrogen and argon, implanted during the deposition process, are also observed. Films aged in air for several months also have copper present at the film surface in some instances.

(ii) Thermal annealing of spectrally selective films (670K, 60 minutes) produces a range of significant changes in film structure. The intensity of oxygen photoelectron emission is reduced implying a reduction in the oxygen content in the film as a result of outgassing, in the form of CO and H_2O. The intensities of the copper, argon and nitrogen signals are also reduced.

(iii) The layer profile of films deposited on borosilicate glass substrates is virtually unaffected by the annealing process. The films deposited on metal substrates, in particular those containing oxygen, undergo major structural changes in response to baking. The carbon surface layer of the film is reduced in thickness and carbon in other layers is observed to diffuse into neighbouring stainless steel regions. Copper layers in the film structure apparently act as diffusion barriers.

There are a number of areas in which more research is required in the context of the thermal switch/gas adsorption project. Film deposition and characterisation needs to be more rigorously undertaken, particularly in the light of the surface analysis results discussed in Chapters 3 and 4. A conceptual link must be forged between the higher dose pressure quartz crystal oscillator studies [2,3] and volumetric adsorption studies [1] and the lower dose pressure surface studies described herein.

The thermal desorption and work function experiments were concentrated on the interaction of benzene with a particular type of a-C:H film and spectrally selective film. This course of action is specifically directed at characterising the thermal switch mechanism discussed in this thesis. There is considerable scope for extending the investigation to cover a variety of types of amorphous carbon and a variety of gases. The role of oxygen in determining film structure and the modes of film degradation is of particular interest. A generalised approach will greatly improve the understanding of amorphous carbon behaviour. The thermal desorption and work function techniques can both be improved with the implementation of pressure gauges which extend the accessible pressure range. This development may provide more favourable conditions for studying benzene adsorption using work function

techniques. In addition, there is no barrier to devising an experimental system which incorporates both QCM and work function techniques.

Another important area to be addressed when integrating experimental results from the range of techniques now available in the laboratory is the problem of standardising experimental conditions. Although superficially a straightforward problem, differences in experimental conditions caused by instrumental effects can significantly change adsorption behaviour. Two examples are standardisation of annealing conditions and recognition of the effect of prior experiments on a given sample.

In conclusion, the work presented in this thesis has significantly advanced the understanding of the gas adsorption behaviour of these a-C:H films. As part of a broader programme of research on evacuated tubular collectors this work has provided several unique and some complementary insights into the important physical mechanisms which determine the characteristics of the system.

References - Chapter 7

[1] S.J. O'Shea, PhD thesis, Department of Applied Physics, University of Sydney, 1989.

[2] Y. Yin, R.E. Collins and B.A. Pailthorpe, J. Appl. Phys., submitted December 1990.

[3] Y. Yin, Personal communication.

EMENDATIONS

Chapter 2, § 2.6.2, p22
It should be noted that Type I isotherms can also represent monolayer adsorption on non - porous surfaces.

Chapter 2, § 2.6.3, p26
Studies of the benzene/a-C:H system in this laboratory have been restricted to the use of volumetric and quartz crystal microbalance (QCM) techniques. Gravimetric measurements of gas adsorption can also be made using quartz spring systems and fine mechanical microbalances (a CAHN balance, for example).

Chapter 3, § 3.6.1, p45, figures 3.8 & 3.9
The X-ray photoelectron spectra shown in figures 3.8 and 3.9 were obtained consecutively from the same sample. Apparent differences in peak structure arise from scaling differences between the two figures.

Chapter 3, § 3.6.1, p46
Samples were analysed freshly prepared, thermally treated and stored in air for 4 months so that film stability could be tested under a variety of conditions. Film stability is a key requirement for commercially produced spectrally selective films to achieve a lifetime of 20 years.

Chapter 3, § 3.6.1, p47, figure 3.11
Secondary ion mass spectroscopy (SIMS) analyses of the surface of the spectrally selective film are included to complement accompanying X-ray photoelectron spectra. In particular, SIMS qualitatively identifies surface constituents, including trace contaminants which can not be detected using XPS. The data presented show a range of CH fragments arising from the a-C:H material, metal ions (Fe, Ni, Cr, Cu) originating from deeper film layers and trace contaminant ions (K, Ca, Mg, Cl etc).

Chapter 4, § 4.1, p55
The spectrally selective films studied in this work are composed of a graded stainless steel/a-C:H layer which has been optimised for maximum optical absorptance in the visible region of the spectrum and a copper layer which has a low thermal (infrared) emittance. The properties of these component parts of the film were developed to provide optimal optical properties; the gas adsorption properties of the system were not considered during development. While a textured/porous film has advantages for reducing reflection etc, any relationship to satisfactory gas adsorption behaviour is purely coincidental. It is this coincidence that has been exploited to incorporate a thermal gas switch in evacuated tubular collectors without the need for reoptimisation of the optical properties of the specrally selective film.

Chapter 5, § 5.7.1, p88, figure 5.7
The two coverage dependent peaks referred to are very intense, narrow peak centred at approximately 322 K and a broader peak with an assymetric shape centred at approximately 332 K.

Chapter 5, § 5.7.1, p90
The total error for the energy calculation was estimated to be ± 15 %. A more appropriate way of presenting the energy data would have been to include an error equivalent to ± 15 % in each of the values. The energy values quoted in Tables 5.1 and 5.2 represent the centre values in a ± 15 % band of values.

The reader should note that the relationship between the adsorption behaviour investigated in this study and behaviour previously observed and the nature of the underlying binding processes is discussed at a later point of the thesis (pp92 - 96).

Chapter 5, § 5.7.3, p93
The data of S. O'Shea is presented in figure 5.13 to summarise the experimental work and theoretical predictions of benzene adsorption behaviour on these a-C:H films. These studies are limited (as explained earlier in the thesis) by experimental constraints such as the ability to measure low pressures accurately andthe affect of co-adsorption of contaminants at adsorptive partial pressures approaching the base pressure of the experimental vessel and over long periods of time. It can be seen that these factors cause the experimental and theoretical values to diverge at low relative pressures. The experiments discussed in this thesis use techniques which remove some of these limitations. The pressure regime used corresponds to the left hand edge of the data shown in figure 5.13. The energy values deduced using Redhead analysis from thermal desorption data should therefore fall in the range of 85 - 95 kJ mol^{-1}, which is indeed the case.

Chapter 5, § 5.7.3, p94
Peak energies are shifted to higher values as film thickness is increased. All films were subjected to the same preparation conditions and post depostion treatments. It is acknowledged that there will be unavoidable minor differences introduced due to the nature of the preparation process. As film thickness is increased the mean energy required to eject adsorbed material is also increased. It is believed that peak energy shifts are caused principally by the time dependence of diffusion processes between deeply buried pores and the film surface. Previous studies suggest that the structure of these films is approaching the percolation threshold which would further increase the effect of film thickness.

Chapter 6, § 6.1.1, p101
The terms "surface" and "bulk" are used in the context of the textured, porous film used in this study. Changes in work function measured using the Kelvin probe reflect the behaviour of the outermost layers of the film, that is, those film and adsorbate atoms close enough to the gap between the Kelvin probe and the film to influence the electric field in that gap. The film "surface" is therefore composed of those atoms which influence changes in work function as measured by the Kelvin probe. The film "bulk" (or more correctly, the "subsurface") is composed of the remaining surfaces accessible to adsorptives.

Chapter 6, § 6.7.1, p124
The adsorption of benzene on a-C:H at ultrahigh vacuum (or even at dose pressures of ~ 10^{-6} torr) has been shown in previous studies to be very limited in comparison with higher pressure adsorption. In this study no changes in work function were observed in response to benzene adsorption which were not found to be directly related to the purity of the adsorptive (in particular the concentration of water in the benzene) The work function responses observed with the purest benzene prepared were very small in comparison to work functin responses observed for adsorptives such as oxygen, nitrogen and water. On the basis of previous experimental results and calculations and all results taken in this study it was concluded that benzene adsorption on the film surface accessible to the Kelvin probe was too small to be measured.

Chapter 6, § 6.7.2, p128
The energy of adsorptionof benzene in this microporous system is enhanced in the micropores for several reasons. Previous studies have shown that the total surface area of these a-C:H films is composed of 65% very narrow, slit - like micropores (width < 7Å) and approximately 20% wider micropores (7Å < width < 20Å) and approximately 15% mesopores and external surface, (see Chapter 2, p27). The dimensions of the very narrow, slit - like micropores are approaching the dimensions of the adsorbate. Energy of adsorption of a benzene molecule in a slit - like pore of similar dimensions is enhanced by as much as a factor of two by the influence of the closely spaced pore walls. In larger pores an adsorbate contact angle can be defined and capillary condensation effects come into effect. Vapour pressures are reduced as indicated by the Kelvin equation and as a result adsorption energies are increased.